ISSN 0377 - 9416

PMAI

Volume 27, 2001

TRANSACTIONS OF
POWDER METALLURGY ASSOCIATION OF INDIA

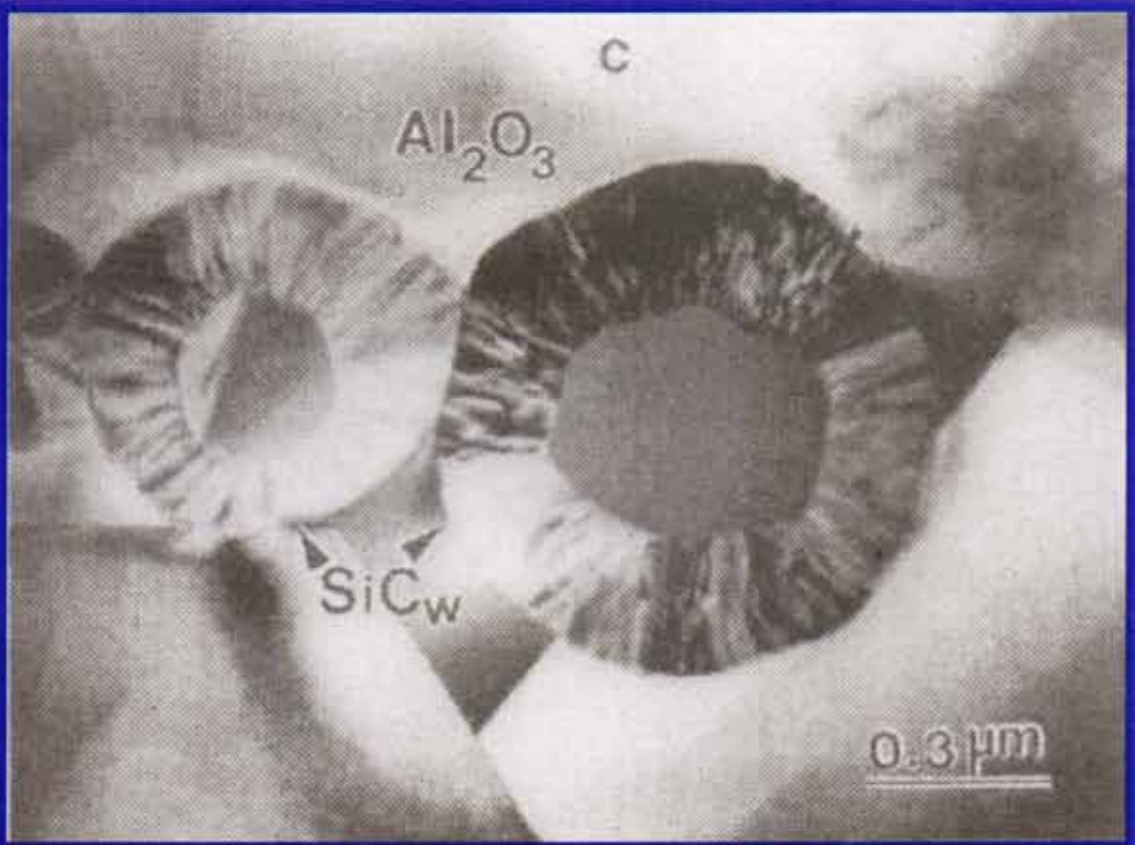

Guest Editors :
Prof. T. R. Rama Mohan
Prof. P. Ramakrishnan

Guest Editors :
Prof. T. R. Rama Mohan
Prof. P. Ramakrishnan

Volume 27
December 2001

Published by

PMAI

Powder Metallurgy Association of India
Department Of Metallurgical Engineering
and Material Science, I.I.T, Bombay,
Powai, Mumbai - 400 076

Neither the Powder Metallurgy Association of India nor the editor
assumes responsibility for opinions expressed by the authors of the papers.

Cover Photograph :
TEM showing matrix - reinforcement interface of composite

EDITORIAL

The Powder Metallurgy Association of India held the 27th National Powder Metallurgy Conference at Jaipur during February 21-23,2001 in conjunction with International Conference on Trends in Mechanical Alloying: Science, Technology & Applications. Although the proceedings of the International Conference "Trends in Mechanical Alloying " was published in 2002 the National Conference papers have not been published and hence this effort of bringing out the volume of Transaction. In addition of R. V. Tamhankar and P. R. Roy memorial lectures, several contributed research papers covering the preparation of powders, whiskers, in-situ composites, metallography of tungsten heavy alloys and nuclear fuel pellets, mechanical properties of powder injection molding mixes, thermal barrier coatings and sintered products were presented by several experts and research scholars. From these thirteen papers have been selected and included in this volume, covering various aspects of powder production, characterization and evaluation of sintered metallic, ceramic and composite materials. This publication will ensure the continuity of the Transactions of PMAI.

T. R. Ramamohan
P. Ramakrishnan

TRANSACTIONS OF **VOLUME 27**

POWDER METALLURGY **DECEMBER 2001**

ASSOCIATION OF INDIA

CONTENTS

POWDER PRODUCTION

1. HIGH –QUALITY SPONGE IRON POWDER FROM INDIAN BLUE DUST FOR P/M APPLICATIONS

TP Bagchi, Ravindra Malewar and Bijoy Sarma 1

2. PRODUCTION OF FINE METAL POWDERS BY LAMINAR GAS STREAMS

Gunther Schulz and K. Krishna Rao 34

3. ALUMINIUM FOAM THROUGH P/M ROUTE

Ravindra Malewar, TP Bagchi and Bijoy Sarma 43

4. PRODUCTION AND CHARACTERIZATION OF IN-SITU CERAMIC MATRIX COMPOSITE FROM INDIGENOUS ALMINO-SILICATES

K.L. Hansda, R.J. Singh, R.R. Dash , M.P. Singh 55

CHARACTERIZATION

5. STRUCTURE – PROPERTY BEHAVIOUR OF Al2O3 – SiC COMPOSITES FABRICATED BY POWDER PROCESSING ROUTE

A. Chakraborty, R. Mitra, S.V. Kamat and K.K. Ray 64

6. MICROSTRUCTURAL MODIFICATIONS OF UO2 FUEL PELLETS THROUGH SILICATE ADDITIVES

R.M. Altekar, U. Basak, V.D. Pandey, I.H. Sheikh, R. Ramachandran, and S. Majumdar. 92

7. OPTICAL METALLOGRAPHIC PRACTICE FOR TUNGSTEN HEAVY ALLOYS SYSTEMS

T.P. Bagchi, N. Arvind Kumar and Bijoy Sarma 102

8. EVALUATION OF INDIGENOUS RAW MATERIALS FOR PREPARATION OF IN-SITU CERAMIC MATRIX COMPOSITES

K.L. Hansda, R.J. Singh, R.R. Dash and M.P. Singh 137

9. EFFECT OF POTASSIUM AND NICKEL ON THE FORMATION OF TiC AND TiN WHISKERS THROUGH CARBOTHERMAL REDUCTION OF TiO2

R.V. Krishnarao, J. Subrahmanyam and V.V. Ramarao 151

10. PHASE EVOLUTION ON CARBOTHERMAL REDUCTION OF 1:2 MOLAR MIXTURE OF MoO3 AND SiO2

Tarasankar Mahata and Beant Prakash Sharma 175

EVALUATION OF SINTERED PRODUCTS

11. INFLUENCE OF DENSITY ON THE ROLLING CONTACT FATIGUE BEHAVIOUR OF SINTERED STEELS

N. Rajiv, N. Govindarajan, R. Gnanamoorthy, K. Gopinath, Y. Miyahsita,and Y. Mutoh 182

12. EFFECT OF ELASTIC PLASTIC DEFORMATION ON THERMAL BARRIER COATINGS

Nilima Roy, Debasish Mahanty, Kersi M. Godiwalla and Ashok K. Ray 188

13. A SIMPLE MODEL FOR VISCOSITY OF PIM MIXES; ISO-VISCOSITY CONTOUR MAPS FOR PIM PROCESSING

J. Janardhana Reddy, M. Vijaykumar, T.R. Rama Mohan and P. Ramakrishnan 202

HIGH-QUALITY SPONGE IRON POWDER FROM INDIAN BLUE DUST FOR P/M APPLICATIONS

TP Bagchi, Ravindra Malewar and Bijoy Sarma

Defence Metallurgical Research Laboratory
(Govt. of India, Ministry of Defence)
Kanchanbagh-P.O.
Hyderabad - 500 058
India.

ABSTRACT

Indian Blue Dust from Bailadila (M.P.) mines enjoys a unique distinction. Entire deposit (estimated as more than 20 million tons) of Blue Dust is fragile hematite ore with no impurities like carbon, sulphur and phosphorus. The ore is also amenable to easy beneficiation to a high-purity " superconcentrate" with about 0.03 silica and alumina as impurities.The "superconecntrate" (available in fine powdered form) is easily reducible to high-quality sponge iron powder using carbon or hydrogen as reductants. Present paper is concerned with production and characterization of hydrogen-reduced sponge iron powder.

In order to improve its properties required for different Powder Metallurgy applications, as-reduced sponge iron powder was subjected to suitable post-reduction treatments. The powder was characterised thoroughly (eg. A.D., T.D., particle size distribu tion and morphology).

The powder was found to be very soft with good compactibility. Its compaction behaviour was also studied. Cylindrical compacts were made by compacting it in a closed-die-both without and with lubricant (zinc stearate). Green densities of the compacts were measured and plotted against respective compaction pressures. Predictor equations (pressure vs.green density) were obtained by curve fitting with goodcorrelation coefficient.

1.0 Introduction

Iron powder is an important raw material for commercial powder metallurgy (P/M) applications [1]. It tops the list of tonnage-consumptions of all types of commercial metallic powders. The trend is likely to continue in future too. This is because of the technocommercial merits of iron powder as compared to those of its non-ferrous counterparts; some of them are listed here.

- Low cost of production.
- Attractive strength-to-weight-to-cost ratio.
- Easy formability to required shapes.
- Possibility to have good mechanical properties (especially—strength).
- Easy alloyability with carbon and other alloying elements leading to production of all types of plain carbon- and alloy steels with their technical attributes in tact.
- Easy availability in bulk quantity with consistent quality.

Apart from P/M industries, a large tonnage of different grades of iron powder is also consumed in pharmaceutical industries, food processing (preservation and enrichment) industries, chemical industries, production of welding rods, flame cutting, electronic and magnetic industries etc. In order to meet these diversified requirements of industries—both P/M and non-P/M—a wide spectrum of iron powders are required to be produced in huge quantum through different methods of production. Most common commercial methods of iron powder production are—

- Atomisation (largest in tonnage production),
- Reduction process
  - Carbothermic reduction process (second largest in tonnage production)
  - Hydrogen reduction process
- Electrolytic process
- Carbonyl process
- Fluidised-bed process.

Present paper is concerned with the production of P/M grade sponge iron powder by hydrogen-reduction route. This process is commonly known as the Pyron Process [2]. The raw material used for this process is mill scale—obtained from steel rolling mills which produce plain carbon steel products like plate, pipe, rod, sheet etc. Although this process produces good quality sponge iron powder for commercial use [3], availability of proper grade of raw material is a constant handicap for the process. The quality and quantity of the product (*i.e.* sponge iron powder) is always dependent on the ready availability of proper grade of raw material (*i.e.* mill scale) with consistent quality and required quantity. This problem may be reduced if high-purity hematite ore powder, available in abundance as a natural ore, is used as the feedstock in lieu of mill scale. It is, however, difficult to find huge natural deposits of such type of fragile and pure iron ore and that is why the Pyron Process has not been a commercially acceptable process elsewhere. Carbothermically reduced sponge iron powder, produced by Höganäs process [1] continues to be the only choice for P/M industries since its inception in the early 1900's. Various grades of Höganäs sponge iron powders are produced by suitable post-reduction treatments to address multifarious requirements of the user industries [4].

In this respect, India is placed favorably because of the huge deposits of Blue Dust—an easily friable hematite (Fe_2O_3) ore—at different iron ore mines scattered over the country. The Bailadila

Iron Ore Mines (M.P.) alone have over 20 million tons (estimated) of this high-quality Blue Dust. Because of millions of years of weathering effects, the hard hematite ore has metamorphosed to this typical fragile Blue Dust which is essentially a pure hematite ore—characterised by its singular absence of carbon, sulphur and phosphorus—with some small fraction of silica and alumina present as mechanical mixture. This ore is amenable to easy pulverisation and beneficiation to a "superconcentrate" with an average impurity level (mainly acid-insolubles) of 0.3%. This superconcentrate powder (almost pure Fe_2O_3) is amenable to easy reduction with the help of using hydrogen or carbon. But in spite of this, the effort of using the Blue Dust as a feedstock for normal blast furnace process of iron extraction failed because of its very fragile nature. Even the use of this ore as pellets or sinter did not prove to be a viable option. Efforts were then concentrated on trying other types of direct reduction processes. The Pyron Process became a natural and obvious choice at this stage. Moreover, the main weak point of the process, *i.e.* perennial dependence on other industries for supply of proper grade of raw materials (mill scale) as per required quantity and specification, is expected to be taken care by ensuring steady supply of feedstock with consistent quality at competitive rate.

This activity has been taken up at Defence Metallurgical Research Laboratory, Hyderabad. Efforts have been launched to establish the process flowsheets for production of different grades of sponge iron powders, both hydrogen-reduced and carbothermically reduced, using Bailadila Blue Dust superconcentrate (courtesy: M/s. National Mineral Development Corporation, Hyderabad) as the input raw material. A part of the activity has been published earlier [5,6]. This sponge iron powder produced showed good formability because of favorable particle morphology (porous and spongy) which promotes good interlocking during compaction and high surface area for mass transfer during sintering. Simultaneous efforts, therefore, have been launched to develop a range of downstream value-added P/M products using this grade of sponge iron powder for commercial exploitation. Initial studies have proved that this powder is suitable for many useful products like—

- Soft magnetic materials [7],
- Low-shrinkage Fe-Cu-Graphite bushes [8],
- High-density strips [9],
- Heavy duty friction materials.

Some more interesting results relating to the production and characterization of hydrogen-reduced sponge iron powder is presented in this paper.

2.0 Powder Production

Flowsheet of the production process (hydrogen reduction and post-reduction treatment) is shown in Fig. 1. This has been standardised by conducting a series of in-house experiments.

2.1 Raw Material

As-mined hematite ore powder was subjected to magnetic beneficiation to obtain the required grade of superconcentrate with low acid-insolubles (<0.3%) carbon (0.001%). Its particle size distribution was determined by laser diffraction technique using Malvern MasterSizer. Clean distilled water was used as dispersion medium. The cumulative particle size distribution is plotted (as a broken line) on a semi-logarithmic scale (Fig. 2). The bi-modal distribution curve indicates that two types of hematite ore powders (coarse and fine) were blended for this particular batch.

2.2 *Hydrogen Reduction*

Iron is known to form three stable solid compounds with oxygen—hematite (Fe_2O_3), magnetite (Fe_3O_4) and wüstite ($Fe_{1-y}O$) where $y \rightarrow 0$ as the reduction process continues towards completion. The reduction process of hematite is thus a three-stage process:

$$3\,(Fe_2O_3)_{solid} + (H_2)_{gas} = 2\,(Fe_3O_4)_{solid} + (H_2O)_{gas} \quad \text{<first stage>}$$

$$(Fe_3O_4)_{solid} + (H_2)_{gas} = 3\,(FeO)_{solid} + (H_2O)_{gas} \quad \text{<second stage>}$$

$$(FeO)_{solid} + (H_2)_{gas} = (Fe)_{solid} + (H_2O)_{gas} \quad \text{<third stage>}$$

Details of kinetics and mechanism of the hematite reduction process is well-documented [10]. The equilibrium diagram of iron and iron oxides (wüstite and magnetite) with hydrogen-water vapour (H_2/H_2O) mixture reproduced in Fig. 3 for reference. Reduction temperature was chosen in such a way that the yield should be α-Fe. Some of the important processing parameters which affects the properties of the product (iron powder) and the process reliability are—

- Reduction intensity*,
- Hydrogen flow rate,
- Dew point of hydrogen used,
- Bed height and
- Packing density.

Effects of these parameters (general trend) on the powder properties are summarised in Table I [11]. All of these parameters required to be optimised to get the best result (*i.e.* maximum metallisation with minimum residual oxygen at lowest possible cost).

The hematite powder was packed loosely in molybdenum boats by hand and fed to a continuous pusher-type electric furnace. Dry hydrogen gas (dew point: 243 K) was passed in counter-current direction through the muffle for reduction. Reduction temperature and -time were controlled suitably so as to yield near-complete (>99%) metallisation of the ore right up to the bottom layer of each boat. After reduction, each boat was pushed to the cooling zone of the furnace (which was kept cool by continuous circulation of cold water). After cooling, the boats were dragged manually from the discharge-end of the reduction furnace through a curtain of flowing hydrogen so as to minimise further oxygen pick-up.

---

*Amongst all these reduction parameters, the temperature-time combination has the most predominant effect on the reduced powder. This synergistic temperature-time combination is denoted as *"reduction intensity"* drawing the analogy of "sintering intensity" which combines the effect of temperature and time of sintering.

Table I. Effect of Processing Parameters on the Iron Powder Produced by Hydrogen Reduction

Reduction Process Parameters	Level	Reduction Kinetics	Effect on Powder Characteristics				
			Particle Size	Sp. Surface Area	Residual Oxygen	Other Possibilities	Productivity
Reduction Intensity							
• Temperature (T) • Time (t)	Higher Prolonged	Fast	Large	Low	Low	Sinter cake formation	Low
• Temperature (T) • Time (t)	Lower Shorter	Slow	Smaller	Higher	Higher	Pyrophoric Powder	Higher
Hydrogen Flow							
• Flow Rate • Dew Point	High Low	Fast	No direct effect	Increased	Low	No re-oxidation during cooling	Increased production cost
• Flow Rate • Dew Point	Low High	Slow	No direct effect	Decreased	High	Re-oxidation at low temperature	Impracticable
Charge							
• Bed Height	High	Slow	No direct effect	No direct effect	High	Bottom layer remains unreduced	Improves marginally
• Bed Height	Low	Improves	No direct effect	No direct effect	Low	Entire charge is reduced	Reduced
• Bed Packing	Tight	Slow	No direct effect	No direct effect	High	Bottom layer remains unreduced	Improves marginally
• Bed Packing	Loose	Improves	No direct effect	No direct effect	Reduced	Entire charge reduced	Reduced

2.3 *Crushing and Milling*

After reduction, the metallised iron powder turns to hard cakes inside the boats because of *in situ* sintering of freshly-reduced nascent surfaces of the powder particles. These hard cakes were subjected to crushing in a conventional jaw crusher followed by further size-reduction using a multi-mill. The products of multi-mill were then sieved through a mesh (100 #, *i.e.* 150 μm). Almost 99% of the pulverised powder passed through the sieve; oversize fraction (~1%) was subjected to recycling. Chemical composition of the iron powder, after milling and sieving, was analysed as—

- Carbon = 0.0009 %
- Sulphur = not detected (<0.002 %)
- Phosphorus = not detected (<0.002%)
- Oxygen (total) = 1.83 %.

The effect of milling time on the oxygen pick-up was studied by milling the powder for different lengths of time. Results show (Fig. 4) the spongy powder particles are not likely to pick-up extra oxygen during milling operations, their very high specific surface area notwithstanding . Hence, the high oxygen content of the sponge iron powder may be attributed to the residual oxygen left behind because of incomplete reduction.

2.4 *Reduction Annealing*

In order to bring down the oxygen level further, the iron powder was subjected to reduction-annealing treatment (973 K) in dry hydrogen (dew point: 243 K) passed in counter-current direction through the muffle of the annealing furnace. The annealing is also helpful in reducing the stress induced in the powder particles during milling and soften the powder particles. This will soften the powder and increase its compactibility. Effect of annealing parameters (time and bed height) on residual oxygen content was studied and the results are shown as bubble diagram (Fig. 5). It may be noted that the residual oxygen content may be reduced to 0.33% by adjusting the bed height and annealing time suitably. Studies are on-going to reduce the residual oxygen content of the annealed powder further by optimising the annealing process.

2.5 *Remilling*

After reduction-annealing, the loose powder forms a hard cake was once again because of unavoidable *in situ* sintering. Hence, it is required to subject the annealed cakes to similar type of milling operations in a jaw crusher and then in a multi-mill. Powder so obtained was analysed for chemical composition. If the oxygen content of the powder is found to be within limits (0.3 % in this case), the yield is taken as acceptable for P/M applications. Otherwise, the powder has to be subjected to reduction-annealing again as indicated in the flowsheet (Fig. 1).

3.0 Powder Characterisation

Every batch (~100 kg) of reduced sponge iron powder was thoroughly mixed before storage in air-tight bags. No passivator was used for the powder as the storage is intended to be of short term. Representative powder samples for testing were obtained by cutting the stream of flowing powder while being poured into the storage bags. These samples were subjected to in-house characterization as per standard methods [12].

3.1 *Particle Size Distribution and Shape*

The particle size distribution of the powder was determined by laser diffraction technique with the help of Malvern MasterSizer using clean distilled water as dispersion medium. The cumulative particle size distribution of the sponge iron powder is shown in Fig. 2 along with that of the original raw material (*i.e.* hematite ore powder). The particle size of the iron powder is decreased considerably because of size reduction during milling.

Particle morphology was observed under scanning electron microscope. The particles are spongy in shape with some internal porosity (Fig. 6). The reason is attributed to the gas-solid reduction process (shrinking-core model). As the reduction proceeds at high temperature, the oxygen atoms are gradually knocked off from the hematite lattice by hydrogen. This creates small pore channels within the reduced metallic layer. These channels provide easy entrance path to the reductant gas (hydrogen) to the reaction interface and exit path of the reduction product (water vapour) as shown schematically in Fig. 7. The reduction process thus continues till complete metallisation is obtained.

3.2 *Chemical Analysis*

Purity of the iron powder is an important factor. As the raw material itself is highly pure in nature, this factor is automatically taken care of to a great extent. There are, however, some alumina and silica particles embedded in the product which come directly from the initial raw material (*i.e.* beneficiated hematite ore powder) itself. The influence of these non-magnetic inclusions is under study now. If their presence proves to be harmful above a certain specified limit, the silica and alumina contents of the initial ore have to be reduced as there is no scope to reduce them in any of the subsequent steps.

Another unavoidable impurity is the oxygen content of the powder. High oxygen content of the sponge iron powder may be controlled by suitable adjustment of sintering and annealing parameters. Care is required to be exercised to reduce the oxygen pick-up during milling by maintaining an inert atmosphere within the milling chamber. The sponge iron powder, however, is highly prone to atmospheric oxygen pick-up during long-term storage, handling and further processing owing to its high surface area. Necessary care is required to be taken to minimize further oxygen pick up (using suitable passivators) if long-term storage is intended.

Chemical composition of the annealed powder samples were determined by the Chemical Analysis Group of DMRL. The results are given in Table II.

3.3 *Other Powder Properties*

Common properties of the annealed powder were evaluated in the laboratory as per standard methods and are summarised in Table II.

Table II

Properties of the sponge iron powder produced from Blue Dust

Property	Average Value	Remarks
Chemistry		
▪ Oxygen content (total)	0.3 %	C, O & S were determined by Leco apparatus. P by wet chemical method. Other impurities by Atomic Absorption Spectrometer (Varion Techtron).
▪ Sulphur	not detectable (<0.002%)	
▪ Phosphorus	not detectable (<0.002%)	
▪ Carbon	0.0009 %	
▪ Acid insolubles	0.3 %	
Powder Properties		
▪ Apparent density	2040 kg/m^3	As per MPIF Standards [12]
▪ Tap density	2590 kg/m^3	
▪ Flow rate	25 s/0.05 kg	
Particle Size		
▪ Median size (D_{50})	134.83 x 10^{-6} m	Results obtained with the help of Malvern MasterSizer S software
▪ Diameter at 10% (D_{10})	84.67 x 10^{-6} m	
▪ Diameter at 90% (D_{90})	197.8 x 10^{-6} m	
▪ Average size ($D_{4,3}$)	138 x 10^{-6} m	
▪ Specific surface area	6.5 m^2/kg	

4.0 Compactibility Studies

Compactibility (or, compressibility) of a powder denotes its ability to get densified under pressure. This property is of immense practical importance for design of pressing tools and ascertaining the capacity of the press required to yield the desired green density. Compactibility of metal powder is dependent on various factors, like—

- Inherent properties of the powder, *eg.*
  - Hardness of the powder particles
  - Particle size distribution
  - Particle shape
  - Intra-particle porosity
  - Non-metallic impurities
- Post-reduction treatment of the powder
  - Milling
  - Annealing
  - Use of solid lubricants
  - Alloying additions.

The compaction response of the sponge iron powder produced was determined over a range of compaction pressures. Since it is rather difficult to comprehend the overall behaviour of the powder when subjected to compaction and sintering from theoretical standpoint, a new phenomenological approach was adopted for data processing (§ 4.2). This approach is expected to supplement, albeit qualitatively, the present knowledge-base of compaction.

4.1 Powder Compaction

For compaction studies, small cylindrical compacts were made in a closed-die (material = hardened die steel, diameter = 0.038 m). About 0.1 kg of powder was weighed with the help of an electronic balance (Make: Mettler, capacity: 2.4 kg, least count: 1.0×10^{-5} kg) for each compaction run.

No lubricant was used for the powder particles, only the die wall and the punch were lubricated with zinc stearate solution (*i.e.* 0.002 kg zinc stearate in 0.1 litre of benzene) during each compaction to reduce die wear.

In order to emulate the realistic processing condition, the powder was compacted in two different presses as per a random sequence of experimental runs. Details of the presses and compaction loads (with corresponding compaction pressures) are tabulated in Table III.

Table III

Details of compaction presses with compaction loads and -pressures

Details of Compaction Press	Compaction Load (ton)	Compaction Pressure (MPa)
Universal Testing Machine (Mohr & Federhaff AG, Mannheim, Germany), Capacity: 60 tons	5	43
	7.5	64.5
	10	86
	12.5	107.5
	15	129
Commercial P/M Press (TH & J Daniel Ltd., England) Capacity: 250 tons	20	172
	25	215
	30	258
	35	301
	40	344

After compaction, the compacts were carefully ejected from the die cavity with a small ejection pressure (less than the least count of the presses). Average diameter of the green compacts was calculated as 0.0381 m with a standard deviation of 0.00006 m. This shows that green compacts experienced some elastic expansion (0.26 %) after ejection. Green densities (GD, kg/m^3) of the compacts were measured metrologically (details omitted).

4.2 Data Analysis

Processing of compaction data is not an easy task. Different types of predictor equations are available in the literature [for example, cf. Ref. 13-23]. It is, however, beyond the scope of the present paper to discuss the merits and demerits of these approaches. A detailed study has been undertaken by one of the authors [24] and the results will be published in future. It would suffice to state that a phenomenological approach was adopted to process the compaction data. The process of analysis is briefly explained here.

A typical compaction pressure (P) vs. green density (GD) curve for metal powder is shown schematically in Fig. 8. The compaction process may be divided into four broad stages [25] as summarised in Table IV. These stages are also shown schematically in Fig. 8 as vertical straight lines.

Table IV

Stages of Powder Compaction

Stage	Segment in Fig. 8	Pressure	Main Process
First	I	Low	Deformation-free displacement of particles.
Second	II	Intermediate	Displacement and rotation of particles caused by plastic deformation at the contact zones.
Third	III	High	System gets consolidated due to plastic deformation of the particle volume. Rate of consolidation, controlled by the strain-capacity of the material, gradually falls with increase in pressure.
Fourth	IV	Very high	Consolidation continues but its rate is reduced drastically due to increased deformation resistance of the system. Not practised in real life as it leads to excessive tool wear and compact cracking during sintering because of closed pore channels.

At low compaction pressures (first stage), a straight line (*i.e.* first-order polynomial), shown in eqn. (1), is usually observed to fit the compaction data with good accuracy. Increasing the degree of the polynomial to higher orders did not improve the accuracy of fitting significantly.

$$GD = A_0 + A_1 * P \quad \ldots (1)$$

At P = 0, equation (1) takes the following form—

$$(GD)_{P=0} = A_0 \quad \ldots (2)$$

This, on differentiating with respect to P, yields—

$$\frac{d(GD)}{dP} = A_1 \quad \ldots (3)$$

For higher compaction pressures, however, a second-order polynomial fits better to the compaction data. Increasing the degree of the fitted polynomials to higher orders or trying other types of equations (logarithmic, exponential, power etc.) did not improve the correlation coefficients further as far as the present set of experimental data are concerned. Proceeding in a similar fashion, the generalised form of the equation may be written as—

$$GD = A_0 + A_1 * P + A_2 * P^2 \quad \ldots (4)$$

As before, at P = 0, equation (4) takes the following form—

$$(GD)_{P=0} = A_0 \quad \ldots (5)$$

and, on differentiating with respect to P, one gets—

$$\frac{d(GD)}{dP} = A_1 + 2 * A_2 * P \quad \ldots (6)$$

Second differential of eqn. (4) with respect to P, yields—

$$\frac{d^2(GD)}{dP^2} = 2 * A_2 \quad \ldots (7)$$

Apparently these (A_0, A_1 and A_2) may look like some *fitted parameters* of unknown theoretical significance. But, these parameters can also be used as some *practical parameters* in comprehending the particulate behaviour during compaction and sintering.

As per eqns. (2) & (5), the parameter 'A_0' may be taken as *Zero-pressure Green Density (ZPGD)*. Sapiro [18] has mentioned about this parameter when studying the compaction behaviour of powder. Its value is observed well above the apparent- and tap density of the powder. Physical significance of ZPGD is yet to be established.

When the pressure is applied, the powder particles are brought closer to each other due to continued plastic deformation and the green density increases proportionately. This direct cause-and-effect relationship is denoted by the linear response parameter 'A_1' and may be designated as *compaction response*. Particle rearrangement is almost completed at this stage.

After reaching the stabilised packing configuration of the particles, the densification continues as a result of many complex phenomena (simultaneously aiding and opposing the densification process) as the compaction pressure is increased continuously. Some of them are listed here:

- The powder particles gradually flow plastically to fill up the inter-particle porosities and thereby leave less and less room to occupy further.
- The particles get work-hardened simultaneously and hinders the plastic flow of the particles.
- The surface roughness of the particles get smoothened because of localised inter-particle friction.
- The thin oxide films surrounding the particles get fragmented; this brings the freshly-exposed metallic surface into intimate contact.
- Mechanical interlocking between the particles increases.

The rate of densification falls in this region because of the inherent resistance offered by the system itself. This *resistance element* is represented by the parameter 'A_2'. Normally, the value of A_2 is negative (denoting resistance to the on-going process) with its value considerably lower than those of A_1 (order of two) and A_0 (order of six). That is why, its effect is not prominent at lower values of P. But at higher values of P, this factor becomes predominant when multiplied by P^2. At this stage, these parameters may be taken as some qualitative indices which may be used for comparison of powder responses under compaction. Detailed study has been undertaken [24] and the results will be published in future.

For this powder, the green density (GD, kg/m^3) data were plotted against respective compaction pressures (P, MPa) for a range of 43 MPa to 344 MPa (Fig. 9). Different types of predictor equations were fitted to these data by linear least-square (LLS) method. All calculations were done with the help of a spreadsheet (Excel 2000™). For these set of data, the best-fit equation (with $r^2 = 0.9425$) takes the following form—

$$GD = -0.0138*P^2 + 9.2613*P + 4305.8 \quad (\text{valid for } 43 \text{ MPa} \leq P \leq 344 \text{ MPa}) \qquad \ldots (8)$$

In order to understand the compaction process better, microstructures of the *green compacts* were developed. The green compacts were impregnated with molten wax and carefully polished with emery paper followed by lapping with diamond paste (0.5 micron). Samples were polished by highly experienced persons so that the pore morphology of the compacts are not distorted. Microstructures of some green compacts, compacted at different pressures, are shown in Fig. 10. The size and distribution of the pores get reduced with increased compaction pressure as expected. At lower pressures, the change of pore size is very prominent [cf. Fig. 10 (a) and (b)]. At higher pressures, however, the change in pore morphology shows a diminishing trend because of the reasons explained earlier. A detailed quantitative metallographic study has been undertaken to correlate these features with compaction pressure. Results will be published in future.

4.3 Compression Ratio

Along with compressibility, the compression ratio (*i.e.* the ratio of green density, GD, of the compact to the apparent density, AD, of the powder used) is also reported as a part of characterisation. Although not of much theoretical significance, the ratio (GD/AD) indicates the depth of die cavity

required to hold the loose powder which is to be compacted to specified green density. In order to complete formal characterisation exercise, the compression ratios (CR) of the powder were calculated and are plotted against their respective compaction pressures (Fig. 11). Predictor equation (P vs. CR) with correlation coefficient (r^2), obtained by LLS curve fitting, is also shown in Fig. 11. Mathematically this plot is equivalent to P vs. GD plot (shown in Fig. 9) with a shift in the scale of y-axis. Hence, no new insight is obtained from this plot.

4.4 Effect of Lubrication

Since the shape of the reduced sponge iron powder particles is highly irregular and spongy (*vide* Fig. 6), it was but natural to expect that the compactibility of the powder would be enhanced by lubricating the powder particles with some solid lubricant before compaction. Another set of compaction experiments were, therefore, designed with lubricated powder. Two batches of lubricated iron powder—one with 0.5% and the other with 1% zinc stearate were prepared for this purpose. Required quantity of zinc stearate powder (commercial grade) was weighed precisely and then dissolved in benzene (LR grade). This solution was then hand-mixed with pre-weighed quantity of iron powder which was subjected to drying in air before compaction.

Cylindrical compacts were made as before using the same Universal Testing Machine (cf. Table III). Die wall and the punch were lubricated with zinc stearate solution (*i.e.* 0.002 kg zinc stearate in 0.1 litre of benzene). Green densities (GD, kg/m^3) of the compacts were metrologically as before.

The compaction data (P vs. GD) were computed and plotted for comparison with those obtained without lubrication (*vide* Fig. 12). These data were generated at lower compaction pressures (43 MPa $\leq$ P $\leq$ 129 MPa) and, as discussed in § 4.2, a 1st –order polynomial [*i.e.* (eqn. (1)] should be adequate to fit the data by LLS curve fitting with good correlation coefficients. The results of curve fitting are tabulated in Table V.

Table V

Results of LLS curve fitting (first order polynomial) to compaction data.
GD = Green density, kg/m^3, P = Compaction pressure, MPa

Green Density Data for Iron Powder	Co-efficient of Predictor equations		r^2
	A_0	A_1	
Without lubricant	4257.4	8.7207	0.9488
With lubricant (0.5%)	4292.4	6.5486	0.9888
With lubricant (1%)	4391.8	6.7993	0.9791

Although the surface of the powder particles are extremely rough and spongy (Fig. 6), the effect of solid lubricant is not so pronounced in imparting good densification of the compacts as expected. On the contrary, it is observed that the compaction response of the sponge iron powder *without* lubricant is *more* than that with lubricant. Even the ZPGD is improved marginally with application of powder lubricant. This is possible because the powder particles are too soft and would prefer to undergo bulk plastic deformation (without the necessity of any lubricant) than get rearranged (with the help of purported lubrication) under the action of compaction pressure. Hence, the effect of lubrication is not pronounced in green density improvement.

The solid lubricant, in fact, plays two opposite roles in the overall compaction process. On one hand, it reduces the inter-particle friction and thereby aids the process by ensuring better particle packing (positive effect). On the other hand, the very presence of low-density lubricant in the inter-particle pores brings down the green density of the compacts (negative effect). In this case, it is observed that the compaction response of the powder with 1% lubricant is marginally better than that with 0.5% lubricant. This means that the positive effect of using 1%-lubricant is greater than its negative effect to such an extent that the resultant is still better than that obtained with 0.5% lubricant. It is, therefore, necessary to strike an optimum percentage of lubricant which would ensure best possible green density. The lubrication response of this powder is also under detailed study now. More clear picture is expected to emerge in future.

5.0 Sinterability Studies

These green compacts (with different green densities to start with) were then sintered in order to study their response to sintering.

5.1 Sintering

The green compacts were sintered in a pusher-type high-temperature electric furnace under dried hydrogen (dew point = 243 K) atmosphere (counter flow). The samples were charged in molybdenum boats with alumina powder packing (to ensure even heat distribution). The samples were sintered at 1673 K for 10.8 ks. After sintering, the boats were pushed to the cooling zone of the furnace. When cooled, the sintered samples were dragged out from the discharge-end of the furnace through a curtain of flowing hydrogen in order to prevent re-oxidation.

5.2 Sintered Density

After cleaning, the samples were observed visually. No distortion in shape or discontinuity was noticed in any of the sintered compacts. The volume of each sintered sample was measured by metrological technique. The mass of each sample was determined with the help of same electronic balance and the density was computed therefrom. As a check, the density was also measured by Archimedes principle for first few samples (with proper wax coating). Since no significant difference in results (sintered density) was noticed, it was discarded because of its associated hassles and metrological method was followed for rest of the samples.

Experimental data (P vs. SD) are plotted in Fig. 13. Proceeding in a similar fashion (§ 4.2), a second-order polynomial [(eqn. (9)] was fitted to these data. The P vs. SD plot shows a trend similar to that of P vs. GD plot (as shown in Fig. 9).

$$SD = 4871.4 + 12.544 * P - 0.0208 * P^2 \quad \text{(valid for 43 MPa} \leq P \leq \text{344 MPa)} \qquad \ldots (9)$$

Microstructures of sintered compacts were also developed to study the effect of compaction pressure and sintering on pore closure and grain formation. Here also, due care was exercised to retain the pore morphology during polishing. Some of the microstructures of sintered samples, compacted at different pressures, are shown in Fig. 14. It is observed that increased compaction pressure aids the sintering process by (i) reduction of overall porosity and (ii) grain growth (because of intimate contact of the particles). Detailed quantitative metallographic studies are in progress.

It is also interesting to note that although the relationship of P vs. density (both GD and SD) is a parabolic one, the relationship between GD and SD can be described through a *linear* equation (Fig. 15). More data, however, are required to comment further in this direction.

These experimental data (P vs. SD) were compared with those of four grades of reduced iron powders available commercially—MH 100.24, NC 100.24, EC 100.24 and SC 100.26. These data were collected from literature [26] and are re-plotted (Fig. 16) here for preliminary comparison. The results of curve fitting (curves are omitted because of clarity) are tabulated in Table VI. From the initial results, it may be observed that the overall densification response of this powder is comparatively better than the reported values; even the parametric response of this powder—in terms of A_0 (zero-pressure density) and A_1 (linear response)—is better. The third parameter, A_2 (resistance element), is higher than that of the other four grades of powder by one- or two orders. Significance of these findings would be understood clearly by conducting more rigorous comparison studies which are on-going.

Table VI

Results of LLS curve fitting (second order polynomial) to sintering data

Sintered Density Data for Iron Powder	Co-efficient of Predictor equations			r^2
	A_0	A_1	A_2	
Present Grade	4871.4	12.544	-0.0208	0.9488
SC 100.26 Grade	4805.3	6.3883	-0.0033	0.9975
EC 100.24 Grade	4284.9	7.6246	-0.0043	0.9956
NC 100.24 Grade	3905	8.0429	-0.0043	0.9958
MH 100.24 Grade	3490.5	8.8837	-0.005	0.9946

SC: Super Compressibility, EC: Extra Compressibility, NC: Normal Compressibility

5.3 Dimensional Changes

Dimensional changes are important from practical point of view [27-30]. The lateral and radial shrinkage of the samples were measured before and after sintering. Average shrinkage values (expressed as percentage of original green dimensions) of this iron powder are much above the expected values [29] of -0.38% (Fig. 17). It is required to bring down the shrinkage level by suitable alloying addition. Effect of addition of 2% copper and 0.8% graphite is being studied now.

At lower compaction pressures (43 to 172 MPa), the longitudinal shrinkages are seen to be more than the corresponding lateral shrinkages. At higher compaction pressures (215 to 344 MPa), the trend is observed to be reversed with reduced difference between the radial and longitudinal shrinkage values. Green compacts obtained at higher compaction pressure are more homogeneous as compared to those obtained at lower compaction pressure. Hence, the shrinkage pattern of high-pressure compacts will be less erratic after sintering.

6.0 Issues to be Addressed

This paper is presented as an interim report of an on-going activity to invite helpful comments and suggestions. Many important issues are yet to be addressed in order to complete the project. Some of them are listed here.

6.1 Optimisation of Reduction Parameters

Since the preliminary experiments on reduction are over, it is now necessary to optimise all reduction parameters (*vide* Table I) by design of experiments.

6.2 Optimisation of Annealing Parameters

Similarly, the annealing parameters (§ 2.3) are also to be optimised by design of experiments. Another important aspect to be ascertained is to specify the maximum allowable oxygen content of the power particles after annealing. It is not necessary to bring down the oxygen content below a certain limit as specified or acceptable by the user from the process economics point of view (any additional step in the flowsheet will increase the cost of the product). In addition to this, some amount of residual oxygen (present as thin layer of reducible oxide scale over the powder particles) and locked-up stress is expected to have a favorable effect on sintering kinetics. This aspect is to be studied.

6.3 Characterisation of Powder

Exhaustive characterisation of the powder is required to create a database. Particular attention is to be focused on its formability studies, i.e. compactibility, sinterability, effect of post-sintering treatments (annealing, coining, infiltration etc.), dilatometric study of dimensional changes with the help of high-temperature dilatometer [31], image analysis of microstructure, toxicity and pyrophoricity of the powder [32, 33].

6.4 Downstream Products

Since the powder has shown good potential for commercial exploitation [5-9], concomitant attempts should be launched to evaluate its applicability (with necessary modifications) in the industries (both P/M and non-P/M). The authors are not equipped with all types of facilities to address

this mammoth task, powder samples are to be sent to various industries who are interested to try this indigenous grade of powder.

6.5 Use of other types of Blue Dust

There are other deposits of Blue Dust or hematite powder ore in India. It is time to try and evaluate those ores also for commercial exploitation.

7.0 Conclusions

- Hematite iron ore from Bailadila mines is a good source of raw material—both in quality and quantity—for production of high-grade sponge iron powder by direct reduction process (Pyron process). Its high level of natural purity ensures high-purity iron powder, virtually free from carbon, sulphur and phosphorus, with controlled level of acid insolubles.

- Availability of proper grade of mill scale in required quantity is an inherent limitation of Pyron process. This can be obviated if hematite iron ore is used in stead.

- The iron powder, produced by hydrogen reduction of this grade of powder ore, was subjected to thorough charactersation for P/M application. Properties are well within the acceptable limits for commercial applications.

- The compactibility of the powder was studied. Powder is soft enough to yield good green density, its highly irregular shape notwithstanding.

- The sintering response is good in terms of densification. Shrinkage values are on higher side at low compaction pressure. It shows a trend to fall with increased compaction pressure.

- Microstructural studies of green- and sintered compacts revealed how the size and distribution of the pores change with increasing compaction pressure.

- Exhaustive database of evaluation results should be created as a forerunner of technology package.

- Intense application engineering is required for downstream consumption of the powder in P/M and non-P/M industries.

- Other types of natually-occuring hematite ore powders should also be tried in the same line for production of sponge iron powder for commercial exploitation.

References

1. Fritz V Lenel, *"Production of Iron Powder by the Reduction of Iron Oxide"*, **Metals Handbook®**, Volume 7, Powder Metallurgy, Ninth Edition, American Society of Metals, Metals Park, Ohio 44073, June 1984, pp. 79-99
2. Harold T Harrison, *"Production of Iron Powder by the Pyron Process"*, ibid., pp. 82-83
3. Website <www.pyroncorp.com>
4. Website <www.hoganas.com>
5. KC Sahoo, DK Lahiri, S Barpanda, GS Bhattacharjee and TP Bagchi, *"Perspectives in Iron Powder Manufacture: A Resource Approach"*, Presented in the 1988 International Powder Metallurgy Conference, Orlando, USA, June 5-10, 1988. Revised version published in **Modern Developments in Powder Metallurgy**, Compiled by P Ulf Gummeson and Donald Gustafason, Metal Powder Industries Federation and the American Powder Metallurgy Institute, Princeton, NJ, USA, Volume 20, pp. 279-292, 1988
6. K Gopalakrishna, N Ravi and TP Bagchi, *"P/M Grade Sponge Iron Powders from Blue Dust—A Comparative Assessment"*, **Trans. Powder Metallurgy Association of India**, Volume 21, December 1994, pp. 42-49
7. TP Bagchi, Bijoy Sarma and TG Vasudev, *"Development of Soft Magnetic Materials Using Hydrogen-Reduced Sponge Iron Powder"*, presented at **Advances in Magnetic Materials and Applications** (16th Technical Meet and National Seminar), organised by Magnetics Society of India, held at University of Madras, Chennai, September, 22-23, 2000 (paper under publication)
8. BP Saha, KP Rao, TP Bagchi and AV Saibaba, *"High-Temperature Sintering of Iron-Copper-Graphite System"*, **Trans. Powder Metallurgy Association of India**, Volume 21, December 1994, pp. 30-34
9. BP Saha, KP Rao and TP Bagchi, *"High-Purity Fully Dense Iron Strips by Powder Rolling"*, **Trans. Powder Metallurgy Association of India**, Volume 21, December 1994, pp. 22-26
10. L von Bogdandy and H –J Engell, **The Reduction of Iron Ores. Scientific Basis and Technology,** Springer-Verlag, Berlin-Heidelberg-New York, 1971
11. F Thümmler and R Oberacker, **An Introduction to Powder Metallurgy,** The Institute of Materials, 1 Carton House Terrace, London SW1Y 5DB, 1993, p. 32
12. **Standard Test Methods for Metal Powders and Powder Metallurgy Products (1998 Edition),** Multimedia CD-ROM, Metal Powder Industries Federation and the American Powder Metallurgy Institute, Princeton, NJ, USA
13. John E. Davidson, *"Compressibility of Metal Powders"*, **Metals Handbook®,** Volume 7, *op. cit.*, pp. 286-287
14. TP Bagchi, KP Rao and N Maitra, *"Predictor Equations for Green Properties of Nickel-Graphite Powder Compacts"*, **Transactions of Powder Metallurgy Association of India,** vol. 25, 1999, pp. 1-9
15. G Portal, E Euvrard, P Tailhades and A Rousset, *"Relationship between compacting pressure, green density, and green strength of powder compacts used in thermal batteries"*, Powder Metallurgy, vol. 42, no. 1, 1999, pp. 34-40
16. R Panelli and F Ambrozio Filho, *"Compaction equation and its use to describe powder consolidation behaviour"*, Powder Metallurgy, vol. 41, no. 2, 1998, pp.131-133
17. Shujie Li, Paul B Khosrovabadi and Ben H Kolster, *"New Compaction Equation for Powder Materials"*, Intl. J. Powder Metallurgy, vol. 30, no. 1, 1994, pp. 47-57

18. I Sapiro, *"Compaction of Powders XI. Application of the General Equation to Both Metal Powders and Ceramic Powders"*, **Adv. Powder Metallurgy & Particulate Materials – 1994, Compaction, Sintering and Secondary Operations,** vol. 3, compiled by Chaman Lall and Albert J. Neupaver, Proc. 1994 Intl. Conf. & Exhibition on Powder Metallurgy & Particulate Materials, Metal Powder Industries Federation, APMI International, Princeton, New Jersey, USA, pp. 41-55
19. Ge Rong-de, *"A New Powder Compaction Equation"*, Intl. J. Powder Metallurgy, vol. 27, no. 3, 1991, pp. 211-216
20. R Agatonović, D Stefanović, V Petrović and MM Ristić, *"Consolidation of iron powder"*, J. Materials Science Letters, vol. 9, 1990, pp. 40-42
21. Roger LK Matsumoto, *"Generation of Powder Compaction Response Diagrams"*, J. American Ceramic Society, vol. 69, no. 10, Oct., 1986, pp. C-246-C247
22. MM Carroll and KT Kim, *"Pressure-density equations for porous metals and metal powders"*, Powder Metallurgy, vol. 27, no. 3, 1984, pp. 153-159
23. Erhard Klar and WM Shafer, *"On Green Strength and Compressibility in Metal Powder Compaction"*, **Modern Developments in Powder Metallurgy,** vol. 9, Powder Metallurgy Principles and Production Processes, (Eds.) Henry H. Hausner and Pierre V Taubenblat, Metal Powder Industries Federation, Princeton, New Jersey, USA,1976, pp. 91-113
24. TP Bagchi, unpublished work
25. Anderj Šalak, **Ferrous Powder Metallurgy,** First Edn., December 1995, Cambridge International Science Publishing, 7 Meadow Walk, Great Abington, Cambridge CB1 6AZ, England, pp. 62-65
26. Ibid., p. 159
27. Ibid., pp. 113-115
28. Randall M German, **Powder Metallurgy Science,** 2nd. Edn., Metal Powder Industries Federation, Princeton, New Jersey, USA, 1994, pp. 266-267
29. Cynthia L Freeby, *"Dimensional Change of Sintered Metal Compacts"*, **Metals Handbook®,** Volume 7, *op. cit.*, pp. 290-292
30. Fritz V Lenel, **Powder Metallurgy: Principles and Applications,** Metal Powder Industries Federation, Princeton, New Jersey, USA, 1980, pp. 212-224
31. F Thümmler and R Oberacker, **An Introduction to Powder Metallurgy,** *op. cit.*, 1993, pp. 236-238
32. Robert P Beliles, *"Toxicity of Metal Powders"*, **Metals Handbook®,** Volume 7, *op. cit.*, pp. 201-208
33. F Thümmler and R Oberacker, **An Introduction to Powder Metallurgy,** *op. cit.*, 1993, pp. 117-119

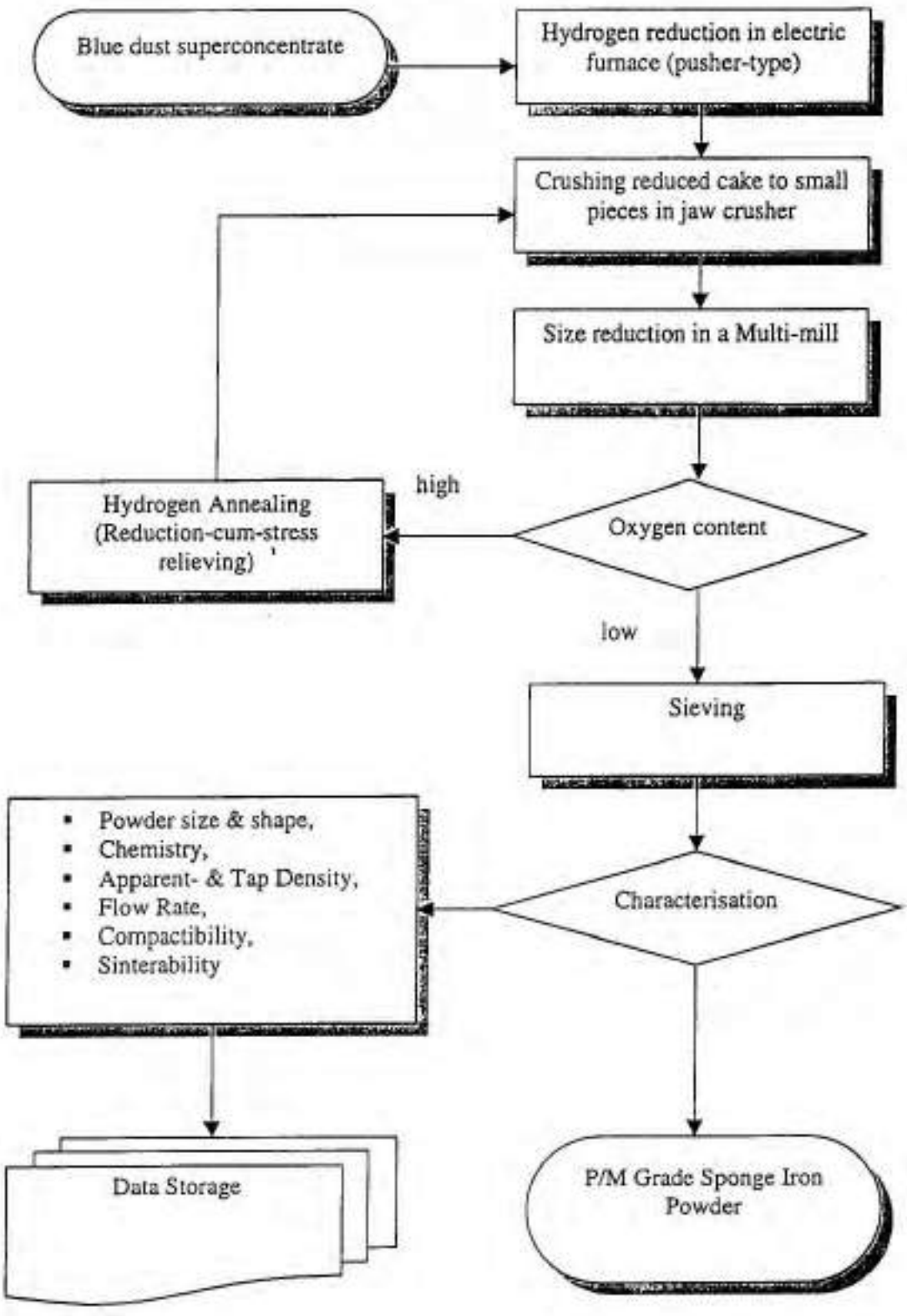

Fig. 1 **Process flowsheet for powder production and characterisation.**

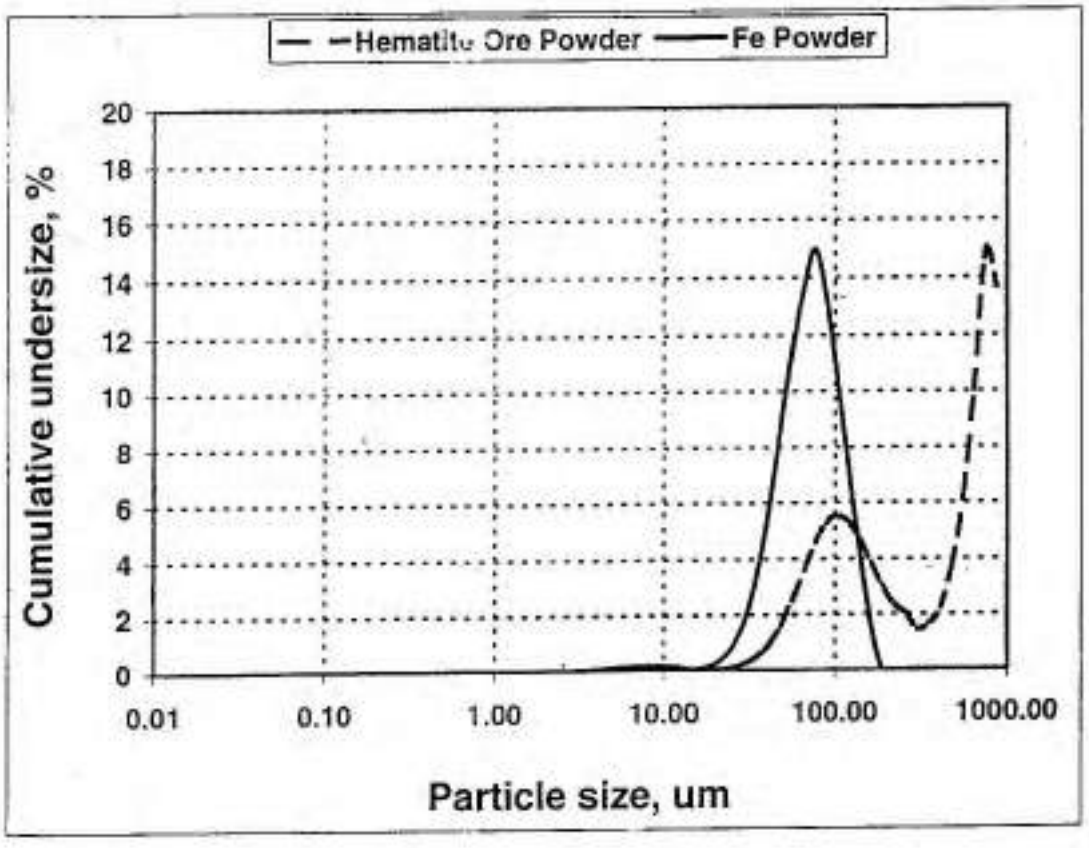

Fig. 2 Particle size distributions of the hematite ore powder and sponge iron powder produced (measured by laser diffraction technique).

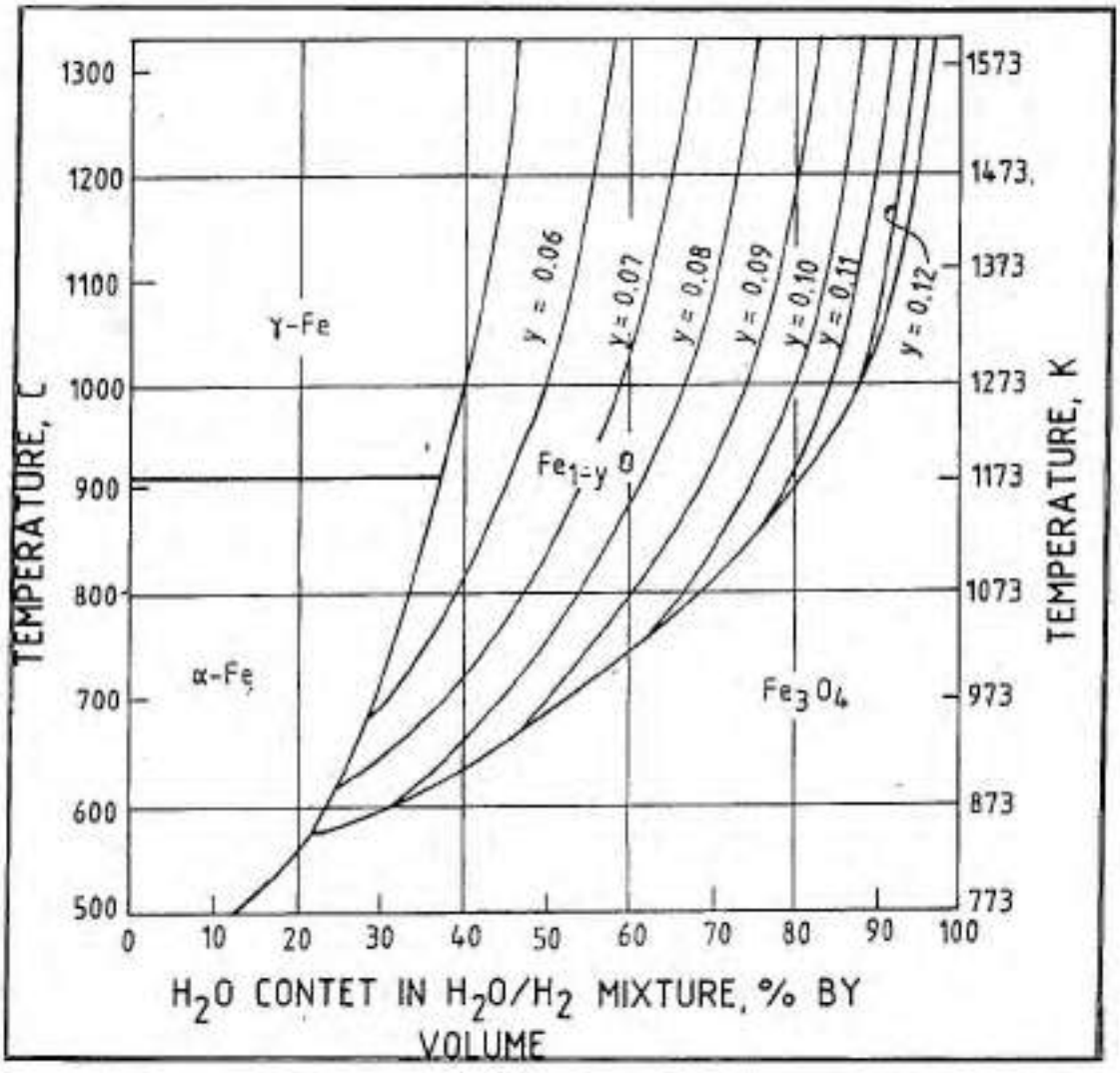

Fig. 3 Equilibrium diagram of iron and iron oxides (wüstite and magnetite) with hydrogen-water vapour mixture (H_2/H_2O).

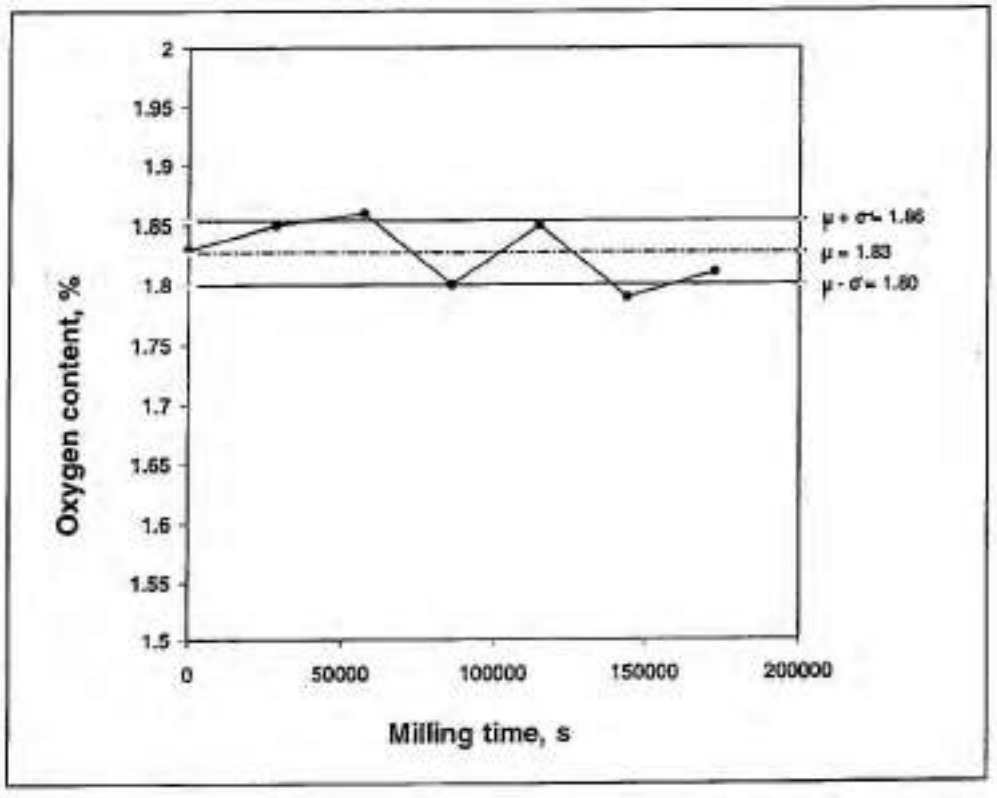

Fig. 4 Effect of milling time on oxygen content of the sponge iron powder. No significant change in the average oxygen content (1.83 %) with increased milling time.

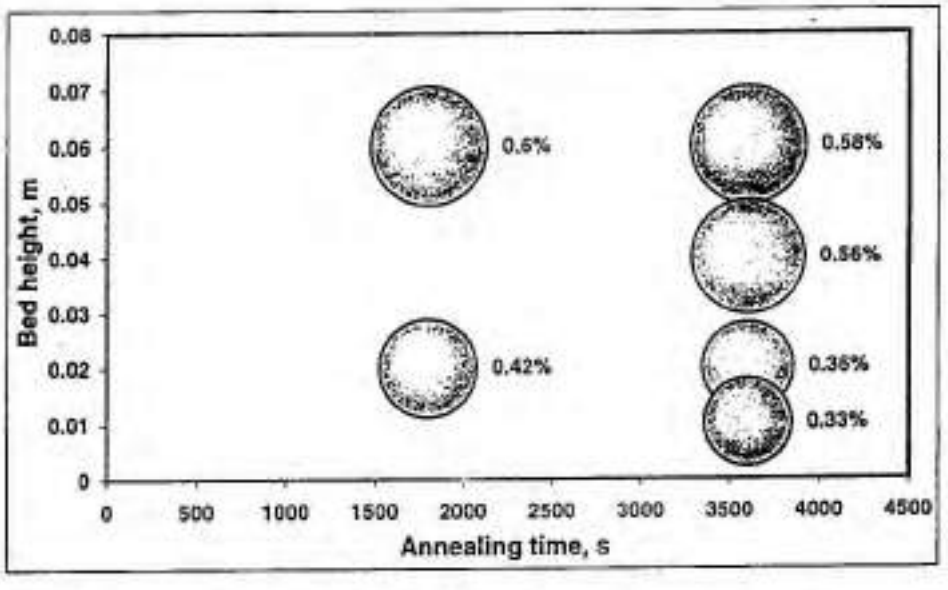

Fig. 5 Effect of annealing time and bed height on the oxygen content (shown as bubbles of proportionate diameters) of the annealed powder.

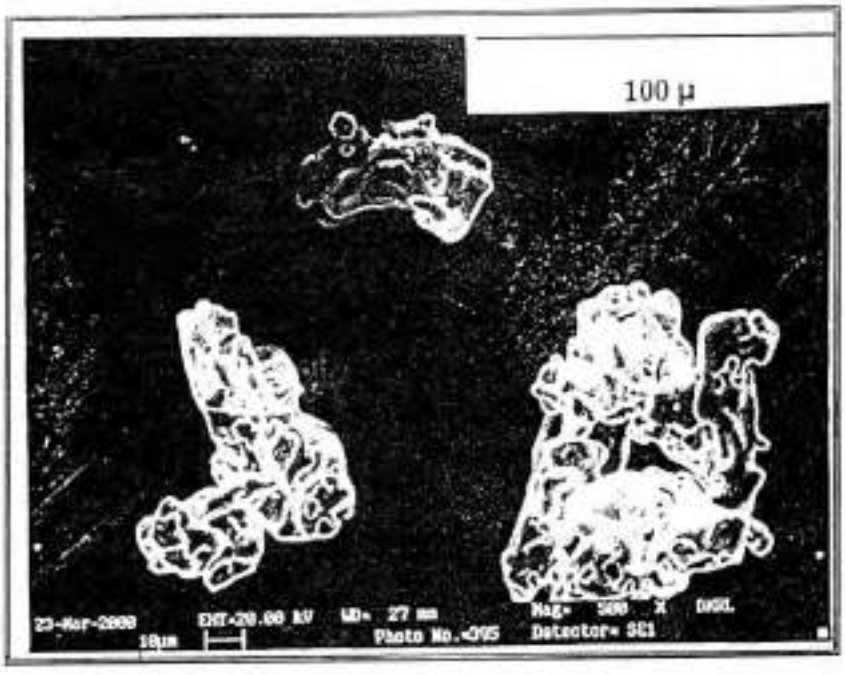

Fig. 6 SEM image of the sponge iron powder particles.

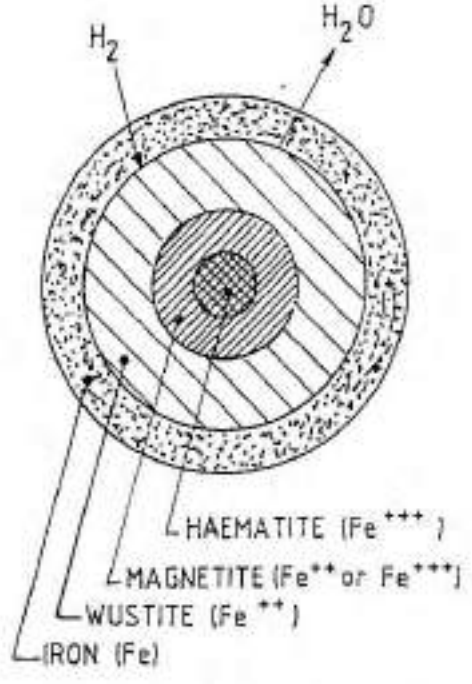

Fig. 7 Pores channels formed on the reduced metallic layer during the course of reduction allow the reductant gas (H_2) to permeate in and the reduction product gas (H_2O) to permeate out which makes the reduced iron porous and spongy.

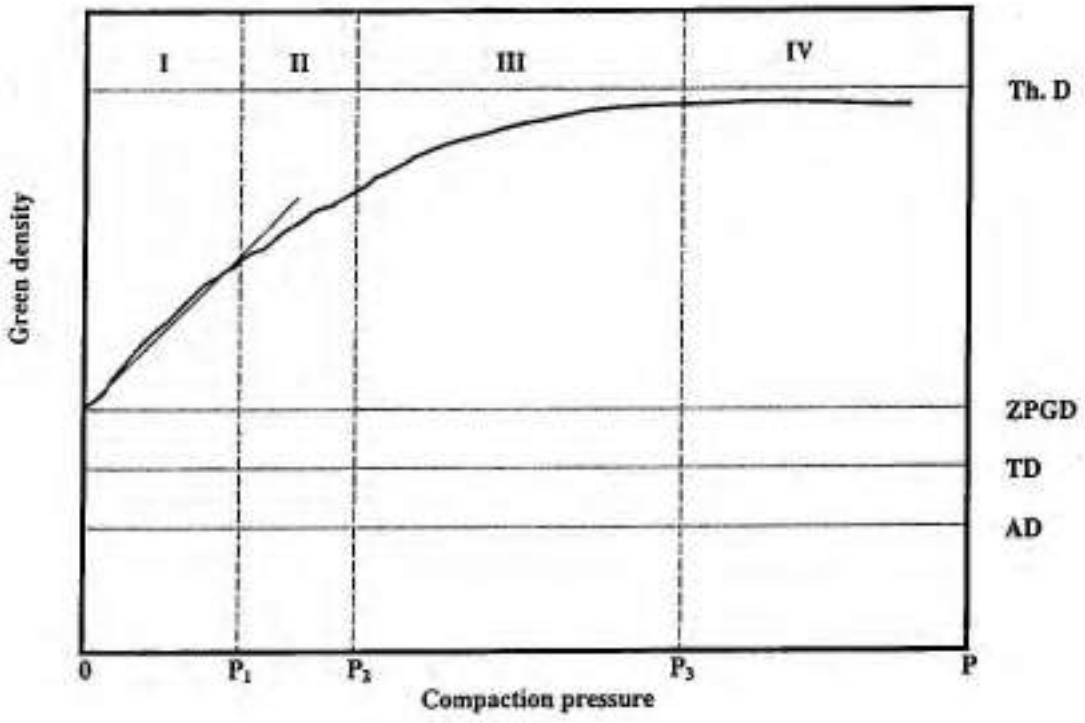

Fig. 8 Schematic representation of variation of green density (GD) of powder compacts along with corresponding compaction pressure (P). AD = Apparent density, TD = Tap density, ZPGD = Zero-pressure green density, Th. D = Theoretical density.

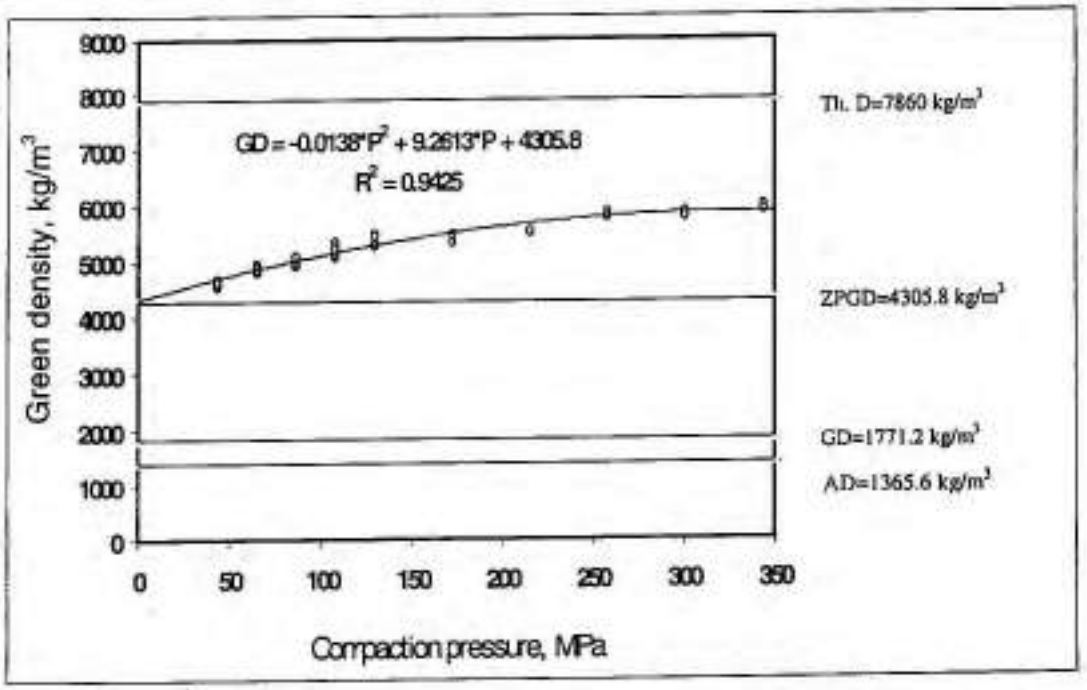

Fig. 9 Variation of green densities (GD) of iron powder compacts along with corresponding compaction pressures (P).

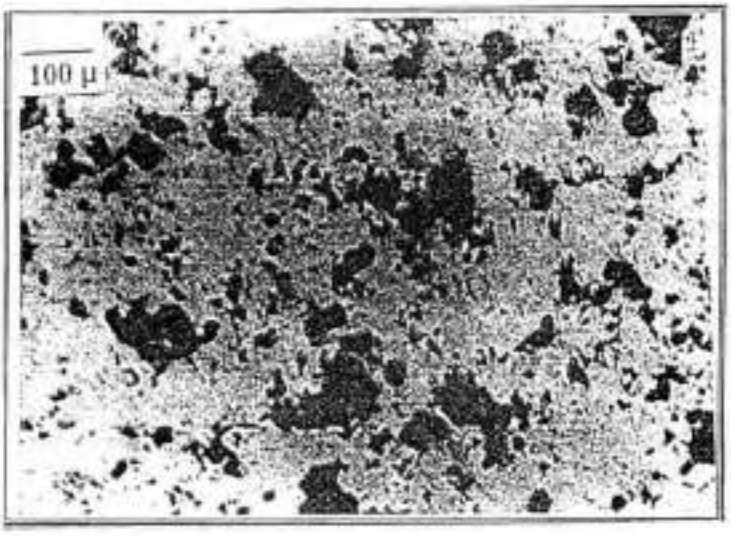

(a) Compaction pressure = 43 MPa

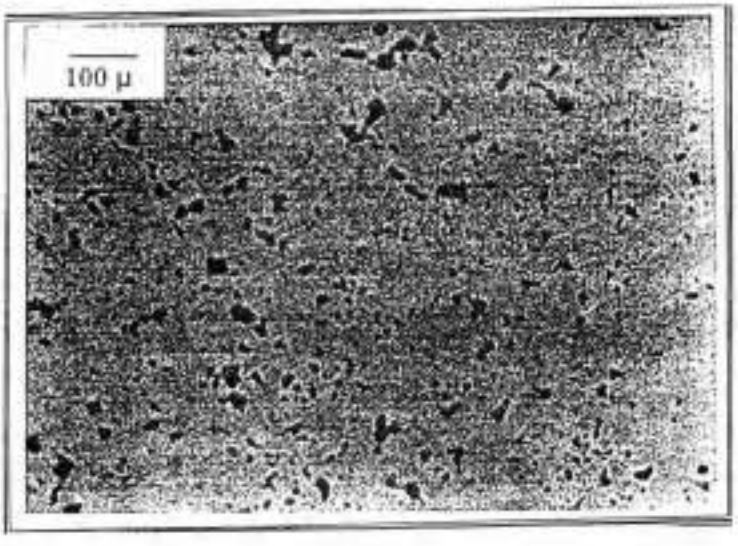

(b) Compaction pressure = 86 MPa

Fig. 10 **Microstructures of the green compacts. Samples were wax impregnated before polishing to retain the pore morphology in tact. The size and distribution of the inter-particle pores get reduced with compaction pressure because of plastic flow of the powder particles. No etchant was used. Magnification: 100X**

(contd...)

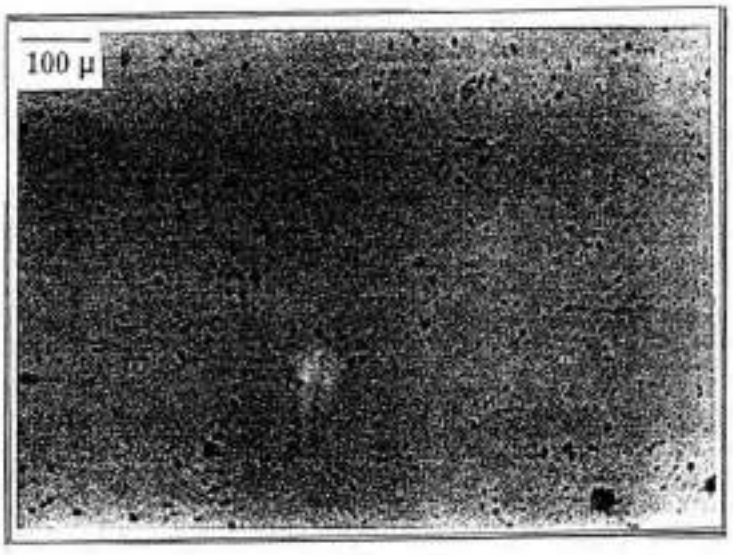

(c) Compaction pressure = 107.5 MPa

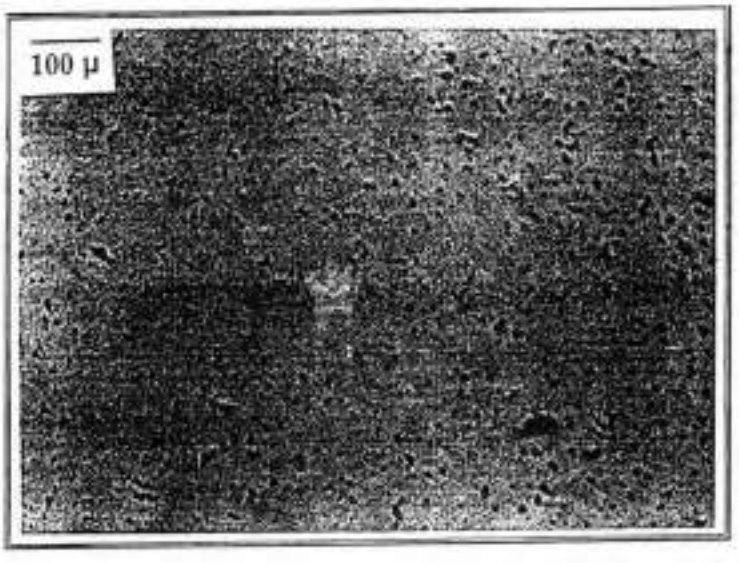

(d) Compaction pressure = 129 MPa

Fig. 10 **Microstructures of the green compacts. Samples were wax impregnated before polishing to retain the pore morphology in tact. The size and distribution of the inter-particle pores get reduced with compaction pressure because of plastic flow of the powder particles. No etchant was used.** Magnification: 100X

(contd...)

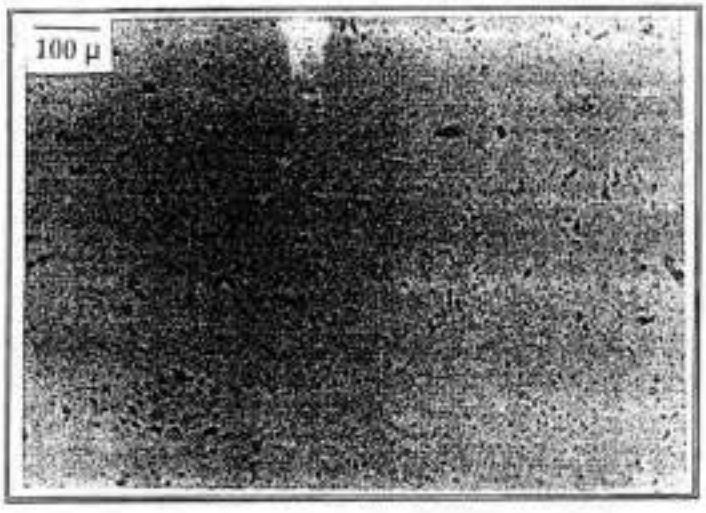

(e) Compaction pressure = 215 MPa

Fig. 10 Microstructures of the green compacts. Samples were wax impregnated before polishing to retain the pore morphology in tact. The size and distribution of the inter-particle pores get reduced with compaction pressure because of plastic flow of the powder particles. No etchant was used. Magnification: 100X

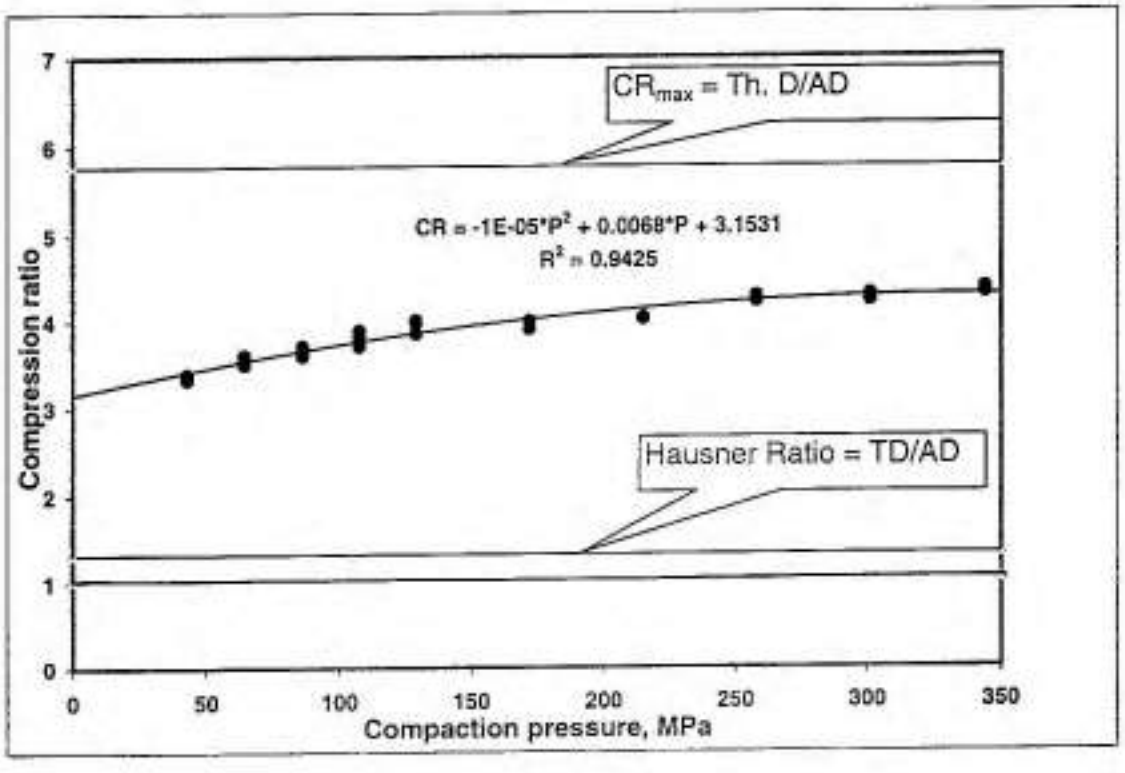

Fig. 11 Variation of compression ratio (CR) with compaction pressure (P).

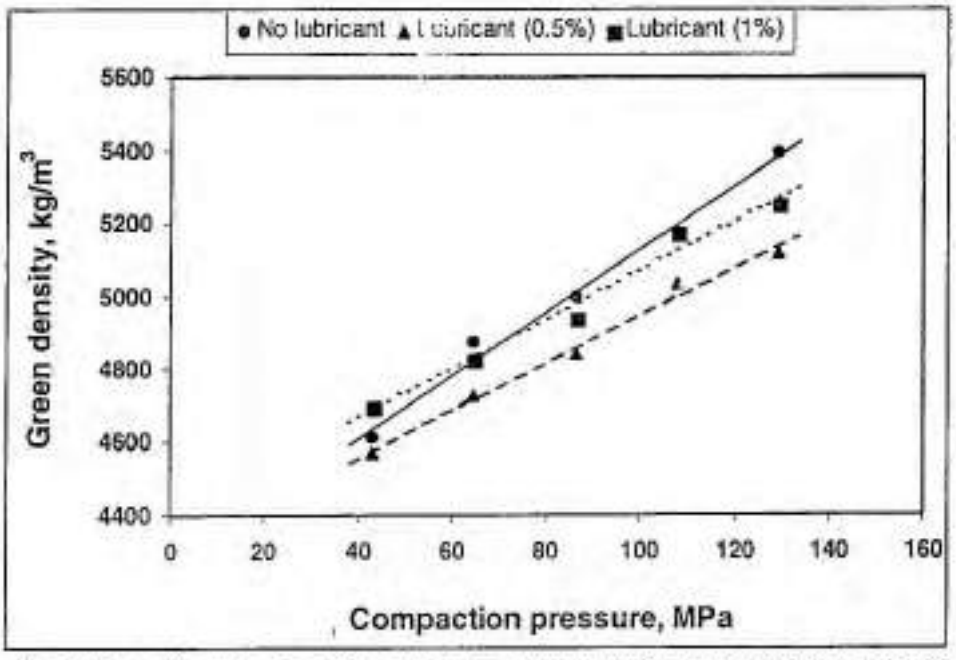

Fig. 12 Variation of green density of iron powder (with and without lubricant) with compaction pressure.

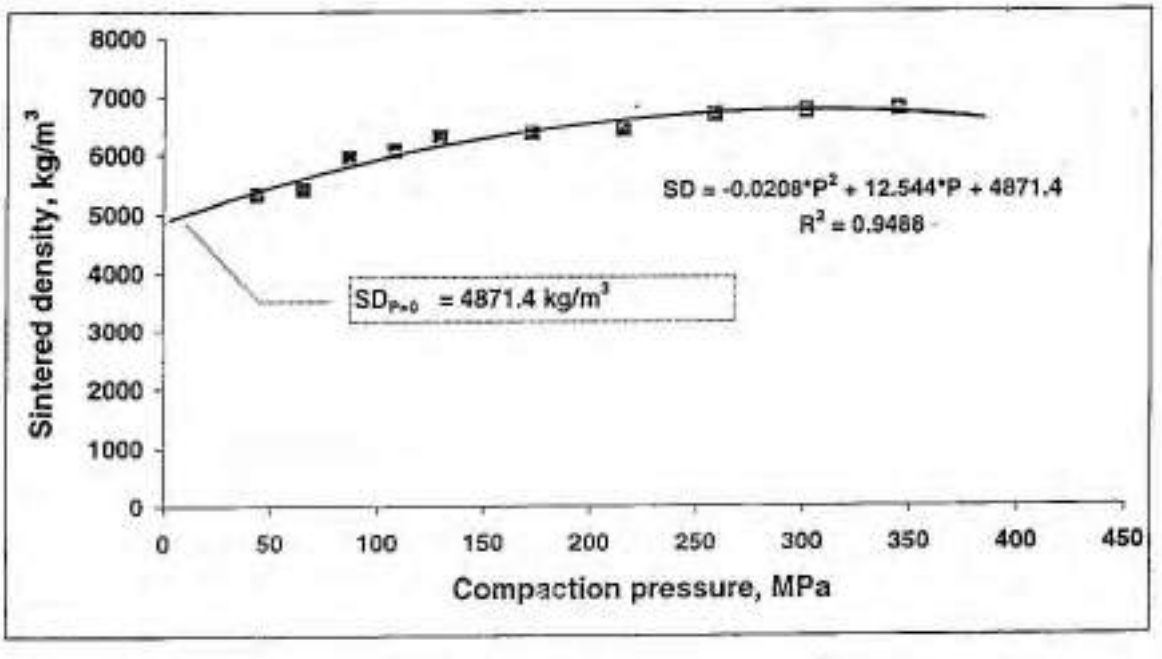

Fig. 13 Variation of sintered densities (SD) of powder compacts along with corresponding compaction pressures (P).

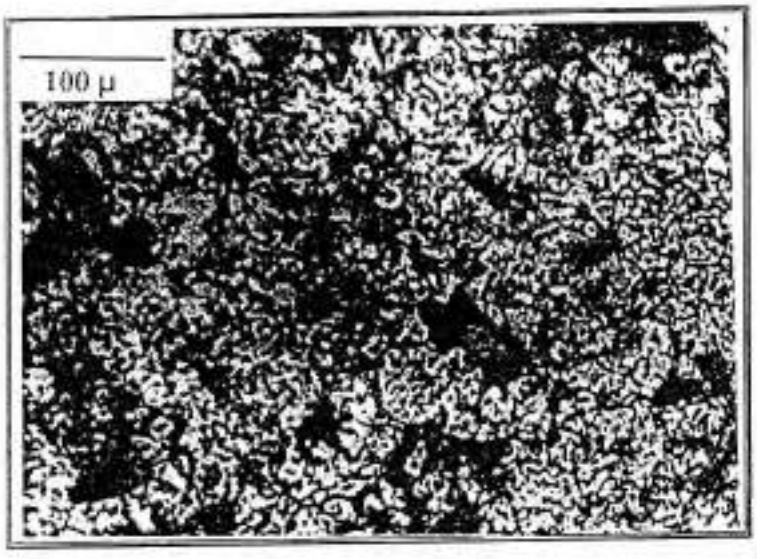

(a) Compaction pressure = 43 MPa

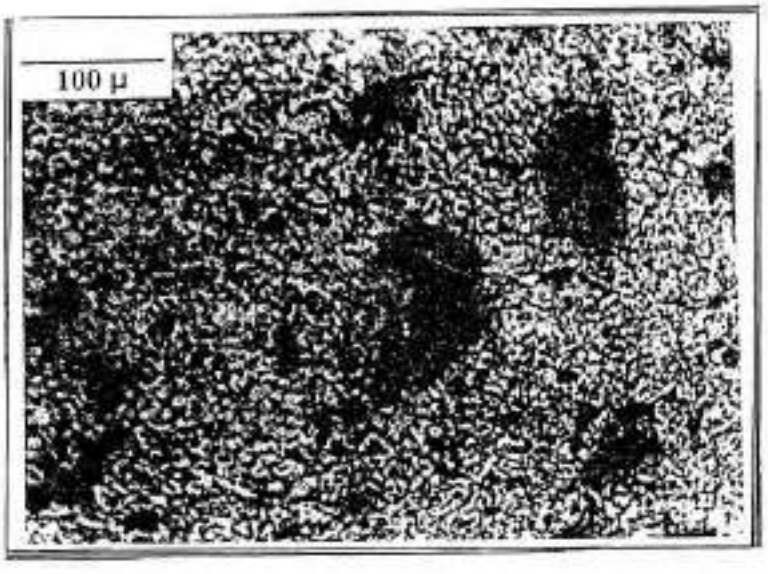

(b) Compaction pressure = 172 MPa

Fig. 14 Microstructures of the sintered (1400 C/hydrogen/3 hr) sponge iron powder compacts.
Etchant: 3%-nital (30 s swabbing), Magnification: 200X

(contd...)

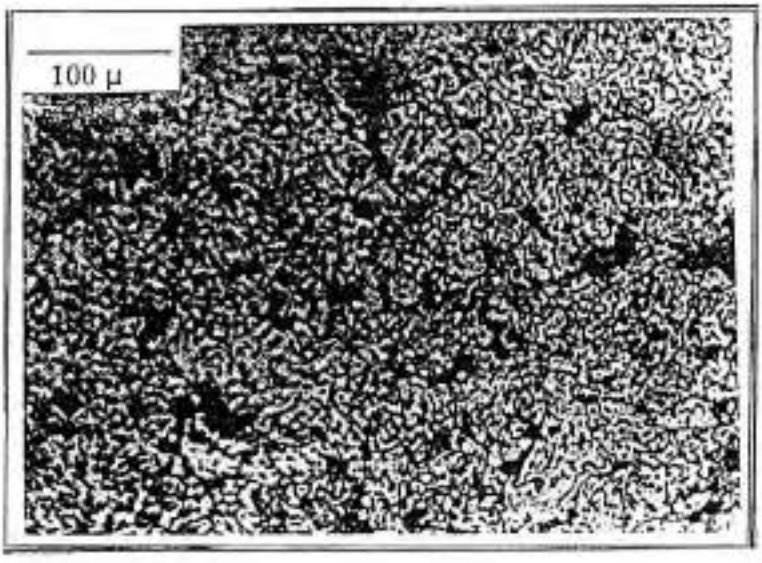

(c) Compaction pressure = 215 MPa

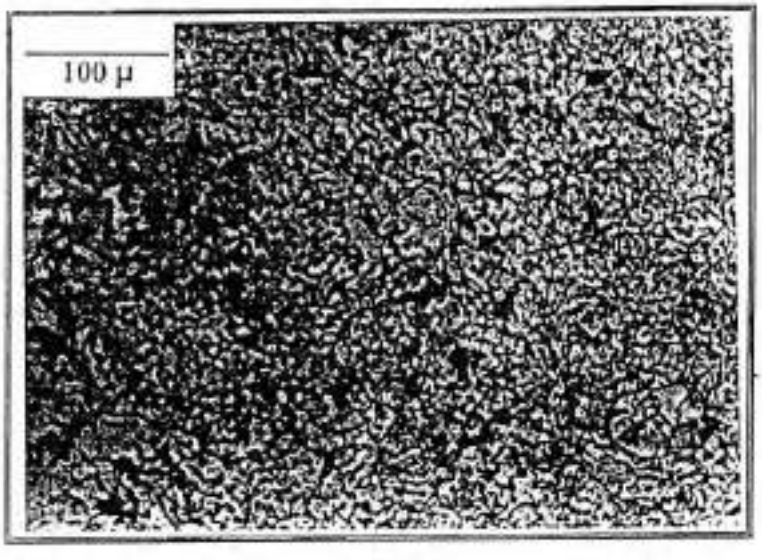

(d) Compaction pressure = 258 MPa

Fig. 14 **Microstructures of the sintered (1400 C/hydrogen/3 hr) sponge iron powder compacts.**
Etchant: 3%-nital (30 s swabbing), **Magnification: 200X**

(contd...)

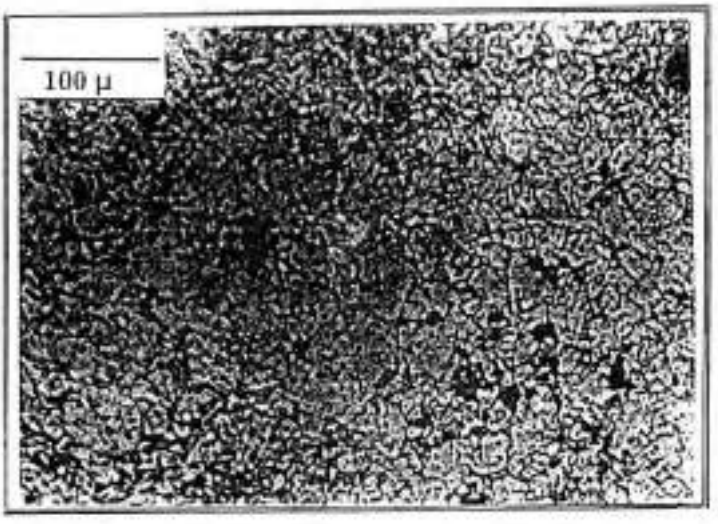

(e) Compaction pressure = 301 MPa

Fig. 14 Microstructures of the sintered (1400 C/hydrogen/3 hr) sponge iron powder compacts.
Etchant: 3%-nital (30 s swabbing), Magnification: 200X

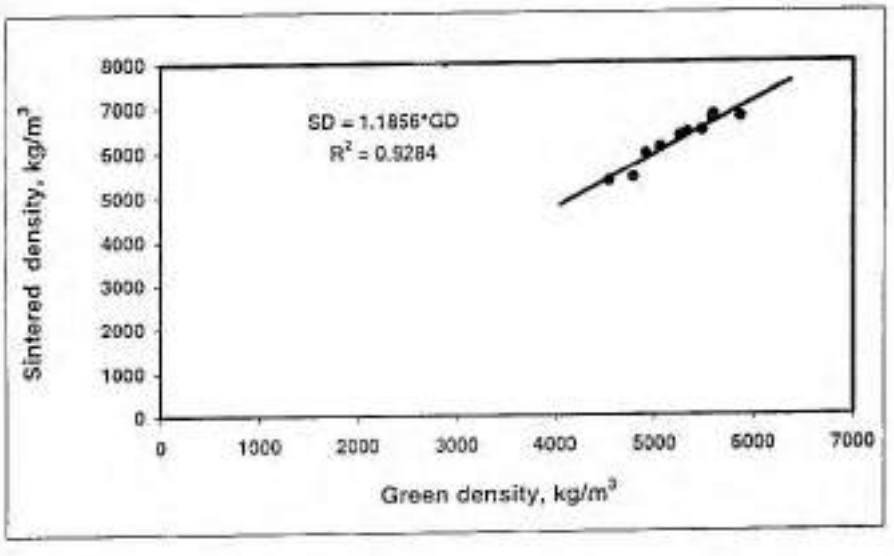

Fig. 15 Variation of sintered densities of powder compacts with their corresponding green densities

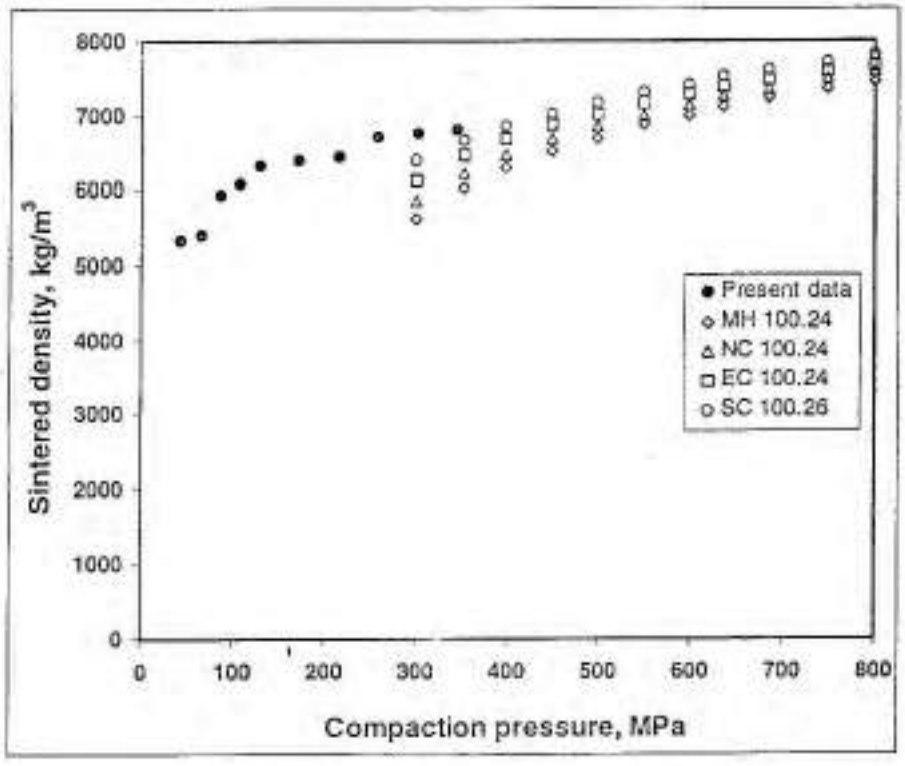

Fig. 16 Comparison of P vs. SD data of different grades of reduced powders (obtained from literature) with those of the present powder (hydrogen-reduced).

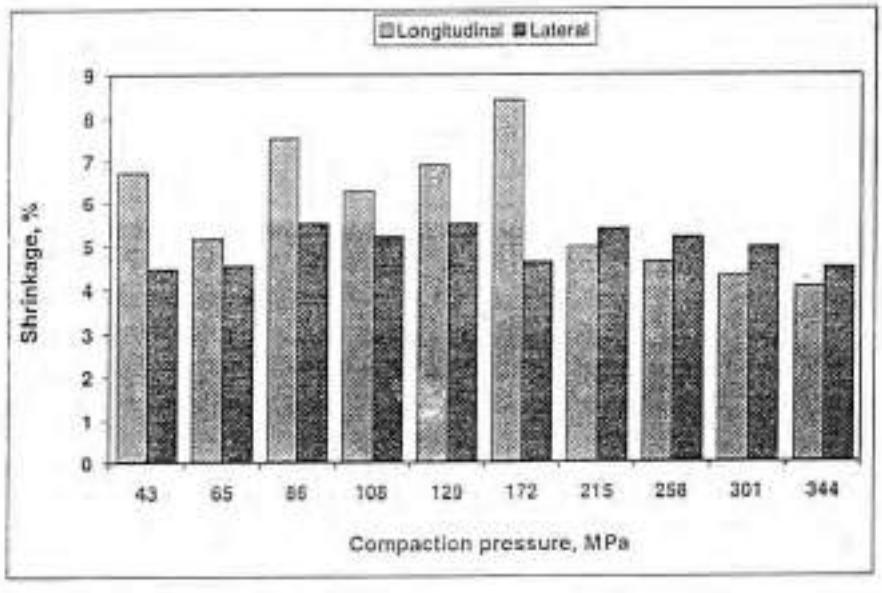

Fig. 17 Variation of linear- and radial shrinkages of sintered compacts with their corresponding compaction pressures.

PRODUCTION OF FINE METAL POWDERS BY LAMINAR GAS STREAMS..

Dr. Gunther Schulz
Wideflow Metal Powder production Engineering, GmbH
Gothaer Str.41. D-99885
Ohrdruf, Germany.

Dr. K.KrishnaRao
Consultant, Shiva Group Companies
213(539/A), Street No.7., Lane.2., Himayatnagar
Hyderabad –500 029

A B S T R A C T.

Conventional Gas atomization processes use turbulent gas flows decelerating while the melt stream accelerates. The nature of interactions between the fluids result in powders with wide particle size distribution and with powders of mean particle diameter of about 50 microns and above. The metal powders by laminar gas streams directly yield fine powders of with mean particle size about 10 microns and with narrow particle size distribution. These fine powders with growing market potential have unique properties and find applications in areas such as Metal Injection Molding (MIM) , Surface Mounted Devices (SMD) solder pastes, Thermal Spraying, Contact Materials, Dental Amalgams, etc. The principle involved, the innovative and patented film forming nozzle system used by Dr. Schulz, one of the authors, for the commercial production of fine powders are outlined.

INTRODUCTION.

Metal Powders are produced commercially by one of four approaches (a) Chemical (b) Electrolytic (c) Mechanical and (d) Atomization. By the 80's however, over 60% by weight (1) of all powders produced are manufactured by atomization and the figure may be higher today. There are many methods of atomization in vogue to-day. However the two-fluid atomization , that is break up of liquid melt with water or gas is the most commercially exploited method. Generally the underlying conditions that dictate the use of either gas or water depend on the size, size distribution, shape and surface morphology of the required powder. In either case a wide variety of ferrous and non-ferrous alloys , stainless steels, specialty alloys are manufactured.

The heart of any atomization unit is the nozzle and many different nozzle designs are in use, their function being to control the flow and pattern of the atomizing medium to provide provide for efficient disintegration of the liquid metal and to produce a powder of the desired properties. These nozzles generally take the form of either an annulus,

The heart of any atomization unit is the nozzle and many different nozzle designs are in use, their function being to control the flow and pattern of the atomizing medium to provide provide for efficient disintegration of the liquid metal and to produce a powder of the desired properties. These nozzles generally take the form of either an annulus, which is concentric around the metal stream or discrete jet, they being available either in free-fall or in confined designs as shown schematically in figure 1.

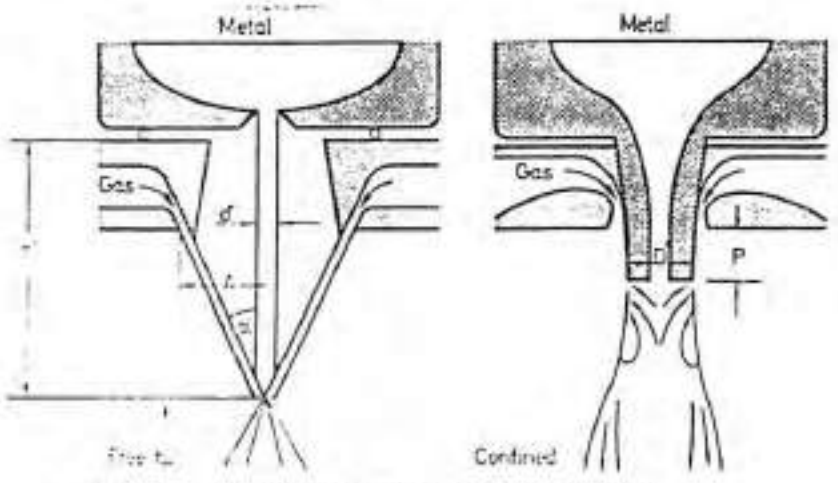

Figure.1. Nozzle systems for gas atomization.

While the free-fall configuration is predominantly followed in water atomization, the confined nozzle design is almost exlusively used in gas atomization. Commercially water atomized powders are typically irregular in shape with a rough dimpled surface texture, whereas the gas atomized powders are typically spherical with smooth surface. In either case, because of the tarbulent nature of interactions between the two fluids and the decelerating different densities and velocities varying with location and time of the atomizing fluid, a wide distribution of particle size with mass median particle diameters in the range of 50 to 300 microns are obtained. The size distribution follows approximately a logarithemic normal distribution and the standard deviations are generally 2.2 and above.

While the relatively coarse powders produced by the two-fluid systems using conventional atomizing nozzles, find applications in P/M component manufacture and other industries, interest in fine powders having median particle size of around 10 microns and lower have developed for applications like Metal Injection Moulding, Thermal Spray, Composite Materials, Catalysts, Conducting plastics , Solder Pastes for surface Mounting devices etc. These powders are also useful as additives in enhancing the strength of sintered parts.

coupled nozzle (4,5). Other variants of nozzle configurations and melt streeam flow have also been adopted to obtain fine powders (6,7,8,9,). In all the above cases, the melt stream which is dimensionally not well defined, is attacked by turbulent jets of the atomizing gas of varying density and speed, giving a fine but broad particle size distribution, thus providing poor yeilds and creating s necessity to classify the powder.

Recently de Laval nozzle principle has been used by T. Mahata, et.all (10) to produce spherical shaped tin powders. 90% of an atomized batch was reported to have particle size between 5 and 20 microns. The investigators used close-coupled annular nozzle, a nozzle configutation originally proposed by Unal (11) The melt nozzle being circular and protruding a short distance beyond the gas exit, as shown in figure 2. In all the above cases, the melt streeam which is dimensionally not well defined, is attacked by turbulent jets of the atomizing gas of varying density and speed, disintegrating the melt stream giving a fine but broad particle size distribution, thus providing poor yeilds and creating a necessity to classify the powder.

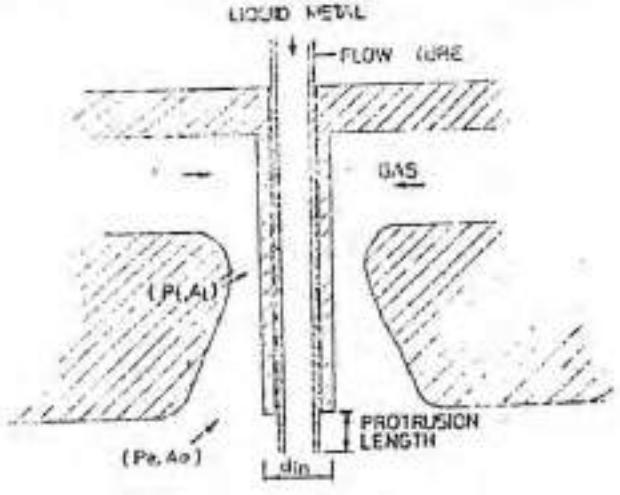

Fig. 2 Schematic of close coupled atomisation nozzle

NANOVAL PROCESS

To get fine powders of mean particle size of about 10 microns, with narrow particle distribution, Walz(12) introduced a new fluid dynamic approach into metal powder atomization using a circular melt nozzle and de Laval nozzle for gas flow. This new approach is later termed as Nanoval process. The basic idea of the process is the use of strictly laminar, self-stablizing gas flow accompanying the melt stream in parallel. Figure 3 (12) shows the nozzle configuration of the above process.

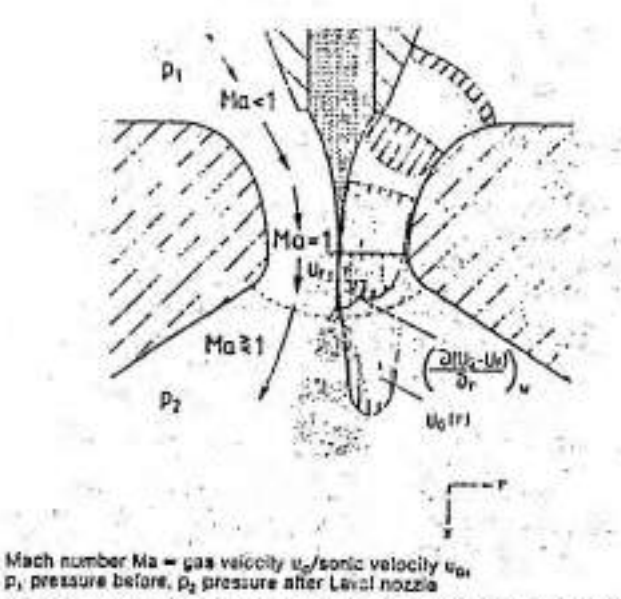

Mach number Ma = gas velocity u_g/sonic velocity u_{gs}
p_1 pressure before, p_2 pressure after Laval nozzle

Fig. 3. Nanoval process for atomization at sonic and supersonic laminar gas flow.

The gas flow with sonic velocities at the narrowest cross-section and with supersonic velocities at the divergent portion of the de Laval nozzle deforms the melt stream at a very increasing speed by virtue of shear stresses between gas and liquid surface until it becomes a thin unstable monofil and bursts into many thinner filaments (13, 14). These in turn disintegrate into small pieces. Under the influence of surface tension spherical melt droplets are formed which cool down and solidify to fine powders. The use of round melt nozzles with de Laval nozzle principle as described above , eventhough give fine powders with narrow size distribution, limits the metal through put to a fairly low levels of about 12 to 30 kgs/hr. (15). Once the melt nozzle orifice diameter is increased to achieve a more melt through put, the particle size of the resulting powder is increased thus defeating the objective of producing fine powders. To overcome this limitation, parallel use of several melt nozzzle systems was proposed. (15). This however increase the refractory costs thus not helping reduce powder costs.

WIDEFLOW MELT FILM NOZZLE SYSTEM

The basic new idea brought to atomizing practice by Dr.Schulz of Wideflow is to use linear nozzle system (16) This allows deploying a melt film with a large surface area, thus enabling efficient transfer of the kinetic energy from the gas to the melt. Since a thin liquid film, under free flow deforms and disrupts instantly, it is required to stabilize the melt film. This happens, in this case using a linear de Laval nozzle as shown under. Figure 4. Is a simplified drwing of the WIDEFLOW nozzle system (16). A vessel,1, containing the atomizing gas at high pressure is separated from the spraying tower 2, which is maintained at a much lower gas pressure by means of a linear de Laval nozzle 3. While going through the converging part of the gas nozzle, the gas accelerates strongly, laminarizing the gas flow. Once the gas enters the pressure drain field of the de Laval nozzle, its way through the nozzle is determined, and there is no possibility of eddies forming. The atomizing gas is expanded from P1 to a pressure of P at the narrowest cross-section, provided that the pressure P2 inside the spraying

tower is lower than P. The ratio P1/P is a constant for a given gas,and is independent of the de Laval nozzle design

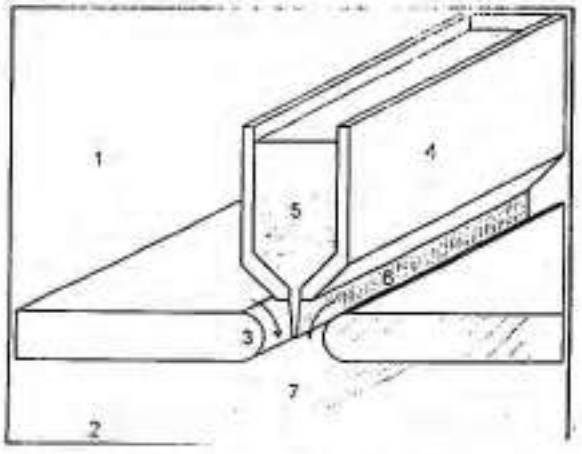

Figure 4. Wideflow melt film nozzle system.

At the narrowest cross-section of the nozzle, gas particles attain sonic velocity. The melt 5, leaves the basically rectangular shaped melt nozzle 4, as a thin melt film 6 which is injected into the gas flow field of the nozzle.The melt film acts as an obstacle within the gas flow and the gas particles stabilize the melt film from both sides in a perfect way. Inside the converging part of the de Laval nozzle the melt film keeps the same width as the orifice of the melt guidance tube. The large surface of the melt film enables a high specific transfer of kinetic energy from the gas to the melt. In the divergent part of the nozzle, the gas pressure drops sharply and the gas cannot stabilize the melt film any more. Hence the gas atomizes the melt with a constant high and uniform specific impulse. The resulting fine particle spray 7, solidifies rapidly forming spherical particles. The schematic diagram of the WIDEFLOW atomizer arrangement is shown in figure 5 (16).

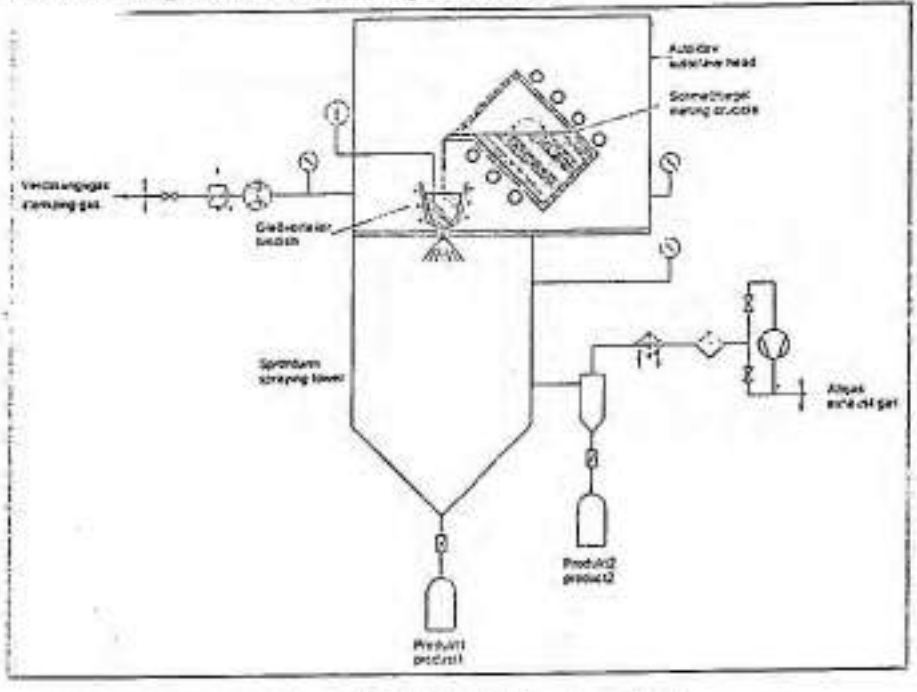

Figure 5. WIDEFLOW Atomizing Plant

SPECIFIC GAS CONSUMPTION.

A very important feature of the wideflow linear nozzle system is the quite low specific gas consumption compared to that of other existing systems. Figure 6 (17) shows the specific gas consumption data of different atomizing nozzle systems as a function of the mean particle diameter of raw powders. Since use of conventional nozzles do not result in fine powders, the results are extrapolated to small particle sizes. The wideflow system requires only 1/3 rd of the gas that a round laminar nozzle system takes and only $1/10^{th}$ of a conventional close-coupled nozzle system, for getting the same mean particle diameter. As is the case for other systems the powder fineness increases with the atomizing gas pressure as well as the gas to metal ratio.

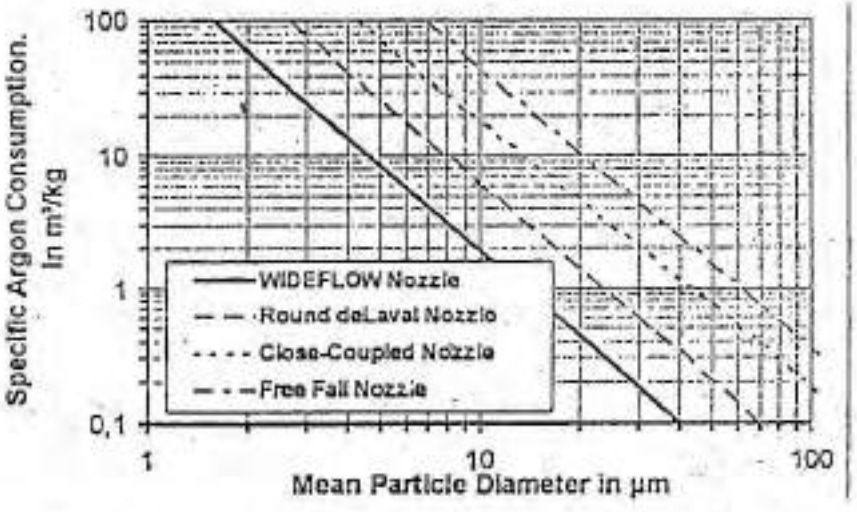

Fig. 6. Specific gas consumption required to produce metal powders of a certain mean Particla diameter d50 using different atomizing technologies (valid for argon gas)

APPLICATIONS.

Me5al injection moulding process in powder metallurgy requires essentially fine metal powders. In general these powders are specified to be 90% or more finer than 20 microns.

Figure 7 (18) shows a typical particle size distribution of 316 L stainless steel powder produced for MIM applications.

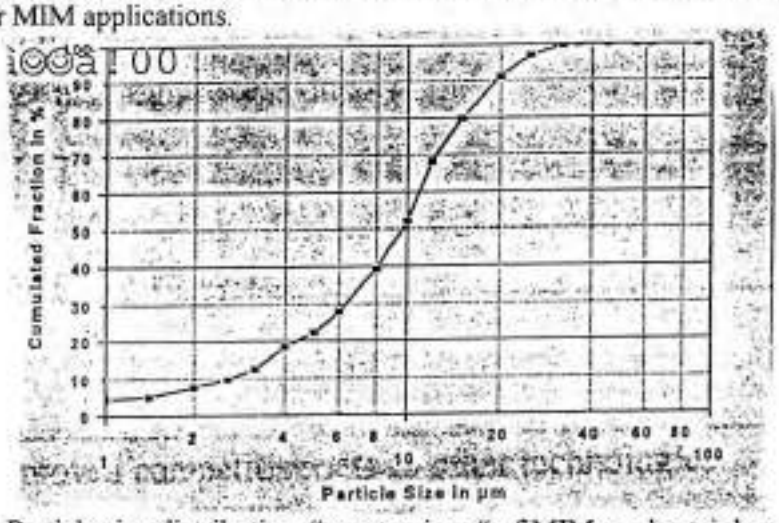

Fig. 7. Particle size distribution " as atomizes " of MIM grade stainless steel 316 L, mean Particle diameter d 50 = 9.8 microns, atomized with 25 bars argon, atomizing rate 600 kgs/hr, melt nozzle slit 0.6 30 mm, specific gas consumption 3.5 kg. Ar/kg stainless powder.

Other materials like (18) nickel-aluminides,iron, nickel and cobalt base alloys, 304, 17-4 PH stainless steels can also be atomized to meet the MIM requirements. Composite materials are another application. Non- metallic dispersoids are often available in small particle sizes and to obtain a homogeneous distribution of the dispersoids in the composite, metallic powders shouild also possess similar sizes.

Contact materials are compound materials based on silver or copper used for disconnectable electrical connections (switches). Suitable materials like Ag, AgSn, AgZn, Cu, Cr, can be in the fine particle form be made available through Wideflow process. Fine powders are also used as solder pastes for soldering SMD. This is an application that requires very narrow particle size distribution and the wideflow process to obtain such powders is most suitable.

Other often very special applications for fine metal powders are catalysts, rapid solidification materials, metallic pigments, rocket fuel (ex. –10 micron solid fuel), batteriess, thermal spraying (HVOF) and laser processes like rapid prototyping, rapid laser manufacturing. Other applications beyond the once mentioned may be found as technical innovations progress.

CONCLUSIONS.

The WIDEFLOW gas atomizing process, using linear de Laval nozzle and linear melt nozzle stabilizes a melt film by an accelerating, parallel gas flow which finally disintegrades into fine powders. Comparing with Nanoval process which uses circular melt nozzle, this new

design gives much higher production capabilities and suggests the possibility of scaling to any desired production levels. Specific gas consumption is shown to be much less compared to other gas atomizing processes. Moderate gas pressures of the order of 2.00 to 2.5 Mpa with nitrogen and Argon are shown to be adequate to produce powders of mean particle size of around 10 microns. Many advanced high-tech applications beyound classical powder metallurgy are indicated.

REFERENCES

1. Alan Lawley " Atomization, The production of Metal Powders." Metal Powder Industries Federation, Princeton, N.J. Publications, 1997, p.8, 14, 15.

2. N.Furukawa, S. Takajo, S. Somiya, T. Masumoto and H. Stabash " P/M in Japan, Status Report." Int. J. Powder Metall (25,No.3) 1989. P.225

3. Y.Seki, S.Okamoto, T. Tasigawa and N.Kawas "Effects ofAtomization Variables on Powder Characteristics in High Pressure Water Atomization Process." Metal Powder Report (45) 1990. P.41.

4. S.A. Miller " Close –coupled gas atomization of metal alloys."al Powder Report(42) 1987. P.702.

5. W.G. Hopkins " Fine Powder: Close-coupled or Open Die Atomization " Metal Powder Report (45) 1990, P.41.

6 I.E. Anderson " Boost in Atomizer Pressure Shaves Particle Size." Advanced Materials and Processes (140) 1991 P.30

7 I. E. Anderson, R.S. Figliola and H. Morton. " Flow Mechanisms in High Pressure Gas Atomization" Materials Science and Engineering (A 148) 1991,P101.

8 C.P.Ashdown, T.G.Bewely and G.B.Kenney " The Tandem Atomization Process of Ultrafine Metal Powder Production." Modern Development in Powder Metallurgy "Metal Powder Industries Federation (20) 1988, P.169.

9 C.F. Ashdown and G.B.Kenney " Ultra fine Alloy Powders for Injection Molding. " Advances In Powder Metallurgy MPI. 3. (1989) P.45.

10 Tarashankar Mahata, B.P.Sharma, S.Narasimhan, P.K.Sinha " Design Aspects of a Close-Coupled Gas Atomizer. " Tran. PMAI. (24) 1997. P.43-49.

11 A.Unal. " Influence of Nozzle Geometry in Gas Atomization of Rapidly Solidified Aluminium Alloys. " Materials Science and Technology (4) Oct. 1988. P.909-915.

Cont'd...

12. WalZ.A. Verfahren Zur Herstellung Von Feinen Metalpulven Sowie Vorrichtung Zur Durchfuhrung des Verrahrens. Patent DE 331134.3. 29-03-1983.

13 L. Gerking, " Powder from Metal and Ceramic Melts by Laminar Gas Streams at Supersonic Speeds. " Powder Metallurgy International (25) 1993. P.59-65.

14 G. Schulz " Nanoval Process Offers Fine Powder Benefits." Metal Powder Report Nov. 1996. P.30.

15 G. Schulz. " Laminar Sonic and Supersonic Gas Flow Atomization – The Nanoval Process " Adv. Powder Metall. Part. Mater. (1) 1996. P. 43-54.

16 Friedhelm Diesch and Gunther Schulz " Gas Atomization of Prealloyed MIM Powders. In Bulk Quantities" Paper Presented at the PM2 Tec '99 Conference, Vancouver, B.C. Canada.

17 Gunther Schulz " Wideflow Atomization—A technique for Gas Atomization and Spray Forming " Proceedings, Spray Deposition and Melt Atomization 2000 (2) 2000. P.521-529.

18 G. Schulz " Wideflow Melt Film Atomization – An Efficient Tool for Direct MIM Powder Production " Paper presented at P/M. World Congress, Kyoto Nov. 2000.

19 G. Schulz " Some Applications of Ultra Fine Gas Atomized Metal Powders Beyond Classical Powder Metallurgy. " Paper Presented at P/M World Congress 2000. Kyoto, Japan.

ALUMINIUM FOAM THROUGH P/M ROUTE

Ravindra Malewar, TP Bagchi and Bijoy Sarma

Defence Metallurgical Research Laboratory
(Govt. of India Minisitry of Defence)
Kanchanbagh - P.O.
Hyderabad- 500 058

Abstract

Light metal foams have recently roused interest as an innovative engineering material with great potential. Production of aluminium foams, the lightest of this family, is being studied by the authors using aluminium powder as starting raw material. A part of this activity is presented in this paper to stimulate discussion.

Effect of raw material (i.e. aluminium powder) on the foaming index of the component was studied in terms of source, chemical composition and size distributions. Foaming agent was also characterized (chemical composition, X-Ray diffraction patterns, size distribution). Process of blending of raw materials with critical parameters involved therin .(type medium, time etc.) is discussed. Effect of compaction processes (both uniaxial die-compaction and cold isostatic compaction) and its effect on the final products were also studied. Foaming cycles and their effects are discussed in details. Effect of foaming index on various process parameters is given with a brief account on concept of foaming index. Results of macroscopic studies are presented. Future course of investigation and possible field of application of this product have been highlighted.

1.0 Introduction

Metal foams are cellular materials with 40% to 90%. porosity. This porosity can be of two types:

- Closed porosity,
- Open porosity or interconnected porosity.

Foams with interconnected porosity are used for filtration purposes. Foams with closed porosity usually exhibit better engineering properties (*e.g.* damping, stiffness etc.) as compared to their open-porosity counterparts. In this paper, the experience of the authors in development of porous aluminium structure (with about 40% open porosity) through powder metallurgy (P/M) route is presented. Process flowsheet is given in Fig.1

2.0 Experimental

2.1 Characterisation of the input materials

2.1.1 Aluminium powder

Aluminium powder from different sources is used for experimentation. Their complete characterisation carried out and results are as below:

2.1.1.1 Source : M/s Metal Powder Company Ltd., Madurai (TN)
Ingot used : 98% purity Al ingot
Atomisation Medium : Argon

Chemical composition

Elements	Wt %
Al	95.5%
Fe	0.91%
Ash	0.8%
Si	1.1-1.5%
Oxides	0.915%

Particle size distribution is shown in Fig. 2

2.1.1.2 Source : M/s Maharashtra Metal Powder Company Ltd., Nagpur (MS)
Ingot used : 99.5% purity Al ingot
Atomisation Medium : Argon

Chemical composition

Element	Wt %
Aluminium	98
Fe	0.25
Si	0.1
Oxygen	0.28

Particle size distribution is shown in Fig.3

2.1.1.3 Source : Defence Metallurgical Research Laboratory, Hyderabad (AP)
Ingot used : 99.87% purity Al ingot
Atomisation medium : Argon

Chemical composition

Element	Wt %
Aluminium	98.76
Fe	0.12
Si	0.02
Oxygen	0.9 - 1.1%

Particle size distribution is shown in Fig.4

2.1.2 *Foaming Agent*

Foaming agents are those compounds that release gas when heated to its Decomposition temperature. The gas generated gets surrounded by the molten material, thus forming cells causing the entire stuff to foam. For aluminium metal foams Titanium hydride is used as a foaming agent.

Chemical formula TiH_2
Decomposition temperature ~400 C

Particle size distribution is shown in Fig.5

X-Ray diffraction study

To assess the presence of any other compounds along with TiH_2 an XRD study conducted. The XRD patterns studied which reveals that mainly it is TiH_2 with very negligible traces of $TiH_{1.971}$ and $TiH_{1.924}$. The XRD pattern is shown in Fig. 6.

2.2 *Process for production of porous aluminium structure*

It involves the following steps

1. Mixing: Aluminium metal powder is mixed with Titanium hydride powder in a typical powder blending m/c (ball mill) so as to ensure a thorough mixing of the two. Mixing time and mixing medium ensured as per the design of experiment. In order to minimise the oxidation of Aluminium metal powder during mixing wet medium of Benzene maintained.

2. Compaction: After the homogenous mixture is formed the powder mix is compacted to yield virtually dense non-porous compact. Compaction carried out in both uniaxial die compaction as well as cold isostatic press. Pressure selected as per the design of experiment.

X'Pert Graphics & Identify

Description:
PMG

Original scan : TiH2
Description of scan:
PMG

Used wavelength	: K-Alpha 1
K-Alpha 1 wavelength(A)	: 1.54056
K-Alpha 2 wavelength(A)	: 1.54439
K-Alpha 2/K-Alpha 1 intensity ratio	: 0.50000
K-Alpha1 wavelength(A)	: 1.54056
K-Beta wavelength (A)	: 1.39222
Peak search parameter set	: As Measured Intensities
Set created	: 1/1/98 08:22
Peak positions defined by	: Minimum of 2nd derivative
Minimum peak tip width (°2Theta)	: 0.00
Minimum peak tip width (°2Theta)	: 1.00
Peak base width (°2Theta)	: 2.00
Minimum significance	: 0.60

d- spacing A	Relative Intensity (%)	Angle (°2Theta)	Peak Height (counts/s)	Background (counts/s)	Tip Width (°2Theta)	Significance
2.54531	100.00	35.23100	2486.07	19.36	0.14000	14.55
2.20719	31.14	40.85067	774.20	16.92	0.12000	3.70
2.12361	0.26	42.53491	6.51	11.21	0.08000	1.00
1.56644	21.60	58.91010	536.99	10.36	0.16000	6.27
1.33745	16.24	70.32988	403.81	13.73	0.18000	5.40
1.28051	7.62	73.96086	189.46	8.81	0.08000	1.08
1.17415	0.06	81.99628	1.47	3.88	0.64000	0.61
1.11091	1.25	87.79594	31.02	6.41	0.24000	1.39
1.04393	0.05	95.09978	1.28	6.32	0.24000	0.61
1.01962	5.66	98.13113	140.72	11.68	0.16000	1.71
1.01674	3.87	98.50526	96.13	12.29	0.16000	0.70

3. Thermal treatment: This compact is then heated to a temperature close to liquidus (melting point of aluminium in case of pure aluminium) temperature. During this thermal treatment hydrogen gas is generated at the decomposition temperature of the foaming agent.

2.3 *A typical comparison between Aluminium powder from various sources and Titanium Hydride in terms of size distribution and total oxygen content*

Source	10 % Fraction	50% Fraction	90% Fraction	SSA (m^2/g)	Oxygen PPM
1. MEPCO	14.11 micron	42.03 micron	91.69 micron	0.0790	915
2.MMPL	15.77 micron	87.80 micron	270.57 micron	0.0594	280
3.DMRL (In House)	29.66 micron	64.78 micron	110.60 micron	0.0488	1100
TiH_2 F.A.	6.01 micron	16.23 micron	32.35 micron	0.1156	NA

Cumulative particle size distribution of aluminium metal powder from various sources are compared with each other and also with that of foaming graph as shown in fig.7 It is evident from this comparison, MEPCO powder in spite of being the most suitable did not serve the purpose due to high oxygen content (see table above). In-house powder that has high oxygen content simultaneously exhibited coarser size distribution. In case of MMPL the powder meets the average requirements.

Above results state that in addition to the particle size, oxygen content plays a vital role. This oxygen most of which is in the form of surface oxide delays the sintering at the contacts thereby allowing generated gas from foaming agent to escape out. The success of the process lies in the fact that the release of gas at decomposition temperature of foaming agent should see the onset of localised liquid formation so as to trap the released gases.

2.4 *Experimental Details*

Constants: Powder source-M/s Maharashtra Metal powder Ltd., Nagpur
Mixing - Wet mixing in benzene medium

Uniaxial die compaction

%TiH_2	Mixing Type	Mixing Time min	Mpa	GD g/cc	F.Temp C	TTT min	FD g/cc	*FI	F/c atm
3	Ball mill	60	4352.3	2.68	660	20	1.6	1.68	Open
3	Ball mill	120	4352.3	2.68	660	20	1.6	1.68	Open
3	Ball mill	180	4352.3	2.68	660	20	1.6	1.68	Open
1.5	Ball mill	60	4352.3	2.68	660	20	2.68	1	Open
1.5	Ball mill	120	4352.3	2.68	660	20	2.68	1	Open
1.5	Ball mill	180	4352.3	2.68	660	20	2.68	1	Open
1	Ball mill	60	4352.3	2.68	660	20	2.68	1	Open
1	Ball mill	120	4352.3	2.68	660	20	2.68	1	Open
1	Ball mill	180	4352.3	2.68	660	20	2.68	1	Open

Cold isostatic compaction

%TiH_2	Mixing Type	Mixing Time min	Kbar	GD g/cc	F.Temp C	T.T.T. min	FD g/cc	*FI	F/c atm
3%	Ball mill	60	3	2.68	660	20	1.6	1.68	Open
3%	Ball mill	120	3	2.68	660	20	1.6	1.68	Open
3%	Ball mill	180	3	2.68	660	20	1.6	1.68	Open

(GD-Green density; F.Temp - Foaming Temp; TTT-Thermal TreatmentTime; FD-Final density; FI- Foaming index)
(Except for the above used powder source, all other sources have failed in showing the propensity to foaming)
Foaming index = Initial density/ Final density
It gives the dimension less figure representing the degree of foaming.

Both uniaxially die compacted and cold isostatically pressed compacts have shown propensity to foaming. As shown in the data tables out of the various attempted in-put process variables percentage of the foaming agent and Thermal treatment time could be optimised to get aluminium metal foam of 1.6 g/cc density. It shows that to get a Aluminium metal foam of 1.6 g/cc both uniaxial as well as cold isostatic press compaction can be made use of.

3.0 Concluding Remarks

Aim of the present activity is to produce Aluminium foam with porosity fraction as high as possible with low specific weight. In all the cases where foaming has been observed, localisation of pores is on the higher side leading to open porosities instead of close ones. This has put restriction on generating the cellular structure. Some of reasons can be attributed to

- Lower green density, or
- Accumulation of gas generated giving rise to big pores, or
- Delayed sintering due to oxide layer on the surface of aluminium powder particles

In all the cases sample was loaded in to the f/c maintained at a given temperature ensuring the sudden rate of heating. Further work is going on to get more uniform porosity with cellular structure.

References

1. H. D. Kunze, J. Baumeister, J. Bamhart, M. Weber -P/M Technology For The Production Of Metal Foams,Pmi Vol. 25, No. 4,1993
2. J. P. Droplet - Low Density Foams Produced From Aluminium Powders, IJPMAPT, vol. 13 , no.3 , July, 1977
3. Chin-Jye(Mike), H. H. Eifert, J. Banhart and J. Baumeister - Metal foams, Advance materials and processes 11, 1998
4. G. J. Davis , Shu Zhen - Metallic foams: Their production, properties and application, JOMS 18,1983

Some applications of metal foams

- *Energy absorption application.* Using suitable elements made of aluminium foam in the crash zones of automobiles, it is possible to induce controlled, programmed deformation with maximum energy consumption.(for side protection also same thing can be exploited)

- *Net weight saving with high stiffness application.* Hollow profiles made of steel or aluminium can be filled with aluminium foam giving rise to better deformation behaviour of these parts during loading. Other parts of the car body or engine can be made of or reinforced with alumunium foam. This gives better stiffness combined with net wt saving.

- *Lightweight application.* Replacement of honeycomb structure with sheets of foamed aluminium will lead to reduced cost and more isotropic properties. The complications involved in making the honeycomb structure out of rolled sheets will be totally eliminated.

- *Damping out the vibration application.* Complex shaped parts of the foamed metals may be used to encapsulate the components, which produce noise out of heavy vibrations. Elastic modulus of the foam materials can be varied by playing with the density of foam. Because of this it is possible to match the resonance frequency of the foamed parts. This will help in restricting the detrimental vibrations.

- *Thermal resistance applications.* Closed cell foamed metal parts can be exploited to encapsulate the component which are hot due to thermal insulation provided by foam.

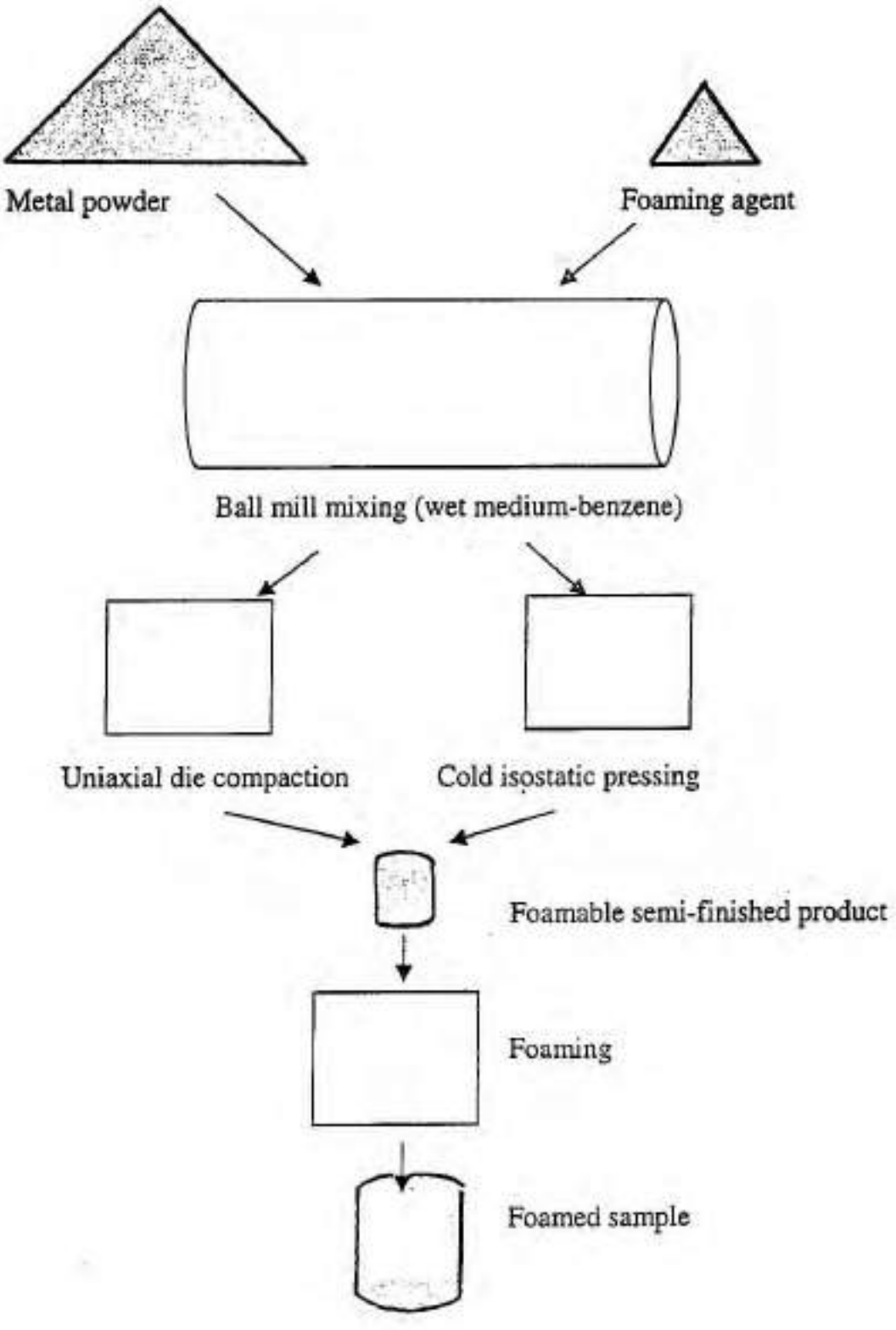

Fig. 1 **Process flowsheet for production of aluminium foams**

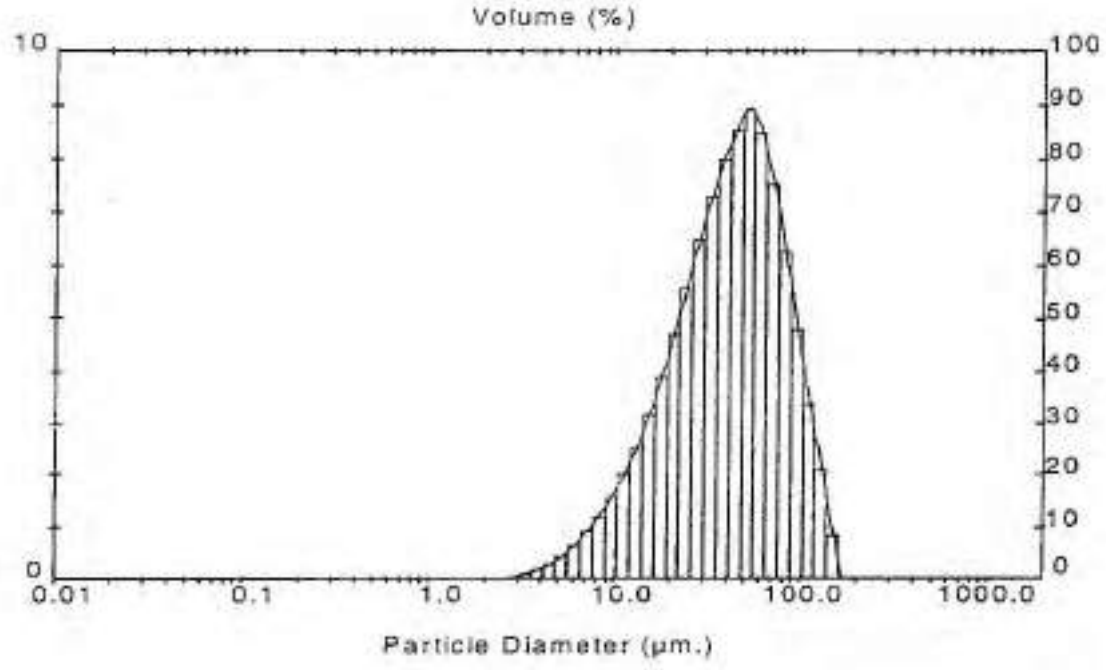

Fig. 2 Particle size distribution of MEPCO aluminium powder

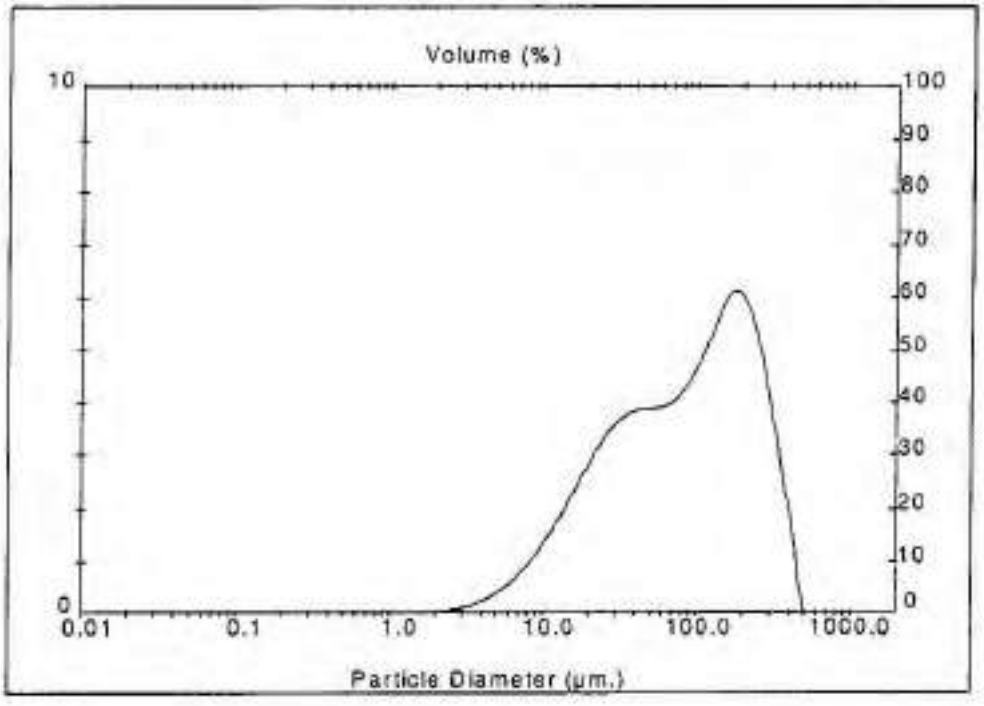

Fig. 3 Particle size distribution of MMPL aluminium powder

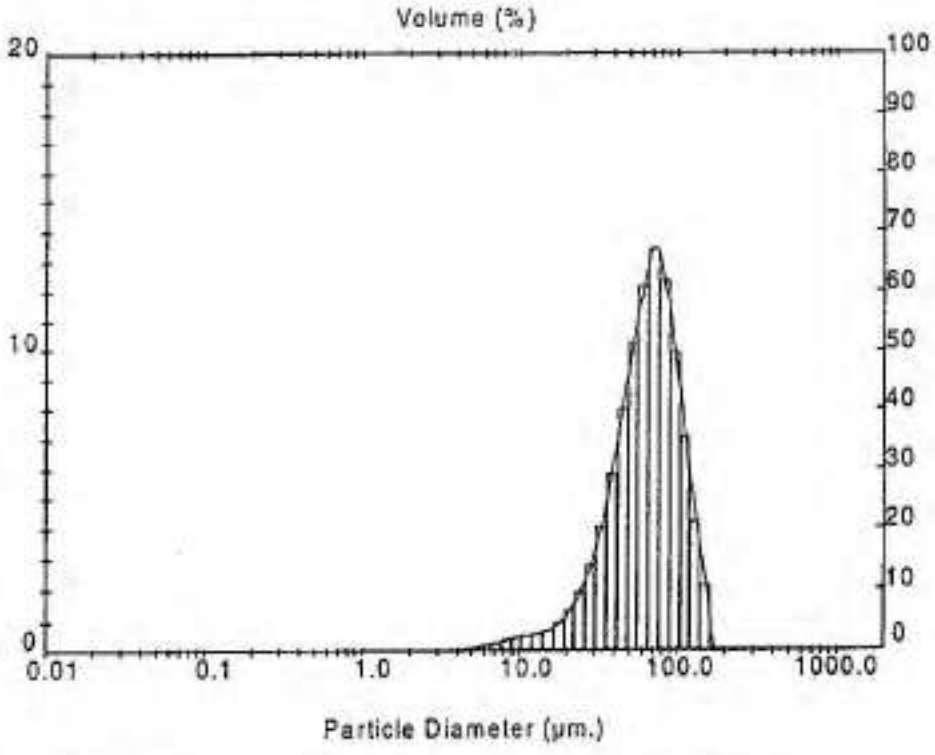

Fig. 4 Particle size distribution of DMRL aluminium powder

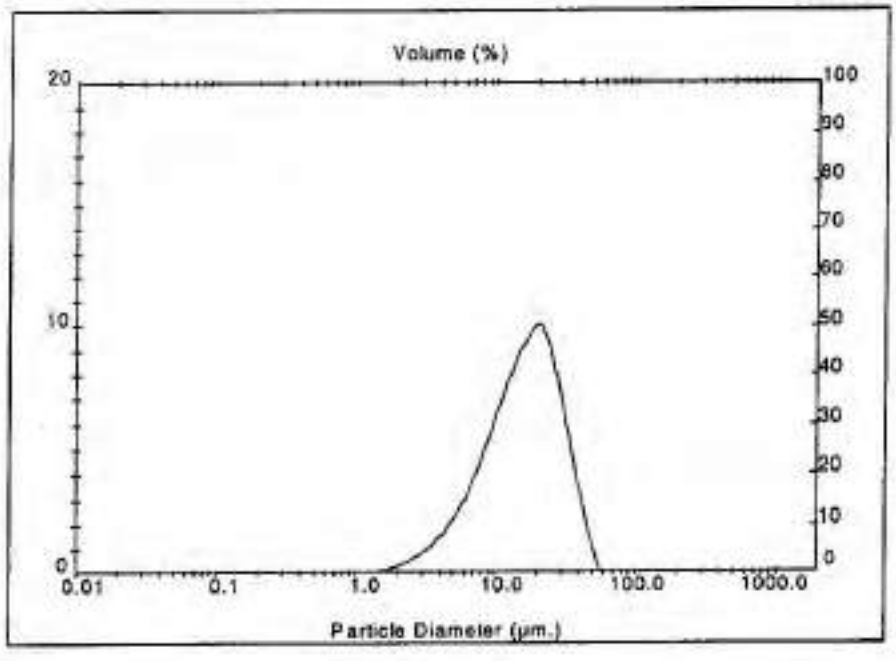

Fig. 5 Particle size distribution of titanium hydride powder

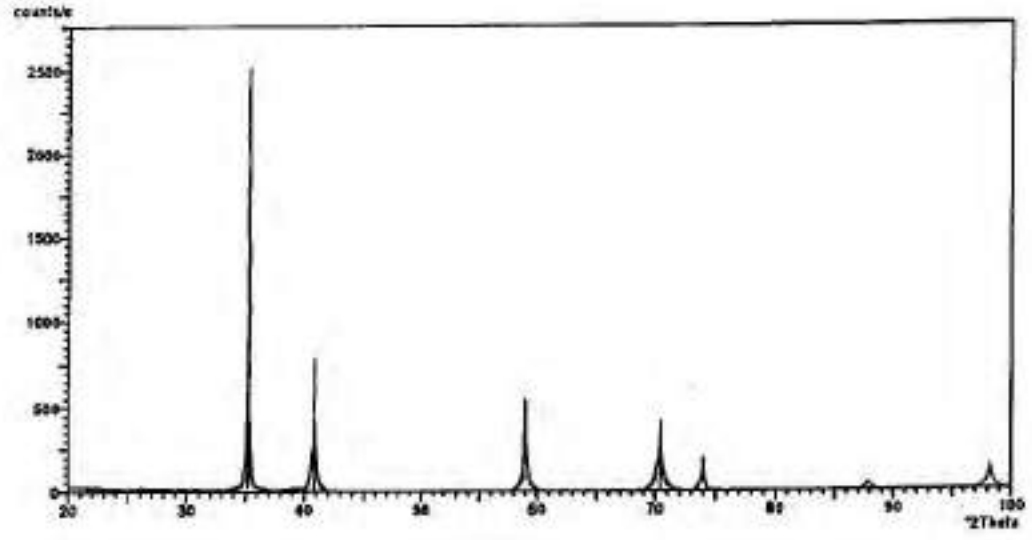

Philips Analytical

Fig. 6. The XRD Pattern of TiH_2

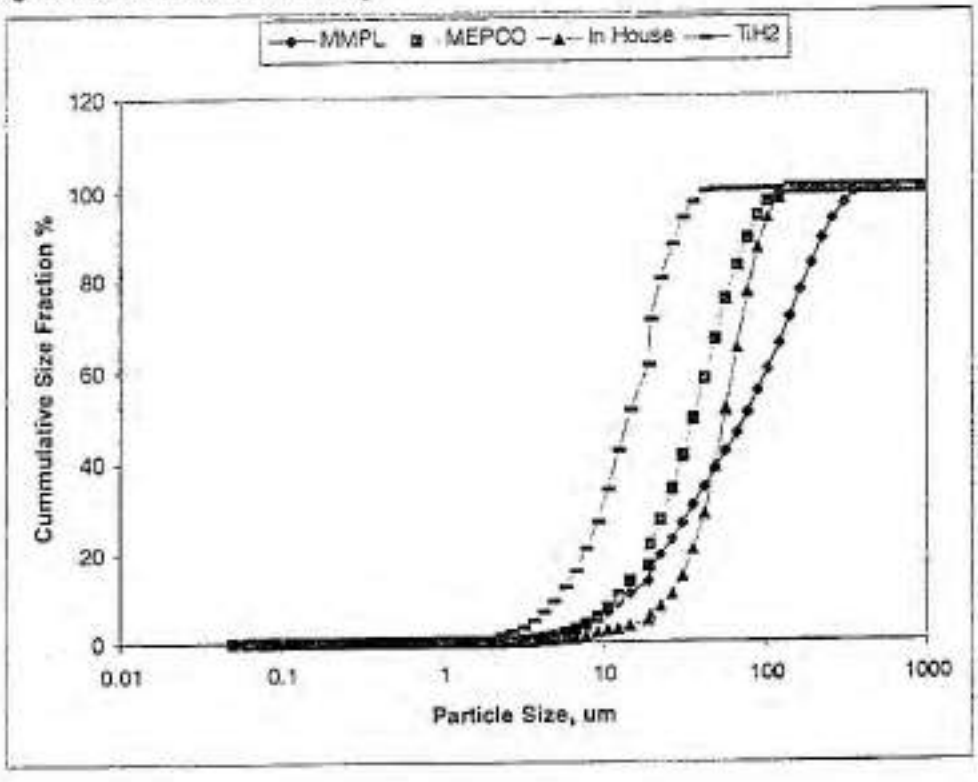

Fig. 7 Comparison of cumulative particle size distributions of all the powder used

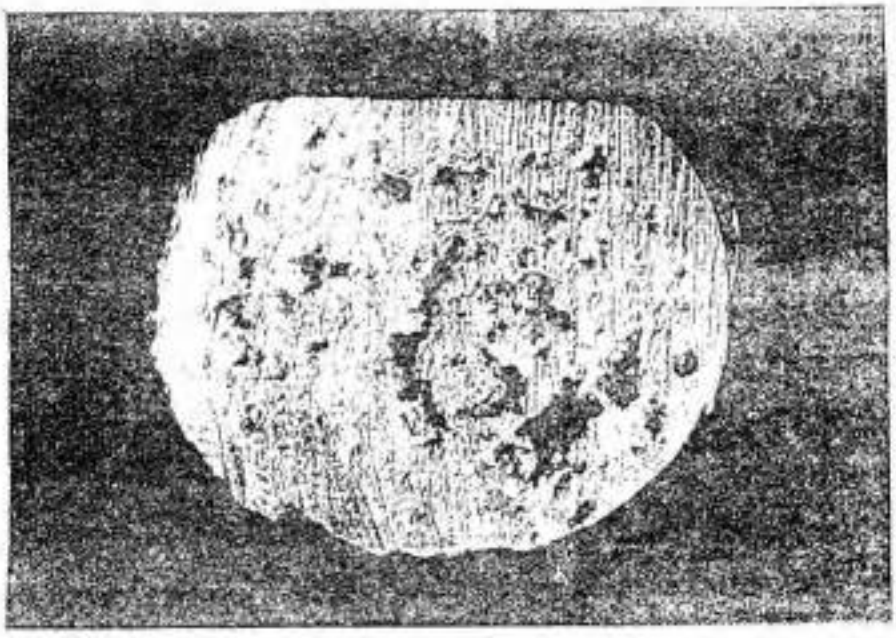

Fig. 8. Transverse section of aluminium
(uniaxial die compacted at 4352.3 MPa, heated at 660 C, 20 min.)

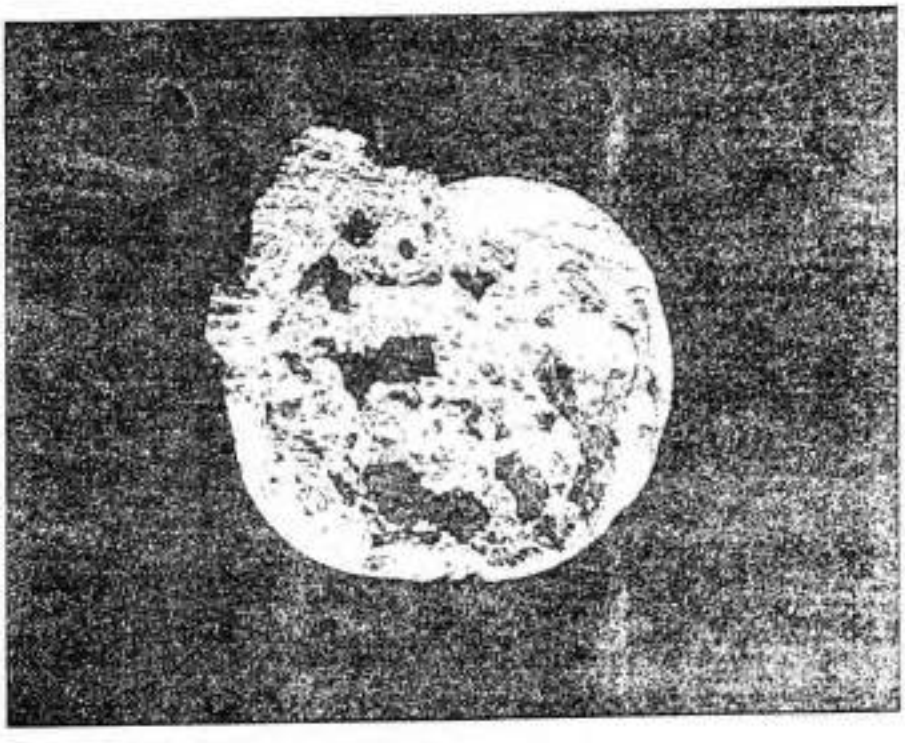

Fig. 9. Transverse section of aluminium
(cold isostatically compacted at 3 kbar, heated at 660 C, 20 min.).

Production and Characterisation of in-situ ceramic matrix Composite from indigenous alumino-silicates

K.L.Hansda* R.J.Singh ** R.R.Dash* M.P.Singh**

* Scientist, National Metallurgical Laboratory (CSIR), Jamshedpur

** Professor, Met. Engg. & Mat. Sci. Dept. Regional Institute of Technology, Jamshedpur

Abstract

Ceramic matrix composite with silicon carbide whisker is an important composite reinforcing material and has gained considerable importance in the current year owing to their enhance mechanical property, high fracture toughness, high temperature creep resistance, slow crack growth etc. Kaolinite with amorphous / crystalline carbon was used for present investigation. Thermal treatment in Dynatech furnace was carried out at 1600°C for two hours in vacuum/ Argon atmosphere. For the characterisation of the product phases, XRD for phase analysis and SEM for structural analysis were used.

The result obtained indicates that higher yield of SiC in the form of whisker (β-SiC) in the matrix of either α-Al_2O_3 or AlN could be possible. The structural investigation revealed the distribution of silicon carbide in the matrix and the product phases such as Al_2O_3 or AlN respectively depending on the type of atmosphere prevailed during high temperature synthesis of these materials. Under certain conditions of temperature - time cycle and type of carbon used, the silicon carbide showed rod type of growth morphology. When amorphous carbon was used as a source material with Kaolinite clay the predominant growth morphology was observed to be Whiskers. However, Crystalline form of carbon on the other hand, exhibited α-SiC growth morphology.

1.0 INTRODUCTION

Alumino-silicates are potential raw materials for the preparation of alumina-silicon carbide and aluminium nitride-silicon carbide CMCs by reaction with either amorphous or crystalline carbon. While alumina-silicon carbide is produced by carbo-thermal reaction, AlN-SiC CMC has been produced by nitridation reaction[1]. At and beyond 1400°C, alumino-silicates become very unstable, thus favouring the reaction of silica and carbon to form silicon carbide which grows as whiskers or particulates depending on the type of carbon source used in the reaction.

India has vast resources of high purity Kaolinite minerals suitable for use in the preparation of the ceramic matrix composites. Kaolinite clays have been found to respond to the high temperature reactions with carbon. The amenability of the carbo-thermal or nitridation reactions is possibly due to structural organisation of the alumino-silicates (Kaolinite type). Additionally selected Kaolinite group of minerals are low in alkalies and

other impurities having distinct advantages over other classes of minerals such as Montmorrillonite, Vermiculite, Beidelite etc.

Due to plentiful availability of relatively purer alumino silicates indigenously, there is a distinct economic advantage in using these materials for the preparation of expensive in-situ ceramic matrix composites[2]. Further, handling of silicon carbide whiskers / particulates is hazardous. The in-situ Al_2O_3-SiC CMC does not create pollution problems[3].

It has been observed by various workers that the mechanical properties of Al_2O_3-SiC and AlN-SiC produced from mechanical mixing are much inferior to those produced from the in-situ CMCs[4]. There is restricted diffusion of Al_2O_3-SiC and AlN-SiC on the formation of solid solution due to covalent nature of the reacting species. Homogeneous solid solution with improved mechanical properties is expected to form since the phases nucleate starting from the same material [5,6]

2.0 EXPERIMENTAL

2.1 RAW MATERIALS

A large number of naturally occurring alumino-silicates were identified for investigation to asses their suitability as feed stock for the preparation of Al_2O_3-SiC and AlN-SiC ceramic matrix composites. The alumino-silicate minerals belonged to the group of montmorillonite, Kaolinite and sillimanite. At the first step, the chemical analysis and DTA studies were undertaken to examine their impurity contents and type of clay group.

2.2 Preparation of CMC

2.2.1 Processing of Raw Materials

The clays were processed through grinding to obtain below 10 micron size. These were thoroughly mixed with carbon using absolute alcohol as medium and finally dried at a temperature of 80-100°C. The dried powder was taken in graphite crucible and heated at various time temperature combinations in the Argon atmosphere. Each graphite crucible contained twenty gms of processed clay mixed with carbon. For the preparation of AlN-SiC CMC pure nitrogen was used instead of Argon following the same process.

2.2.2 Characterisation

The characterisation of produced CMCs was made using XRD and SEM techniques. The chemistry and high temperature reactions were optimised based on the characterisation.

Upscaling of the production of CMC in 2 kg scale was undertaken successfully in a graphite resistance high temperature (2500°C) atmosphere controlled furnace.

3.0 RESULTS AND DISCUSSIONS

3.1 Preparationof CMC from Alumino-Silicate Minerals

Several alumino-silicate minerals were examined chemically to study its suitablity for use as raw materials for the preparation of CMCs. [Table I] gives the chemical compositions of the raw material. The DTA studies are shown in the Fig.1 and Fig.2 depicts the DTA of china clay. The possible reaction between alumino-silicate and carbon (amorphous or crystalline) is as follows :

$$SiO_{2(S)} + 3C\ (s) = SiC\ (s) + 2\ CO\ (g)$$
$$2Al_2O_3 + 3C\ (S) = 2Al_4O_4C(S) + 2\ CO\ (g)$$
$$Al_6Si_2O_{13}(S) + 6\ C(s) = 3Al_2O_3(S) + 2SiC(S) + 4\ CO\ (g)$$
$$SiO_2(S) + CO\ (g) = SiO(g) + CO_2\ (g)$$
$$SiO\ (g) + 2\ C(S) = SiC(S) + CO\ (g)$$

3.2 Characterisation of CMC :

The phases formed as a result of reaction with amorphous carbon (purity 99.9%) have been observed to comprise mainly α-Al_2O_3 and β-SiC vide XRD figure (3). Figure 4 depicts the XRD of aluminium nitride and silicon carbide ceramic matrix composite. Further, it has been observed that when amorphous carbon has been added as precursor, whiskers have mainly grown in the matrix, while crystalline carbon favoured the growth of rod shaped and particulate SiC vide SEM figures 5 and Fig.6 respectively.

4.0 CONCLUSIONS

- Mined Neyveli clay can be successfully used for the preparations of Al_2O_3-SiC and AlN-SiC CMCs
- β-SiC and α- SiC maybe produced depending on the type of carbon source using amorphous or crystalline form of carbon
- Attractive economic return is envisaged as CMCs have been prepared from abundantly available indigenous sources of the feed stock.
- Pollution / health hazards arising from in-situ Al_2O_3-SiC or AlN-SiC CMCs is lowered down as handling of individual whiskers or particulates is being avoided

ACKNOWLEDGEMENT

The authors gratefully acknowledge the guidance and keen interest of Prof.P.Ramachandra Rao, Director, National Metallurgical Laboratory in the present investigation. The authors are also thankful to Prof. R. Yadav, Principal, R.I.T Jamshedpur for his kind permission to present and publish this paper in PMI – Tech Meet, 2001.

SELECTED BIBLIOGRAPHY

1. M.R.Pendugonda, A.C.D Chaklader, Alumina-silicon carbide composites from Kaolinite-carbon precursons by hot pressing, Solid State Phenomena 1989 Vol 839, pp 457-470.
2. P.K.Rohatgi, Cast Metal Matrix composites Metals Hand Book ASM International 1988, 9th Edition , Vol. 15, pp 840-854.
3. S.F.Moustafa,Technical note, Canadian Metallurgical Quarterly 1994, Vol 33, No.3, pp 259-264
4. P.K.Rohatgi, International Material Reviews, 1994, vol 30, No.I
5. H.Lagale and D.J.Lioyd, Micro structural analysis of Al-SiC composites Canadian Metallurgical Quarterly 1989 Vol.2, No.2, pp 145-152.
6. J.A.Zhang, L.C.Zhang, Y.W 1992, Particle effects of friction and wear of aluminium matrix composites, Jr.of Mat. Sci.30, 1995 pp 5995-6004
7. D.J.Lloyd Particle Reinforced Aluminium and Magnesium Matrix Composites "International Materials Reviews 1994, Vol 39, No.1
8. Surappa M.K & Rohatgi P.K "Preparation and Properties of Cast al-Allys Ceramic Particulate Composites" J.Mater Sci, 1981, 16(4) 983
9. Avigdor Zangvil & Robert Rub "Phase Relationship in SiC-AlN System" Jr.Am.Ceram.Soc.71 (10) 884-90 (1988)

Table 1 : Chemical analysis of Raw Materials

Chemical Constituents (%)	China Clay (%)	Orissa Kaolinite Clay (%)	Sillimanite Rock (%)	Sillimanite Sand (%)	Minestone (M) (%)	Shell Material (N) (%)
Al_2O_3	37.66	30.05	50.50	60.15	17.46	28.32
SiO_2	44.80	58.85	37.00	33.2	66.16	53.01
ZrO_2	Trace	Trace	Trace	Trace	Trace	Trace
$Fe_2O_3$1.54	1.30	1.02	1.15	6.22	5.16	
Tio_2	0.60	0.90	0.30	Trace	n.f.	n.f.
CaO0.50	0.50	0.36	1.2	1.41	3.72	
MgO	Trace	0.50	0.47	1.25	0.40	0.75
Na_2O	Trace	Trace	0.30	0.20	n.f.	n.f.
K_2O	n.f.	Trace	0.07	0.06	0.93	0.41
Lol	14.33	12.0	9.86	1.11	-	-
Fixed Carbon	-	-	-	-	8.08	37.04
Moisture	-	-	-	-	0.34	2.74

Table 2. Chemical Analysis of Gujrat clays

Samples Marked	Chemical constituents %								
	SiO_2	Al_2O_3	Fe_2O_3	TiO_2	CaO	MgO	Na_2O	K_2O	LOI*
H_1	42.0	19.20	7.20	1.20	4.23	3.12	4.1	2.22	16.70
H_2	41.00	19.00	8.0	1.30	4.95	2.96	4.14	2.30	16.30
H_3	43.8	14.60	8.8	1.50	4.7	2.90	4.28	2.29	17.0
H_4	43.50	14.50	7.6	1.4	5.07	3.1	4.1	2.47	18.2
H_5	44.0	15.25	8.00	1.25	4.45	2.96	4.33	199	17.50

*LOI Loss on Ignition

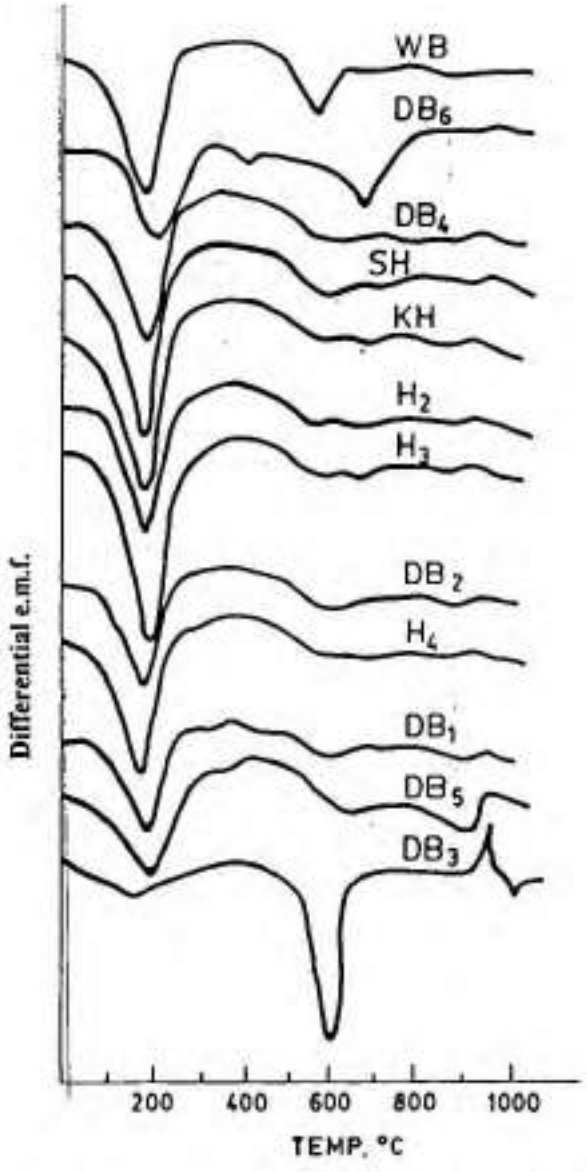

Fig -1 : DTA OF SOME TYPICAL INDIAN CLAYS

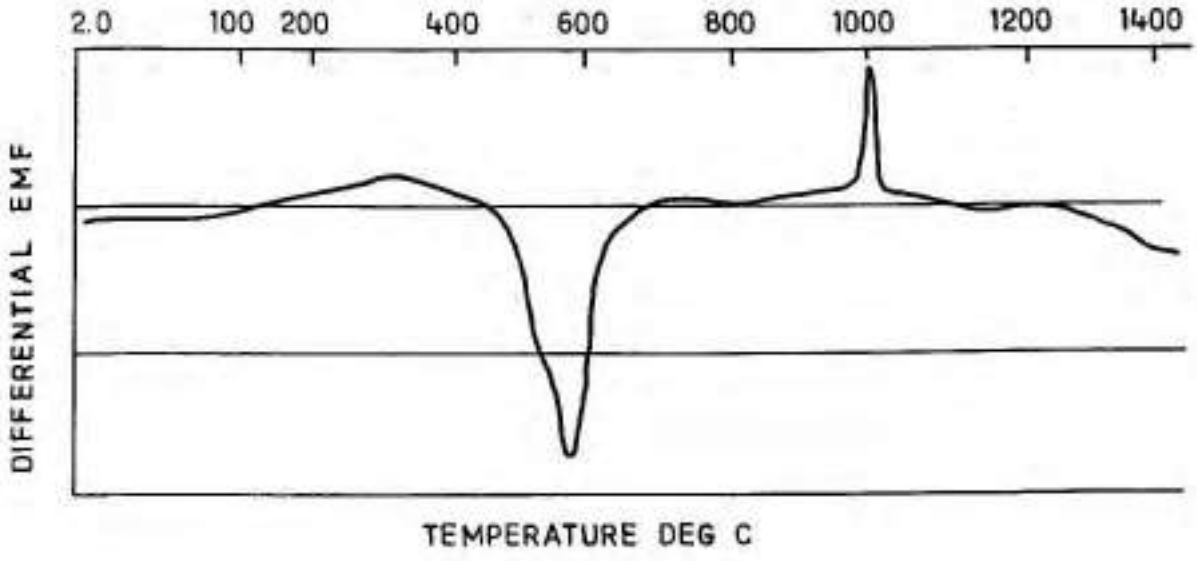

Fig 2. Differential Thermal Analysis of China clay

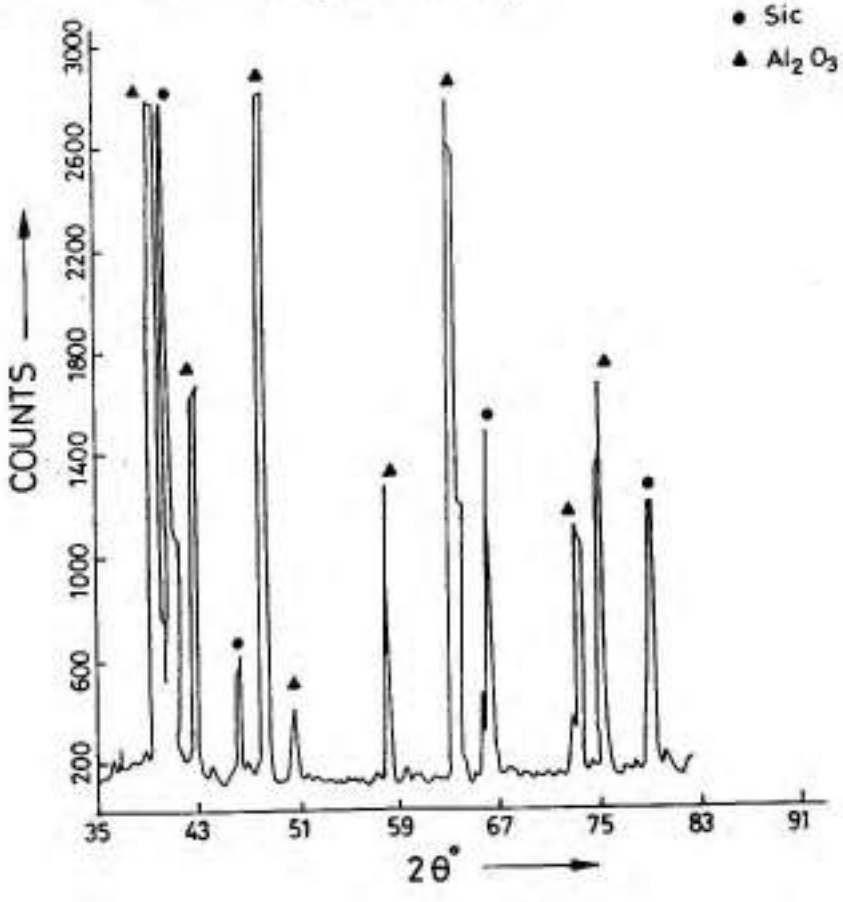

Fig. 3. : XRD pattern of alumina - silicon carbide composite

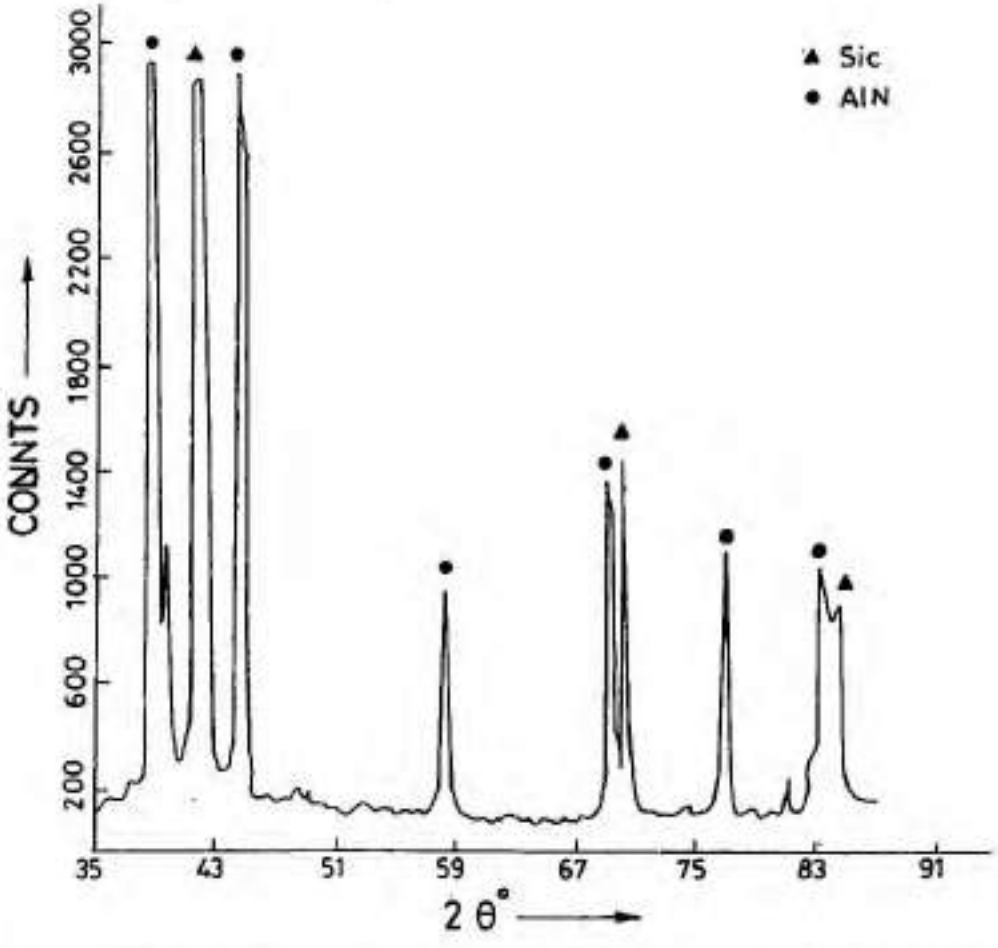

Fig. 4. : XRD pattern of aluminium nitride and silicon carbide composite.

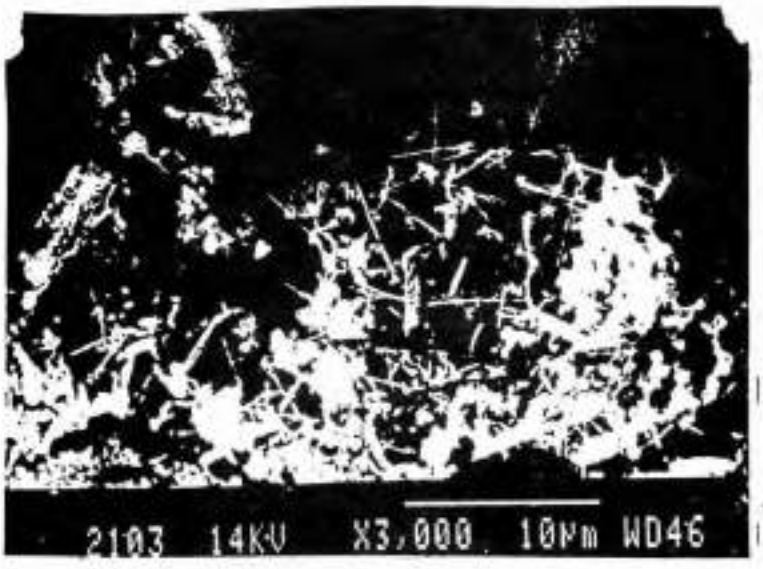

FIG. 5. IN-SITU FORMATION OF Al_2O_3 - SiC BY USING AMORPHOUS CARBON.

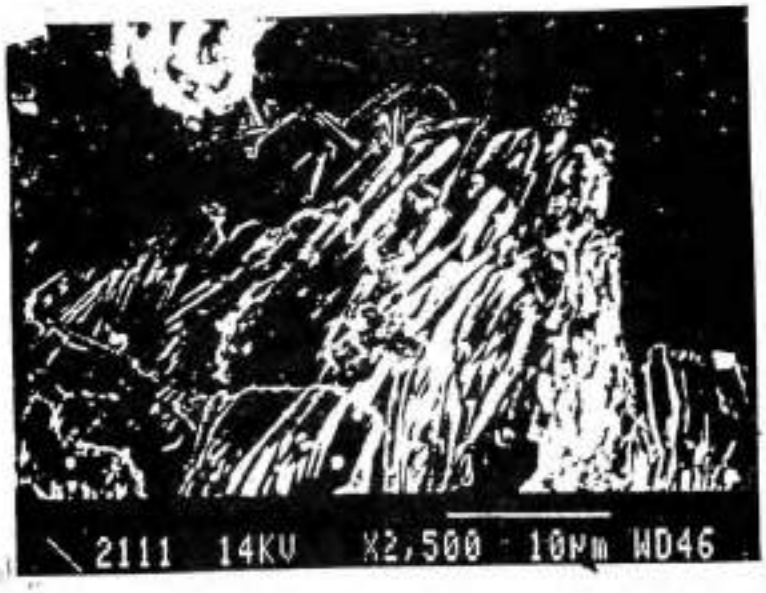

FIG. 6. IN-SITU FORMATION OF Al_2O_3 - SiC BY USING ACTIVATED CHARCOAL.

STRUCTURE - PROPERTY BEHAVIOUR OF Al_2O_3 - SiC COMPOSITES FABRICATED BY POWDER PROCESSING ROUTE

A. Chakraborty, R. Mitra, S.V. Kamat and K.K. Ray*
Defence Metallurgical Research Laboratory, Hyderabad
*Indian Institute of Technology, Kharagpur

ABSTRACT

Silicon Carbide reinforced Alumina matrix (Al_2O_3-SiC) composite is a potential structural system, because of its improved mechanical and thermal properties as compared to those of the monolithic matrix. In this study, efforts were directed to understand the role of different morphologies of discontinuous second phase SiC reinforcement on the structure - property behaviour of Al_2O_3-SiC composites fabricated by powder processing route. Initially, three different morphologies of discontinuous SiC reinforcement were selected, namely, SiC particulate (SiC_p), SiC platelet (SiC_{PL}) and SiC whisker (SiC_w). For all these three morphologies, 25 vol% of SiC reinforcement was optimized for their incorporation in the Alumina matrix. Vacuum hot pressing route was established to process dense Al_2O_3-SiC composites having uniform distribution of the second phase for all the three composites. The composites were characterized by evaluating their mechanical properties (flexural strength, fracture toughness, hardness and elastic modulus) at both room and elevated temperature. For all the systems, improvements in the properties of the composites were observed in comparison with that of the monolithic matrix. To understand the reasons

behind these improvements, the roles of different strengthening and toughening mechanisms were studied by analyzing the fractographic data and the crack path - second phase interaction behavior for the three systems. Interfaces of all the composites were observed by carrying out thorough TEM studies. Finally, the fractographic data and the mechanical properties were correlated with the microstructural and interfacial results to observe the effect of different morphologies of SiC reinforcements on the structure - property behaviour of these composites.

INTRODUCTION

There has recently been a resurgence of interest in ceramics for a variety of high performance structural applications, ranging from high temperature gas turbines and adiabatic diesel engines to cutting tools and other wear-resistant parts [1]. In each case the applications make use of the beneficial properties of ceramics, including high stiffness, strength and hardness, low density and good resistance to corrosion, oxidation, wear and erosion at high temperatures. In most structural applications, the primary disadvantage of ceramics is their inherent lack of toughness, which renders them sensitive to sudden catastrophic failure in response to accidental overloading, contact damage or rapid temperature changes. This has led to attempts for developing ceramic matrix composites (CMC) which provide

the best possible toughness and thermal shock resistance without significant loss of other desirable properties [2].

A variety of strategies has been adopted in the search for greater toughness. These include incorporation of metallic and/or ceramic fibers and/or whiskers [2-5]; incorporation of more or less equiaxed second-phase particles, both ductile [6-9] and brittle [10-11]; control of grain size, porosity or other microstructural features [12,13]; and transformation toughening by the incorporation of tetragonal ZrO_2 (zirconia) particles [14,15]. Second phase particles can play a number of roles. They can deflect cracks out of their paths [16,17], can bridge the crack behind the crack tip [18], cause them to bow between obstacles [19], cause them to bifurcate [20], or cause the nucleation of additional microcracks ahead of the primary crack [21]. Among the various CMC systems studied so far, Silicon carbide reinforced Alumina (Al_2O_3 - SiC) is considered to be one of the most successful material, primarily due to the achievement of significant property enhancement for the Al_2O_3 matrix at both room and elevated temperature by incorporation of SiC reinforcement [22,23].

PRESENT STUDY

The present work is concerned with establishing the structure - property behaviour of Al_2O_3 - SiC composite systems incorporated with three different morphologies of SiC reinforcement, namely : i) SiC

particulates (SiC_p), ii) SiC platelets (SiC_{pl}) and iii) SiC whiskers (SiC_w). The morphology of the reinforcement is believed to play an important role in dictating the degree in improvement of properties of the monolithic matrix [24]. Secondly, the change in morphology of the reinforcement is also responsible for giving rise to differential crack path and fracture behaviour in the composite system [25]. Since Al_2O_3 - SiC composite is a proven potential system, in this study, efforts are directed for studying the role of these three different morphologies on structure - property relations on these composites.

EXPERIMENTAL

High purity Al_2O_3 and SiC reinforcement were used in the present study. Table 1 shows the source and average particle size / aspect ratio of all the raw materials in as received condition. The process flow chart followed for fabricating the Al_2O_3-SiC composites is illustrated in Figure 1. Al_2O_3 and the three SiC reinforcement were taken in required proportions (25 vol% each) and then wet blended in an ultrasonic mixer. The blended powder was vacuum hot pressed using a GCA, USA make hot press at temperatures between 1800°C and 1850°C and pressure of 30 MPa. For the sake of comparison, pure Al_2O_3 without any reinforcement was also processed following the pressureless sintering route. The x-ray diffraction patterns of

all the three as received SiC reinforcement are shown in Figure 2, where it is seen that all are having β phases.

Flexural strength was measured on a Instron 1185 Testing machine using 3 point bend specimens. A loading rate of 0.5 mm / min was used during testing of all the samples. The test samples were prepared in the form of rectangular bar specimens having dimensions as : 40mm (Span : L) x 5 mm (Breadth : B) x 5 mm (Width : W). The flexural strength, σ, was calculated as,

$$\sigma = 3 P_{max} L / 2BW^2 \qquad \ldots\ldots\ldots (1)$$

where, P_{max} is the maximum load obtained from the load displacement curve.

Table 1 : Source, purity and size of the raw materials in as received condition

Sl. No.	Material	Source	Purity level (%)	Av. Particle size (μm) / Range of aspect ratio
1.	Al_2O_3	M/s Baikowski International, USA	99.8	1.06
2.	SiC_p	M/s Superior Graphite Co., USA	99.6	1.91
3.	SiC_{pl}	M/s Tateho Chemical Co., Japan	99.2	4 - 10
4.	SiC_w	-Do-	98.2	20-200

Fracture toughness (K_{IC}) was determined using single edge notched beam (SENB) specimen (under 3 point bend loading) having following dimensions : Span (L) = 40mm, Breadth (B) = 5 mm and Width (W) = 10 mm. The notch in the SENB specimen was made using a ISOMET diamond

wheel having a thickness of ~ 100 μm which resulted in a notch root radius of ~ 60 μm. The notch depth was maintained at about 0.5 to 0 .55W (Figure 3). The fracture toughness values were calculated using the following equation [27],

Table 2 : Properties of the composites in comparison with monolithic matrix

Properties / Designation	% Theoretical density	Hardness (GPa)	Fracture Toughness (MPa√m)	Flexural Strength (MPa)	Elastic Modulus (GPa)
Al_2O_3	99.6	16.2 (0.2)	2.6 (0.3)	276 (10)	375 (5)
ASP	98.1	18.1 (0.3)	4.1 (0.4)	410 (14)	415 (7)
ASPL	94.7	15.9 (0.4)	5.6 (0.6)	390 (19)	385 (9)
ASW	98.1	18.6 (0.3)	6.6 (0.6)	610 (18)	430 (8)

****Standard deviations on mechanical properties are given in brackets in Table 2**

$$K_{IC} = (P\,L / B\,W^{3/2})\,.\,f(a/W), \text{ with,}$$

$$f(a/W) = 3\,(a/W)^{1/2}\,[1.99 - (a/W)\,\{1 - (a/W)\}\,\{2.15 - 3.93\,(a/W) + 2.7\,(a/W)^2\}] \times [2\,\{1 + 2(a/W)\}\,\{1 - (a/W)\}^{3/2}]^{-1} \quad \ldots\ldots\ (2)$$

"a" and "P" being the respective notch tip radius and the max. load obtained from the load displacement curve

The fractured specimens were examined using both JEOL and LEO scanning electron microscopes. Indentation tests were carried out for studying the crack path - microstructure interaction behaviour. An indentation load of 30 kg was used by using a Vicker's hardness tester (Wolport, Germany) in order to generate the crack paths from the corners of the indentation mark.

RESULTS AND DISCUSSION

Figure 4 shows the effect of volume fraction of SiC whiskers on both green and sintered densities of the Al_2O_3 - SiC_w composite. It is observed that beyond a volume fraction of 25%, both green and sintered densities start decreasing to a considerable extent. It is generally known that higher loading of whiskers decrease the matrix densification rate (Figure 5), which gives rise to the lower density of the composite [28]. The same was observed to be true for the other composites and hence, the volume content of the SiC reinforcement was fixed at 25% for all.

The respective SEM pictures of as received SiC reinforcements are shown in Figure 6. It is observed that the SiC particles are equiaxed in nature. On the other side, Both SiC whiskers and SiC platelets are observed to have specific aspect ratio. Although majority of the SiC whiskers are observed to be of rod shaped nature having specific length to diameter ratios, the SiC platelets have various types of shapes. The latter fact is primarily responsible for inadequate density of the Al_2O_3 - SiC_{pl} composite, due to lower packing density obtained from these various shaped platelets.

The respective optical micrographs of deagglomerated SiC particulates and whiskers using both acetone and butanol are shown in Figures 7 and 8. It is observed that butanol has produced a better deagglomeration effect. This has happened essentially due to the occurrence of a steric hindrance effect originating from the bulkier chain of butanol than

the other deagglomerating media [29]. Secondly, the evaporation rate of butanol is also lower than the other media and this is also another reason for achieving better deagglomeration effect by using butanol. Hence the same was employed for all the raw materials.

The scanning electron micrographs for polished Al_2O_3 (matrix), Al_2O_3 - SiC_p (ASP), Al_2O_3 - SiC_p (ASPL) and Al_2O_3 - SiC_w (ASW) composites are shown in Figure 9. It is observed that all the composites have uniform distribution of the respective reinforcement phases in the matrix. This has primarily happened due to the employment of effective processing steps like ultrasonication and deagglomeration of the green composite slurry mixture. There is also very little evidence of porosity (excepting for the ASPL batch), which is reflected in the high % theoretical density achieved for the composites (Table 2). This could be attributed to the employment of optimized vacuum hot pressing temperature.

Figure 10 illustrates the back scattered electron image as well as the relevant elemental maps obtained from EPMA for the ASPL composite. This figure shows that the SiC reinforcement has retained its chemical identity in the composite after processing. Identical behaviour was also observed for both ASP and ASW composites. The prevention of oxidation of the SiC reinforcement during processing could be attributed to the high level of vacuum (10^{-5} torr) used during the hot pressing operation. The TEM pictures of the interface regions of all the composites are depicted in Figure

11. Clean reaction free interfaces are observed for all the composites. This is again due to the employment of optimized vacuum hot pressing parameters, which did not allow the matrix and the reinforcement phases to react chemically.

The values of the elastic modulus for Al_2O_3 as well as for the composites are given in Table 2. It is seen that the modulus values for all the three composites are enhanced as compared to that of the monolithic matrix. This is in agreement with the rule of mixture theory, since SiC has higher modulus than Al_2O_3. There are several theoretical models for the estimation of elastic modulus of composite materials such as the iso - strain and iso - stress rule of mixtures [30], modified Tsai - Halpin [31] and Hashin - Shtrikman rules [32]. The iso - strain and iso - stress rule of mixtures are most suitable for continuous fibre reinforced composites for loading in the direction of the fibres and perpendicular to the direction of the fibres, respectively. For composites with discontinuous reinforcements, models such as the modified Tsai - Halpin [30] which takes into account the tensile transfer of loads at the particle ends as well as the particle aspect ratio are more appropriate. This model predicts the elastic modulus of the composite (E_c) as,

$$E_c = \{E_m (1 + 2 s q V_p)\} / (1 - q V_p) \text{ with, } q = \{(E_p / E_m) - 1\} / \{(E_p / E_m) + 2 s\} \quad \ldots\ldots\ldots (3)$$

where, E_m and E_p are the elastic modulus of the matrix and reinforcement, respectively; s is the aspect ratio of the particle reinforcement; V_p is the volume fraction of the reinforcement. The theoretical modulus values calculated for all the composites based on this "modified Tsai - Halpin model" are observed to be in well agreement with the experimentally determined ones (excepting for the ASPL composite, which produced lower experimental value due to the presence of porosity).

Similarly, like stiffness, both strength and fracture toughness values are also observed to be improved for the composites as compared to those of the corresponding unreinforced matrix. Due to the presence of clean matrix - reinforcement interfaces and also due to higher modulus of SiC than that of Al_2O_3, the load transfer mechanism from matrix to reinforcement has functioned efficiently and this is primarily responsible for the strength enhancement. However, the degree in increase in all the properties is observed to be the highest for the whiskers, then followed by platelets and particulates, respectively. This is in agreement with the fact that whiskers, due to their single crystal nature, possess higher strength and modulus than the others.

SEM fractographs of the fractured surfaces for monolithic matrix and the composites are illustrated in Figure 12. The fracture is intergranular in nature in the case of unreinforced Al_2O_3 (Fig. 12d), whereas mostly transgranular and partly intergranular features are observed for the

composites. This is in agreement with a few earlier research activities [33,34]. Pull out phenomena could be observed for both ASPL and ASW materials, but the same is observed to be absent for ASP composite. This is essentially due to the fact that both whiskers and platelets, due to their single crystal nature, possess superior mechanical properties than those of the polycrystalline particulates, and as a result, the former can remain unfractured and get pulled out at the wake of the crack. These pulled out whiskers / platelets can impart considerable bridging forces at the rear of the crack and thus, enhance the fracture toughness of the matrix. The fractographs of the composites also show that there is considerable refinement in the Al_2O_3 grain size. This matrix grain refinement behaviour is also considered to play important role in enhancing the strength of the composite [35]. However, the degree in matrix grain refinement is observed to be the highest for the whiskers and then followed by platelets and particulates, respectively. This is primarily due to the fact that the whiskers, due to their higher aspect ratio, inhibit the matrix densification rate to the higher extent and consequently, give rise to higher matrix grain refinement behaviour.

The crack path behaviour (showing the paths of the cracks originating from the corners of indentations) for all the materials are shown in Figure 13. It is seen that the path in monolithic Al_2O_3 is fairly straight without any significant deviation. This has happened due to the absence of

any reinforcement phase. However, considerable crack bridging and crack deflection phenomena could be observed for both ASPL and ASW composites. On the other side, these behaviour were observed to be of much lesser extent in ASP material. This could be attributed to the lower toughness value obtained for the ASP composite. ASPL also exhibited crack branching behaviour. On the other side, cracking behaviour of an SiC_p could be evidenced in TEM. The frequency vs. Deflection angle plot for all the three materials is shown in Figure 17. It can be seen that ASW composite has the highest median angle of deflection, due to the higher aspect ratio of the whiskers than the others. This observation is in agreement with the theoretical model predicted by Faber et al. [23,36].

CONCLUSIONS

1. Dense Al_2O_3 - 25 vol% SiC composites with three different morphologies of SiC, namely SiC_p, SiC_{pl} and SiC_w, could be fabricated having uniform distribution of reinforcement throughout the matrix by employing uniaxial vacuum hot pressing route. EPMA results ensured that all the three morphologies of SiC had retained their chemical identity in the respective processed composites primarily due to high level of vacuum (10^{-5} torr) and optimized sintering temperature employed during the vacuum hot pressing operation.

2. The elastic modulus values of all the three Al_2O_3 - SiC composites were observed to be significantly higher than that of monolithic Al_2O_3. The

experimentally obtained elastic modulus values for the composites agree very well with the same calculated theoretically based on modified Tsai - Halpin model.

3. The increase in strength for all the composites in comparison with that of monolithic matrix is observed to be primarily due the occurrence of matrix grain refinement phenomenon and efficient functioning of load transfer mechanism from matrix to the reinforcement phases. The functioning of load transfer phenomenon can be attributed to the presence of strong and reaction - free clean interfaces in all the composites. However, the strength enhancement is observed to be the highest for the whiskers, then followed by platelets and particulates, essentially due to higher load bearing capacity of the single crystal whiskers.

4. All the composites exhibited higher fracture toughness as compared to that of monolithic matrix. The marginal increase in fracture toughness for ASP composite is due to the presence of microscopic crack deflection phenomenon. However, the large increase in toughness in ASPL and ASW composites could be attributed to significant crack deflection, crack bridging and pull-out behaviour. Whiskers, due to their higher aspect ratio, exhibited greater toughening behaviour originating primarily from the higher crack deflection phenomenon.

ACKNOWLEDGEMENTS

The authors are thankful to Dr. D. Banerjee, Director, for his encouragement and permission to publish this work. The authors also thankfully acknowledge the funds received from Defence Research & Development Organisation, Delhi, India for carrying out this research work.

REFERENCES

[1]M.H. Vande Voorde and M.R. Nedele, "CMCs : Research in Europe and the future potential of CMCs in Industry", *Ceramic Engineering & Science Proceedings*, **17** [4] 3-21 (1996).

[2]K. Knowles, "Ceramic Matrix Composites"; pp 95-99 in *Ceramic Technology International*, 1992.

[3]K.M. King, "Advanced Ceramic and Metallic Composites", University of Cambridge, UK, 1990.

[4]K. K. Chawla, "Ceramic Matrix Composites", Chapman & Hall, 1993.

[5]B.A. Bender, D. Lewis III, W.S. Coblenz and R.W. Rice, "Electron microscopy of ceramic fibre – ceramic matrix composites – comparison with processing and behaviour", *Ceramic Engineering & Science Proceedings*, **5** [7-8] 513-529 (1984).

[6]S.T. Oh, T. Sekino and K. Niihara, "Microstructure and mechanical properties for Alumina / Copper nanocomposites", *Ceramic Engineering & Science Proceedings*, **18** [3] 329-336 (1997).

[7]T. Sekino, T. Nakajima and K. Niihara, "Mechanical and magnetic properties of Ni-dispersed Alumina-based nanocomposites", *Materials Letters*, **29** [1-3] 165-170 (1996).

[8]Y. Waku, M. Suzuki, Y. Oda and Y. Kohtoku, "Influence of particle size and volume percent of flaky Mo particles on the mechanical properties of Al_2O_3/Mo composites", *Metallurgical and Materials Transactions*, **27A** [10] 3307-3317 (1996).

[9]W.B. Chou and W.H. Tuan, "Toughening and Strengthening of Alumina with silver inclusions", *Journal of the European Ceramic Society*, **15** [4] 291-295 (1995).

[10]D.W. Richerson, *Composite Engineering Handbook*, Edited by P.K. Mallick. Marcel Dekker Inc., New York, 1997.

[11]D. Zhang, H. Yang, R. Yu and W. Weng, "Mechanical properties of Al_2O_3-SiC composites containing various sizes and fractions of fine SiC particles", *Journal of Materials Science Letters*, **16** [4] 877-878 (1997).

[12]K.W. Chae, D.Y. Kim, B.C. Kim and K.B. Kim, "Effect of Y_2O_3 additions on the densification of an Al_2O_3-TiC composite", *Journal of the American Ceramic Society*, **76** [7] 1857-1860 (1993).

[13]X. Lin and P.D. Ownby, ""Mechanical behaviour, microstructure and phase composition of free sintered Al_2O_3-B_4C whisker composites", *Ceramic Engineering & Science Proceedings*, **17** [3] 273-277 (1996).

[14]R.C. Garvie, "Structural applications of ZrO_2-bearing materials", pp 465-479 in *Advances in Ceramics : Science and Technology of Zirconia II*, Volume 12, Edited by N. Claussen, M. Ruhle and A.H. Heuer, The American Ceramic Society, Columbus, Ohio, USA, 1983.

[15]N. Claussen and M. Ruhle, "Design of transformation-toughened ceramics", pp 137-167 in *Advances in Ceramics : Science and Technology of Zirconia*, Volume 3, Edited by A.H. Heuer and L.W. Hobbs The American Ceramic Society, Columbus, Ohio, USA, 1981.

[16]Y.S. Chou and D.J. Green, "Silicon carbide platelet / Alumina composites : III, Toughening Mechanisms", *Journal of the American Ceramic Society*, **76** [8] 1985-1992 (1993).

[17]S.G. Seshadri, M. Srinivasan and K.M. Keller, "Numerical computation of the toughening increments due to crack deflection in particulate composites", *Ceramic Engineering & Science Proceedings*, **8** [7-8] 671-681 (1987).

[18]M.Y. He, D.J. Wissuchek and A.G. Evans, *Acta Materialia* **45** [8] 2813-2820 (1997).

[19]F.D. GAC, "Is there anything of practical value hidden amongst the composite-toughening theories?! – A Jim Mueller Perspective", *Ceramic Engineering & Science Proceedings*, **11** [7-8] 551-570 (1990).

[20]C.C. Wu, S.W. Freiman, R.W. Rice and J.J. Mecholsky, "Microstructural aspects of crack propagation in ceramics", *Journal of Materials Science*, **13** [12] 2659-2670 (1978).

[21]A.G. Evans and K.T. Faber, "Toughening of ceramics by circumferential microcracking", *Journal of the American Ceramic Society*, **64** [7] 394-399 (1981).

[22]W. Gu, J.R. Porter and T.G. Langdon, "Anelastic creep recovery of alumina reinforced with SiC whiskers or particulates", pp. 307-318 in *Advances in Ceramic Matrix Composites II : Ceramic Transactions*, Volume 46, Edited by J.P. Singh and N.P. Bansal. The American Ceramic Society, Ohio, USA, 1994.

[23]K.T. Faber and A.G. Evans, "Crack Deflection Processes – I. Theory", *Acta Metallurgica* **31** [4]565-576 (1983).

[24]P.F. Becher and G.C. Wei, "Toughening behaviour in SiC whisker reinforced Alumina", *Journal of the American Ceramic Society*, **67** [12] C267-C269 (1984).

[25]G.C. Wei and P.F. Becher, "Development of SiC whisker reinforced Ceramics", *American Ceramic Society Bulletin*, **64** [2] 298-304 (1985).

[26]Y.S. Chou and D.J. Green, "Silicon Carbide Platelet / Alumina Composites : II, Mechanical Properties", *Journal of the American Ceramic Society*, **76** [6]1452-1458 (1993).

[27]ASTM Standard E 399-83, p. 500, in *Annual Book of ASTM Standards*, Section 3, Philadelphia, PA, USA, 1990.

[28]T.N. Tiegs and P.F. Becher, "Sintered Al_2O_3-SiC whisker reinforced Composites", *American Ceramic Society Bulletin*, **66** [2] 339-345 (1987).

[29]D.H. Napper, in *Polymeric Stabilization of Colloidal dispersions*, Academic Press, London, 1983.

[30]K.K. Chawla, p 177, in *Composite Materials : Science and Engineering*, Edited by B. Ilschner and N.J. Grant. Springer - Verlag, New York, 1987.

[31]H. Lagace and D.J. Lloyd, "Microstructural analysis of Al-SiC Composites", *Canadian Metallurgical Quarterly* **28** [2] 145-152 (1989).

[32]Z. Hashin and S. Shtrikman, *Journal of Mechanics and Physics of Solids*, **2** [1] 126-134 (1973).

[33]K.W. White and L. Guazzone, "Elevated – temperature toughening mechanisms in a SiC_w / Al_2O_3 Composite", *Journal of the American Ceramic Society*, **74** [9] 2280-2285 (1991).

[34]T. Hansson, R. Warren and J. Wasen, "Fracture toughness anisotropy and toughening mechanisms of a hot pressed alumina reinforced

with silicon carbide whiskers", *Journal of the American Ceramic Society*, **76** [4] 841-848 (1993).

[35]J. Otsuka, S. Iio, Y. Tajima, M. Watanabe and K. Tanaka, "Strengthening mechanism in Al_2O_3 / SiC particulate composites", *Journal of Ceramic Society of Japan*, **102** [1] 29-34 (1994).

[36]K.T. Faber and A.G. Evans, "Crack Deflection Processes – II. Experiment", *Acta Metallurgica*, **31** [4] 577-584 (1983).

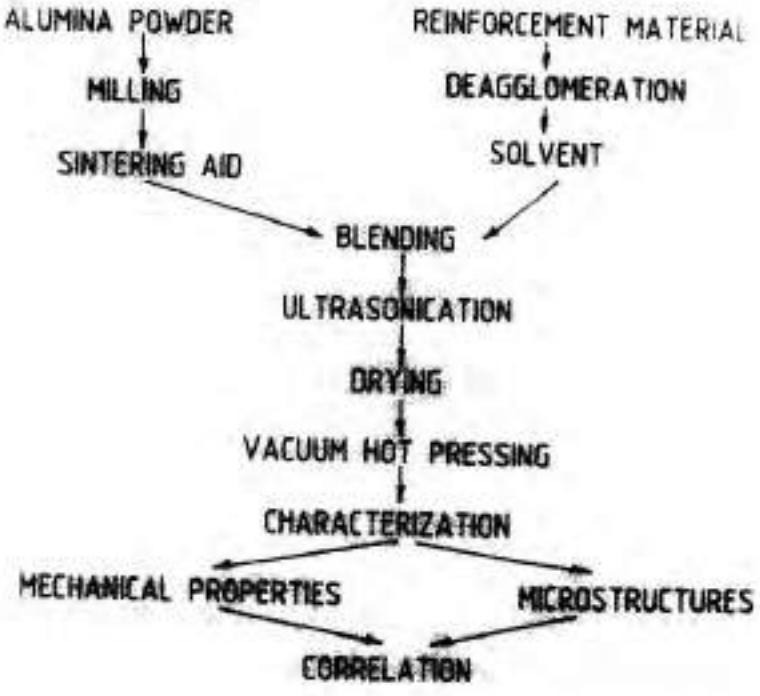

Figure 1 : Process flow chart for fabrication of the composites

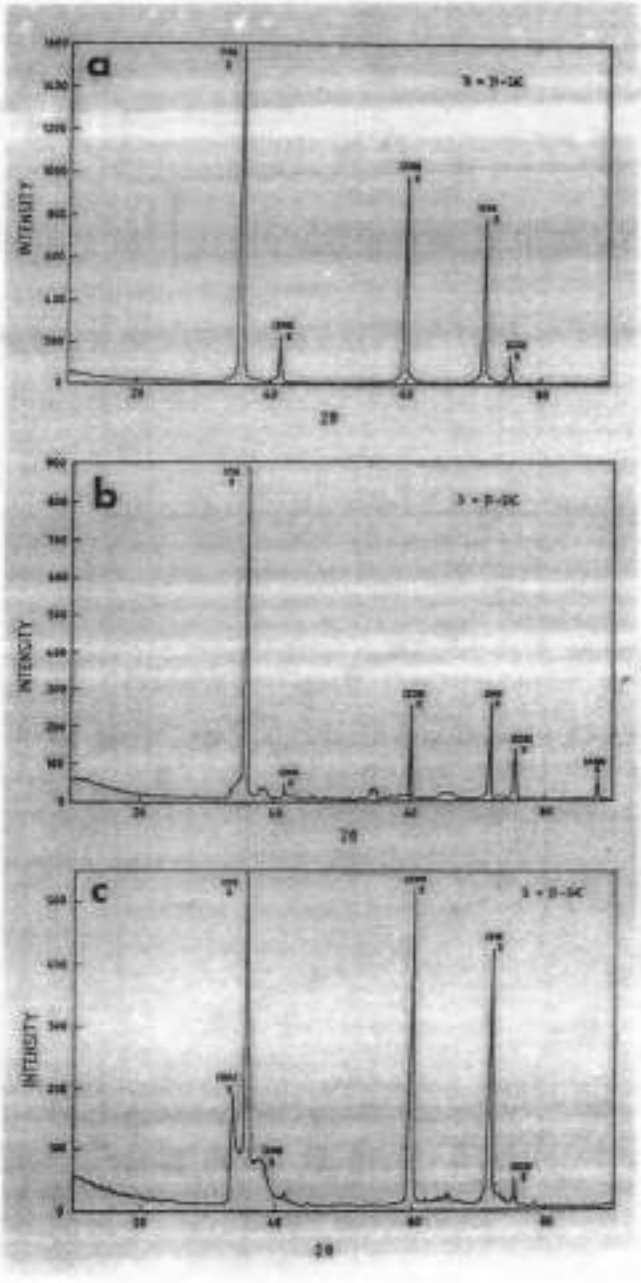

Figure 2 : X ray diffraction patterns of as received : a)SiC_{β}, b)SiC_{β} & c)SiC_{α}

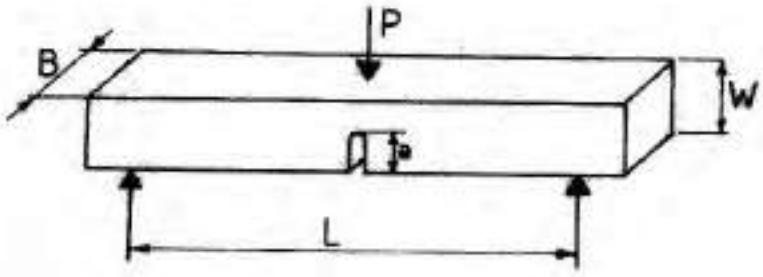

Figure 3 : Schematic diagram of the SENB fracture toughness test sample

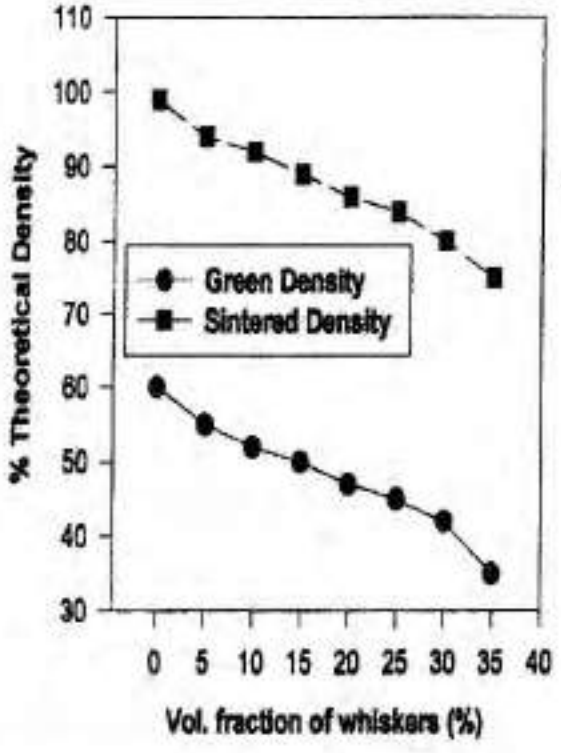

Figure 4 : Effect of volume fraction of SiC whiskers on both green and sintered density of Al_2O_3-SiC_w composites

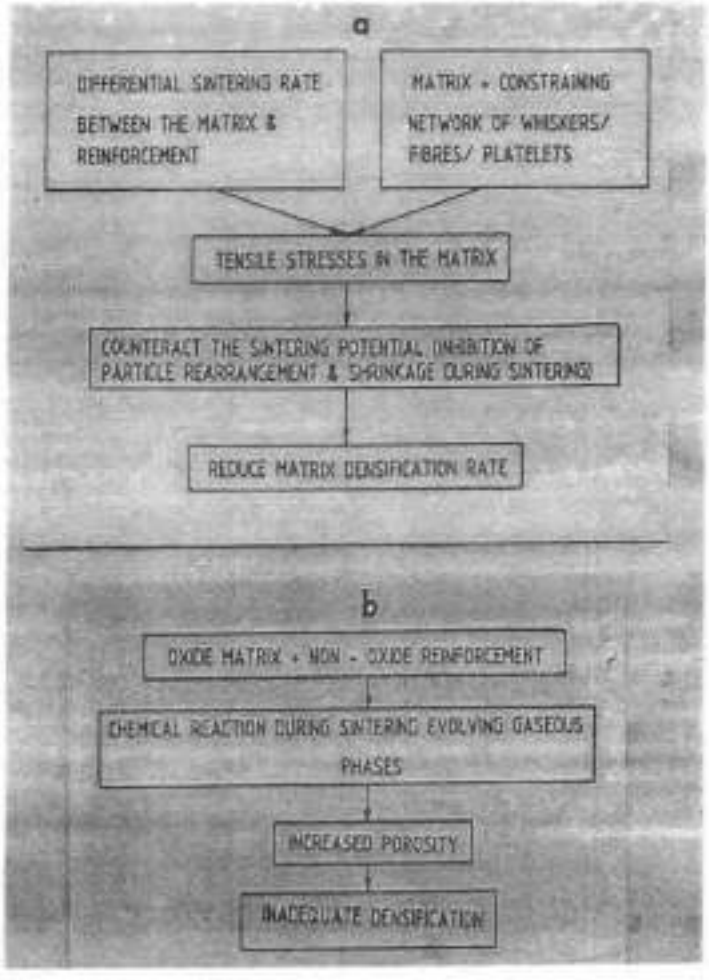

Figure 5 : Critical issues during sintering of Al_2O_3-SiC_w composites in regards to : a)stress generation & b)chemical reaction

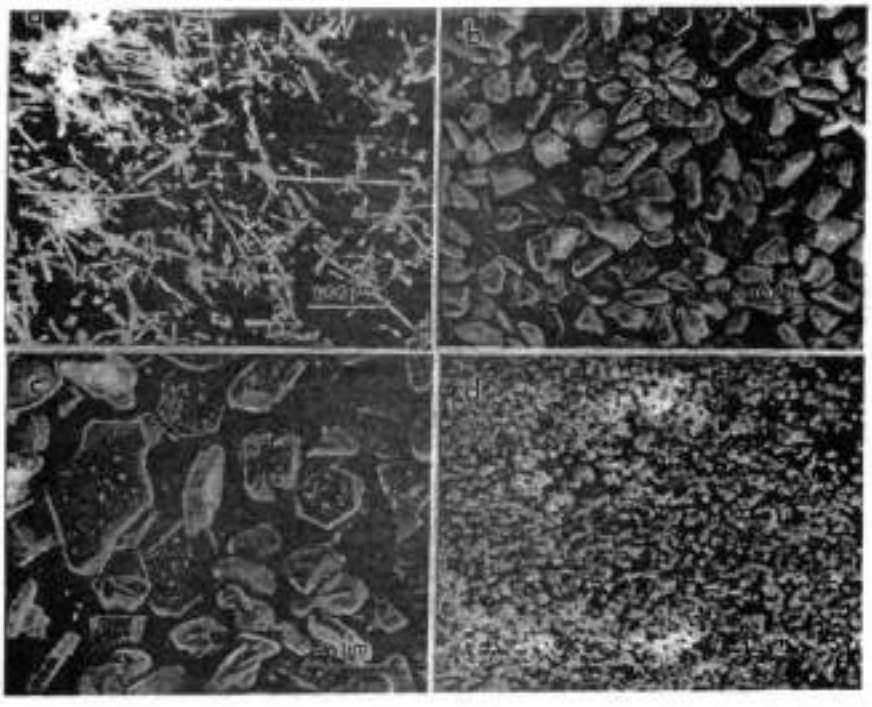

Figure 6 : SEM pictures of as received : a)SiC_w, b)SiC_p, c)SiC_{pl} & d)SiC_p

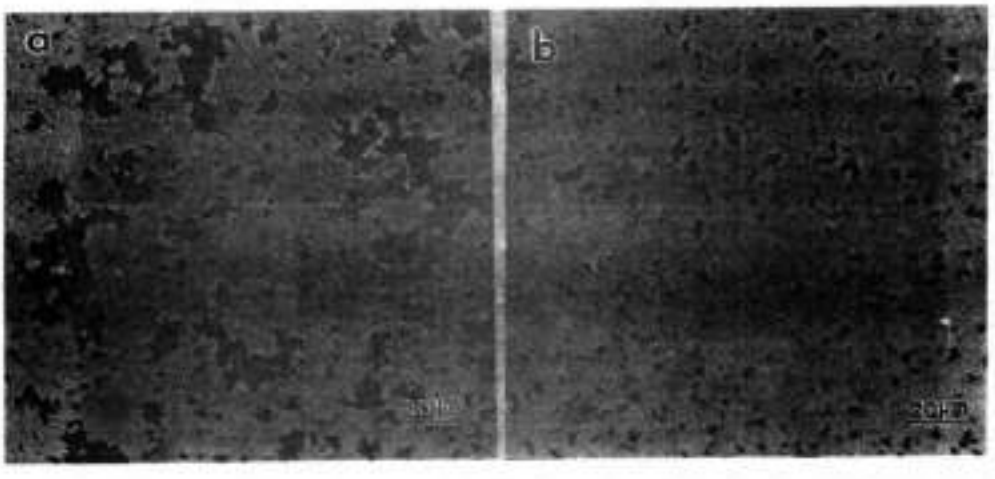

Figure 7 : Optical micrographs showing deagglomerated SiC particles in : a)acetone and b)butanol medium

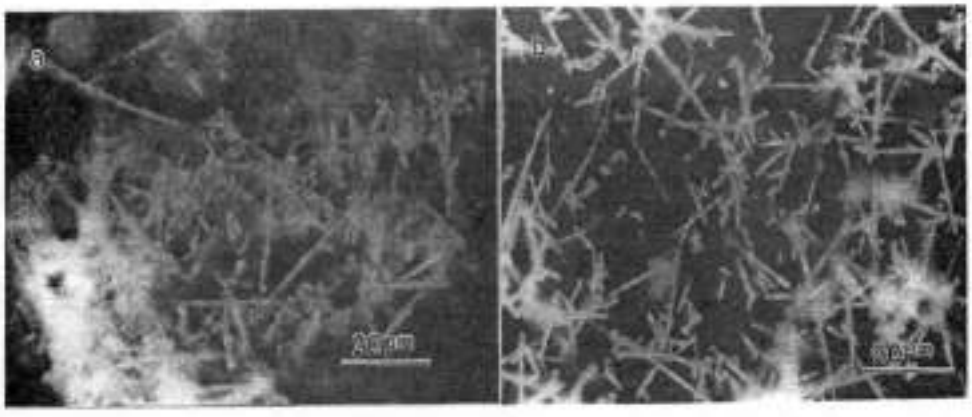

Figure 8 : Optical micrographs showing deagglomerated SiC whiskers in : a)acetone and b)butanol medium

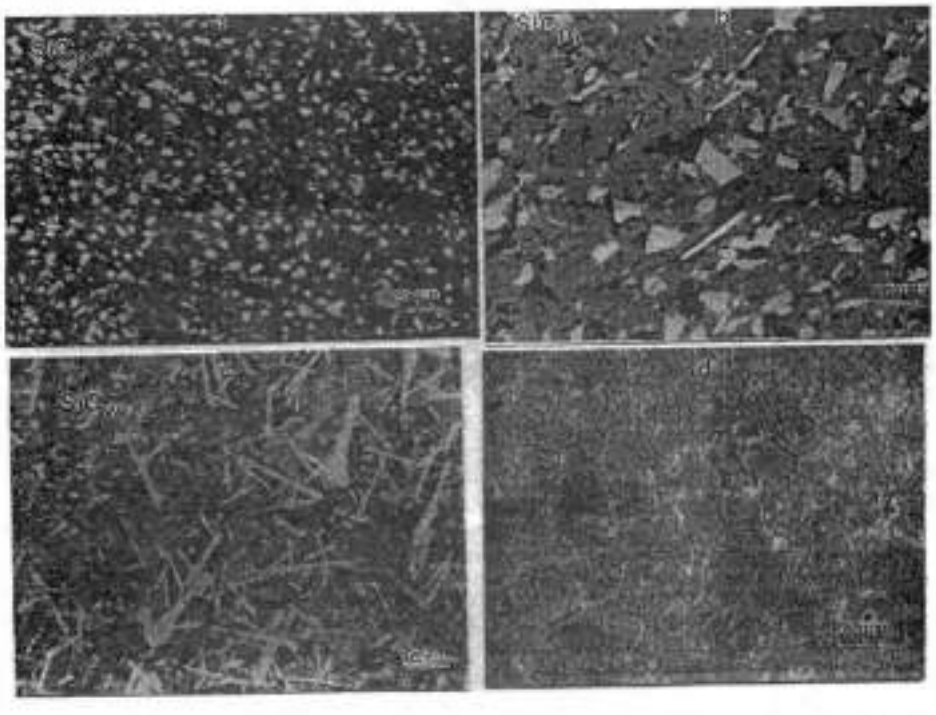

Figure 9 : SEM pictures of polished and etched surfaces of : a)ASP, b)ASPL, c)ASW & d)Al_2O_3 samples

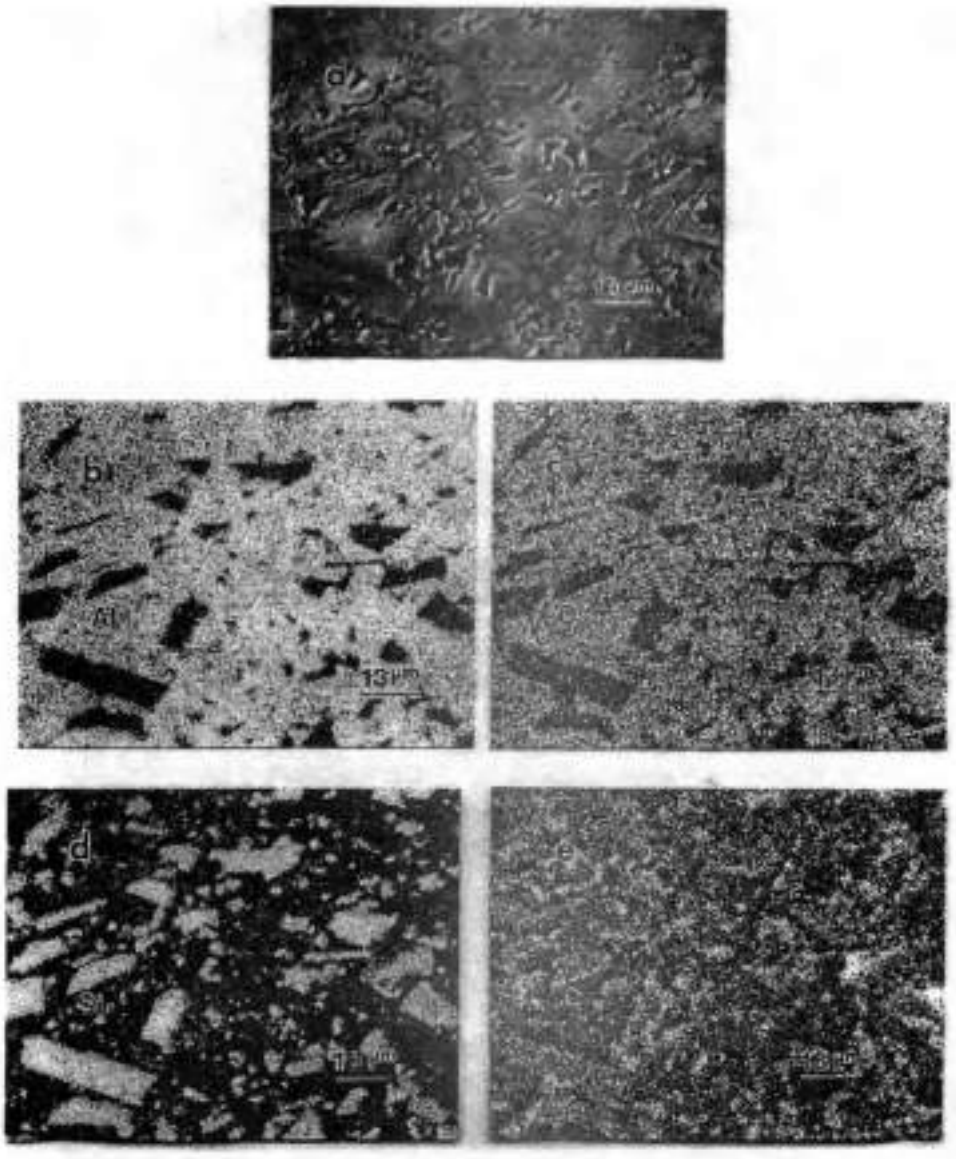

Figure 10 : a)BSE image of ASPL composite; Elemental maps of : b)Al, c)O, d)Si & e)C

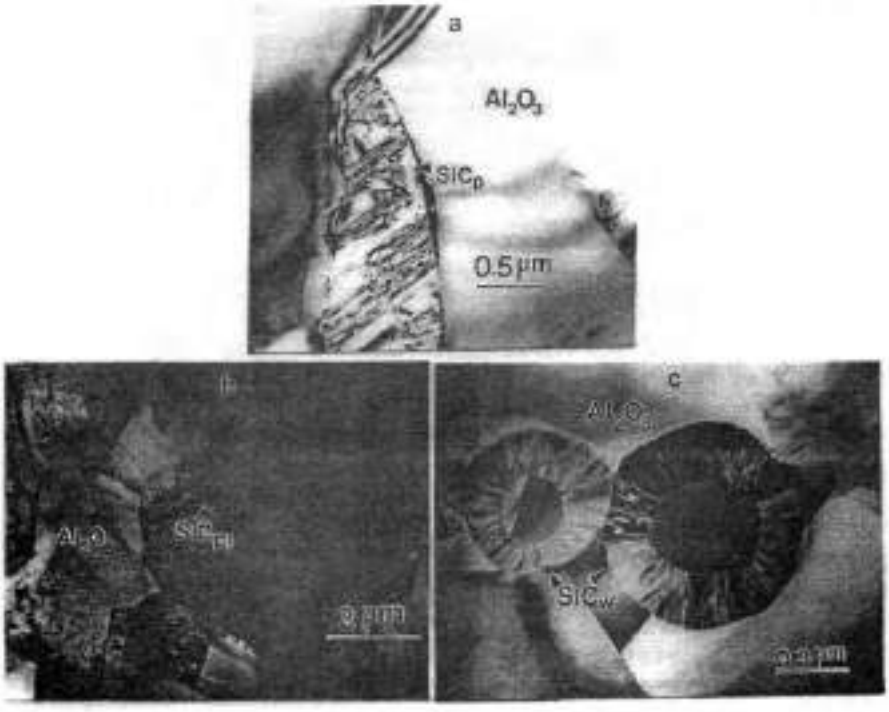

Figure 11 : Transmission electron micrographs showing matrix - reinforcement interfaces for : a)ASP, b)ASPL & c)ASW composites

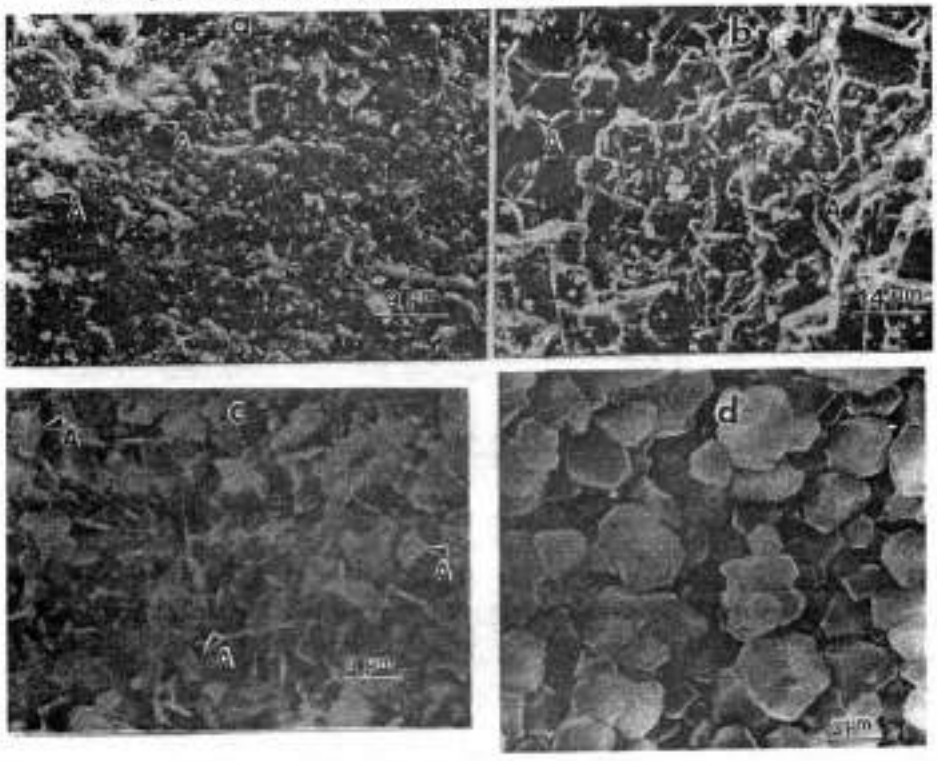

Figure 12 : SEM fractographs of : a)ASP, b)ASPL, c)ASW & d)Al_2O_3; (A : Al_2O_3 grain)

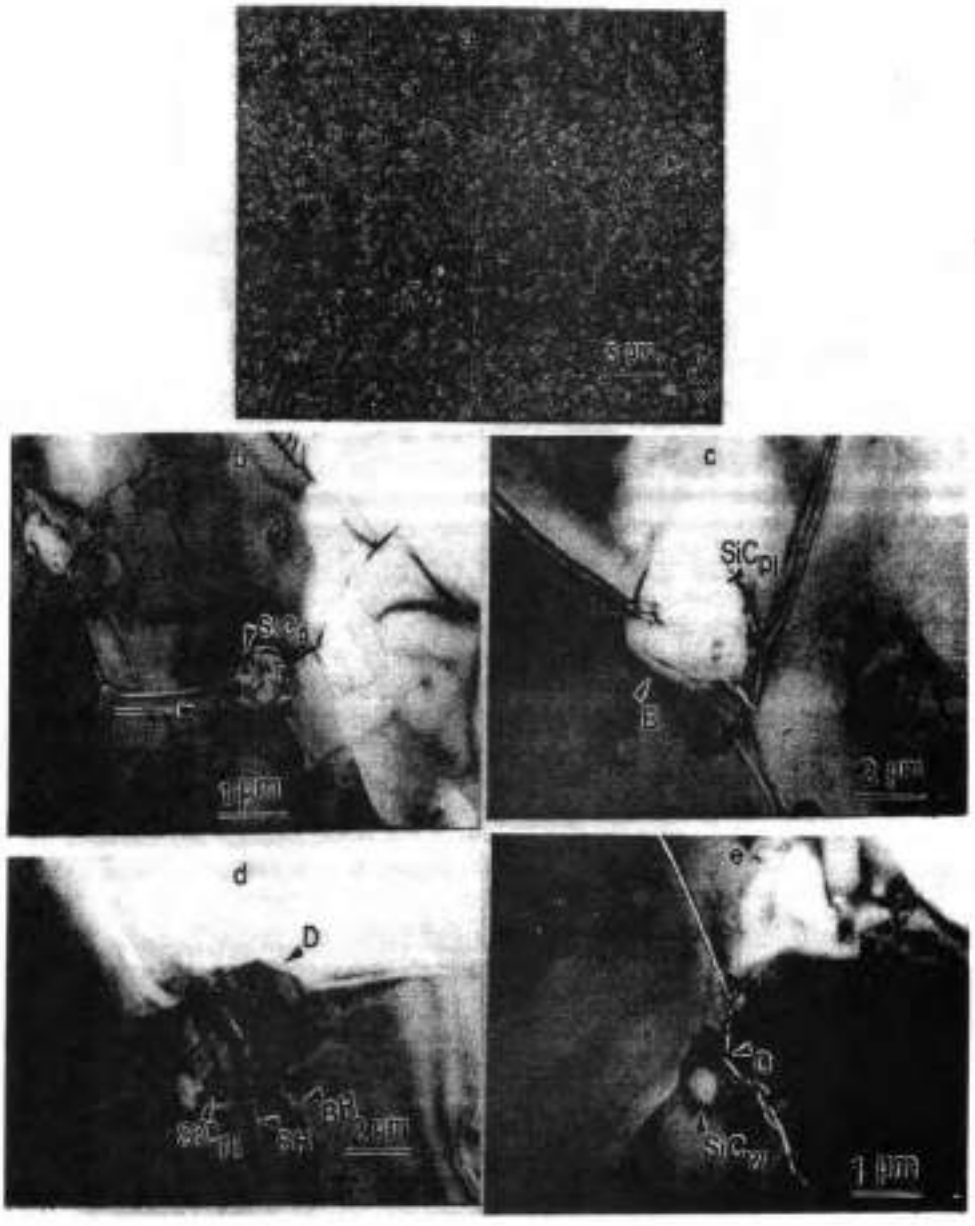

Figure 13 : Crack path behaviour in : a)Al_2O_3, b)ASP, c)ASPL, d)ASPL and e)ASW Composite ("B" : Crack Bridging; "D" : Crack Deflection & "BH" : Crack Branching)

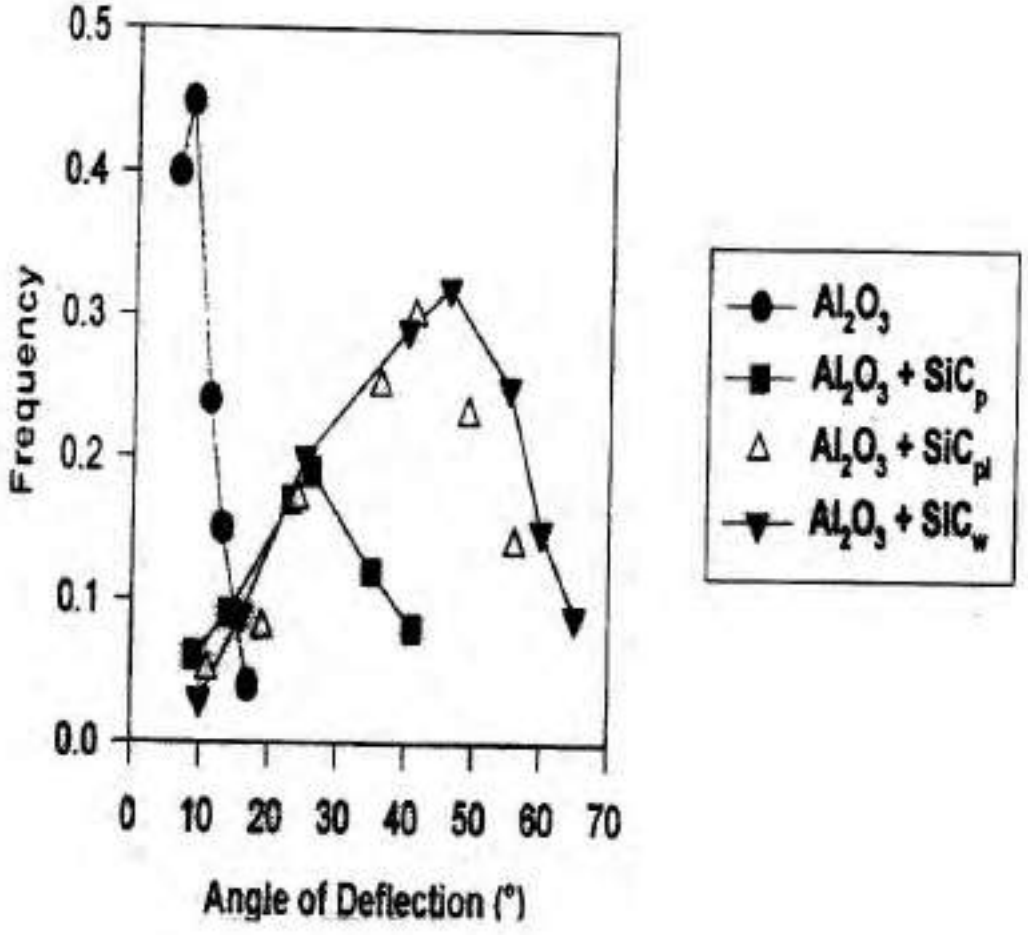

Figure 14 : Frequency vs. Deflection angle curves for all the materials

MICROSTRUCTURAL MODIFICATIONS OF UO_2 FUEL PELLETS THROUGH SILICATE ADDITIVES.

R.M Altekar, U Basak, V.D.Pandey, I.H.Sheikh, R.Ramachandran, and S. Majumdar.
Radiometallurgy Division
Bhabha Atomic Research Centre
Mumbai 400 085

ABSTRACT

Fuel cycle economy, better fuel utilization and reduced waste volume generation are the driving forces for the development of new generation fuels which can be operated for extended period to achieve high burn-up. Greater reliability of these fuels during extended burn-up is to be ensured by modifying the fuel pellet microstructure in terms of large grains, controlled porosity, better grain boundary conditions etc. to reduce fission gas release, swelling and in-pile densification. The present paper deals with fabrication of UO_2 pellets using mechanically as well as synthetically prepared mixed silicates namely Ti-Si-O, Nb-Si-O, Mg-Si-O,and Zr-Si-O respectively as additives. Effect of these additives on the density and microstructure of the pellet is discussed. The conventional P/M process involving milling and mixing of UO_2 powder with oxide additives followed by cold-compaction and sintering at 1650 ^{0}C in N_2- 8%H_2 atmosphere was followed for the fabrication of the UO_2 pellets. The sintered pellets were subjected to density and porosity measurements and microstructural evaluations.

INTRODUCTION

The natural uranium dioxide fueled pressurised heavy water reactors (PHWRs) and low enriched UO_2 fueled light water reactors (LWRs) are being operated at maximum burn-up of 0.7 and 3 at% respectively. Increase in burn-up improves the fuel cycle economy, by maximising fuel utilization and also reduces waste volume generation. However fission gas release, pellet-clad interaction, corrosion of the clad etc. are some of the factors, which affect and limits the performance of the fuel at high burn-up. Fuels with large grains and modified grain boundary conditions are reported to have better in-service performance in water-cooled reactors. Additions of small quantities of certain metal oxides like TiO_2, Nb_2O_5, MgO, and ZrO_2 etc. in the form of dopants or additives to the base material UO_2 , bring about some microstructural changes in terms of large grains and controlled porosity desirable for high burn-up fuel.[1,3,4,6] These dopants, within their solubility limits, form solid solution with baseUO_2 matrix and enhance densification & grain growth leading to large grain size at comparatively low temperature [5].They also improves other physical properties such as creep[7]. In large grain, the migration distance of fission gas atoms from interior of the grains to the grain boundaries is larger and as a result, the fission gas release is greatly reduced. However, reduction in fission gas releases due to large grain obtained by doping UO_2 with oxides like TiO_2, Nb_2O_5 etc. are found to be valid only in steady state reactor operation. Under transient conditions, due to sudden rise in temperature, such pellets have shown high fission gas release and swelling[2] A dopant containing silicate of these oxides are found to be effective in reducing fission gas releases even under transient condition[7]. Some other additives also form stable compounds with corrosive fission products and these compounds are retained in the fuel matrix and hence reduces chemical attack on the clad material form inside.

The objective of this paper is to evaluate the comparative effectiveness of the addition of the dopants constituents either as physical mixtures or as synthetically prepared silicate compound with UO_2 powder. The evaluation was done in terms of density and microstructure of the UO_2 pellets.

EXPERMENTAL

High purity metal oxides Titania, Niobia, Magnesia and Zirconia were respectively mixed with silica powders in 1:1 weight ratio and milled for two hours in ball mill. A part of these batch mixtures were subjected to tableting and air calcinations at 1300^{0}C for two hours. The clinkers thus formed were crushed to fine powders. These powders both as mixed (mechanically prepared) and as heat treated (synthetically prepared) were added to UO_2 powders to have a master mix of UO_2 and oxide mixture or compound in 1:1 weight ratio. The master mix was diluted by adding more UO_2 powder and blended for four hours to get final blend of UO_2 with 0.1w/o of dopants in UO_2. Eight different batches were made. Individual powder batches were precompacted to 75 MPa pressure. The precompacts were granulated and finally compacted at 300 MPa. Green pellets of 12 mm diameter and 7-9mm height were made. These pellets were sintered at 1650^{0}C for fours hours in Nitrogen-8%Hydrogen atmosphere. The process flow –sheet for the fabrication of doped UO_2 pellets is shown in Fig. (A) The sintered pellets were characterized for

density and porosity measurements by liquid displacement method. One pellet of each composition was mounted, polished and subjected to microstructural analysis.

Fig. (A)
The process flow sheet for the fabrication of doped UO_2 Fuel pellets.

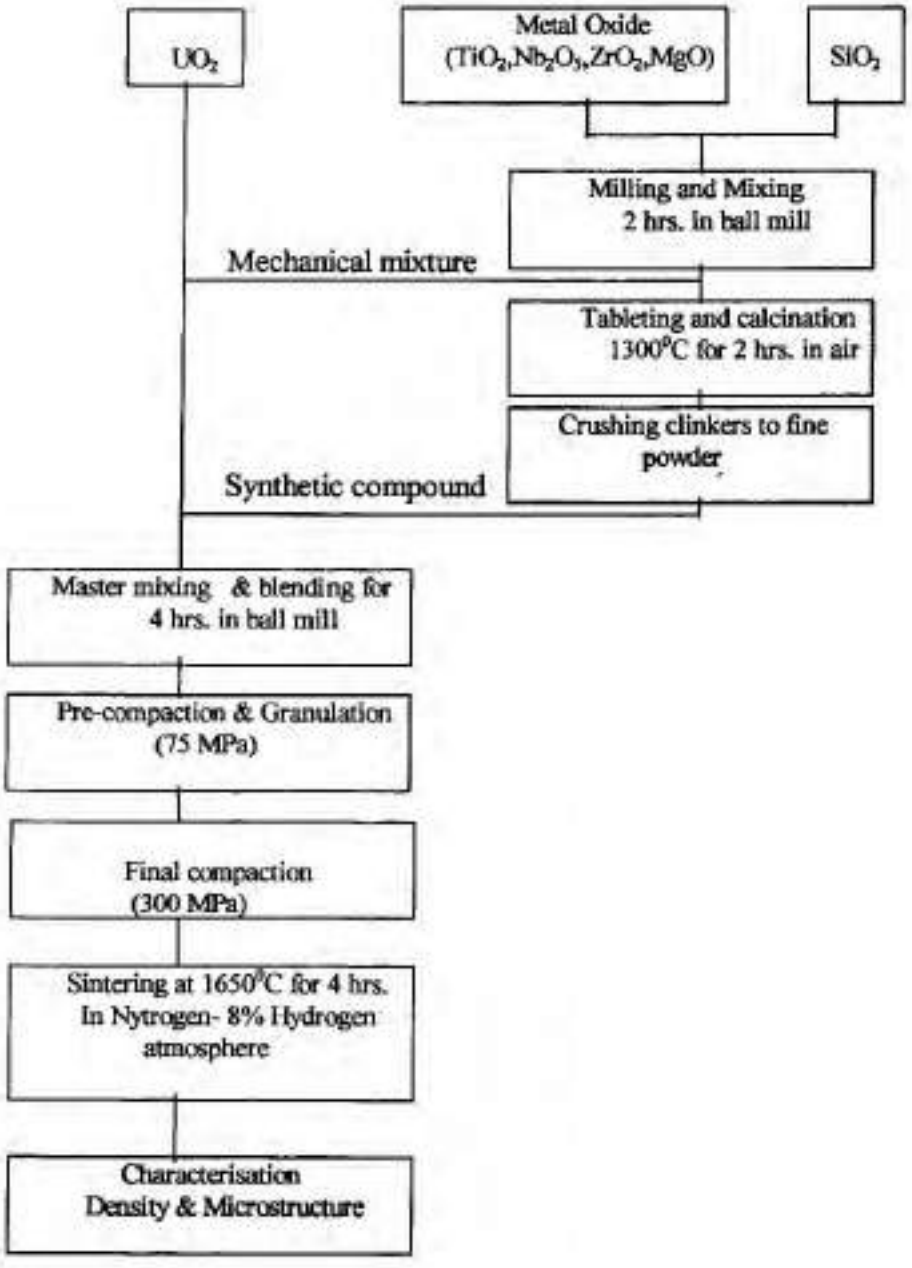

RESULTS AND CONCLUSIONS

The Table 1(a) and 1(b) shows the characteristics of sintered UO_2 pellets doped with mechanically prepared dopants and synthetically prepared dopants respectively.

Table 1(a)
The characteristics of sintered UO_2 pellets doped with mechanically Prepared dopants.

Composition	Density		Porosity		Average Grain Size micron
	gm./cc	%T.D.	Closed (%)	open (%)	
UO_2+ 0.1 w/o $TiO_2 + SiO_2$	09.98	91.07	08.92	0.01	52
UO_2+ 0.1 w/o $Nb_2O_5 + SiO_2$	10.66	97.25	02.74	0.01	35
UO_2+ 0.1 w/o $ZrO_2 + SiO_2$	10.11	92.24	7.75	0.01	15
UO_2+ 0.1 w/o $MgO + SiO_2$	09.70	88.53	11.45	0.02	08

Table 1(b)
The characteristics of sintered UO_2 pellets doped with synthetically prepared dopants

Composition	Density		Porosity		Average Grain Size micron
	gm./cc	%T.D.	Closed (%).	open (%)	
UO_2+ 0.1 w/o Ti -Si- O	10.41	94.95	05.04	0.01	88
UO_2+ 0.1 w/o Nb -Si- O	10.67	97.39	02.60	0.01	40
UO2+ 0.1 w/o Zr- Si- O	10.47	95.53	04.46	0.01	25
UO_2+ 0.1 w/o $MgO + SiO_2$	10.14	92.52	07.47	0.01	35

Photomicrograph of Sintered UO_2 pellets doped with Synthetically and mechanically prepared dopants

Fig. 1(a) UO_2 + 0.1 w/o (TiO_2+SiO_2)

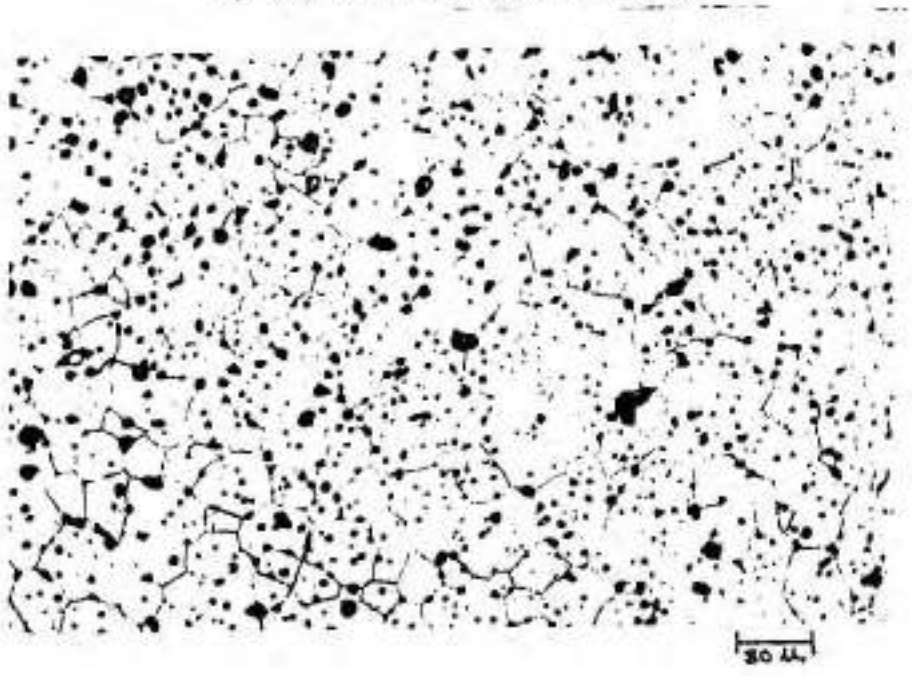

Fig. 1(b) UO_2 + 0.1 w/o (Ti-Si-O)

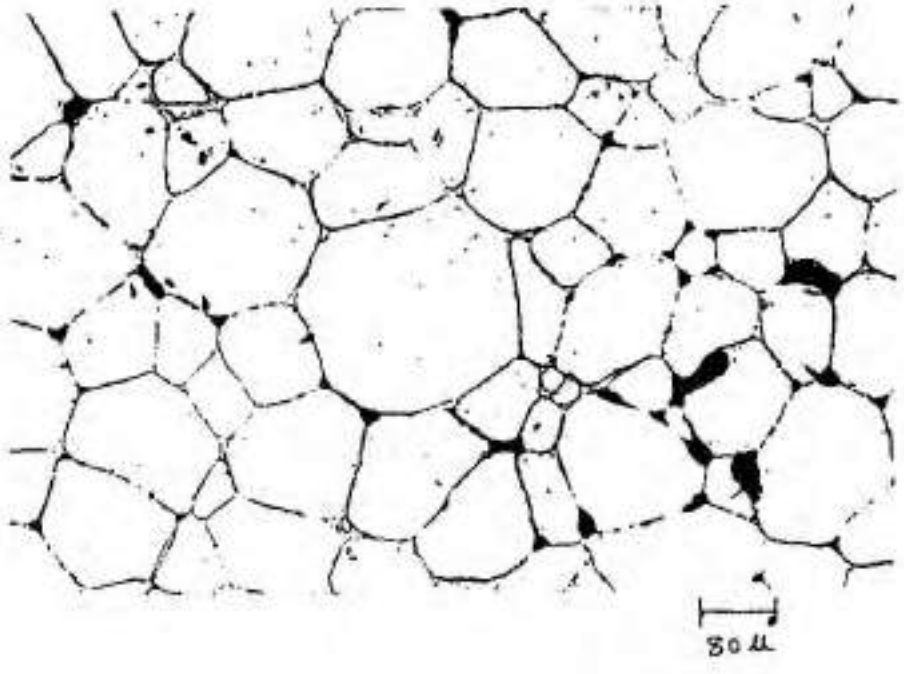

Fig. 2(a) $UO_2 + 0.1$ w/o (Nb_2O_5+SiO_2)

Fig. 2(b) $UO_2 + 0.1$ w/o (Nb-Si-O)

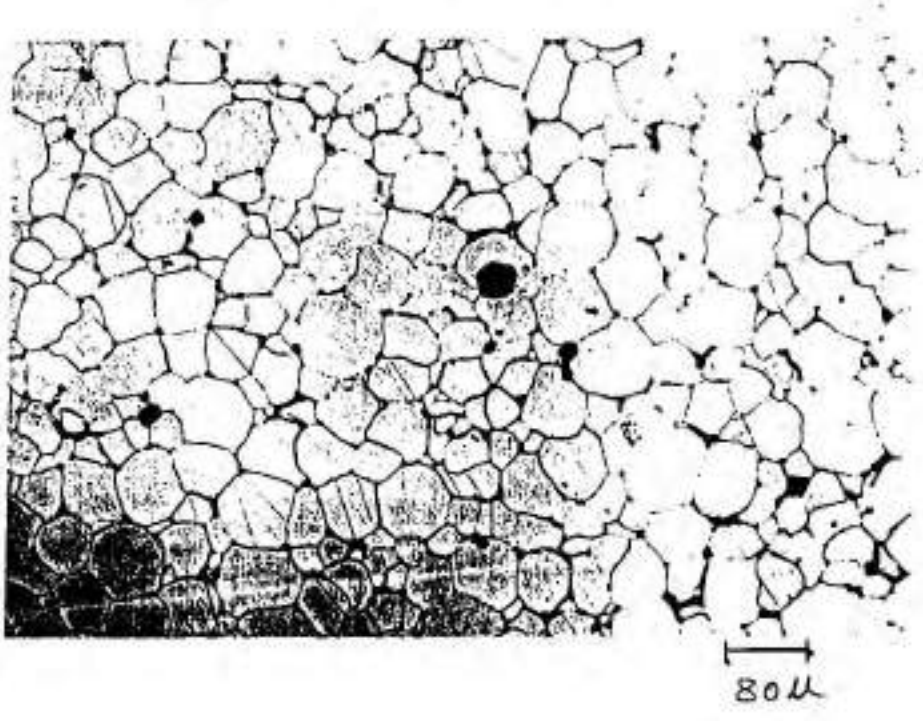

Fig. 3(a) UO_2 + 0.1 w/o ($MgO+SiO_2$)

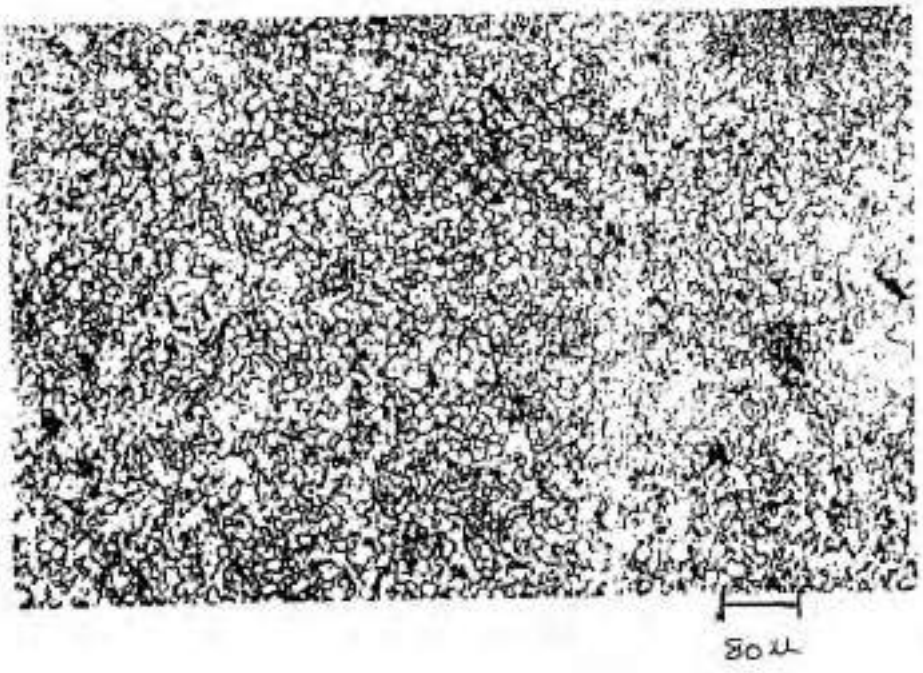

Fig. 3(b) UO_2 + 0.1 w/o (Mg-Si-O)

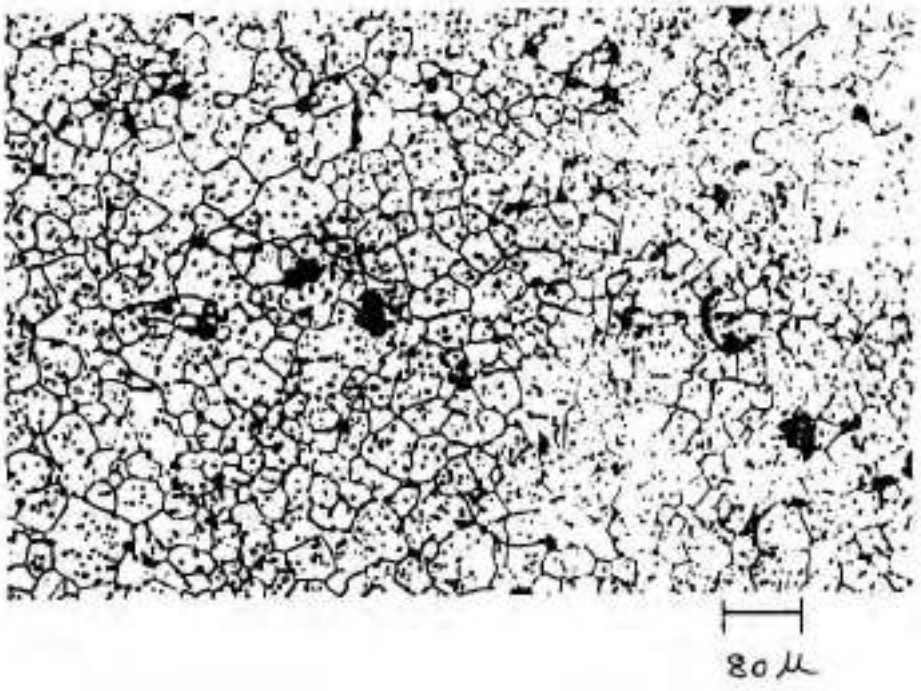

Fig. 4(a) UO_2 + 0.1 w/o (ZrO_2+SiO_2)

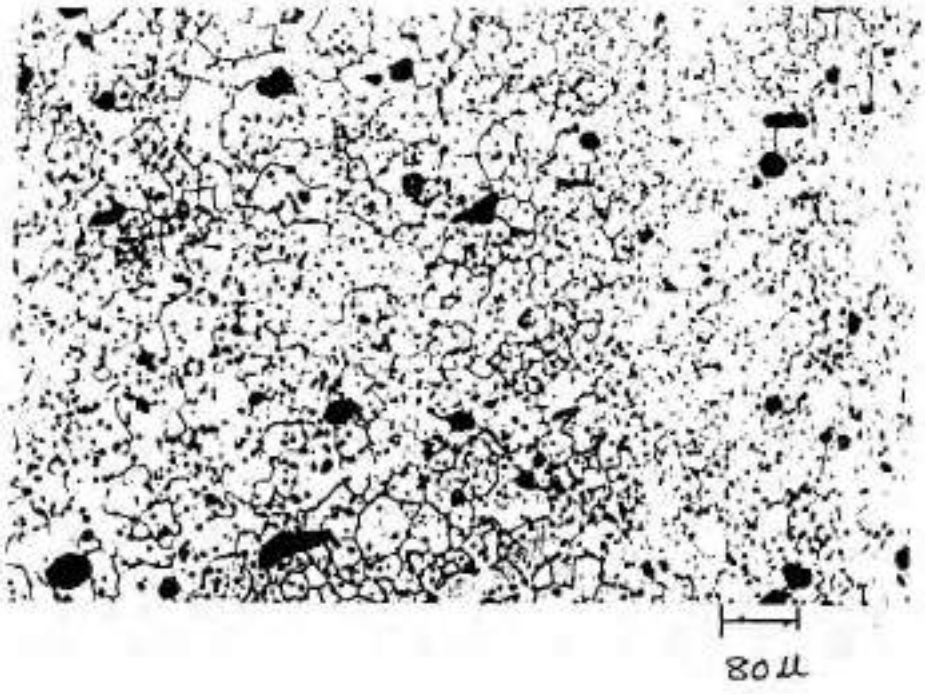

Fig. 4(b) UO_2 + 0.1 w/o (Zr-Si-O)

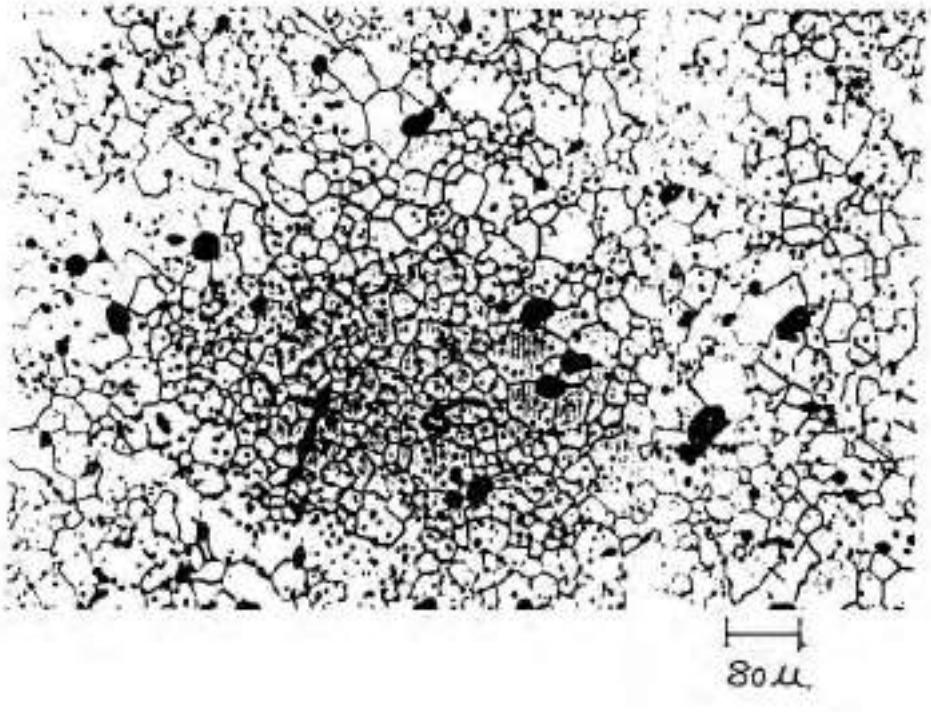

Higher sintered densities (around 3 to 4 % T.D.) and large grain sizes are obtained for UO_2 pellets doped with synthetically prepared silicates, similar results were obtained for Al-Si-O doped UO_2 pellets.[4] This may be attributed to the liquid phase sintering in case of synthetically prepared dopant leading to enhanced diffusivity [5]. In case of UO_2 pellets doped with either mechanically or synthetically prepared Nb-Si-O, no significant change in sintered density was noticed. In case of Nb_2O_5+SiO_2 a part of sintering might have taken place by ionic diffusion since a part of Nb^{5+} is reduced to Nb^{3+} in Nitrogen + Hydrogen atmosphere and substitute U^{4+}ion in lattice. Hence uranium diffusivity has been increased leading to higher density, as defect concentration are much more as compared to other dopants. Ti^{4+} also reduces to Ti^{3+} in Nitrogen + Hydrogen atmosphere. However Ti^{3+} segregates mostly at grain boundary leading to much larger grain growth.

The photomicrograph of sintered UO_2 pellets (figure 1,2,3,and 4) shows single-phase equiaxed grain structure. Higher grain sizes are also obtained in case of pellets doped with synthetically prepared dopants Average grain size of 88 μm has been obtained with Ti-Si-O dopant compared to 52 μm obtained from mechanically prepared TiO_2+ SiO_2 dopant. (Figure 1(a) & 1(b)) Similarly average grain size of 25 μm has been found with Zr-Si-O dopant compared to 15 μm obtained from mechanically prepared ZrO_2+ SiO_2 dopant. (Figure4(a) &4(b)) For Mg-Si-O doped pellets grain sizes were 8 μm and 35 μm respectively. (Figure3(a) &3(b)) The higher grain size obtained from synthetically prepared dopants may be attributed to the segregation of silicates to the grain boundary, forming a viscoplastic layer which provides an effective path for grain boundary diffusion.[6,7] The formation of this viscoplastic layer also contributes to increased creep rate of fuel which in term reduces pellet clad interaction at high burn-up.

CONCLUSIONS

1. High density and large grain size are obtained for UO_2 pellets doped with synthetically prepared silicates. They are much more effective compared to the dopants added through mechanical mixture.

2. In case of mechanically added dopants, ionic diffusivity is also responsible for densification and grain growth. While silicate dopants (synthetically prepared) do not dissolve in UO_2 matrix, contributing to densification and grain growth by liquid phase sintering.

3. UO_2 pellets doped with such silicates are reported to be much effective in retaining fission gas release in steady state as well as in transient conditions. Additionally they also form a viscoplastic layer at the grain boundary, which increases the creep rate.

ACKNOWLEDGEMENT

Authors are grateful to the Director, Nuclear Fuels Group for his keen interest in this work and permission for publication of this paper . Authors thanks the staff members of Oxide Fuel Section for their co-operation during fabrication of pellets.

REFERENCES

1. K. C. Radford, J. M. Pope Journal of Nuclear Materials Vol. 116 (1983) pp 305.
2. J. B. Ainscough, F. Rigby, S. C. Osborn Journal of Nuclear Materials Vol. 52 (1974) pp 191
3. J. B. Ainscough, F. Rigby, Journal of Nuclear Chemistry Vol. 36 (1974) pp 1531
4. R. M. Altekar, U. Basak, S. Majumdar, D. K. Bose paper ' Effect of Alumino-silicate dopant on fabrication and microstructure of UO2 fuel pellets' presented at 26th PMAI conf. at Chennai Feb. 2000.
5. T. Matsuda et. al. IAEA- TECDOC 1036 TCM on Advances in Fuel Pellet Technology for improved performance at High burn-up, Tokyo Japan , Oct. 29 – Nov. 1, 1996 pp 9.
6. C. Duguay et. al. IAEA-TECDOC 1036 TCM on Advances in Fuel Pellet Technology for improved performance at High burn-up, Tokyo Japan , Oct. 29 – Nov. 1, 1996.
7. M. Hirai et.al. proc. 1997 Int. Topical meeting on LWR fuel performance, Portland, Oregon March 2-6, 1997 pp 490

OPTICAL METALLOGRAPHIC PRACTICE FOR TUNGSTEN HEAVY ALLOY SYSTEMS

TP Bagchi*, N Arvind Kumar and Bijoy Sarma

Defence Metallurgical Research Laboratory
(Govt. of India, Ministry of Defence)
Kanchanbagh – P.O.
Hyderabad – 500 058.

Abstract

Optical metallography is a powerful tool for characterisation of metal and alloy products. This is true for Powder Metallurgy (P/M) products too. However, the sample preparation techniques are different from the conventional ones. A part of our experience relating to tungsten heavy alloy (WHA) systems is presented here.

WHA systems contain essentially two distinct entities with widely varying microhardness levels. The soft one (275-300 VPN) is known as matrix and the hard ones (400-450 VPN) are tungsten grains cemented therein. This makes sample preparation rather difficult. Grinding or polishing of hard tungsten grains leave deep scratch on the soft phase (matrix) which is difficult to remove subsequently. Conversely, grinding or polishing of softer phase leaves the tungsten grains unattended. This problem gets aggravated when there are some pores in the matrix whose morphology is likely to get distorted during grinding and polishing. Proper care and skill require to be exercised to circumvent these problems.

The hardness difference is, however, helpful as it imparts relief to the tungsten grains over the soft matrix which, in turn, provides required contrast to identify the phases clearly without etching. Further etching (Murakami solution) provided no additional metallographic information. Efforts have been made to etch WHA samples with different colours for enhanced contrast and aesthetics.

1.0 Introduction

Optical metallography is used extensively for characterisation of metal and alloy products [1,2]. This is true for powder metallurgy (P/M) products too [3,4]. However, the sample preparation techniques of P/M products are different from those of conventional ones. Most of the common P/M products have some porosities within—intentional or unavoidable. These porosities have a significant influence on the end-properties and, thereby, the performance of the products; so much so that it becomes essential to study and interpret the pore morphology (*i.e.* shape, size and distribution) also while examining the microstructure of the base product. It is, however, very difficult to prepare a representative metallographic sample of a P/M part without tampering with the original pore morphology. The pore morphology is bound to get distorted or shrouded because of localised plastic deformation of the surface material, particularly in the vicinity of the pores, during grinding and polishing operations.

Sample preparation is, therefore, regarded as an important step in P/M metallography. Proper care and skill, developed over years of diligent work, are essential to address the problem of retention of pore morphology [5]. This is explained schematically in Fig. 1. A typical surface pore and its contour is shown in Fig. 1(a). After grinding, the actual pore size may appear to be reduced or increased when observed under microscope.

Apparent reduction of pore size:

The surface material around the pore may undergo plastic deformation and close the pore partially and give a wrong picture of the pore morphology as shown in Fig. 1(b). The grinding debris may also block the pore as shown in Fig. 1(c) and lead to the same error.

Apparent enhancement of pore size:

If the surface material around the pore is hardened, small chips may come out as debris during grinding and *increase* the pore contour size [Fig. 1(d)]. In the case of softer metals, pores are more likely to be rounded during polishing (or even during etching) and, once again, would give a wrong picture of the pore morphology (both shape and size) as shown in Fig. 1(e).

This problem is tackled by impregnating the P/M samples with epoxy resin, wax or some low-melting point metals. The surface pores thereby get plugged in. This helps in retention of original pore morphology during polishing.

Despite these technical difficulties, optical metallography is used quite extensively, and successfully, in P/M activities. One such interesting area is development and production of tungsten heavy alloy systems (in short, WHA) where metallography has already proved to be a powerful tool [6-17].

The present authors are working in the area of WHA metallography for many years as a part of their continuous endeavour towards development and production of different types of WHA systems. A part of that experience is presented here with some selected examples of microstructures (both in colour and black-&-white) of a wide range of WHA samples. Some un-resolved problems are also placed for discussion.

2.0 Sample Preparation

The microstructures of WHA systems contain essentially two distinct entities. The predominant one (with rounded shape) is *tungsten grains* (or, *particles*). These grains are cemented in a superalloy phase (usually—W-Ni-X, X=Fe, Co, Mn, Cu etc.) known as *matrix*. There is a wide difference in the microhardness values of these entities (Table I). This makes sample preparation rather difficult. Grinding or polishing of hard tungsten grains leave deep scratches on the soft phase (matrix) which is difficult to remove subsequently. Conversely, grinding or polishing of softer phase leaves the tungsten grains unattended. It rather difficult to make the surface to be examined perfectly polished, so that the incident light does not get scattered, and the reflection is perfect. Experience and dexterity of the persons who prepare the samples play a predominant role in WHA sample preparation for meaningful metallographic investigation.

Table I

Average microhardness values of the phases present in WHA microstructure

Name of the phase	Percentage of area Covered (approx.)	Microhardness, VPN)
Tungsten grain	75%	400-450
Matrix	25%	275-300

2.1 Cutting

Representative metallographic specimens for are gently cut out of the bulk WHA samples with the help of common cutting machines (*eg.* hacksaw, lathe, shaping machine, band saw, abrasive cutter etc.). Appropriate coolants are used to prevent localised heating of the samples during cutting which might tamper with the original microstructure. Care should also be exercised to inhibit any violent mechanical action which might lead to distortion of microstructure. Usually samples of ¼ inch (0.00635 m) to 1 inch (0.0254 m) size is preferred for metallographic study. Samples of very small or very and large size are not selected for operational difficulties. The edges of very small samples tend to get rounded off during polishing whereas it is extremely tedious and time-consuming to make very large sample totally scratch-free. After having cut a specimen, a level surface is produced by shaping or filing.

Normally, the liquid-phase sintered WHA samples are free from porosity and, hence, no impregnation is required at this stage. However, in certain cases, there may be some porosity in the matrix (as in the case of undersintered and oversintered samples). In such cases, the samples are impregnated in order to retain the pore morphology in tact. As per our experience, wax is a relatively cheap and yet effective impregnating agent which was used in this study. Epoxy resin did not improve the quality of microstructure much when compared to that with a wax-impregnated sample. The effect of using a low melting point metal as impregnating agent for WHA is under study.

2.2 *Mounting*

The specimens may be of odd geometry with sharp edges and it becomes difficult to hold the sample by hand during polishing. It is, therefore, customary to mount the specimens with bakelite or cold-setting resins before polishing.

Cold-setting resins are essentially mixtures of a resin and hardener which are available commercially under different trade names. These resins are used to mount the samples at room temperature. No external pressure or heating is necessary for the resins to set and, hence, there is no chance of microstructural distortion of the specimens during mounting. Non-availability of proper cold-setting resins, high cost and short shelf-life, however, stand in the way of their extensive use.

In the present study, samples were mounted with bakelite. Bakelite, a *thermosetting* resin, sets to become hard under the simultaneous action of heat (~390 K) and pressure (~4200 psi or 29 MPa), normally applied using a mounting press. After cooling, the sharp edges of the bakelite mount are rounded off to prevent damage of abrasive papers or polishing cloth during subsequent operations.

2.3 *Grinding and Polishing*

The mounted specimen is then ground successively on fine emery papers. The emery papers are placed on a glass plate of ~¼ inch (0.00635 m) thickness and the specimen is given a steady to and fro motion by hand, until an even system of parallel scratches is obtained.

While switching from coarser- to finer emery papers, the sample is rotated at an angle of 90° to ensure complete removal of scratches of the coarser paper. After grinding the sample on a fine emery paper (Grade: 000), normally the sample is taken for final polishing in a lap wheel. This sample is thoroughly rinsed in running water to remove the loose debris of emery paper grinding and then polished in a rotating wheel with a soft polishing cloth (velvet, selvyt or blazer cloths) impregnated with suspension of alumina powder in water. In some cases, diamond paste (size: 5 and 0.5 micron) is also used for final polishing.

After polishing, the sample (with a scratch-free mirror-finish surface) is thoroughly cleaned with alcohol and dried with the help of a hair drier. The samples are not etched normally as the polished samples reveal the required features quite well. In most of the cases, no extra feature is revealed by etching the polished WHA specimen. This aspect has been discussed later (§ 3.4).

As polished specimens are then observed under a metallurgical microscope. Details are available in standard textbooks [1,2]. Since metallic samples are opaque, they are examined by reflected light. In this study, a Leica inverted microscope (Model name: Metallovert, U.K.) was used with attached camera for photography with auto-exposure. Normally samples were observed under 100X and 200X magnifications. In some cases, microstructures at 500 X magnification are also reported. Beyond 500X, the clarity of the microstructure was observed to get impaired considerably. Other types of microscopes (SEM, TEM etc.) are, however, available to go in for high magnification and resolution.

3.0 Metallographic examination

Different types of metallographic samples of WHA system were prepared and examined by the authors. Because of their prolonged experience in this activity, special skill has developed to address different types WHA systems with diversified properties and pre-treatments. Some interesting microstructures of WHA systems are presented here for discussion.

3.1 Liquid-phase sintering

Tungsten heavy alloys are produced by liquid-phase sintering [18,19]. It is, however, extremely difficult to ascertain the narrow range of temperature where the system would be subjected to liquid-phase sintering temperature properly. Microstructural investigation plays an important role in identifying the proper temperature range for complete liquid phase sintering.

3.1.1 Undersintering (Stage 1)

When the alloy is sintered well below the required liquid-phase sintering temperature, the tungsten grains retain there original irregular shape (mostly) with no well-defined matrix. One such undersintered microstructure is shown in Fig. 2.

3.1.2 Undersintering (Stage 2)

If the sintering temperature is increased further (but still below the required liquid phase sintering temperature), the tungsten grains grow further due to dissolution and reprecipitation process. But the viscosity of the liquid-phase (which, when frozen, forms the matrix) at that temperature may not sufficient to fill-up all the pore channels completely. As a result, there will be some pores in the matrix indicating undersintering as shown in Fig. 3.

3.1.3 Oversintering (Stage 1)

When the sintering temperature is increased above the required level, the viscosity of molten matrix phase will increase and the liquid phase will try to come down to the bottom part of the compact under the action of gravity. The excess supply of matrix phase at the bottom will then pull the tungsten grains apart from each other to a considerable extent. The microstructure (Fig. 4) will show matrix phase with more area fraction with separated tungsten grains embedded in it. This will lead to a density gradient along the cross section and low mechanical properties of the alloy system.

3.1.4 Oversintering (Stage 2)

When the alloy is sintered at still higher temperature, the tungsten grains grow in size further because of continued and thermally-enhanced dissolution and reprecipitation process. At the same time, higher sintering temperature will also impart higher fluidity to the liquid phase—so much so that even the liquid matrix phase will ooze out of the labyrinth of pore channels due to gravitational pull. Thus, the alloy would be depleted of matrix when frozen leading to large matrix porosity (Fig. 5).

3.1.5 Proper Sintering

Both undersintering and oversintering are equally undesirable as they severely impair the mechanical properties of WHA systems. Hence, after identification of undersintering- and oversintering temperatures for a particular alloy system, an intermediate temperature has to be chosen (tentatively) for proper liquid-phase sintering. After some initial trials, the exact range of liquid-phase sintering temperature is ascertained. Metallography, once again, plays the main role in such cases to check whether the sample has really undergone complete liquid phase sintering. A typical liquid phase sintered microstructure (shown in Fig. 6) contains rounded tungsten grains cemented in a pore-free matrix.

Having identified the proper range of liquid phase sintering temperature with the help of metallography, bulk production of heavy alloy products may continue. The metallographic examination should be continued for future batches of products at a suitable sampling frequency in order to ensure proper liquid-phase sintering of the subsequent batches. Any departure from the expected liquid-phase sintered microstructure (*i.e.* undersintering or oversintering) should be reported to the production department for corrective measures. Metallography thus becomes a powerful QC tool in the area of heavy alloy production also.

3.2 Development of new heavy alloy systems

Although classical heavy alloy system (90W-7Ni-3Fe) is used widely, recently trends have been observed to develop other types of non-classical heavy alloy systems, *viz.* W-Ni-Mn, W-Ni-Co, W-Ni-Cu, W-Ni systems for improved performance [20]. Optical metallography proves to be a very useful tool in this endeavour too. Although the techniques of sample preparation for these new WHA systems are *mostly* the same, each sample would require some inherent intricacies to be addressed for getting the desired results. The details are omitted here.

3.2.1 W-Ni-Mn system

Metallographic technique was used extensively for development of W-Ni-Mn alloy system through liquid-phase sintering. Gradual development of this alloy (from undersintered to properly sintered) is shown through a series of microstructures (Fig. 7-10). Undersintered samples showed a microstructure with elongated manganese grains (Fig. 7 and Fig. 8). When the sintering temperature was increased further, tungsten grains grew in size further with some matrix porosity (Fig. 9). After some more trials, proper sintering temperature was established and a complete liquid-phase sintered microstructure was obtained (Fig. 10).

Another batch of W-Ni-Mn was produced using a manganese powder with high (~1%) oxygen content. The oxide inclusions are observed to be evenly distributed throughout the matrix (Fig. 11). In many specialised applications, it is required to distribute some designed discontinuities (like: pores, oxide inclusions) in the matrix of WHA system. This has been achieved with a modified sintering schedule where the oxide inclusions were scavenged at the periphery leaving the core matrix almost clean (Fig. 12).

3.2.2 *W-Ni-Co systems*

W-Ni-Co system is also gaining prominence due its propensity to exhibit adiabatic shear band (or, shear localisation) when subjected to high strain-rate (~10^5 to 10^6 per second) deformation [20]. Such alloys were developed and were subjected to microstructural investigations by preparing specimens using similar polishing techniques. The temperature of liquid phase sintering was ascertained by repeated trials. Optical metallography played an important role in alloy development exercise as before. Microstructure of an undersintered sample (Fig. 13) is clearly distinguishable from that of a properly sintered one (Fig. 14). The latter will have well-defined and rounded tungsten grains embedded in the matrix.

Having identified the required temperature of liquid phase sintering, a complete batch of W-Ni-Co rods were produced. Selected samples from that batch were subjected to microstructural evaluation and certification for process stabilisation. Here, metallography plays the role of a powerful quality control (QC) tool. Microstructure of a sample taken at random from the stabilised batch is shown in Fig. 15 (colour). This microstructure may be taken as a model for clearance of future batches from QC angles.

3.2.3 *W-Ni-Cu systems*

W-Ni-Cu is another interesting WHA system. This alloy has been developed at DMRL [6]. Microstructures of liquid-phase sintered alloy is shown in Fig. 16 (undersintered) and Fig. 17 (properly sintered). Undersintered microstructure shows irregular tungsten grains embedded in a matrix with clearly visible pores, whereas the properly sintered one shows well-grown rounded tungsten grains in a pore-free matrix.

3.2.4 *W-Ni systems*

The self-diffusion tungsten atoms is too sluggish to form bonds between tungsten particles by solid-state diffusion. That is why liquid phase sintering is usually resorted to for consolidation of tungsten powder particles. Solid-state sintering process can, however, be activated by doping the tungsten powder with nickel [21, 22]. Nickel provides a easy diffusion path for migration of tungsten atoms at relatively lower temperatures (*i.e.* within the realm of solid-state sintering). One such tungsten specimen (doped with ~0.2% Ni) was produced by solid-state sintering with a density of 18700 kg/m^3 (~97% theoretical density). Microstructure of the sample is shown in Fig. 18. The matrix is observed to be free from visible porosity. W-Ni alloy find application in radiation shielding [23].

3.3 *Mechanically deformed samples*

The embedded tungsten grains and the matrix pores both undergo shape deformation when subjected to mechanical working. It becomes more difficult to retain their shapes in tact during preparation of metallographic specimens. Microstructures of some worked WHA specimens, prepared with due care and patience, are presented here.

3.3.1 *Rolled samples*

WHA systems are amenable to deformation by rolling [24,25]. One such WHA rod (60W-28Ni-12Fe) was subjected to direct rolling up to 30% deformation [26]. Microstructure of the rolled samples (longitudinal) is shown in Fig. 19 (unetched). It is observed from the microstructure that the tungsten grains are elongated along the direction of rolling.

3.3.2 *Deformed under low strain-rate*

Heavy alloy samples were subjected to low strain-rate deformation using a Dartec machine [27,28]. Lateral and longitudinal samples (as shown schematically in Fig 20) were cut from the deformed piece for microstructural investigation. The microstructures of the deformed samples are reproduced here (vide Table II and Figs. 21 & 22).

Table II

Details of samples deformed in Dartec machine

Strain Rate	Sample Identity	
	Lateral	Longitudinal
1×10^{2} per second	Fig. 21a	Fig. 22b
5×10^{-3} per second	Fig. 22a	Fig.22b

It is interesting to note that under high strain-rate (1×10^{2} per second), the sample undergo a differential mode of deformation. Tungsten grains near the surface get flattened because of the impact load applied on them (Fig. 21a). The severity of this impact gradually gets moderated as one proceeds from the surface to the central zone. The microstructure of the longitudinal section (Fig. 21b) corroborates this. The grains at the top region are observed to be of higher aspect ratio than those at the bottom (*i.e.* at the central portion of the sample).

This trend is observed to be reversed when the sample is deformed under low strain rate (5×10^{-3} per second). The tungsten grains at top portion near the surface will have sufficient time to transmit the compression load to the bottom layer by physical movement and readjustment. Hence, these grains do not get deformed much in shape as shown in Fig. 22a. The central zone of the sample, on the other hand, had to withstand maximum deformation because of the transmitted compression load both from top and bottom. The tungsten grains get elongated thereby in the lateral direction (Fig. 22b).

3.3.3 *Deformed under high strain-rate*

Heavy alloy samples were subjected to deformation under hydrodynamic conditions, *i.e.* very high strain rates (~10^6 per second). The tungsten grains undergo severe deformation near the surface. This severity gets reduced as one moves towards the central zone. Microstructures of such samples, reproduced in Fig. 23(a-d), illustrates this point.

3.4 Effect of Etching

Normally the tungsten heavy alloys are etched by immersing the polished samples in freshly-prepared Murakami's reagent 10 g KOH in 100 ml distilled water or 10 g of $K_3(CN)_6$ in 100 ml of distilled water) for one minute. Some of the etched microstructures are given in Fig. 24 (W-Ni-Co, sintered) and rolled sample (Fig. 25) whose unetched version is shown in Fig. 19. In our opinion, this etchant does not reveal any new feature which was otherwise shrouded after polishing. It only attacks the tungsten grains in a selective fashion. It is even not sensitive to reveal the orientation of the primary tungsten grains within the secondary ones. It is, therefore, necessary to develop proper etchant for WHA systems.

3.5 Effect of Polishing

The shortcomings of Murakami's reagent can the compensated to a great extent by improved polishing technique utilizing the existing difference in hardness of the tungsten grains and that of the matrix. Manipulating the speed of the polishing wheel and applied pressure, it is possible to impart some relief to the tungsten grains over the softer matrix. This, in turn, provides required contrast to identify the phases clearly without etching. Effect of specialized polishing technique is shown in Fig. 26b (high contrast microstructure with relief effect of tungsten grains) in contradistinction with Fig. 26a (conventional polishing leading to low contrast). The same is shown under higher magnification (500 X) in colour print with improved contrast (Fig. 27).

3.6 Colour etching

Colour etching is a well-established technique in the field of colour metallography [29]. Lehwald *et al.* [30] had developed a colour tint etchant for polycrystalline tungsten (not WHA system) which is sensitive to grain orientation. The present authors are trying to develop suitable etchants for imparting some colour tints to the heavy alloy microstructures. Some typical colour microstructures, obtained with the help of a special type of etchant (patent being applied for), are reproduced here (*vide* Table III and Figs. 28-31).

Table III

Etching times for colour tinting of microstructures

Alloy system	Etching Time, days	Microstructure shown in
90W-7Ni-3Co	5 days	Fig. 28
90W-7Ni-3Co	7 days	Fig. 29
90W-6Ni-4Co	5 days	Fig. 30
90W-6Ni-4Co	7 days	Fig. 31.

Tungsten grains turn green after five days of etching. There are, however, some small red patches on the grains. These red patches increase in size when etched for seven days. Further studies are in progress.

4.0 Scope of future study

4.1 Normally, five distinct entities are believed to be present in the microstructure of a properly sintered heavy alloy system, *eg.*

- Primary tungsten grains,
- Secondary tungsten grains,
- Superalloy matrix with typically 20-30 % tungsten dissolved in it,
- Brittle intermetallic films precipitated at the tungsten-matrix interface,
- Pore at the central zone of some tungsten grains.

Present-day metallographic techniques require improvement to reveal all these features with clear contrast.

4.2 Image analysis of the optical microstructures of tungsten heavy alloy systems would be an interesting study to measure different features (*eg.* percentage of matrix area, grain size distribution, contiguity etc.) quantitatively and relate them with the mechanical properties. Attempts in this direction did not yield any fruitful result because of poor optical contrast between the tungsten grains and the matrix phase. Image analysis software differentiates any particular feature from others present in the field based on its grayness. The observed grayness of tungsten grains and the corresponding matrix phase is almost of same order and it is difficult to separate them from each other digitally. This inherent problem, however, was circumvented by the by two innovative techniques—

i) using specially developed software for analyzing features with poor optical contrast, or
ii) using special techniques (like back-scattered electron images) to enhance the contrast between the features so that the tungsten grains become darker than its corresponding matrix (Fig. 32).

Investigations in this direction are in progress and would be published in due course.

5.0 Conclusions

- Optical metallography is a powerful tool for development and production of WHA systems.
- WHA systems contain two distinct entities with widely varying microhardness levels—matrix (275-300 VPN) and tungsten grains (400-450 VPN). This makes sample preparation difficult. Proper care and skill is required to polish this type of samples.
- In order to derive full benefit of metallography, proper care has to be exercised in sample preparation by retaining the micro-features (like: pores, oxide inclusions) morphology in tact.
- It a required to develop suitable etchants for WHA system. Most widely used etchant (Murakami's reagent) does not reveal anything beyond what is observed under as-polished condition.
- Deep polishing can increase the contrast between the tungsten grains and matrix. It also possible to impart some relief effect on the tungsten grains through deep polishing.
- Colour tinting can be imparted with suitable etchant.

Acknowledgements

The authors would like to thank the authorities of DRDO (Govt. of India, Min. of Defence) for funding this activity through a project, Dr. Dipankar Banerjee, Director, Defence Metallurgical Research Laboratory for his kind permission to publish this work and Mr. N Maitra for his constant interest in this activity. The help rendered by Dr. Abhijit Dutta (Dartec studies), Dr. K Muraleedharan & Dr. P Ghosal (SEM images), Mr. AV Saibaba, Mr. K Subba Rao, Mr. MT John, Mr. Y Sundara Raju and Mr. D Pratap Reddy are also thankfully acknowledged.

References

1. George F Vander Voort, **METALLOGRAPHY : Principles and Practice**, McGraw-Hill Book Company, New York, 1984
2. George L Kehl, **Metallographic Laboratory Practice**, McGraw-Hill Book Company, Inc., 1949
3. Leander F Pease III, *"Inspection and Quality Control for P/M Materials (Metallography and Microstructure"*, **Metals Handbook**, Ninth edition, Vol. 7, Powder Metallurgy, American Society of Metals, Metals Park, Ohio 44073, USA, 1984, pp. 485-489
4. WJ Huppmann and K Dalal, **Metallographic Atlas of Powder Metallurgy**, Verlag Schmid GmbH, P.O.B. 1722, D-7800 Freiburg, Germany, pp. 145, 1986
5. W Schatt, Pulvermetallurgie, **Sinter- und Verbundwerkstoff**, 2nd Edition, VEB Deutscher Verlag für Grundstoffindustrie, Leipzig, 1985 (quoted in Ref. 4, p. 21)
6. N Arvind Kumar, A Saibabu, TP Bagchi and N Maitra, *"Development of Microstructure and Properties of W-Ni-Cu System Through Liquid-Phase Sintering"*, Presented at 24th National Powder Metallurgy Conference, Powder Metallurgy Association of India, Pune, February 18-19, 1998
7. J Lankford, H Couque, A Bose and CE Anderson, *"Microstructure Dependence of High-Strain-Rate Deformation and Damage Development in Tungsten Heavy Alloys"*, **Shock-Wave and High-Strain-Rate Phenomena in Materials**, (Eds.) Marc A Meyers, Lawrence E Murr and Karl P Staudhammer, Marcel Dekker Inc., New York 10016, USA, 1992, Ch. 11, pp. 137-145
8. Timothy J Macabe and James A Mullendore, *"Microstructure Morphology Aspects and the Relationship to Mechanical Properties of Tungsten Alloys"*, **Tungsten & Tungsten Alloys – 1992**, Proc. First International Conf. on Tungsten and Refractory Metals, (Eds.) Animesh Bose and Robert J Dowding, Metal Powder Industries Federation, Princeton, NJ, 1992, pp. 407-418
9. Wang Qingquan, Zhang Binru, Lin Guobiao, Zhou Guoan and Lai Heyi, *"Effect of Molybdenum Addition on Properties and Microstructure of W-Ni-Fe Heavy Alloys"*, ibid., pp. 431-435
10. RL Woodward and RG O'Donnell, *"Microstructural Influences on the Ductility of Tungsten Alloys"*, ibid., pp. 389-396
11. A Bose, H Couque and J Lankford, Jr., *"Influence of Microstructure on Shear Localisation in Tungsten Heavy Alloys"*, ibid., pp. 291-298
12. RM German, A Bose and SS Mani, *"Sintering Time and Atmosphere Influences on the Microstructure and Mechanical Properties of Tungsten Heavy Alloys"*, Metall. Trans. A, Vol. 23A, January, 1992, pp. 211-219
13. Barry H Rabin, Animesh Bose and Randall M German, *"Characteristics of Liquid Phase Sintered Tungsten Heavy Alloys"*, Int. J. Powder Metall., Vol. 25, No. 1, 1989, pp. 21-27
14. Jong-Ku Park, Suk-Joong L Kang, Kwang Yong Eun and Duk N Yoon *"Microstructural Change during Liquid Phase Sintering of W-Ni-Fe Alloy"*, Metall. Trans. A, Vol. 20A, June 1989, pp. 837-845
15. BH Rabin and RM German, *"Microstructure Effects on Tensile Properties of Tungsten-Nickel-Iron Composite"*, Metall. Trans. A, Vol. 19A, June 1988, pp. 1523-1532
16. RM German, LL Bourguignon and BH Rabin, *"Microstructure Limitations of High Tungsten Content Heavy Alloys"*, J. Metals, August, 1985, pp. 36-39

17. RM German, *"The Contiguity of Liquid Phase Sintered Microstructures"*, Metall. Trans. A, Vol. 16A, July, 1985, pp. 1247-1252
18. RM German, **Sintering Theory and Practice**, John Wiely & Sons Inc., New York, USA, 1996
19. RM German, **Liquid Phase Sintering**, Plenum Press, New York, 1985
20. WD Cai, Y Li, RJ Dowding, FA Mohamed and EJ Lavernia, *"A Review of Tungsten-Based Alloys as Kinetic Energy Penetrator Materials"*, **Reviews in Particulate Materials**, Vol. 3, 1995, pp. 71-132
21. RM German, **Powder Metallurgy Science**, second edition, Metal Powder Industries Federation, Princeton, NJ, 1994, pp. 272-274
22. S Gowri and JA Lund, *"An Alternative Model for Activated Sintering in W-Ni and Similar Systems"*, **Tungsten & Tungsten Alloys – 1992**, *op. cit.*, pp. 143-154
23. In-Hyung Moon, Yong-Ho Suh, Ju Choi and Young-Hwan Kim, *"Radiation Shielding Capability of Ni Activated Sintered Tungsten Compact"*, **ibid.**, pp. 479-483
24. James R Spencer and Dennis P Buttleman, *"Tungsten Heavy Alloy Sheet"*, **Tungsten and Tungsten Alloys– Recent Advances**, Proc. Symp. by the Refractory Metals Committee, 120th Annual Meeting of The Minerals, Metals & Materials Society, New Orleans, Louisiana, Feb., 17-22, 1991, (Eds.) Andrew Crowson and Edward S Chen, TMS, Warrendale, Pennsylvania, pp. 75-78
25. CA Lavender and WE Gurwell, *"Effect of Rolling Schedule on the Ductility of 80% Tungsten Heavy Alloy"*, **Tungsten & Tungsten Alloys – 1992**, *op. cit.*, pp. 69-78
26. A Saibabu, unpublished data
27. TP Bagchi, Abhijit Dutta and N Maitra, *"Susceptibility of Shear Localization in Two Tungsten Heavy Alloy Systems"*, P/M Science & Technology Briefs (to be published)
28. Abhijit Dutta, TP Bagchi and N Maitra, *"Propensity for Adiabatic Shear bands in W-7Ni-3Fe Heavy Alloy System Under High Strain Rates"*, P/M Science & Technology Briefs, Volume 2, No. 2, 2000, pp. 14-18
29. E Beraha and B Shpigler, **Color Metallography**, First printing, American Society for Metals, Metals Park, Ohio 44073, August 1977
30. Seighart Lehwald, Wulf Erley and Heribert Wagner, *"An Orientation-Sensitive Colour-Etching Technique for Polycrystalline Tungsten"*, Practical Metallography, vol. 9, September, 1972, pp. 510-515.

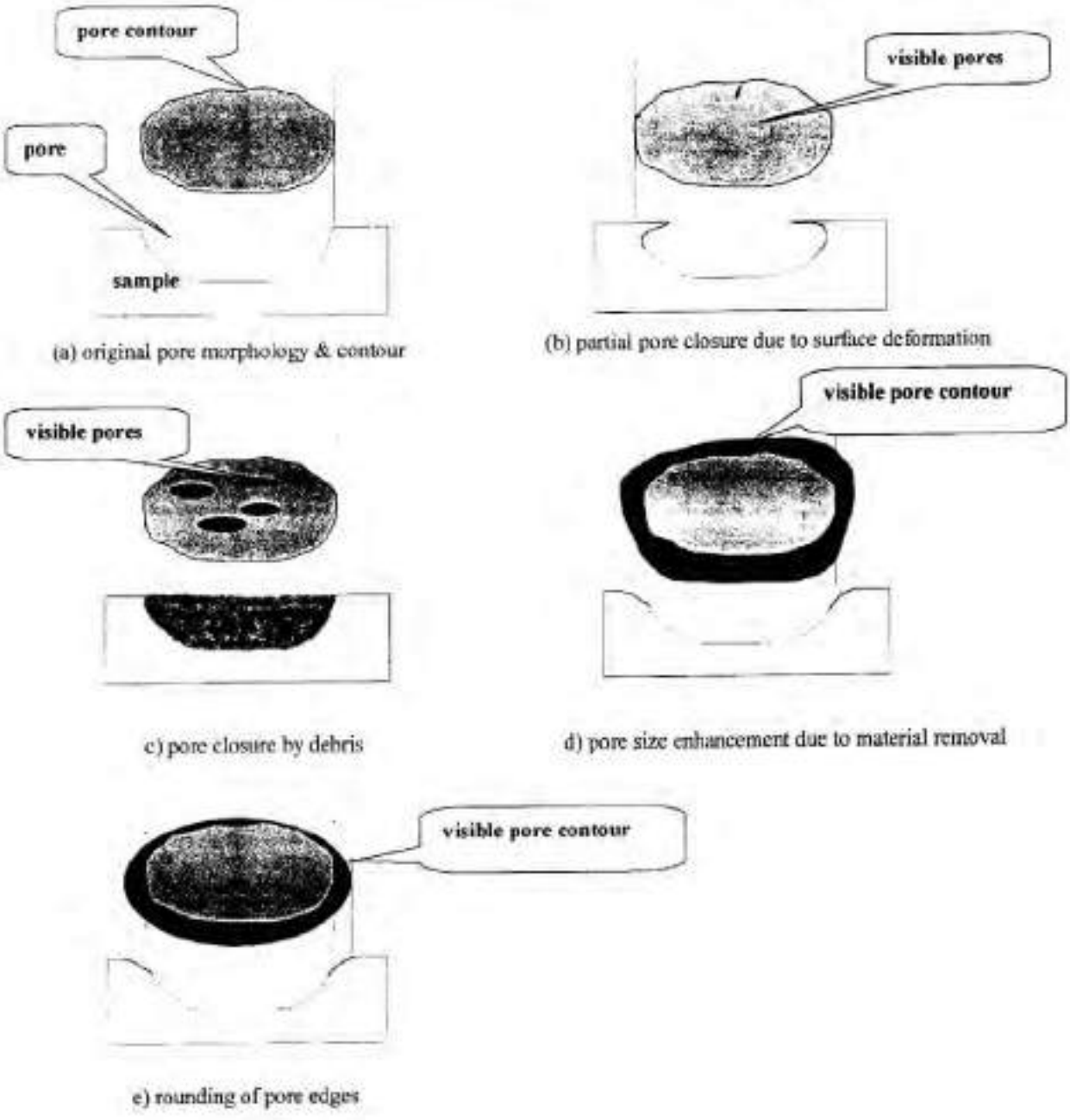

Fig. 1 Different types of shape changes of a surface pore during polishing of P/M metallographic specimens

Fig. 2

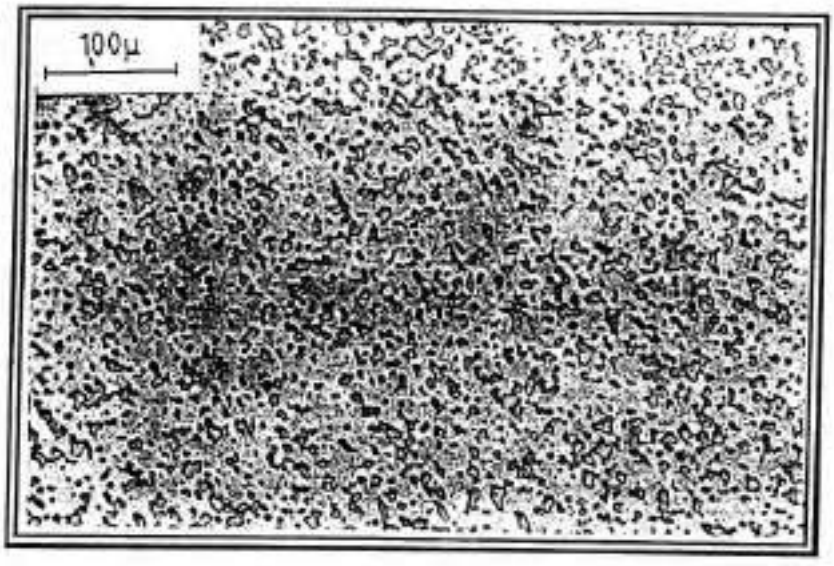

Microstructure of a completely undersintered heavy alloy system.
Primary tungsten grains observed. Matrix not prominent.
Etchant: nil Magnification: 100 X

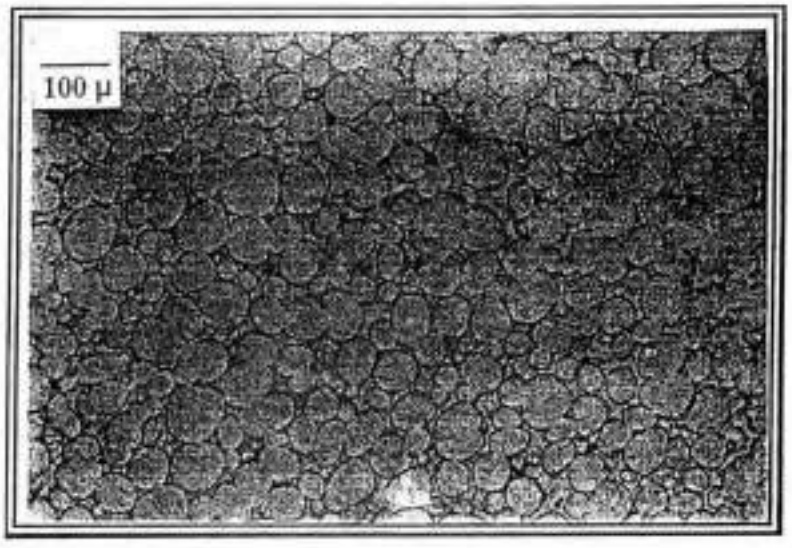

Fig. 3 Microstructure of undersintered heavy alloy system with small matrix porosity.
Etchant: nil Magnification: 100 X

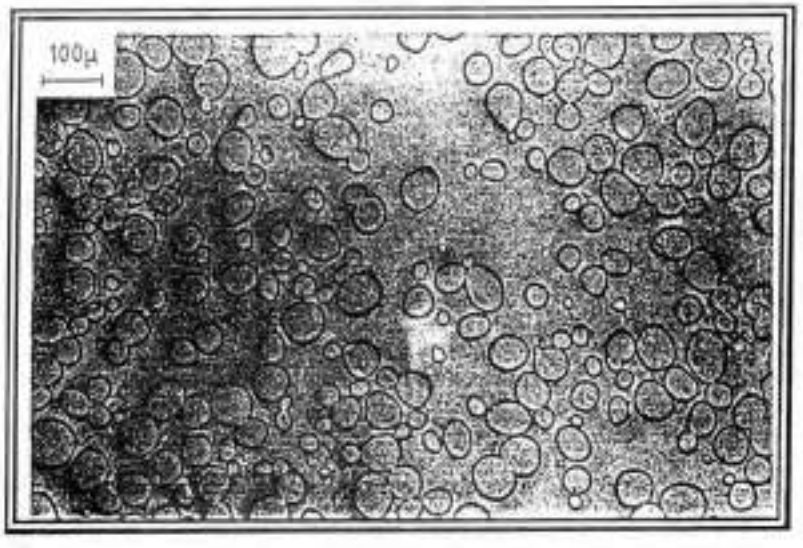

Fig. 4 Microstructure of oversintered heavy alloy system with large volume fraction of matrix with tungsten grains separated.
Etchant: nil Magnification: 100 X

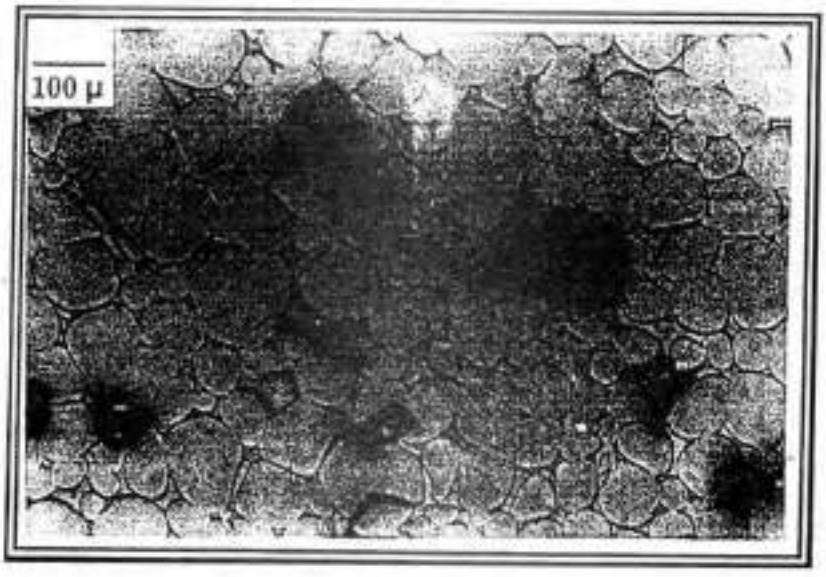

Fig. 5 Microstructure of oversintered heavy alloy system with large matrix porosity.
Etchant: nil Magnification: 100 X

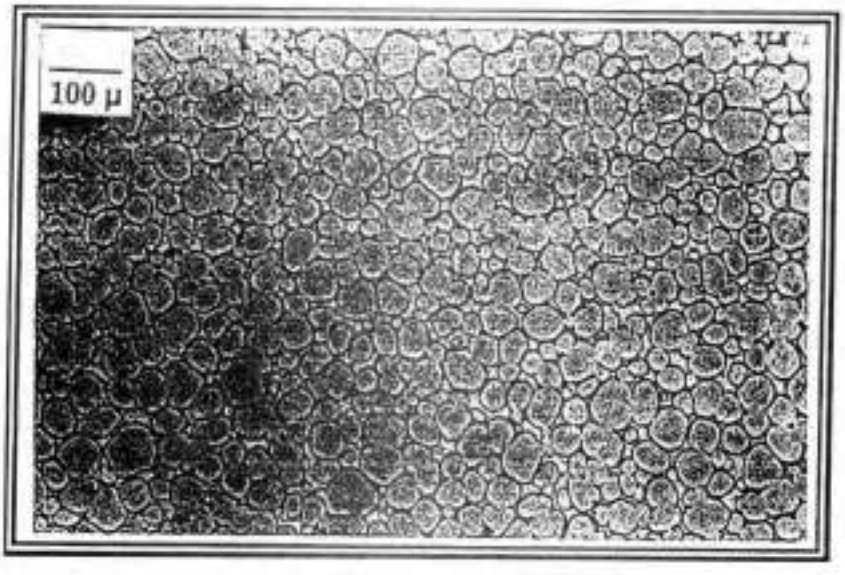

Fig. 6 Microstructure of properly sintered heavy alloy system with no matrix porosity.
Etchant: nil Magnification: 100 X

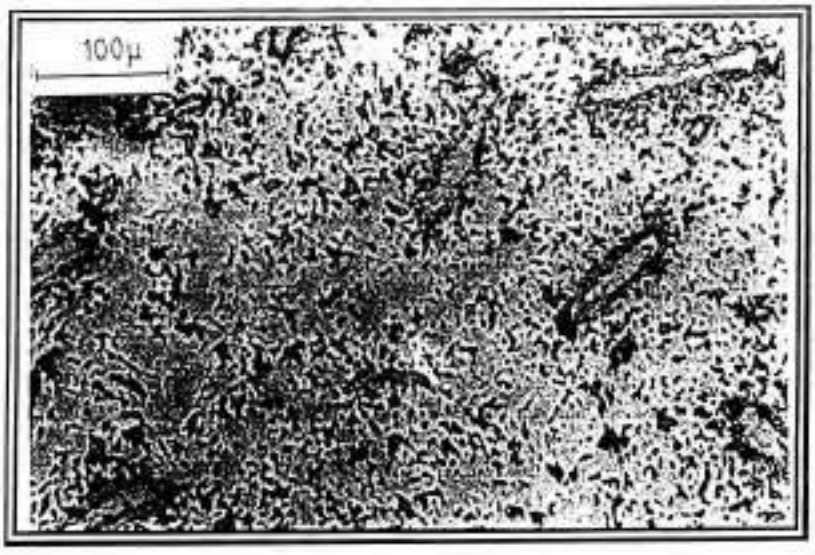

Fig. 7 Microstructure of undersintered 90W-6Ni-4Mn tungsten heavy alloy samples. (1300 C/wet hydrogen/90 min.).
Etchant: nil Magnification: 100 X

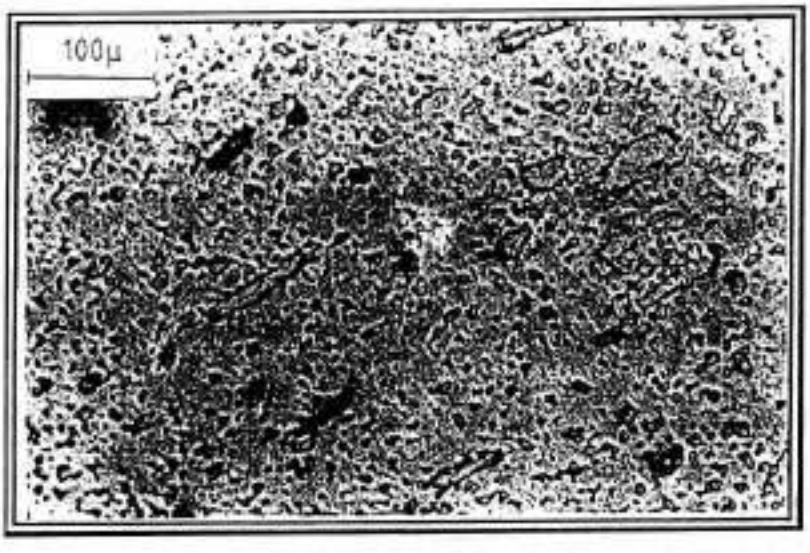

Fig. 8 Microstructure of undersintered 90W-6Ni-4Mn tungsten heavy alloy samples. (1350 C/wet hydrogen/90 min.).
Etchant: nil Magnification: 100 X

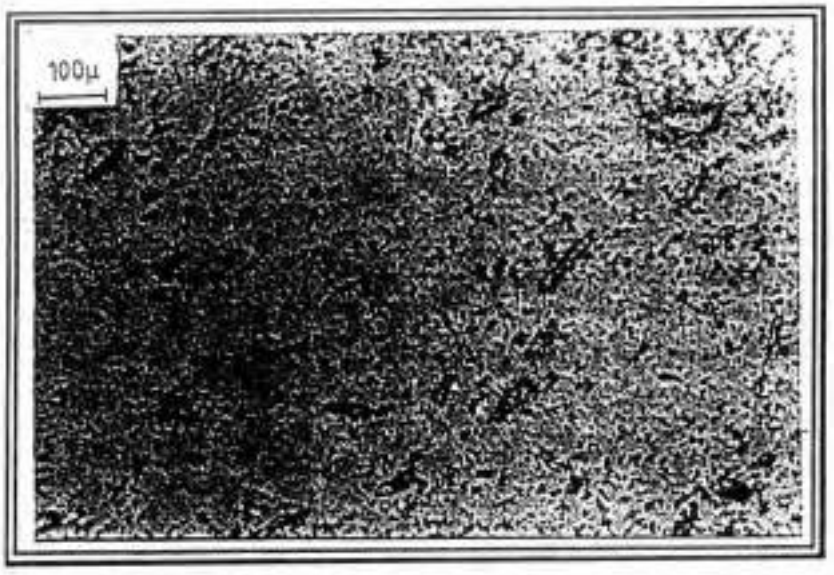

Fig. 9 Microstructure of undersintered 90W-6Ni-4Mn tungsten heavy alloy samples. (1400 C/wet hydrogen/90 min.).
Etchant: nil Magnification: 100 X

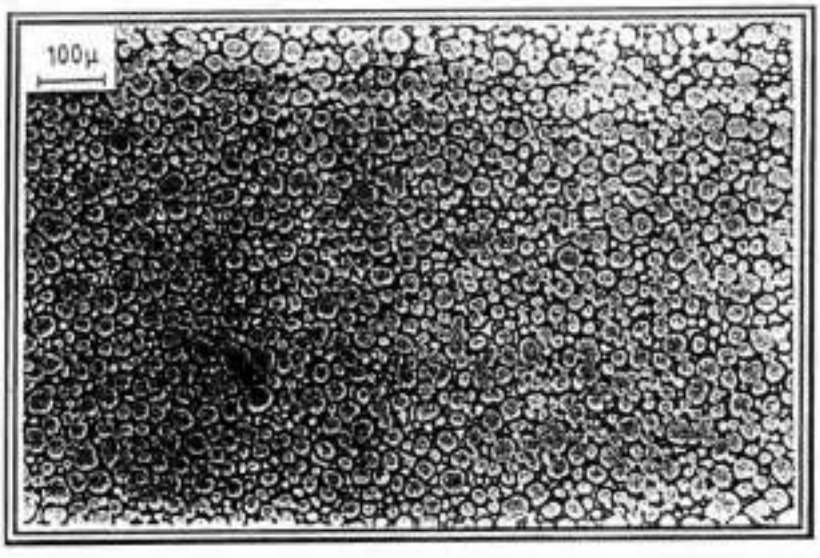

Fig. 10 Microstructure of properly sintered 90W-6Ni-4Mn tungsten heavy alloy. (1450 C/wet hydrogen/90 min.).
Etchant: nil Magnification: 100 X

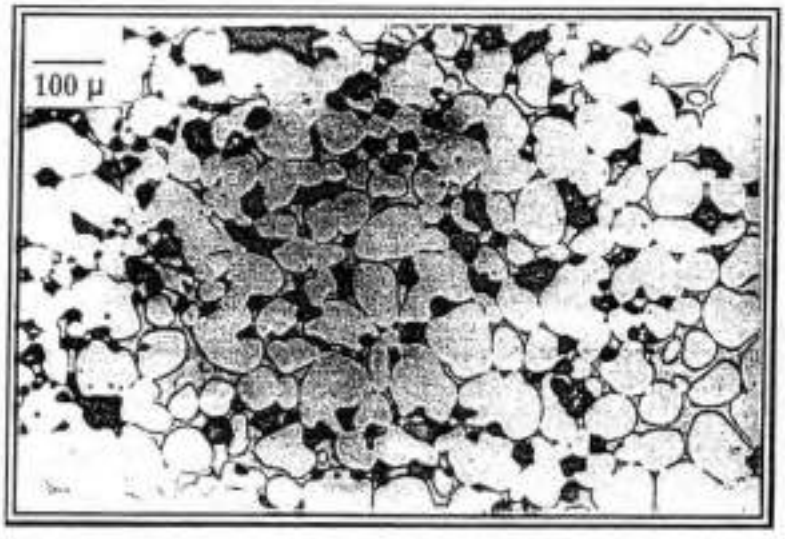

Fig. 11 Microstructures of new-matrix tungsten heavy alloy samples (90W-6Ni-4Mn). Liquid-phase sintered sample. Evenly distributed oxide inclusions in the matrix
Etchant: nil Magnification: 100 X

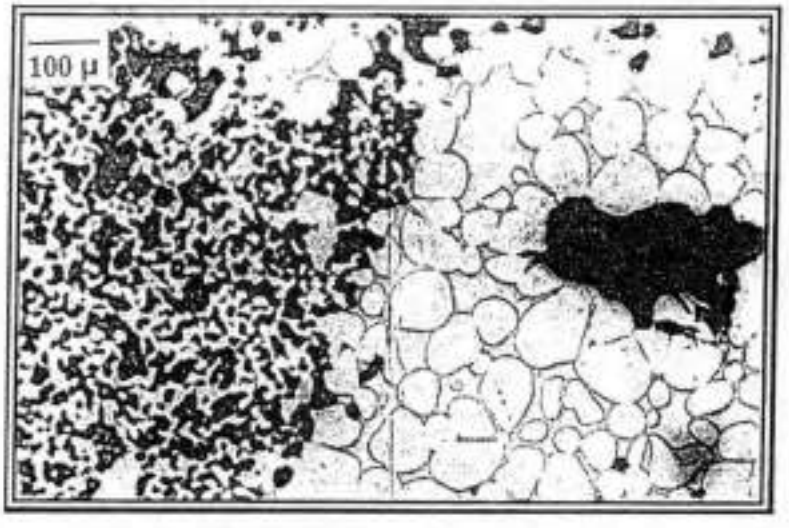

Fig. 12 Microstructures of new-matrix tungsten heavy alloy samples (90W-6Ni-4Mn). Liquid-phase sintered sample. Scavenging the oxide inclusions at the periphery by controlled sintering
Etchant: nil Magnification: 100 X

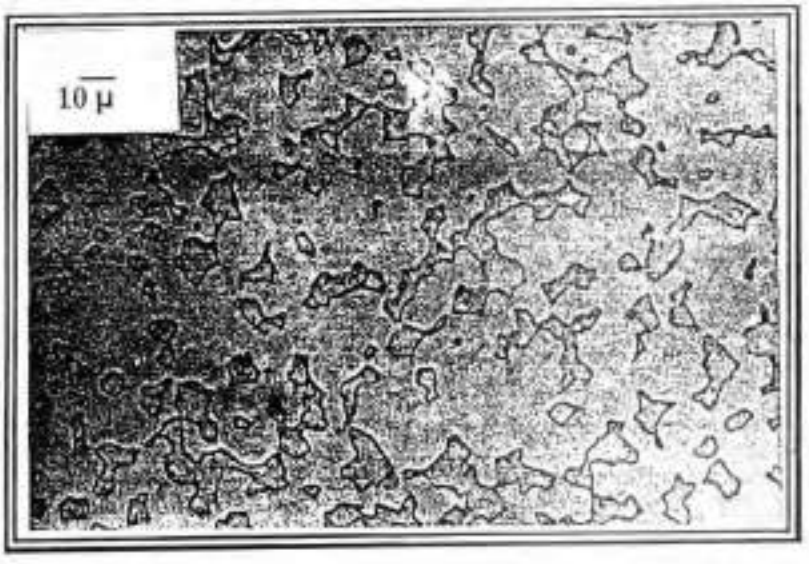

Fig. 13 Microstructure of undersintered tungsten heavy alloy samples (90W-7Ni-3Co).
Etchant: nil Magnification: 500 X

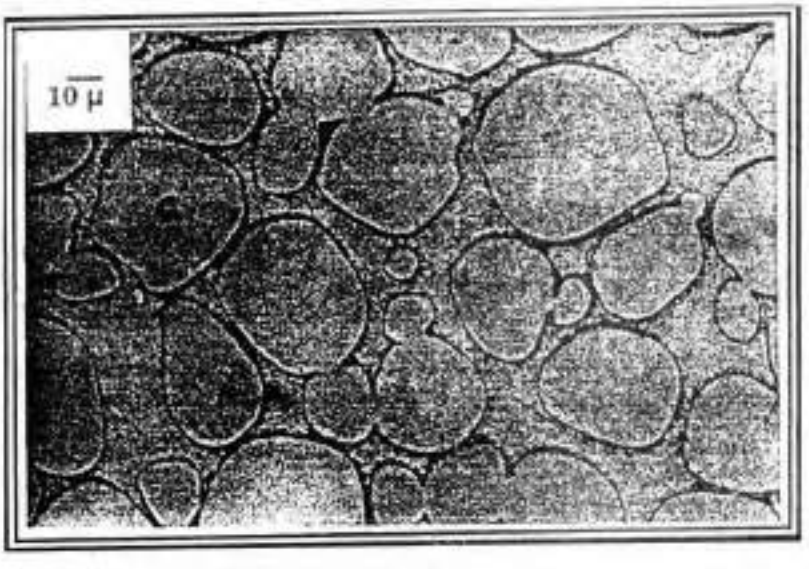

Fig. 14 Microstructure of fully sintered tungsten heavy alloy samples (90W-7Ni-3Co).
Etchant: nil Magnification: 500 X

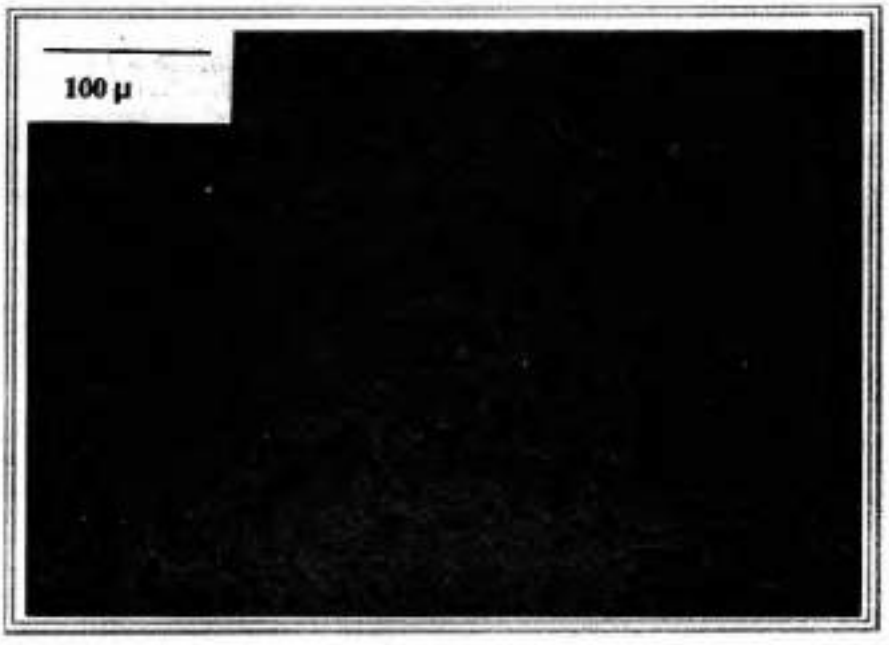

Fig. 15 Colour Microstructure of liquid-phase sintered 90W-7Ni-3Co Heavy Alloy System.
Etchant: nil Magnification: 200 X

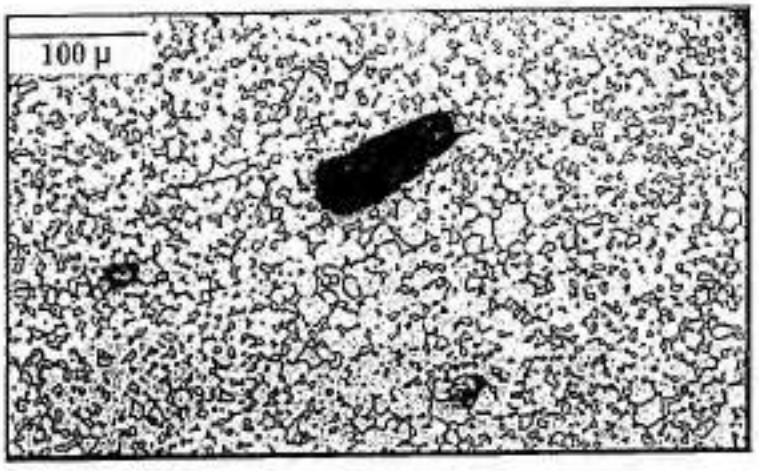

Fig. 16 Microstructure of undersintered 90W-7Ni-3Cu tungsten heavy alloy samples.
Etchant: nil Magnification: 200 X

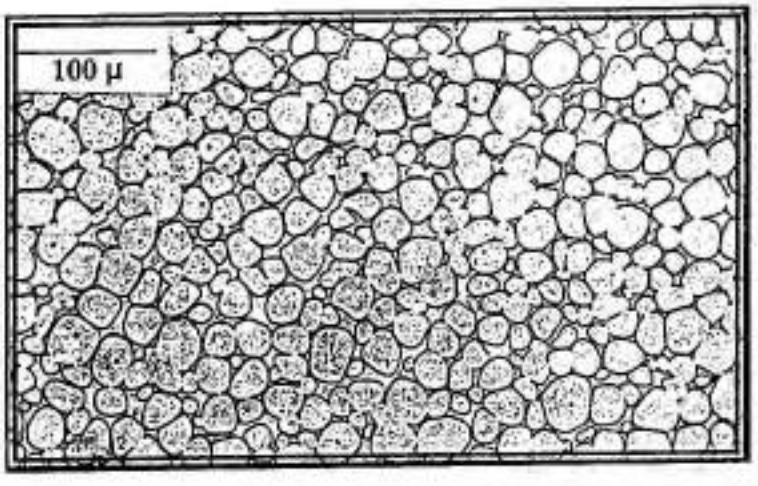

Fig. 17 Microstructure of fully sintered 90W-7Ni-3Cu tungsten heavy alloy samples.
Etchant: nil Magnification: 200 X

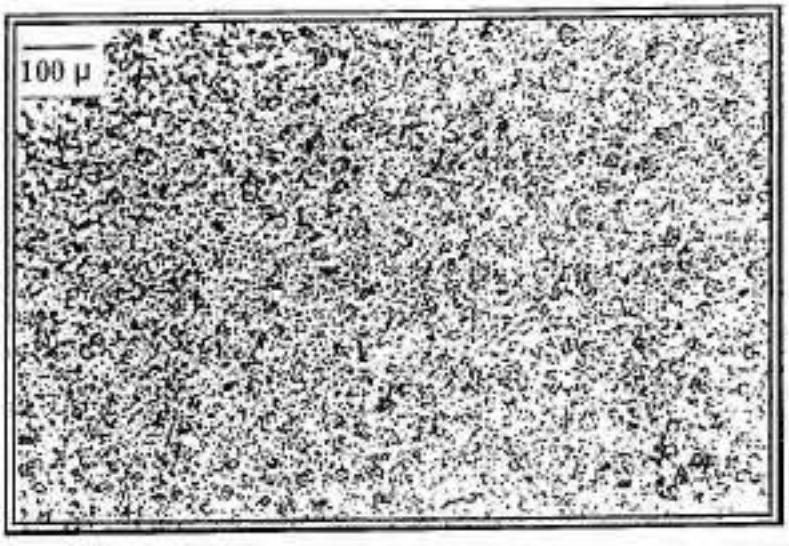

Fig. 18 Microstructure of tungsten samples after solid-state sintering (Ni-activated). Density : 18700 kg/m^3
Etchant: nil Magnification: 100 X

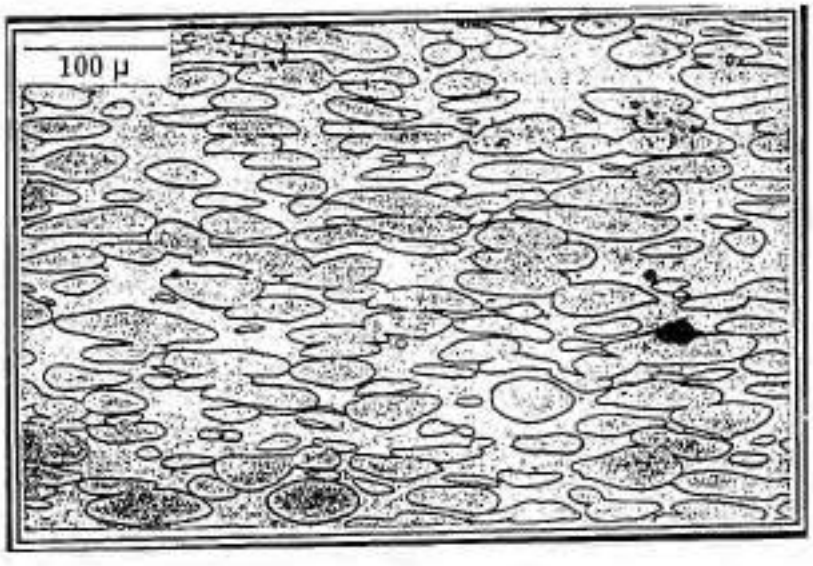

Fig. 19 Microstructures of cold-rolled (30% deformation) tungsten heavy alloy samples (60W-28Ni-12Fe). Transverse section.
Etchant: nil Magnification: 200 X

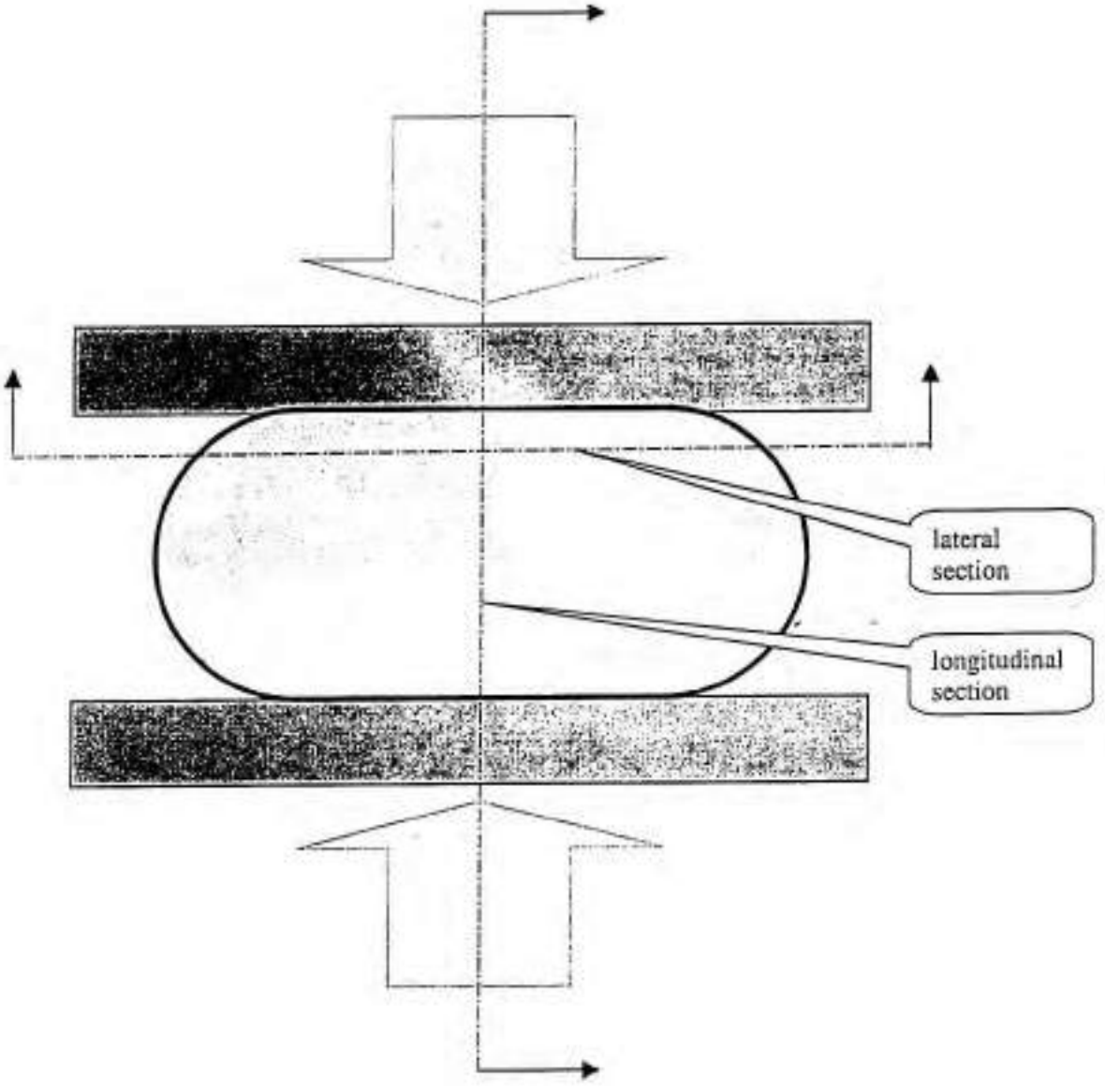

Fig. 20 Application of load on heavy alloy sample in Dartec machine (schematic). The sample gets flattened under compression. Samples were cut along longitudinal- and lateral sections for metallographic investigation.

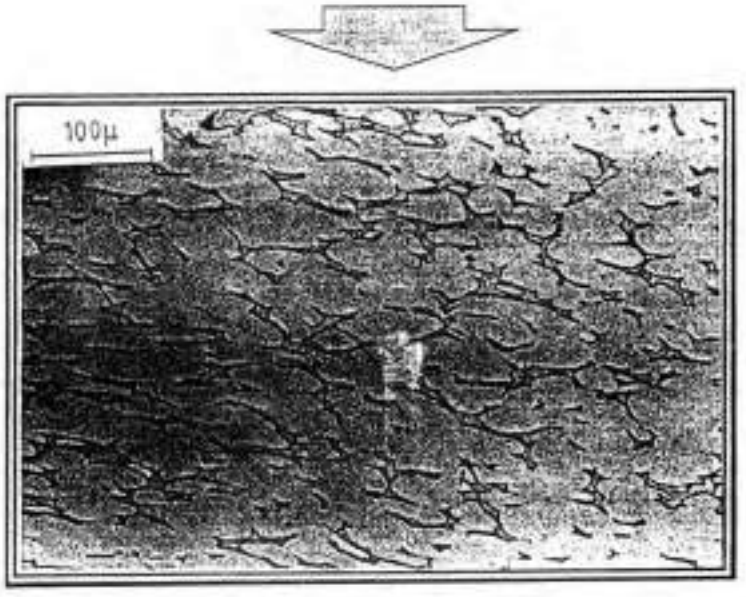

Fig. 21a Microstructure of 90W-7Ni-3Fe Heavy Alloy System (lateral)
Sintered, heat treated & swaged. Deformed at $\dot{\varepsilon} \approx 100$ per second.
Etchant: nil Magnification: 200 X

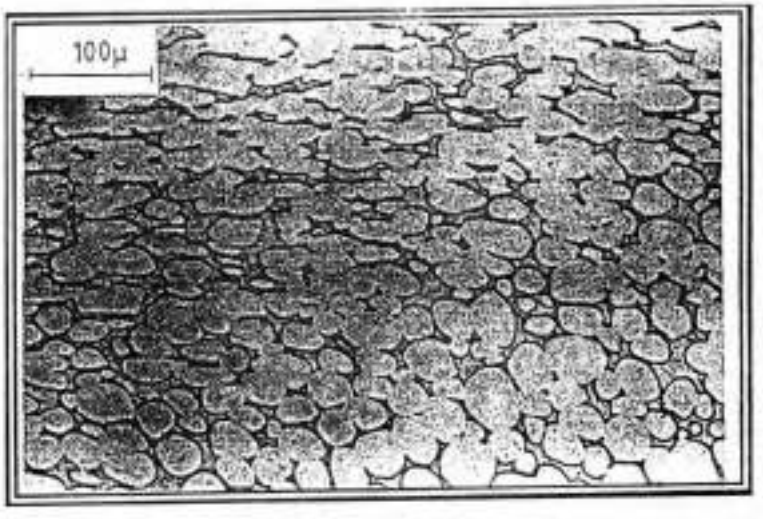

Fig. 21b Microstructure of 90W-7Ni-3Fe Heavy Alloy System (longitudinal)
Sintered, heat treated & swaged. Deformed at $\dot{\varepsilon} = 100$ per second.
Etchant: nil Magnification: 200 X

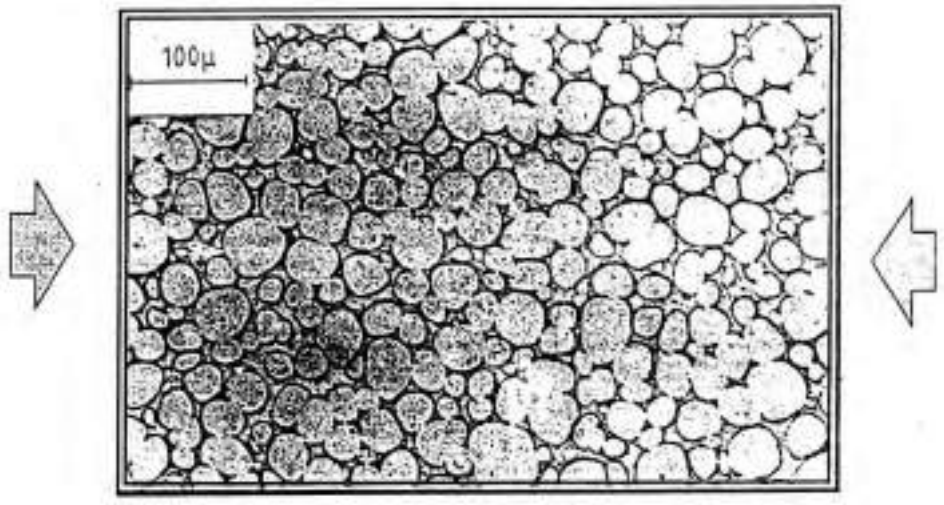

Fig. 22a Microstructure of 90W-7Ni-3Fe Heavy Alloy System (lateral)
Sintered, heat treated & swaged. Deformed at $\dot{\varepsilon} = 0.001$ per second.
Etchant: nil Magnification: 200 X

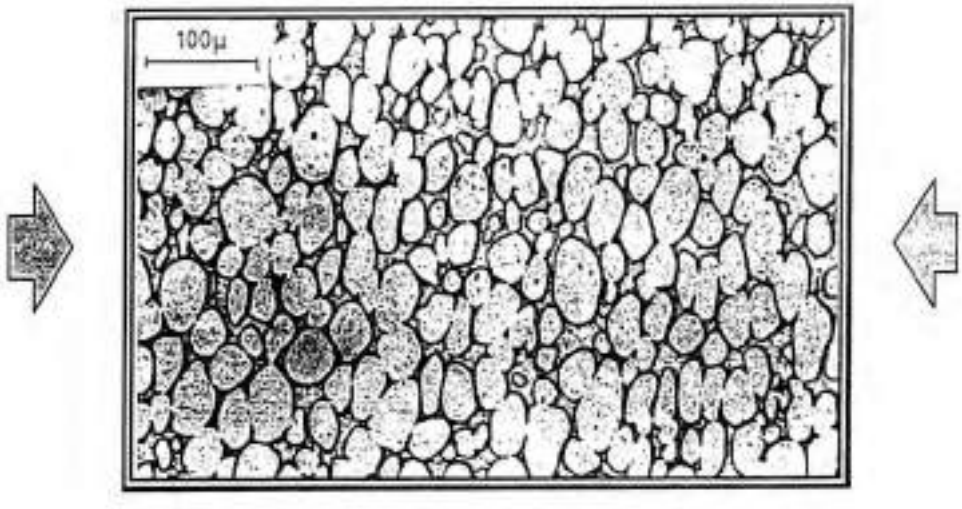

Fig. 22b Microstructure of 90W-7Ni-3Fe Heavy Alloy System (longitudinal)
Sintered, heat treated & swaged. Deformed at $\dot{\varepsilon} = 0.001$ per second.
Etchant: nil Magnification: 200 X

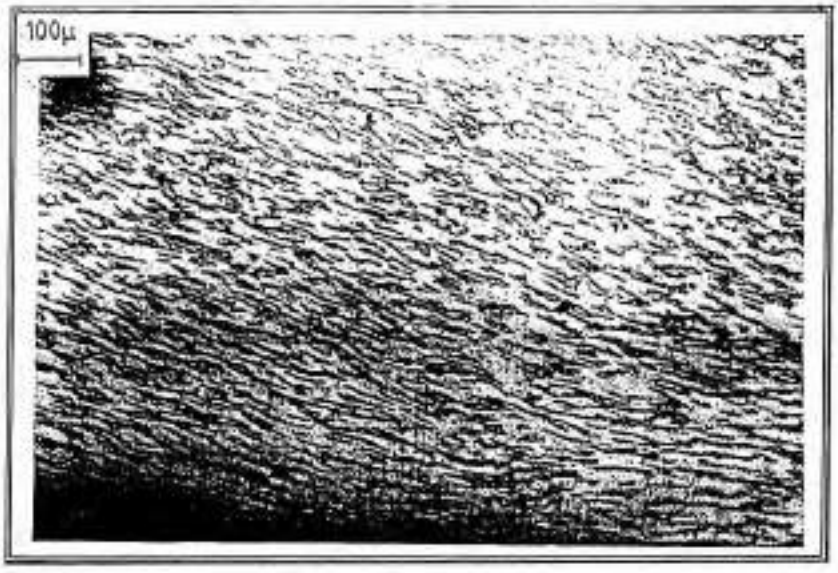

(a) Elongated W grains indicating highest degree of deformation at the surface.

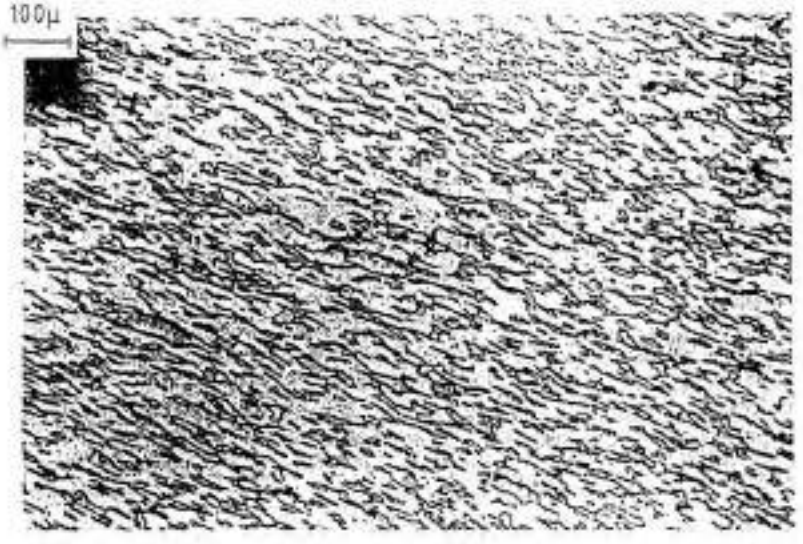

(b) Elongated W grains indicating high degree of deformation near the surface

Fig. 23 Microstructure of heavy alloy sample after high strain-rate deformation ($\dot{\varepsilon} = 10^6$ per second).
Etchant: nil Magnification: 100 X

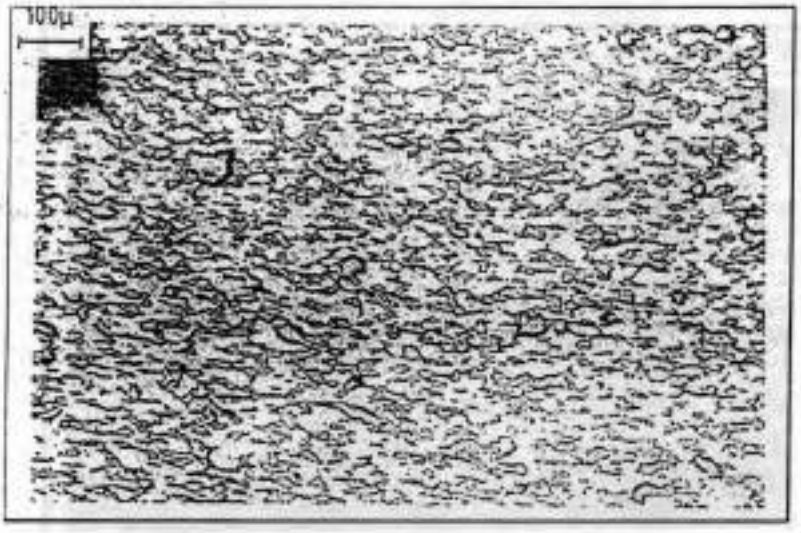

(c) Aspect ratio of W grains reduced indicating lower degree of deformation as one approaches from surface to core region

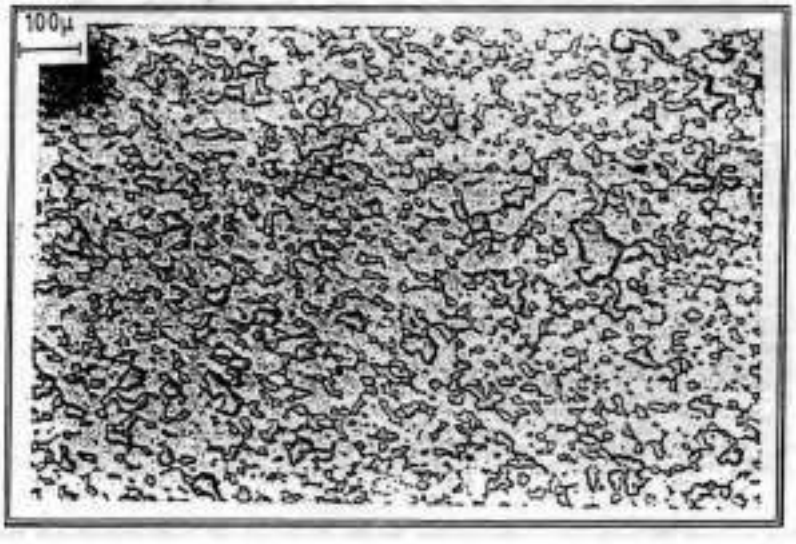

(d) Aspect ratio of W grains further reduced indicating still lower degree of deformation at the core region

Fig. 23 Microstructure of heavy alloy sample after high strain-rate deformation ($\dot{\varepsilon} = 10^6$ per second).
Etchant: nil Magnification: 100 X

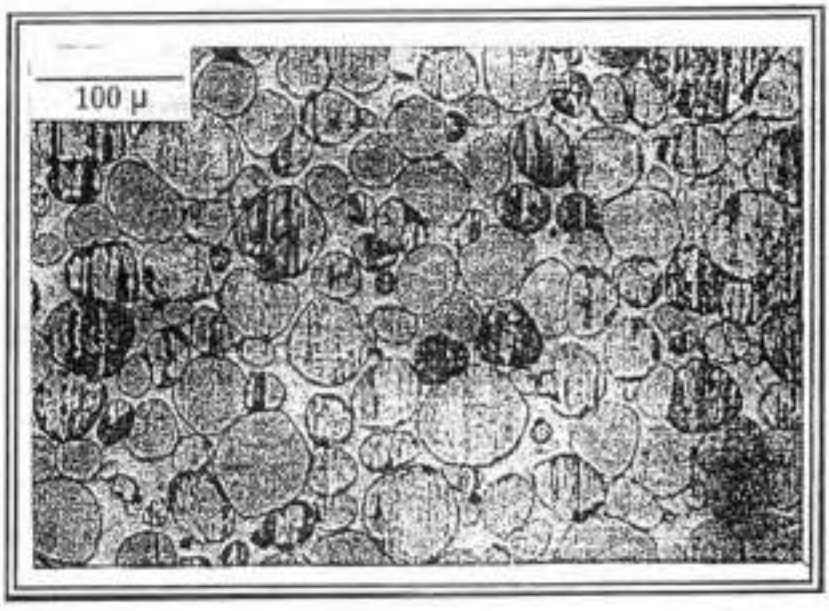

Fig. 24 Microstructures of sintered tungsten heavy alloy samples (90W-7Ni-3Co). Some of the tungsten grains remained unattacked.
Etchant: Murakami's reagent (1 min. dipping) Magnification: 100 X

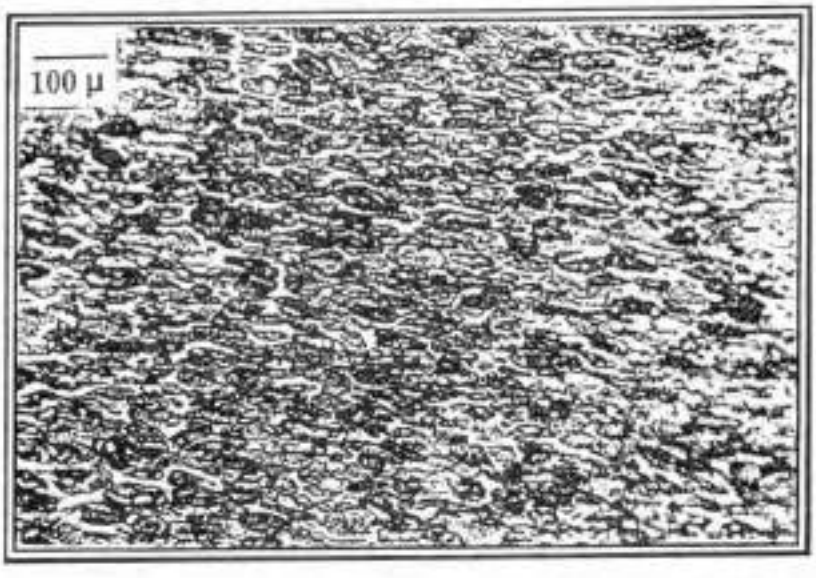

Fig. 25 Microstructures of cold-rolled (30% deformation) tungsten heavy alloy samples (60W-28Ni-12Fe). Transverse section. Etched version of the microstructure shown in Fig. 19
Etchant: Murakami's reagent (1 min. dipping) Magnification: 100 X

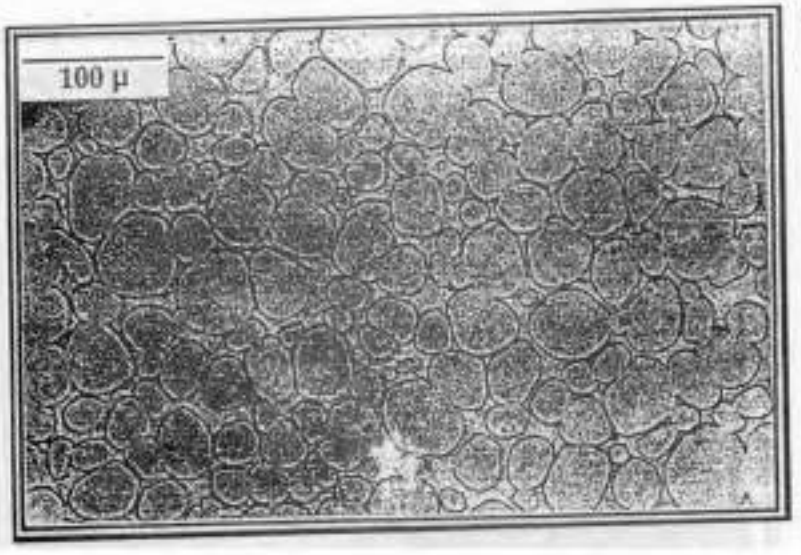

(a) Tungsten grains observed with low contrast

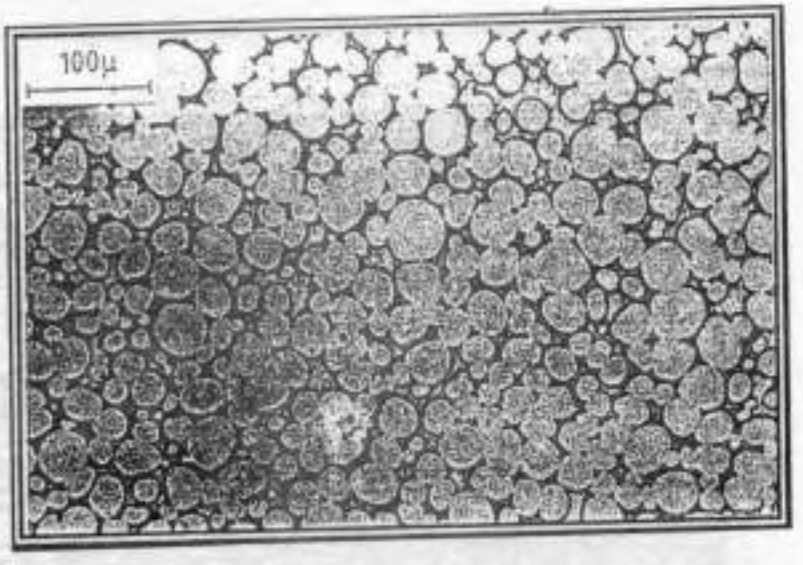

(b) Tungsten grains observed with relief effect.

Fig. 26 Effect of improved polishing technique for better-contrast microstructure of 90W-7Ni-3Fe Heavy Alloy System (Sintered, heat treated & swaged). Etchant: nil Magnification: 200 X

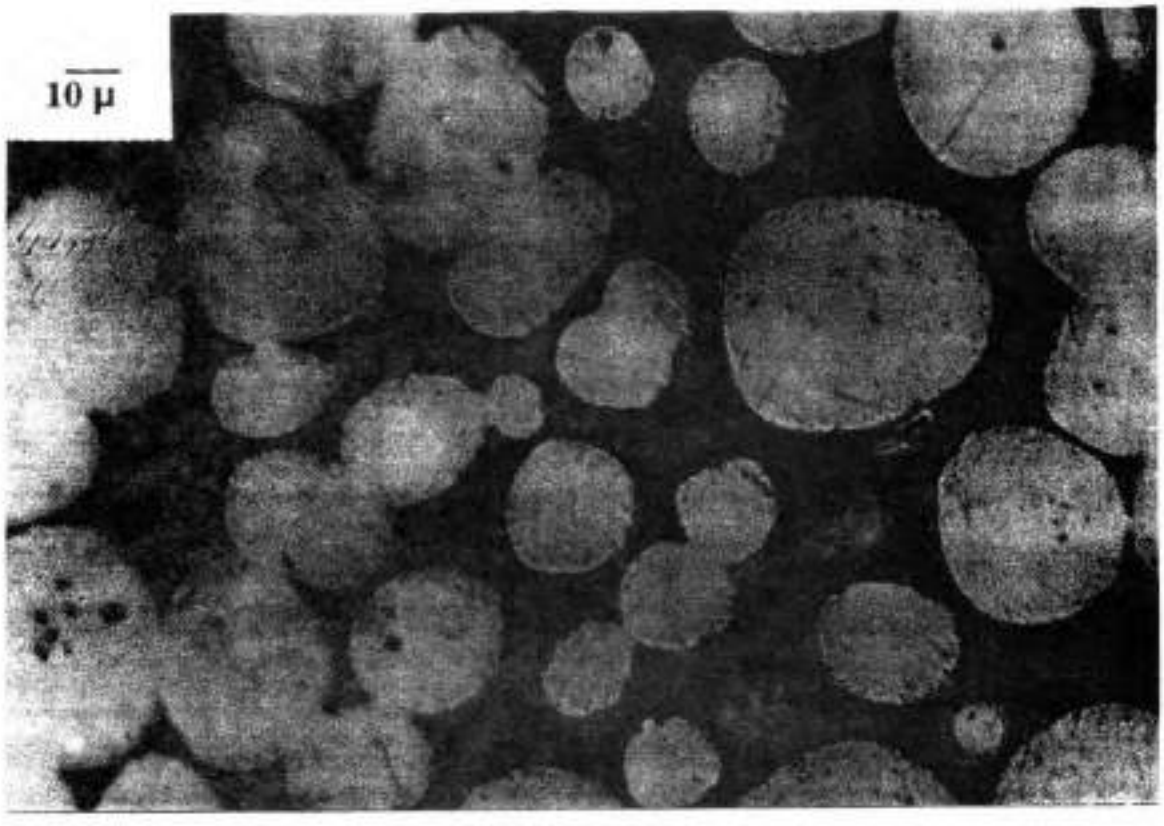

Fig. 27 Colour Microstructure of 90W-7Ni-3Co Heavy Alloy System.
Liquid-phase Sintered. Deep polished for better contrast
Etchant: nil Magnification: 500 X

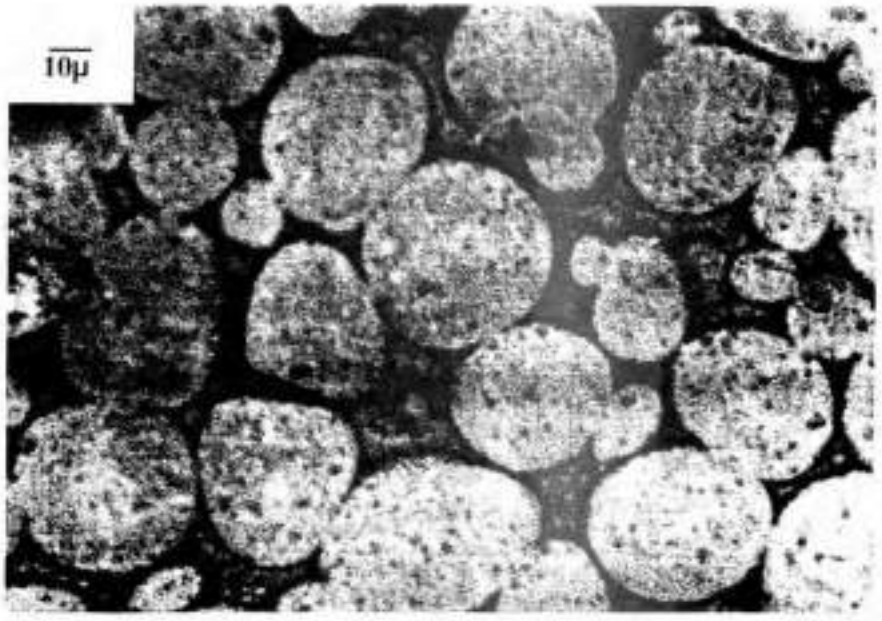

Fig. 28 Colour Microstructure of 90W-7Ni-3Co Heavy Alloy System, Liquid-phase Sintered.
Etching time: 5 days Magnification: 500 X

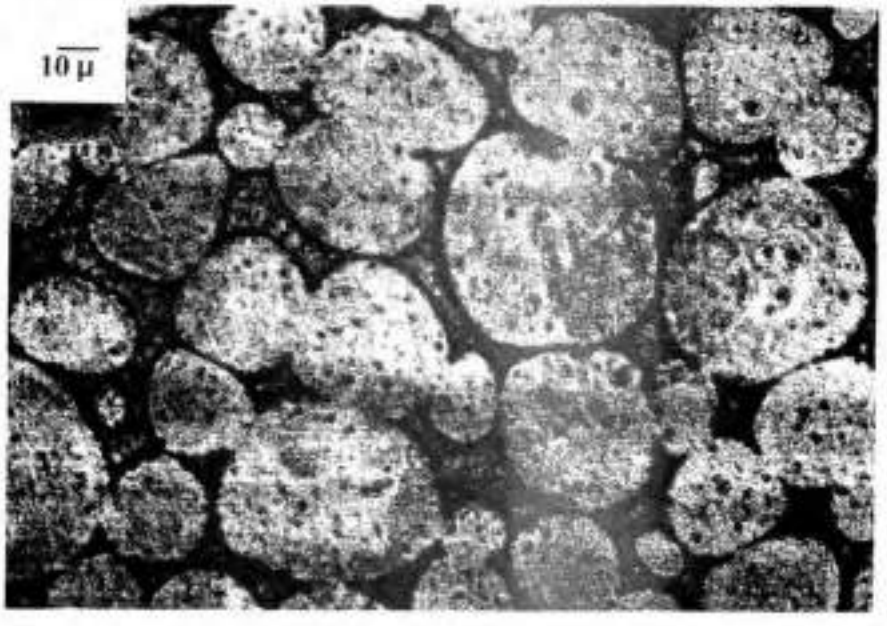

Fig. 29 Colour Microstructure of 90W-7Ni-3Co Heavy Alloy System.
Liquid-phase Sintered.
Etching time: 7 days Magnification: 500 X

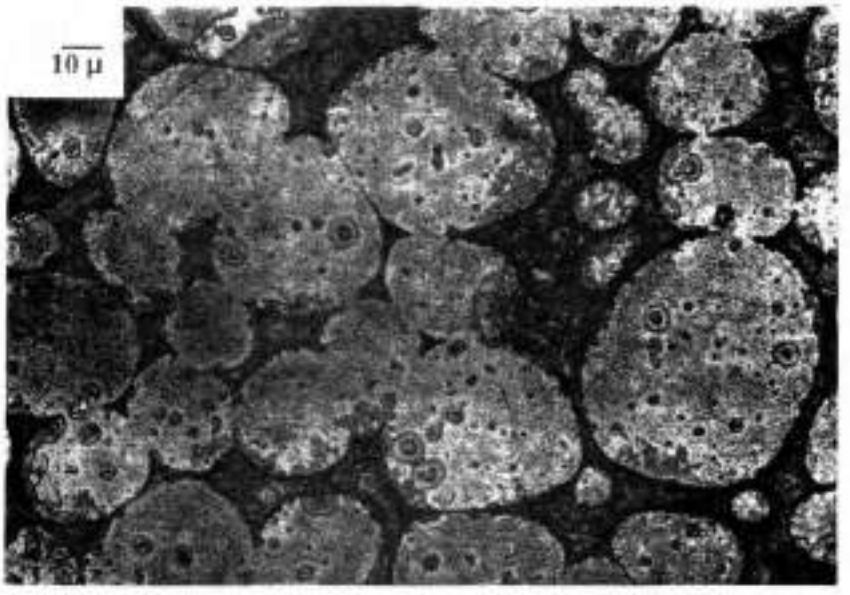

Fig. 30 Colour Microstructure of 90W-6Ni-4Co Heavy Alloy System.
Liquid-phase Sintered.
Etching time: 5 days Magnification: 500 X

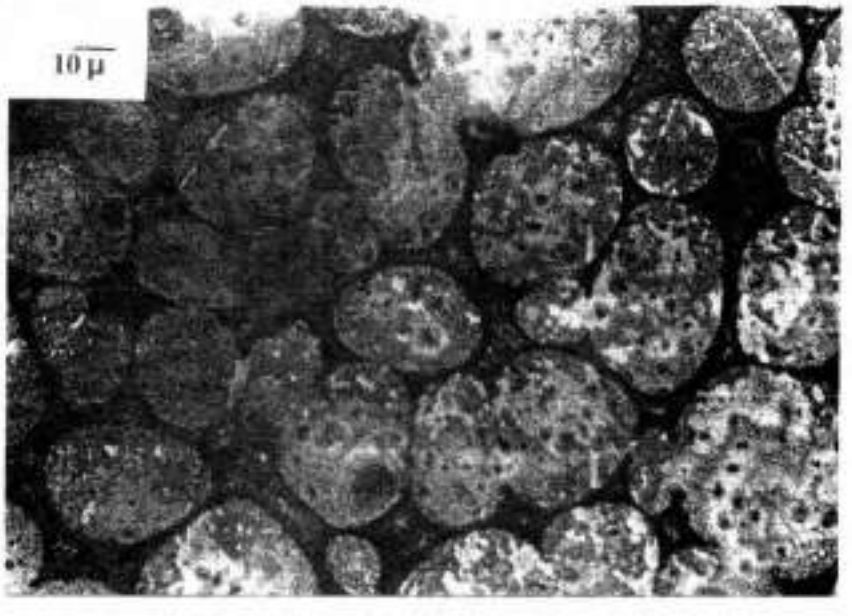

Fig. 31 Colour Microstructure of 90W-6Ni-4Co Heavy Alloy System.
Liquid-phase Sintered.
Etching time: 7 days Magnification: 500 X

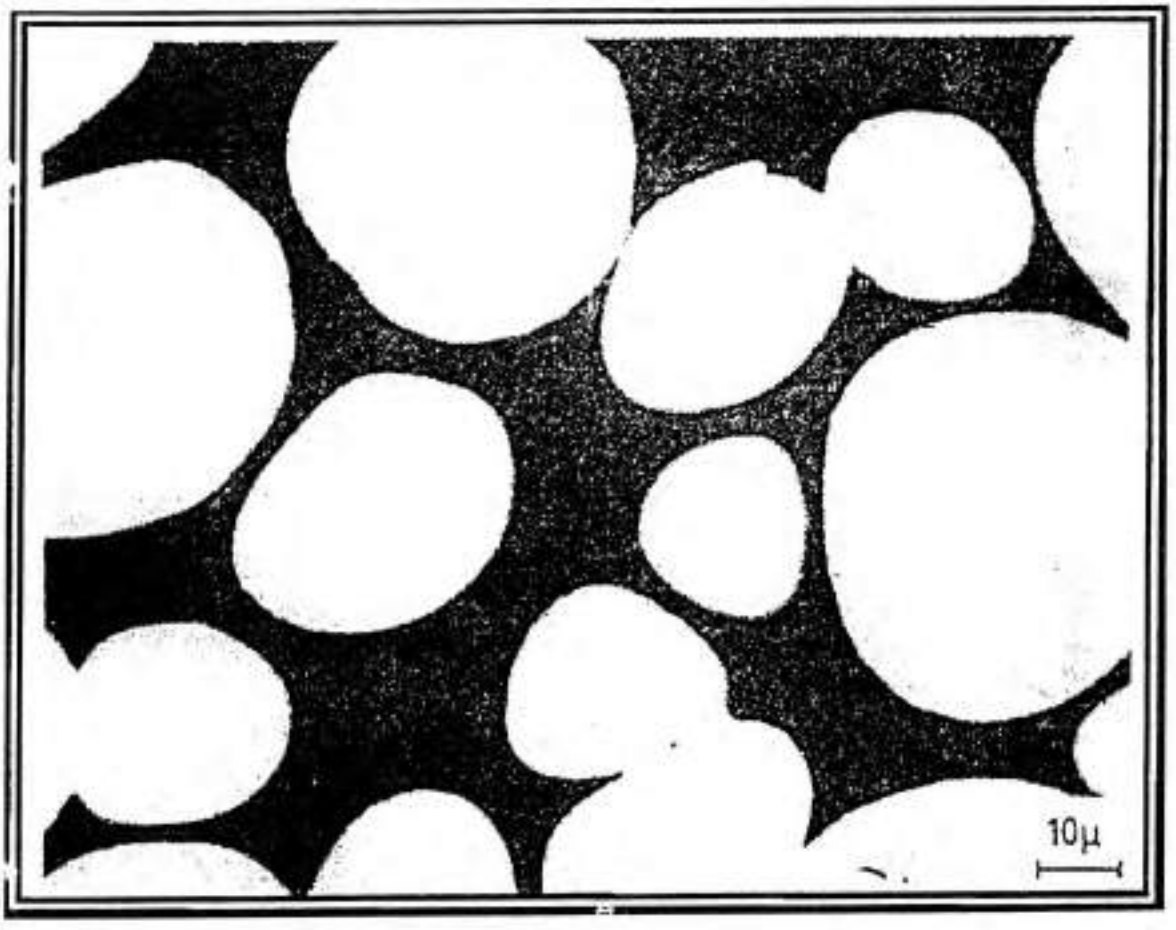

Fig. 32 Back Scattered Electron (BSE) image of 90W-7Ni-3Fe Heavy Alloy with high contrast between tungsten (white) and matrix (black). Etchant : nil.

Evaluation of indigenous raw materials for preparation of in-situ Ceramic Matrix composites

K.L.Hansda* R.J.Singh** R.R.Dash* M.P.Singh**

* Scientist National Metallurgical Laboratroy (CSIR) Jamshepur

** Professor. Met. Engg. & Mat. Sci.Dept. Regional Institute of Technology, Jamshedpur

Abstract

Raw materials suitable for the production of in-situ ceramic matrix composites are scarce. In the present investigation indigenously available clays have been undertaken to study its amenability particularly Al_2O_3-SiC with a source of carbon such as crystalline or amorphous varieties. The suitability of the clays have been assessed through the study of chemical analysis, differential thermal analysis and electron diffraction.

The detailed evaluation of various alumino-silicates have revealed that structurally these alumino-silicates contain varying proportion of different structural units. A particular alumino-silicate has been observed to contain montmorillonite in combination with Kaolinite, Saponite Beidelite etc. Some of the alumino-silicates have been observed to be richer in montmorillonite and some are richer in Kaolinite alumino-silicate of montmorillonite group and has been characterised by high gel and swelling properties. These were basically formed to contain either Na or Ca as exchangeable cations in the structural lattice of the montmorillonite. However, Kaolinite type of clay was characterised by very low gel and swelling property and also characterized by the differential thermal analysis. The presence of two endothermic picks at about 150 and 500-600°C are characteristics of montmorillonite group alumino-silicates[1]. However, Kaolinite type of clay has been characterised by the presence of third exothermic peak at about 900-1000°C. The appearance of this peak was indicative of formation of mullite. The Al_2O_3-SiC CMC could be produced substantially utilising the Kaolinite type of clay.

INTRODUCTION

The preliminary investigation has been undertaken to study the amenability of the indigenously available clays for formation of in-situ ceramic matrix composite particularly Al_2O_3 –SiC with a source of carbon such as crystalline or amorphous varieties. At the first step a large number of clays were collected from the state of Gujarat Orissa, Kerala, Maharashtra, Bihar etc. where a varieties of quality clays are known to exist. The suitability of the clays have been assessed through the study of chemical analysis, differential thermal analysis and electron diffraction[2,3,4]. Chemical analysis of the clays were the main focus to identify the clays for this study. Forty two numbers of the clays were collected and investigated for the preparation of in-situ CMC.

EXPERIMENTAL TECHNIQUES : METHODS & MATERIALS

Three types of raw materials have been identified for the preparation of Al_2O_3 - SiC in-situ CMC. This includes

A clay of montmorillonite group
A typical Kaolinite clay
Colliery minestones

Characterization of the raw materials

Chemical Analysis
Particle size analysis
Identification of phases through XRD
Differential Thermal Analysis
Electron diffraction analysis

The main experimental procedures for this study were evaluation and chemical constituents of clays such as Silica, Alumina, Iron Oxide, Calcium Oxide, sodium and potassium oxides and Titanium oxide. The chemical analysis have been presented in the form of statistical bar charts to give (Fig I) by an over view of the chemistry of the Indian clays. The particle size analysis was performed using standard sieves. The differential thermal analysis of the clays were conducted to evaluate the thermal reactions endothermic or exothermic, to have an assessment of the behaviour of clays during high temperature synthesis for the formation of ceramic matrix composites Electron diffraction analysis of the clays were conducted to reveal the crystalline or amorphous nature of the clays and the mineralogical composition of the crystalline clays[5-6].

Processing of the Clays:

The clays in the as-mined condition were ground below 44μm using a laboratory scale pulveriser and each ground clay was dried at 110°C for two hours to remove surface moisture.

Chemical Analysis:

The clays were chemically analysed for the important chemical constituents particularly aluminium oxide , calcium & Magnesium oxide, sodium and potassium oxide, silica which would determine finally upon high temperature synthesis the amount of silicon carbide loading in the matrix of alumina. The chemical analysis was performed using standard methods .

Differential Thermal Analysis

For the characterisation of the raw materials differential thermal analysis study was carried out on the as received samples using netsch apparatus upto 1100°C heating at a uniform rate of 5°C per minute.

Electron Diffraction Studies

For electron diffraction examination clays in powder form were treated with distilled water. The suspensions were vibrated and left undisturbed for some time. A former film is prepared on a grid and a drop of the colloidal suspension is placed on the formvar film and dried. The samples were then examined in Finch type cold cathode high voltage (45-65 KV) Electron Diffraction camera. The photographs were taken with the help of the camera and "d" values were determined. The minerals were identified using the "d" values.

Preparation of Al_2O_3 – SiC CMC

Preparation of CMC from clay minerals namely Montmorillonites and Kaolinite were examined for their amenability towards carbo-thermal reaction. For carbo-thermal reaction calculated amount of graphite based on stoichiometric calculation was well mixed in the solid state followed by mixing with absolute alcohol. The liquid mix was dried at 80°C for 8 hours, finally ground and packed in graphite crucibles. The powder mixture was heated in a potassium resistance furnace at 1500°C in Argon Iolar-I atmosphere and cooled to room temperature in the atmosphere of Argon.

Chemistry of Clays

In the first step, frequency distributions of the clay property levels have been investigated which gives the general information about the chemistry of the clays. Fig. 2 shows the distribution of silica in the clays. There is a definite peak around 47% but there have been clays which contained as low as 38 % and as high as 62 %.

The distribution of iron oxide has been shown in fig. 3 having, a peak around 11 per cent of iron oxide. A few clays have been found to contain maximum of 17 per cent and some of these as low as 1 to 3 per cent of iron oxide. The iron oxide in clays should be very low for preparation of Al_2O_3-SiC in-situ ceramic matrix composite for improved properties .

Particle Size Analysis

The particle size analysis of all the clays investigated have been done and was observed that majority of the clays contained 80 per cent below 44μm . The particle size analyses of some of the clays have been presented below in Table 1.

All other clays investigated showed similar particle size classification and in the average contained around 80 per cent below 44 micron. For preparation of ceramic matrix composites from the clays, there should be below 10 μm. Further comminution is , therefore, necessary.

Understanding Clay Properties

In order to characterise the clays as feed stocks for the preparation of ceramic matrix composites some other properties were investigated which have been shown in Table 2. These properties indicated the behaviour of the clays during high temperature synthesis of CMC.

Majority of the clays investigated, records high pH, Gel-value and swelling except DB_3, and H_4 which are comparatively less plastic indicating that majority of the clays belonged to montmorillonite one. Na/Ca ratio were on the higher side indicating predominantly sodium as exchangeable cation. The fusion point or the sintering range has been observed to be lower in all the clays except H_3, H_4 WB, SH, KH, DB_3 and DB_5. Clays with higher swelling Gel value have been observed to have high swelling indicating higher plasticity. The lower Na/Ca ratio has been observed with clays marked H_3, H_4 and DB_3.

Electron Diffraction Studies of Clays

Electron diffraction photographs of some crystalline clays have been shown (vide figures 4,5& 7) by the well defined rings. The electron diffraction pattern marked china clay has been depicted in Fig.8. The clays marked DB_3, DB_5 and H_3 are characterised by the absence of crystallinity (vide figure no. 9,10 & 11)

Table 3 gives the electron diffraction analysis of twelve numbers of clays, nine of which are crystalline and hence their mineralogical composition could be determined by measuring the "d" values while three of the clays are amorphous and their compositions could not be determined. However, the composition could be assessed from the physico-chemical properties.

RESULTS AND DISCUSSION

In the first step, frequency distributions of the clay property levels have been investigated which gives the general information about the chemistry of the clays. Fig.1a shows the distribution of silica in the clays. There is a definite peak around 47 percent but there have been clays contained as low as 38 per cent and as high as 62 percent.

The distribution of iron oxide has been shown in fig 1b, there has been a peak around 11 percent of iron oxide. A few clays have been found to contain maximum of 17 percent and some of these as low as 1 to 3 percent of iron oxide. The iron oxide in clays should be very low for preparation of Al_2O_3-SiC in-situ ceramic matrix

composite for improved properties. Iron oxide is considered an impurity in the CMC which deteriorates the high temperature properties.Fig 1c. depicts the distribution of titanium oxide of Indian clays. The majority of the clays have been observed to contain 1.0 to 1.5 per cent of titanium oxide. A few clays have been observed to contain 1.0 to 1.5 percent of titanium oxide. A few clays have been found to contain as high as 4 to 6 percent of TiO_2.

The predominance of calcium oxide in the clays have been revealed through fig. 1.d. The majority of clays are found to contain 2 to 3 percent of calcium oxide. There are clays which have been found to contain as high as 5 to 6 percent of it. Calcium oxide helps sintering of the produced CMC and 2 to 3 percent of it is beneficial as sintering aid.

Fig 1.e shows abundance of Sodium oxide of the Indian clays so that the sodium/calcium ratio is slightly greater than one in majority of the indigenously available clays. Both sodium oxide and potassium oxide are harmful since these are highly fusible and lower the refractoriness of the clays.

Fig 1.f shows the distribution of magnesium oxide in the clays and found to contain 2.5-3.0 percent of it. Presence of MgO is not harmful in the clays since around 2.0 percent of it is deliberately added to CMC as a sintering aid. Both CaO and MgO are economic as sintering aids compared to high cost of yittria (Y_2O_3) used for sintering of ceramics or ceramic matrix composites.

The distribution of aluminium oxide has been presented in fig. 1g. There has been a peak around 18.0 percent. However, there are clays in which upto 30.0 percent of Al_2O_3 has been recorded. Ratio of Alumina to silica has been a deciding factor for selection of clays in the preparation of ceramic matrix composites (Al_2O_3 – SiC). Free Silica is undesirable since it does not help formation of in-situ CMC (Al_2O_3 –SiC) instead, free silica forms silicon carbide which may appear not in chemically combined form with Alumina.

CONCLUSION:

- All the clays investigated showed higher silica & lower Alumina of montmorillonite class
- Iron oxide has been found to be on the higher side a very undesirable impurity
- Alkali oxides, such as sodium and potassium oxides are the unwanted chemical ingredients which favour the formation of glassy phase detrimental for the preparation of CMc
- Alkaline earth metal oxides such as Calcium or Magnesium present in the clays act as dopants in the sintering of the CMC

- The predominant exchangeable cation in the clays was found to be sodium and majority of the clays were plastic showing higher gel and swelling
- The clays recorded higher pH in the alkaline range.
- Clays were finer, eighty percent of which pass below 44 m necessitating further comminution to below 10 m.
- Differential thermal analyses showed endothermic and exothermic peaks characteristic of the montmorillonite type of clays with the exception of a clay marked DB_3 and china clay which depicted an exothermic peak at around 1000°C indicative of Kaolinite group of clay.
- Majority of the clays were crystalline as revealed by electron diffraction analysis and montmorillonite was found to be a common constituent.
- A few clays marked DB_3, H_3 and H_5 were amorphous.
- The amenability of montmorillonite type of clay towards formation of Al_2O_3-SiC by carbothermal reaction was poor. However, Kaolinite type of clay had better response towards high temperature synthesis of in-situ Al_2O_3-SiC/AlN-SiC CMCs.

ACKNOWLEDGEMENT

The authors gratefully acknowledge the guidance and keen interest of Prof.P.Ramachandra Rao, Director, National Metallurgical Laboratory in the present investigation. The authors are also thankful to Prof. R. Yadav Principal R.I.T. Jamshedpur for his kind permission to present this paper in PMI-Tech.Meet 2001.

SELECTED BIBLIOGRAPHY

1. R.Grim "applied Clay Mineralogy" ch # 2, Vol.2
2. A.Chrysanthou,T.Sanchuan"Preparation of Ceramic composite powders from waste colliery minestones" Jr.of Materials Science 29,(1994) 1382-1387.
3. A.C.D. Chaklader, S.Das Gupta, Edmond C.y.Lin, Al_2O_3-SiC composites from Alumino-Silicate precursors" J.AM.Ceram.society 75(8) 2283-85 (1992)
4. A.C.D.Chaklader,E.C.y.lin, and S.Das Gupta "In-situ production of silicon carbide reinforced ceramic compoistes". U.S.pat No.5011799, April 1991.

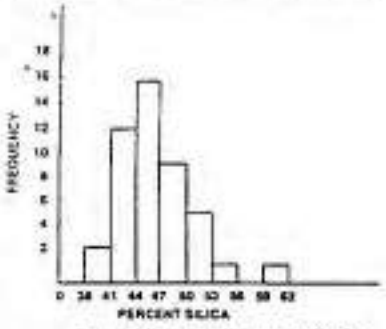

1.a : FREQUENCY DISTRIBUTION OF SILICA IN INDIAN BENTONITES

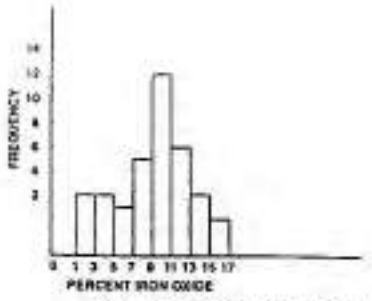

1.b. : FREQUENCY DISTRIBUTION OF IRON OXIDE

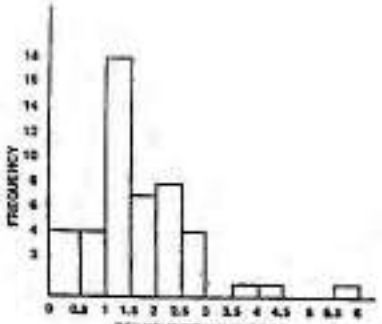

1.c : FREQUENCY DISTRIBUTION OF TITANIUM OXIDE

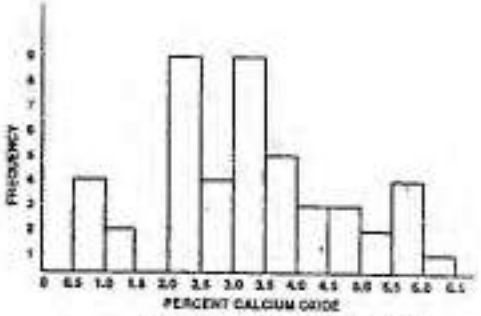

1.d : FREQUENCY DISTRIBUTION OF CALCIUM OXIDE

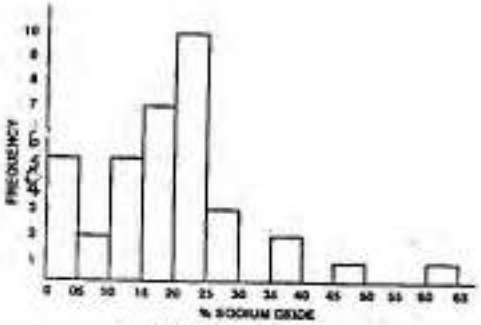

1.e : FREQUENCY DISTRIBUTION OF SODIUM OXIDE

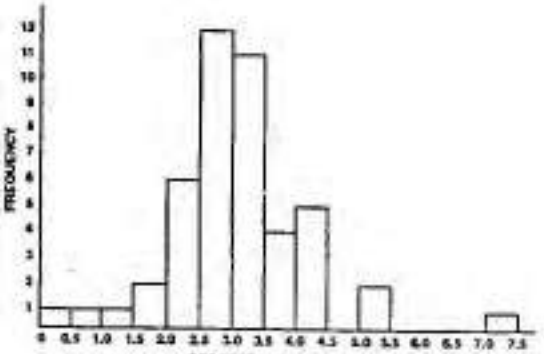

1.f : FREQUENCY DISTRIBUTION OF MAGNESIUM OXIDE

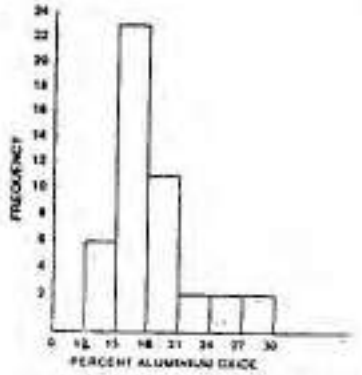

Fig. 3.3.1.g : FREQUENCY DISTRIBUTION OF ALUMINIUM OXIDE

Fig 1 : Statistical Presentation of Chemistry of - Indian Clay

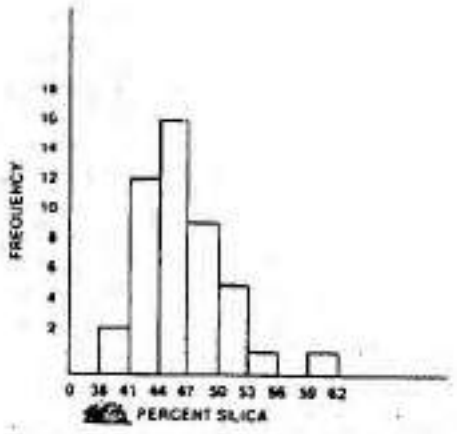

Fig 2 : Frequency Distribution of Silica in Indian Clay

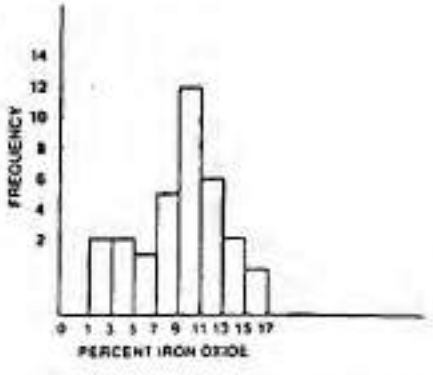

Fig 3 : Frequency Distribution of IronOxide in Indian Clay

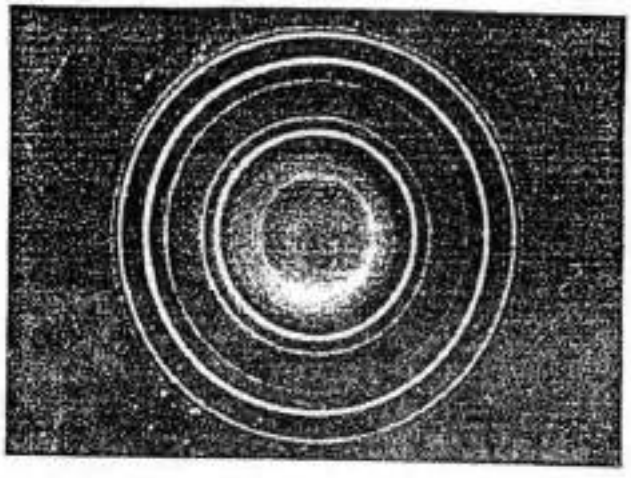

Fig 4 : Electron difraction Pattern of mont-morillonite clay marked V/B

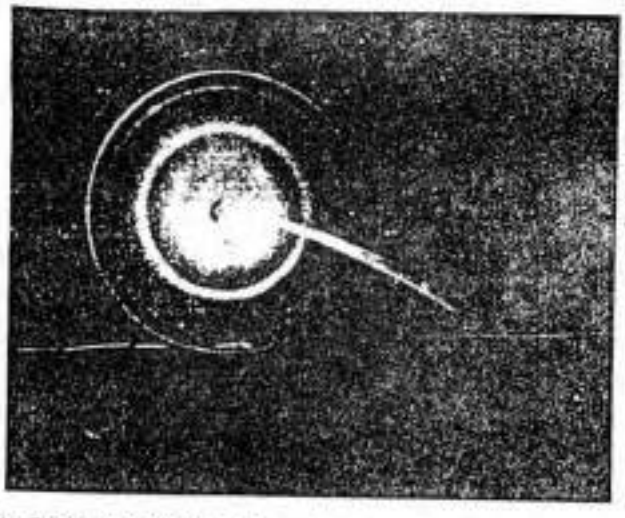

Fig 5 : Electron diffraction pattern of clay marked kH

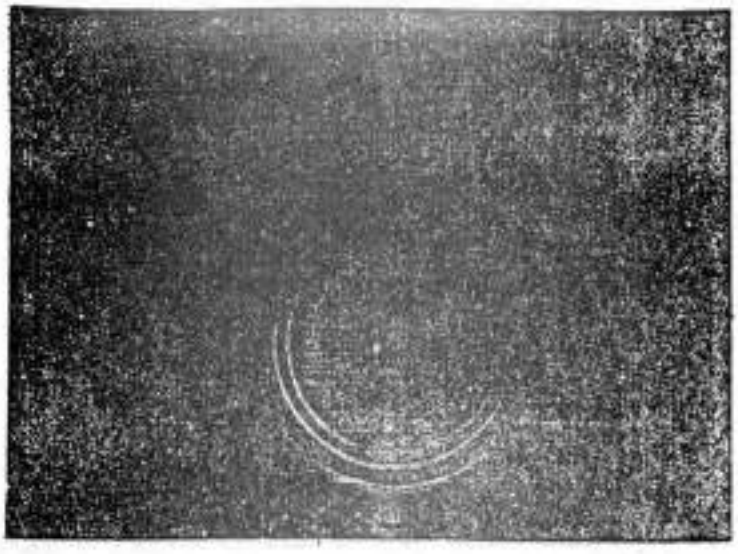

Fig. 6 : Electron diffraction pattern of clay marked H_4

Fig 7 : Electron diffraction pattern of clay marked B_8

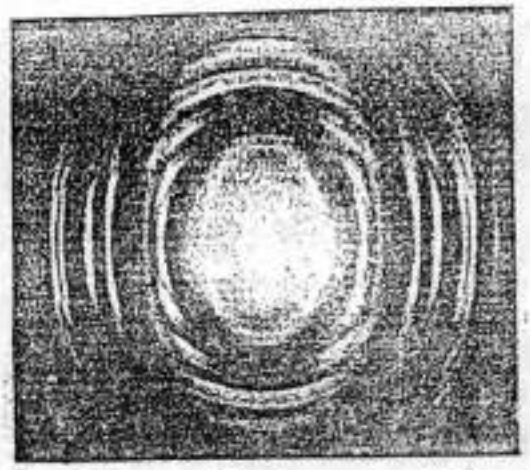

Fig 8 : Electron diffraction pattern of china clay

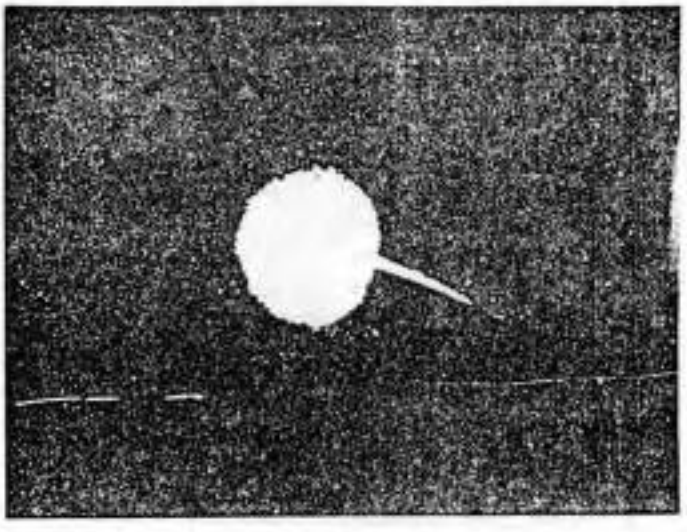

Fig 9 : Electron diffraction pattern of clay marked DB_3

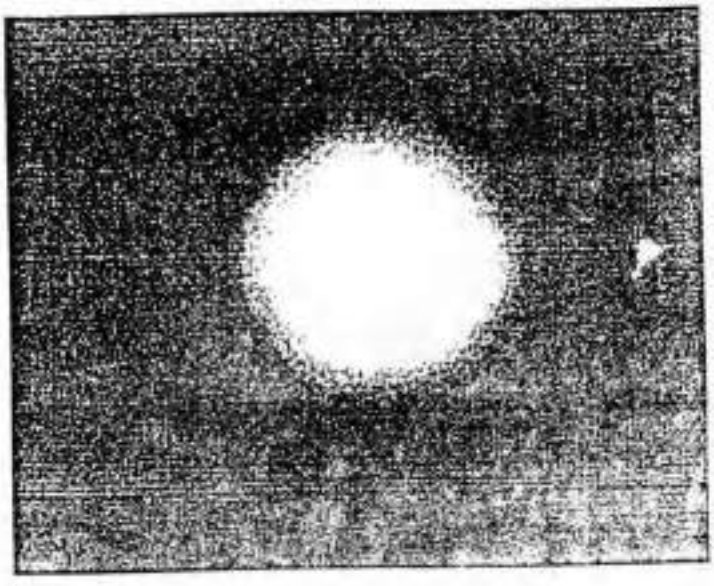

Fig.10: Electron Diffraction of Clay Marked DB_5

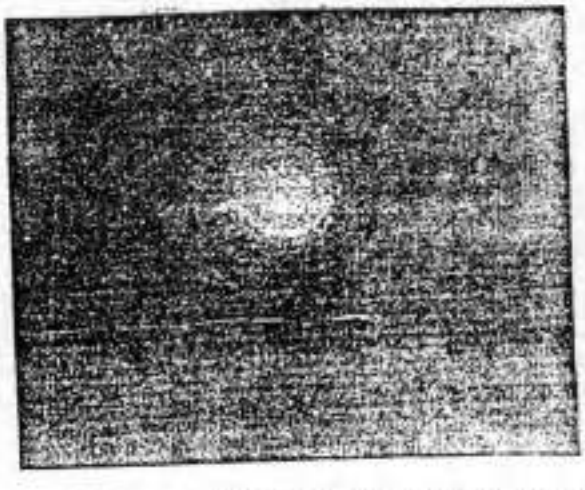

Fig 11: Electron diffraction pattern of clay marked H_3

Table 1 : *Particle Size Analyses of some clays*

Samples of Clays	Particle Size Classification %			
	105 µm	75µm	53 µm	-44 µm
H_1	1.52	2.92	10.04	85.44
H_2	1.56	2.84	10.16	85.28
H_3	1.84	5.12	12.52	80.36
H_4	1.89	4.24	10.80	83.00
H_5	1.80	4.28	10.82	83.12

Table 2 : *Some properties of Indian clays*

Sl. No. of clays	Properties					
	Moisture %	pH	Na/Ca ratio	Sintering range °C	Gel value	Swelling
H_1	10.1	9.6	1.236	900-950	53	8.33
H_2	9.2	9.4	1.923	975-1025	57	14.28
H_3	10.3	10.1	1.0	1150-1200	72	16.2
H_4	11.1	9.8	0.405	1050-1100	38	10.5
H_5	10.1	8.9	0.289	930-980	32	12.5
WB	9.8	10.8	1.79	1050-1100	95	25.0
SH	9.6	9.3	1.35	1080-1150	85	20.0
KH	9.9	10.2	1.57	1020-1100	90	21.5
SK	10.8	9.9	1.65	1050-1100	92	21.4
DB_1	9.6	8.9	1.45	1000-1050	93	20.8
DB_2	9.9	9.5	1.58	980-1050	94	20.9
DB_3	9.6	8.1	0.42	1120-1200	15	7.5
DB_4	9.8	9.1	1.36	1100-1150	85	19.6
DB_5	9.7	8.6	1.23	1100-1120	87	19.0

Table 3 : *Mineralogical composition of the clays*

Mineralogical compositions of some typical clays. Determined from the Analyses of 'd' spacing of Electron Diffraction Structures.	
Clays marked	Mineralogical composition from Electron Diffraction studies
DB_1	Montmoriilonite, illite, talc saponite, crystabolite, diaspore, hectorite, quartz, halloysite
WB	Montmorillonite, kaolinite, vermiculite, quartz, illite, talc, diaspore, crystabolite.
SH	Montmorillonite, crystabolite, halloysite, talc, quartz, saponite
KH	Illite, Montmorillonite, crystabolite, hectorite, diaspore, saponite, halloysite
H_4	Montmorillonite, Crystabolite, halloysite, talc, kaolinite, illite, diaspore
DB_2	Montmorillonite, halloysite, vermiculite, talc, saponite kaolinite, quartz
DB_6	Montmorillonite, crystabalite, nontronite, kaolinite, diaspore, talc
SK	Montmorillonite, Vermiculite, illite, nontronite, saponite, quartz
H_2	Montmorillonite, cyrstabalite, diaspore illite, quartz
DB_3, DB_5 & H_3 are amorphous clays.	

Effect of Potassium and Nickel on the Formation of TiC and TiN Whiskers through Carbothermal Reduction of TiO_2

R.V.Krishnarao, J.Subrahmanyam and V. V. Ramarao

Defence Metallurgical Research laboratory
Kanchanbagh, Hyderabad-500058 India

Abstract: TiC and TiN whiskers were produced through carbothermal reduction of TiO_2 in the presence of potassium (K_2CO_3) and nickel ($NiCl_2$). Effect of potassium, nickel and heating rate on the formation of whiskers was studied. Potassium was found to be an essential constituent for whisker formation. Nickel acts as a catalyst for whisker formation in the presence of potassium only. The yield of TiC and TiN whiskers was maximum at 1000-1200°C and at 920-1000°C respectively. At higher temperatures, formation of particulates was the dominant process. Increase in K_2CO_3 concentration during fast heating and decrease in K_2CO_3 concentration during slow heating was found to be beneficial in increasing the formation of TiC whiskers. A vapour-liquid-solid growth mechanism of whisker formation was identified. Initially K_2CO_3 dissociates and K_2O rich liquid form by reaction between K_2O and TiO_2. This potassium titanate react with $NiCl_2$ and form a complex K-Ni-Ti droplet. Continuous supply of TiO/TiO_2,CO, and N_2 , to this droplet lead to the precipitation of TiC/TiN whisker.

1. INTRODUCTION

Due to high strength, and oxidation resistance, SiC whiskers are widely considered to be an attractive reinforcing agent for various materials. However, SiC whiskers have some limitations because of their high chemical stability. Except SiC whiskers, there are very few types of whiskers commercially available on a large scale. There is a need to produce new whisker materials on a large scale.

Titanium carbide (TiC) and titanium nitride (TiN) are technologically very important materials. TiC is used for cutting tool applications, armour, and as composites for tape heads in the electronic industry, because of its high hardness (20-30GPa), good tensile strength (500-600MPa) and moderate fracture toughness (4-4.5MPaM$^{1/2}$). TiC has a high melting point (3067°C), low thermal expansion co-efficient 7.9X $10^{-6}K^{-1}$ and good thermal and electrical conductivities. TiN is extremely hard (8 to 9 on the Mohs scale), abrasion resistant comparable to diamond. It possesses high melting point (2950°C), gold colour and high electrical conductivity. It is stable at high temperatures in inert atmospheres. According to thermodynamic calculations TiN should be compatible with SiC, Al_2O_3, ZrO_2, Si_3N_4 and TiB_2 [1]. TiN whiskers are said to have better chemical stability toward iron aluminides and nickel aluminides than has SiC [2]. They may be useful in these aluminides and other metal matrix composites.

Single crystals of TiC can be produced by the Verneuil technique [3-5], floating zone process [6-9], precipitation from molten metals [10] and chemical vapor deposition [11-15]. The catalytic effect of various metals and refractory oxides on the growth of TiC

whiskers by CVD was reported by Kato and Tamari et al [16-18]. The growth, morphology and structure of TiC whiskers obtained by CVD from $TiCl_4+CCl_4+H_2$ system have been discussed in detail by Wokulski et al [19,20].

There are several reports on the formation of TiN whiskers [21-27]. They are essentially based on chemical vapour deposition using a set of reagents: $TiCl_4$, N_2, and H_2. Kamiya et al [26] prepared TiN fibers by nitridation of TiO_2 fibers prepared by a solgel method. By exposing to NH_3 for 5h at 1100°C the TiO_2 fibers were completely converted into TiN fibers. The production of TiN whiskers by reaction of sodium titanium bronze ($Na_x TiO_2$), with excess sodium cyanide (NaCN) at 1000°C is reported by Bamberger et al [1, 27].

Literature of recent patents [28-30] revealed the process of carbothermal preparation of TiC and TiN whiskers via a VLS mechanism. They used TiO_2, carbon, and MCl (M=Li, Na, or K) as raw materials, and Ni as a catalyst. TiN whiskers formed in nitrogen, whereas argon is used for TiC whiskers. Influence of various parameters on the yield and whisker morphology has been reported by Ahlen et al [31]. The carbothermal reduction of titania (TiO_2) to form TiC/TiN can be represented by the following overall reactions.

$$TiO_2\,(s) + 3C\,(s) \rightarrow TiC\,(s) + 2CO\,(g) \quad (1)$$

$$TiO_2\,(s) + 2C\,(s) + 1/2N_2\,(g) \rightarrow TiN\,(s) + 2CO\,(g) \quad (2)$$

But the actual formation of TiC/TiN is complex, as many intermediate steps are involved [32]. When alkali metal chloride and metallic catalyst are added, the reactions

that actually take place are more complex and difficult to predict and, thus also difficult to study. In this work we have used TiO_2 and carbon black as precursor materials. The influence of K_2CO_3, $NiCl_2$ catalyst, and heating rate on the formation of TiC and TiN whiskers was studied.

2. MATERIALS

Laboratory reagent grade TiO_2 powder was obtained from Glaxo laboratories (India) Ltd, Bombay-400025. Laboratory reagent grade $NiCl_2$ was supplied by Qualigens Fine Chemicals, Bombay-400075, India. Specpure K_2CO_3 was procured from Johnson Matthey Chemicals Limited, Hertfordshire, England. Carbon black of grade N220 was obtained from Philips Carbon Black Ltd., Durgapur, India.

3. EXPERIMENTAL

Various types of powder mixtures were prepared by dry ball milling for 5 h. For TiC synthesis, TiO_2, carbon black, $NiCl_2$, and K_2CO_3 were taken in weight ratio (TiO_2 : C: $NiCl_2$: K_2CO_3= 20 : 9 : 5 : x), where x= 2.5/5.0/7.5. Its equivalent molecular ratio is (TiO_2 : C: $NiCl_2$: K_2CO_3= 1 : 3 : 0.15 : x), where x= 0.072/0.144/0.216. For TiN synthesis, TiO_2, carbon black, $NiCl_2$, and K_2CO_3 were taken in weight ratio (TiO_2 : C: $NiCl_2$: K_2CO_3= 20 : 6 : 5 : x), where x= 2.5/5.0/7.5. Its equivalent molecular ratio is (TiO_2 : C: $NiCl_2$: K_2CO_3= 1 : 2 : 0.15 : x), where x= 0.072/0.144/0.216.

$NiCl_2$ solution was prepared by dissolving 5 g of $NiCl_2$ in 30 ml of de-ionised water. Similarly 5 g of K_2CO_3 was dissolved in 30 ml of de-ionised water to make a solution of K_2CO_3. Twenty grams of TiO_2 powder was added to $NiCl_2$ solution taken in a

500ml capacity glass beaker. After thorough mixing K_2CO_3 solution was added. The mixture was dried in an oven at 110°C. The dried mix and 9 g of carbon black were taken in an agate pot and dry ball milled for 5 h. this powder mixture was designated as TNKC5. After reviewing the results, further two more TNKC powder mixes were prepared to study the effect of concentration of K_2CO_3 on the formation of TiC whiskers. The mixes containing 2.5 g and 7.5 g of K_2CO_3 are designated as TNKC2.5 and TNKC7.5 respectively.

To study the effect of each constituent on the formation of TiC whiskers, three more mixes were prepared. The powder mix containing TiO_2 and carbon black only was designated as TC. Other two mixes containing (i) TiO_2, carbon and, $NiCl_2$, and (ii) TiO_2, carbon and K_2CO_3 are designated as TNC and TKC, respectively. Finally one more mixture of TiO_2 and K_2CO_3 in 1:3 molar ratio was prepared and designated as TK.

Cylindrical graphite holders of 2.5-mm wall thickness and 10-mm inner diameter were filled with the powder mixtures. The holders were closed with graphite stoppers and placed in the hot zone of high-temperature graphite resistance furnace (ASTRO, U.S.A., Model 1000-3060-FP20). The furnace was evacuated to a moderate vacuum (5 X 10^{-2} torr) and back filled with 1atm. argon for TiC experiments or 1atm. nitrogen for TiN experiments.

TiC experiments were conducted at 920°, 1000°, 1100°, 1200°, and 1300°C for 40 min. The temperature was maintained with a Model 939A3 Honeywell radiation pyrometer. The heating rate employed was ≈ 40°C min^{-1}.TNKC2.5 and TNKC7.5 were

pyrolysed at 1000 and 1100°C for 40 min. To study the effect of heating rate, TNKC2.5, TNKC and TNKC7.5 were subjected to slow heating at a rate of 10°C min^{-1}. The reaction temperature and dwell time was 1100°C and 20 min respectively. A sample of TK was pyrolysed in nitrogen at 1150°C per $45min^{-1}$. TiN experiments were conducted at 815°, 883°, 920°, 1000°, and 1100°C for $45min^{-1}$ in nitrogen.

The reacted samples were ground in an agate mortar and analysed by X-ray diffraction (XRD) and scanning electron microscopy (SEM). A Philips X-ray diffractometer, Model PW3710, with Cu K_a radiation through Ni filter was used. The morphology of the reacted powders was examined with a Model ISI-100A International Scientific Instruments SEM. Energy Dispersive X-ray Analysis (EDX) was done by ISIS Linc, Oxford system connected to an SEM, Leo440i, England. Scanning Electron Probe Microanalysis (SEPMA) was carried out with CAMECA (model CAMEBAX-MICRO, France) equipment.

4. RESULTS

Titanium carbide: Depending on the temperature of reaction the samples existed in the form of loose or an agglomerated powder. After reaction at 920°C the samples appeared like unreacted powders. Upto a reaction temperature of 1000°C, they were in the form of loose powders. At 1100°C the sample of TNC formed a weak cylindrical shape. After reaction at 1300°C TNKC, TNC, TKC and TC formed thin cylindrical agglomerates.

TiC formed in all samples at all reaction temperatures. Typical XRD patterns obtained for TNKC5 are shown in Fig. 1. Peaks of small intensity corresponding to Ni_3C were also observed at 920°C. Ni_3C as well as NiTi ($Ni_{2.67}$ $Ti_{1.33}$) were observed at 920 and 1000°C in TNC. Peaks from unreacted constituents were observed at 920°C in all four systems. The intensities of TiC peaks increased with increase in reaction temperature.

The morphology of TNKC5 samples reacted at different temperatures is shown in SEM micrographs (Fig. 2). At 920°C thick whiskers were observed. The whisker content increased with reaction temperature upto 1100°C. At 1200°C agglomeration of whiskers was observed. At 1300°C the formation of particles is the dominant process (Fig. 2(c)). It appears that the whiskers formed at lower temperatures got converted into thick and short particles. Similar results were observed in TKC also, but very few whiskers were formed. No whiskers were formed in TC and TNC samples at any temperature. In TNC, particulates coarser than that formed in TC were observed.

Upon increasing the K_2CO_3 content from 2.5 to 7.5, whisker formation increased drastically (Fig. 3). But with slow heating rate whisker formation was very sluggish in TNKC7.5 (Fig. 4(a)). In case of slow heating rate, low concentration of K_2CO_3 was beneficial for the formation of whiskers (Fig. 4(c)). Whiskers bearing spherical tips (Fig. 4(c)) suggest that the whiskers are grown by vapor-liquid-solid (VLS) mechanism. Spheroidization of particulates was observed in slowly reacted samples.

Potassium titanate whiskers were formed by the reaction between K_2CO_3 and TiO_2 in TK (Fig. 5). Energy dispersive X-ray (EDX) analysis confirmed the presence of Ti, and C in whisker stems and spherical tips. In the EDX of spherical tips, peaks of potassium and nickel were also observed (Fig. 6). The peak of aluminium in Fig. 6 is from the sample holder. Though the compositions varied, all whisker tips contained Ti, C, K, and Ni. The typical composition of a TiC whisker tip is given in Table. 1. The EPMA anlysis also confirmed the presence of Ni, Ti, and C in whisker tip (Fig. 7). The depletion of Ti in whisker tip reveals the formation of a nickel-titanium alloy (Fig. 7(d)).

Titanium nitride: Upto a reaction temperature of 883°C the samples appeared like unreacted powders. At 1100°C all the three sample were in gold colour. TiN was formed in all samples at all reaction temperatures. Typical XRD patterns of TNKC5 are shown in Fig. 8. At 815°C the intensities of TiN peaks were small. At this temperature peaks corresponding to unreacted TiO_2 (rutile) were also observed in TNKC7.5. Above 920°C peaks corresponding to TiN only were seen. The intensities of TiN peaks increased with increase in reaction temperature.

The morphology of TNKC2.5 samples reacted at different temperatures is shown in SEM micrographs (Fig. 9). At 815°C thick whiskers were observed. The whisker content increased with reaction temperature. Maximum formation of whisker was observed at 1000°C (Fig. 9(b)). At 1100°C agglomeration of whiskers and formation of particulates can be seen (Fig. 9(c)).

Similar results were observed in TNKC5 also. But the formation of whiskers at 815°C is slightly more than that formed in TNKC2.5 (Fig. 10(a)). At 920°C maximum quantity of whiskers were formed. In this system at 1000°C itself formation of totally particulates was observed. Typical particulates formed at 1100°C are shown in Fig. 10(b)). In TNKC7.5 at temperature as low as 815°C large number of whiskers were formed (Fig. 11(a)). But at 920°C whiskers, and particulates were formed. At 1000°C and 1100°C particulates only were formed.

Ti, and N were identified in whisker stems and spherical tips. In the EDX of spherical tips, peaks of potassium and nickel were also observed (Fig. 12). Though the compositions varied, all whisker tips contained Ti, N, K, and Ni. The EPMA anlysis also confirmed the presence of Ni, Ti, and N in whisker tip (Fig. 13).

5. DISCUSSION

From the above results it is very clear that whiskers are formed in the systems containing K_2CO_3. But in TKC very few whiskers were formed. Though K_2CO_3 is an essential constituent, $NiCl_2$ acts as a catalyst for maximization of formation of TiC whiskers.

The progress of reactions (1) and (2) depends on the intimate contact between the reactants which is essential for complete conversion of TiO_2 into TiC [33]. There is lot of literature on catalysis of carbon gasification [34]. Iron, cobalt and nickel acts as a strong catalyst for gasification of carbon in carbon-carbon dioxide reaction [35], and in

water vapor and hydrogen [36]. By introduction of metal atoms into the structure, more carbon monoxide is produced. So more quantity of CO is available in TNC. Koc et al [33] suggested that the continuous supply of CO and argon gas flow during carbothermal reduction is required for complete conversion of TiO_2 to TiC, and for lowering the thermodynamic onset of temperature of the overall reaction by taking away the product gas CO. Due to the catalytic effect of Ni, coarse and well defined particles of TiC were formed in TNC. But no whiskers were formed in TNC.

The morphology of whiskers formed in TKC and TNKC suggest that they were grown by VLS mechanism. In TKC system, K_2CO_3 dissociates into K_2O and CO_2. K_2O can form a thin liquid layer around TiO_2 particle and react with it. The reaction between K_2O and TiO_2 can lead to the formation of rod shaped titanate [37]. The formation of potassium titanate whiskers has been studied in detail by Lee et al [38], and Watanabe et al [39]. In TK system the formation of potassium titanate whiskers (Fig. 5) confirm the existence of a low melting liquid. In TKC system, TiC whiskers must have grown from such K_2O rich liquid. This requires a continuous supply of TiO or TiO_2 and CO to the liquid. So very few whiskers were formed in TKC. The important role of potassium is formation of a low melting liquid. When Ni is added, a complex K-Ni-Ti liquid droplet containing Ni-Ti alloy is forming. This is confirmed from EDX, and EPMA. For the precipitation of TiC crystal, continuous supply of CO is required to this liquid droplet. The presence of Ni, in TNKC increases the availability of carbon as CO and facilitates the growth of TiC/TiN whiskers from a complex K-Ni-Ti liquid droplet.

When K_2CO_3 content increased from TNKC2.5 to TNKC7.5, the formation of TiC whiskers increased drastically (Fig. 3). Due to the increase in K_2O more and more nucleation sites of K_2O rich liquid could be available. But in same TNKC7.5 very few whiskers were formed upon slow heating (Fig. 4(a)). During slow heating, before the sample reaches the reaction temperature large quantity of K_2O melt engulfs the entire powder mix and causes agglomeration and formation of lumps or spherical particles. In slowly heated TNKC2.5 as the content of K_2CO_3 was less the extent of formation of lump or spherical particles was less. So during slow heating, decrease in K_2CO_3 content was beneficial in forming TiC whiskers.

Similarly the increase in K_2CO_3 content from TNKC2.5 to TNKC5, increased the formation of TiN whiskers (Fig. 10). Due to the increase in K_2O more and more nucleation sites of K_2O rich liquid could be available. So in TNKC7.5 still more TiN whiskers were formed at 815°C itself (Fig. 11(a)). But the temperature of formation of particulates was decreased with increase in K_2CO_3 content. The formation of particulates is dominant process at and above 1000°C in TNKC5 and TNKC7.5. In these systems, before the sample reaches the reaction temperature large quantities of K_2O melt engulf the entire powder mix and causes agglomeration and formation of lumps or spherical particles. Therefore no whiskers were formed at higher temperatures.

4. CONCLUSIONS

Potassium has strong positive effect on the formation of TiC/TiN whiskers during the carbothermal reduction of TiO_2. Nickel acts as a catalyst for whisker formation in the presence of potassium only. High yield of TiC whisker was observed in the temperature range of 1000-1200°C. Maximum yield of TiN whisker was observed in the temperature range of 920^0 –1000^0C. At higher temperatures formation of particulates is the dominant process. Increase in K_2CO_3 concentration increased the whisker growth during fast heating. During slow heating a decrease in K_2CO_3 concentration increases the whisker growth. A vapour-liuquid-solid growth mechanism for the formation of TiC/TiN whiskers was identified.

ACKNOWLEDGMENTS

The authors thankfully acknowledge the financial support received from the Defence Research & Development Organisation, Govt. of India in order to carry out the present research study. We are grateful to the director, DMRL, for his constant encouragement and permission to publish this work.

REFERENCES

1. C. E. Bamberger, P. Angelini, and T. A. Nolan, J. Am. Ceram. Soc. 72 (1989), P.587.
2. T. A. Nolan, L. F.Aallard, D. W. Coffey, C. R. Hubbard, R. A. Padgett, M.H. Rawlins and R. W. Nixdorf, J. Am. Ceram. Soc. 74 (1991) P. 2769.
3. W.S. Williams, J.Appl.Phys. 32 (1961), P. 552.
4. G.E. Hollox and R.E. Smallman, J. Appl. Phys. 37 (1966), P.818.
5. F.W. Vahldick, J Less-common Metals. 12 (1967), P.429.
6. W. Precht and G.E Hollox, J. Crystal Growth. 3 (1968), P.818.
7. R.N. Storey and R.A. Laudise, J. Crystal Growth. 6 (1970), P.261.
8. M.E. Parker and M.J. Murray, J. Crystal Growth. 16 (1972), P.240.
9. Y. Kumashiro, A. Itoh and S. Misawa, J. Less-Common Metals. 32 (1973), P.21.
10. Higashi, Y. Takahashi and T. Atoda, J. Crystal Growth. 33 (1976), P.207.
11. T. Takahashi, K. Sugiyama and J. Itoh, J. Electrochem. Soc. 117 (1970), P. 541.
12. J.J. Nickl and M. Reichle, J Less-common Metals. 24 (1971), P.63.
13. J.J. Nickl and R. Vesper, J Less-common Metals. 25 (1971), P.275.
14. K. Hamamura, H. Yamagishi and S. Nagakura, J. Crystal Growth. 26 (1974), P.255.
15. K.Sugiyama, H. Mizuno, S. Motojima and Y. Takahashi, J. Crystal Growth. 46 (1979), P.788.
16. Kato, M. Yasunaga and N. Tamari, J. Crystal Growth. 37 (1977), P.293.
17. N. Tamari and A. Kato, J. Crystal Growth. 46 (1979), P.221.

18. Kato, and N. Tamari, J. Crystal Growth. 49 (1980), P.199.

19. Z. Wokulski, J. Crystal Growth. 82 (1987), P.427.

20. Z. Wokulski and K. Wokulska, J. Crystal Growth. 62 (1983), P.439.

21. M. I. Aivazov and V. F. Melekhin, Inorg. Mater. (Engl. Transl.) 3 (1967), P.1835.

22. A. Kato and N. Tamari, J. Cryst. Growth. 29 (1975), P.55.

23. K. Sugiyama, Y. Takahashi and S. Motojima, Chem. Lett. 4 (1975), P.363.

24. Zb. Bojarski, K. Wokulska and z. Wokuluski, J. Cryst. Growth. 52 (1981), P. 290.

25. A. N. Pilyankevich, V. s. sinel'nikova, L. V. strashinskaya, T. I. Shaposhnikova and S. Ya. Golub, Sov. Powder Metall. Met. Ceram. (Engl. Transl.), 16 (1977), P. 768.

26. K. Kamiya, T. Yoko and M. Bessho, J. Mater. Sci. 23 (1987), P. 937.

27. C. E. Bamberger, D. W. Coffe and T. A. Nolan, J. Mater. Sci. 25 (1987), P. 4992.

28. T. Kida, U.S. Patent, 5, 256, 243, Oct.26, (1993).

29. M. Nygren, M. Johnsson, N. Ahlen and M. Ekelund, Europ. Patent. EP 0 754 782 A1, Jan 22, (1997).

30. R. D. Nixdorf and M. H. Rawlins, U.S. Patent. No. 4 888 084, (1989).

31. N. Ahlen, M. Johnsson, and M. Nygren, J. Amer. Ceram. Soc. 79 (1996), P. 2803.

32. R. Koc, Ceram. Engg. & Sci. Proc. 18 (1997), P.703.

33. R. Koc., and J. S. Folmer, J. Am. Ceram. Soc. 80 (1997), P. 952.

34. P. L. Walker, Jr., M. Shelef, and R. A. Anderson, in Chemistry and Physics of Carbon, P. L. Walker Jr. (ed): Marcel Dekker Inc., New York, 4 (1968), P.287.

35. J. T. Gallagher, and H. Harker, Carbon 2 (1964), P.163.

36. D. W. Mckee, Carbon 12 (1974), P.453.

37. M. Heon Um, C. T. Lee, and H. Kumazawa, J. Mater. Sci. Lett. 16 (1997), P. 344.

38. J. K. Lee, K. H.lee, and H. Kim, J. Mater. Sci. 16 (1996), P. 5493.

39. A. Watanabe, Y. Takeuchi, and G. Saeki, J. Am. Ceram. Soc. 68 (1985), P. C-308.

Table. 1. EDX analysis of TiC whisker tip of TNKC2.5 slow heated to 1100°C

Element	Element%	Atomic%
C k	00.65	02.77
K k	00.36	00.47
Ti k	57.31	60.73
Ni k	41.67	36.03
Total	100.00	100.00

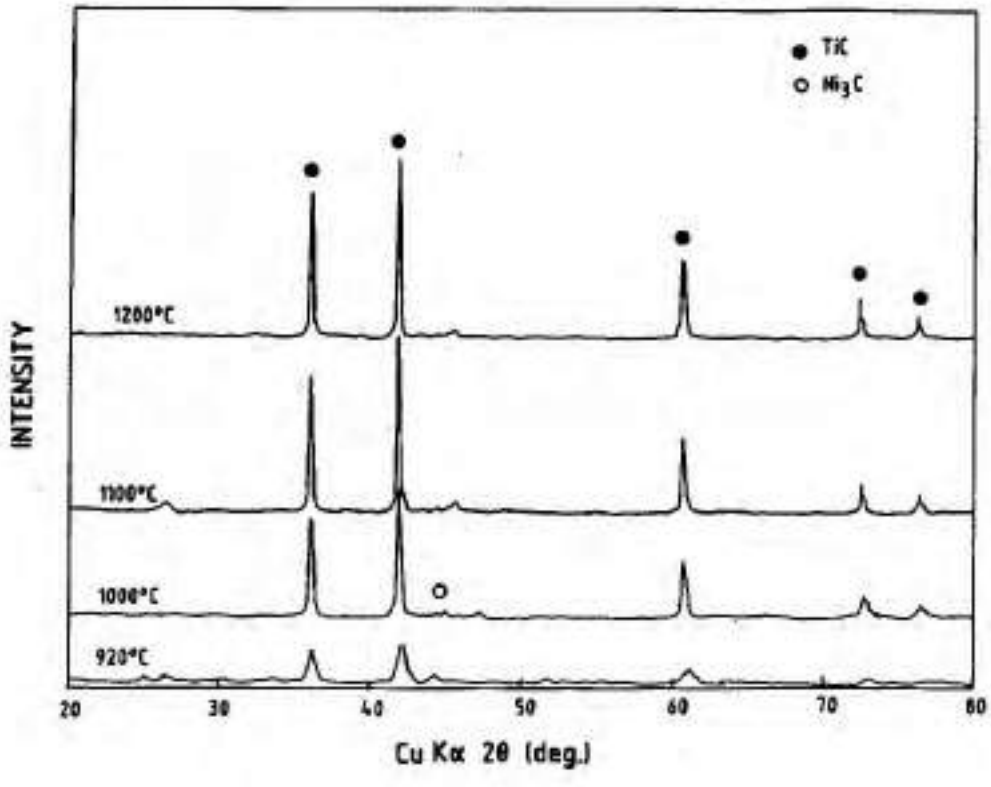

Figure. 1. XRD patterns of TNKC5 reacted at different temperatures.

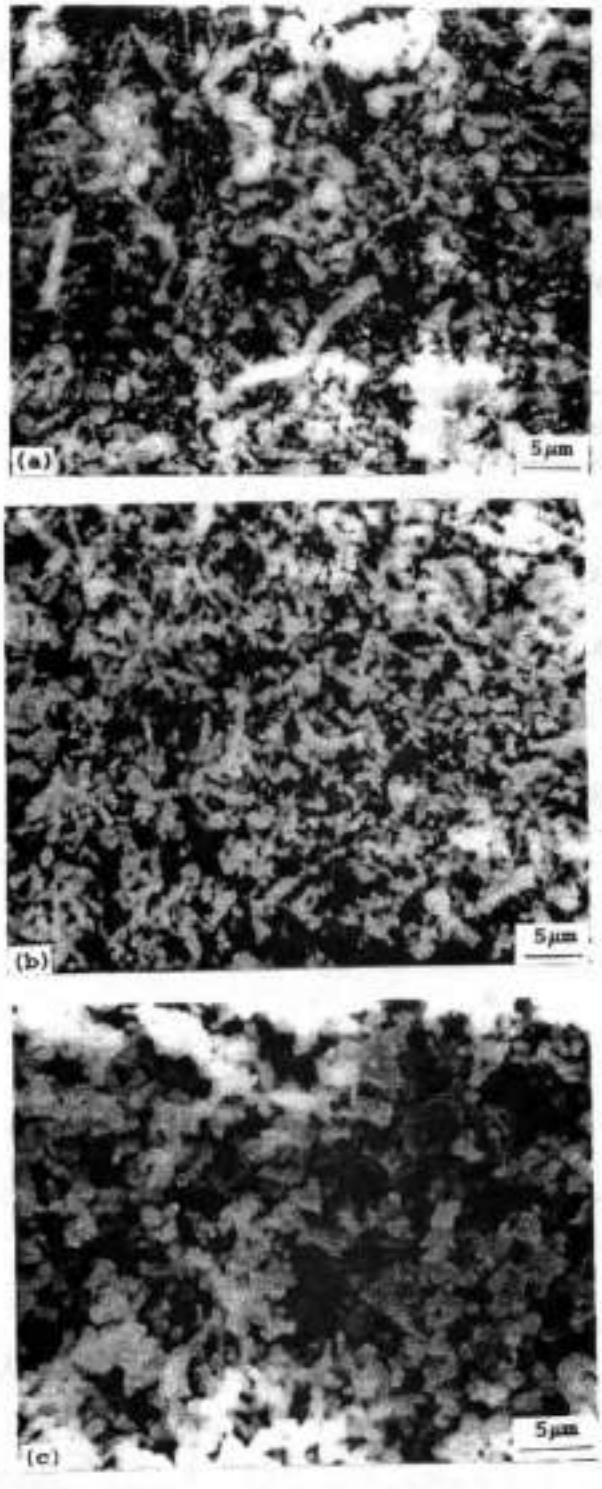

Figure. 2. Morphology of TiC formed in TNKC5 at (a) 920°C, (b) 1100°C, and (c) 1300°C.

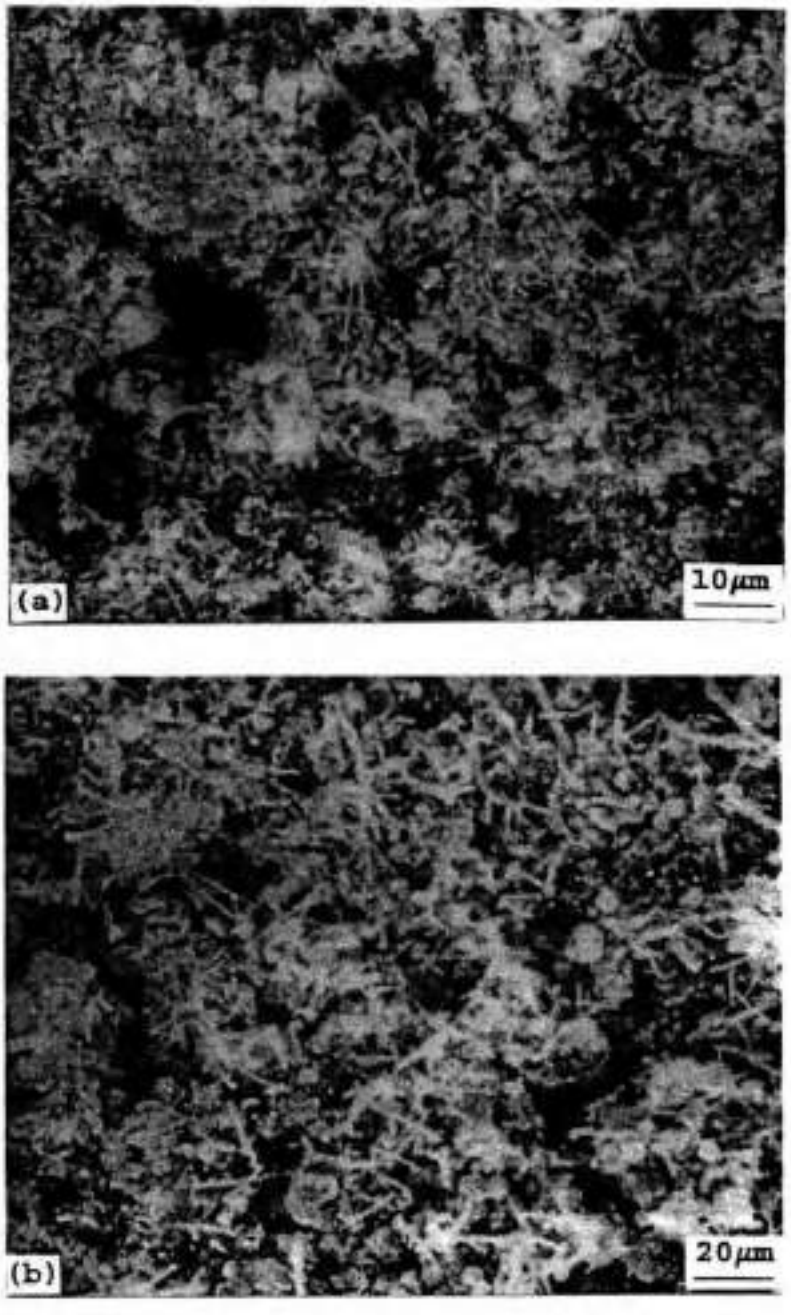

Figure. 3. Morphology of TiC at 1100°C in (a) TNKC2.5, (b) TNKC7.5.

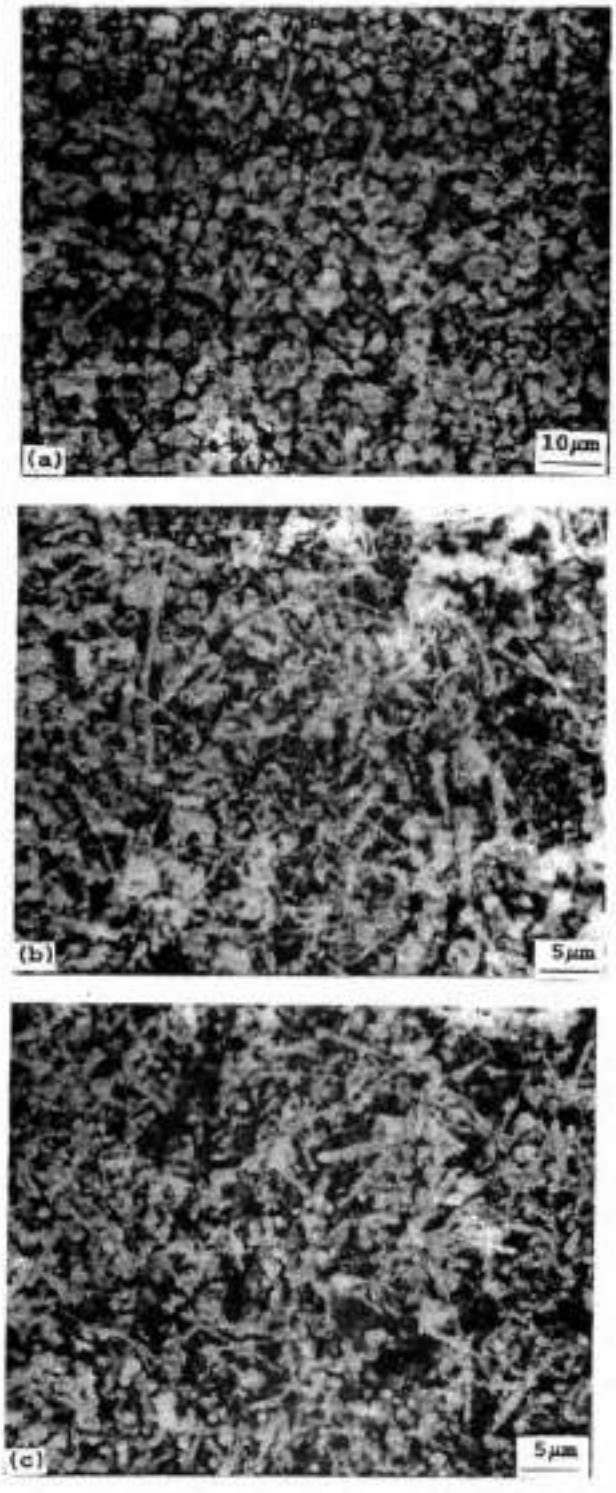

Figure. 4. Morphology of TiC at 1100°C in (a) TNKC7.5, (b) TNKC5, and (c) TNKC2.5.

Figure. 5. SEM of potassium titanate whiskers formed by the reaction between K_2CO_3 and TiO_2 in TK at 1150°C.

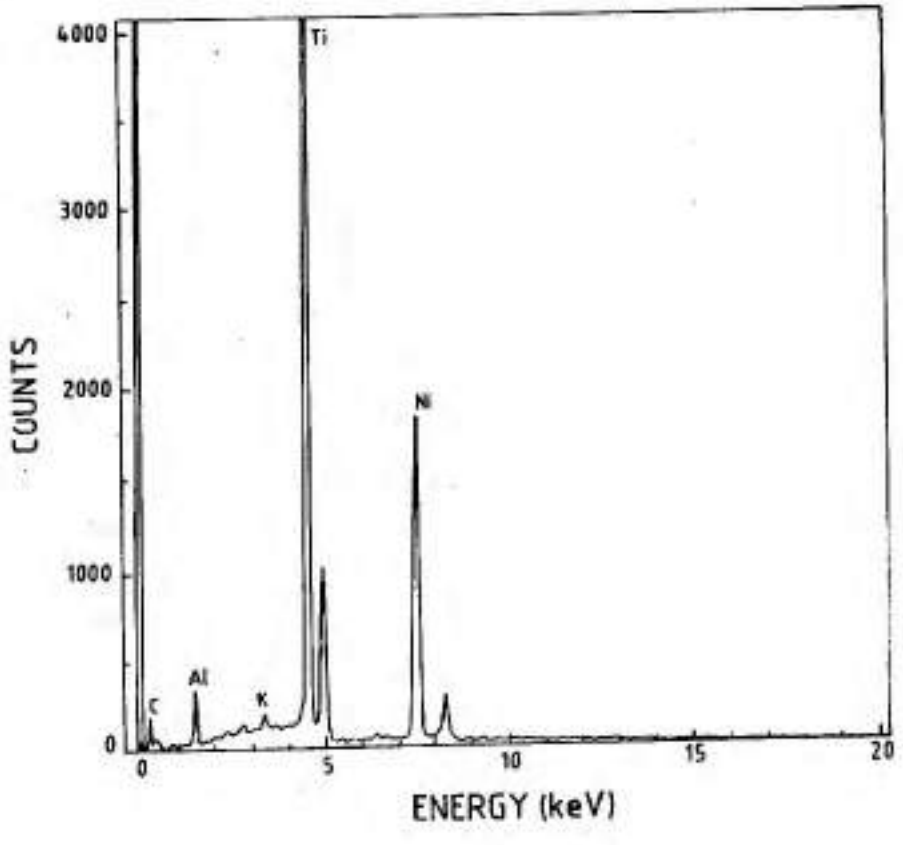

Figure. 6. EDX of spherical tip of TiC whisker formed in TNKC2.5 after slow heating to 1100°C.

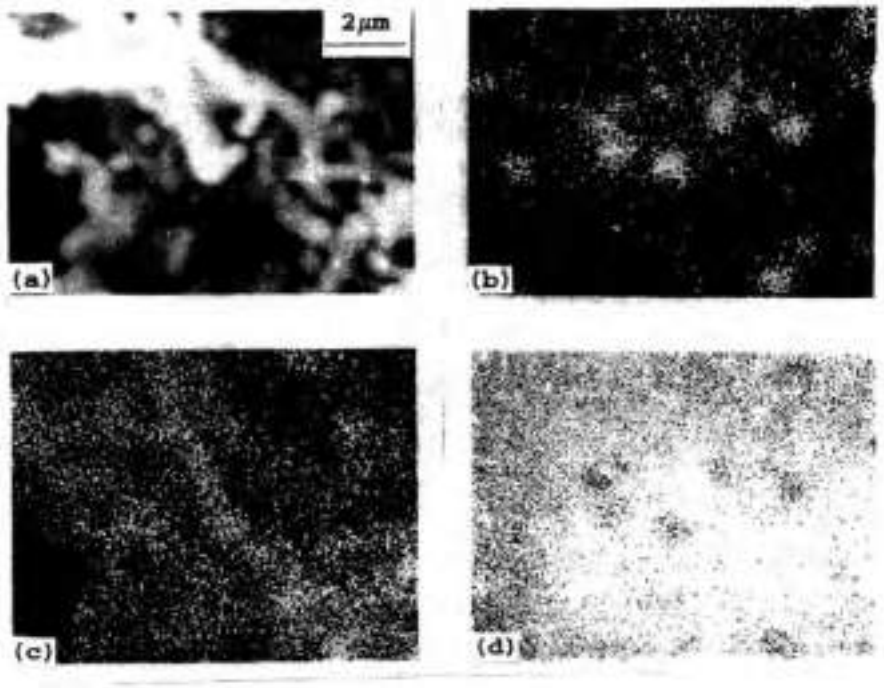

Figure. 7. EPMA anlysis of TiC whisker formed in TNKC2.5 after slow heating to 1100°C. (a) SEM, (b) Ni X-ray map, (c) C X-ray map, and (d) Ti X-ray map.

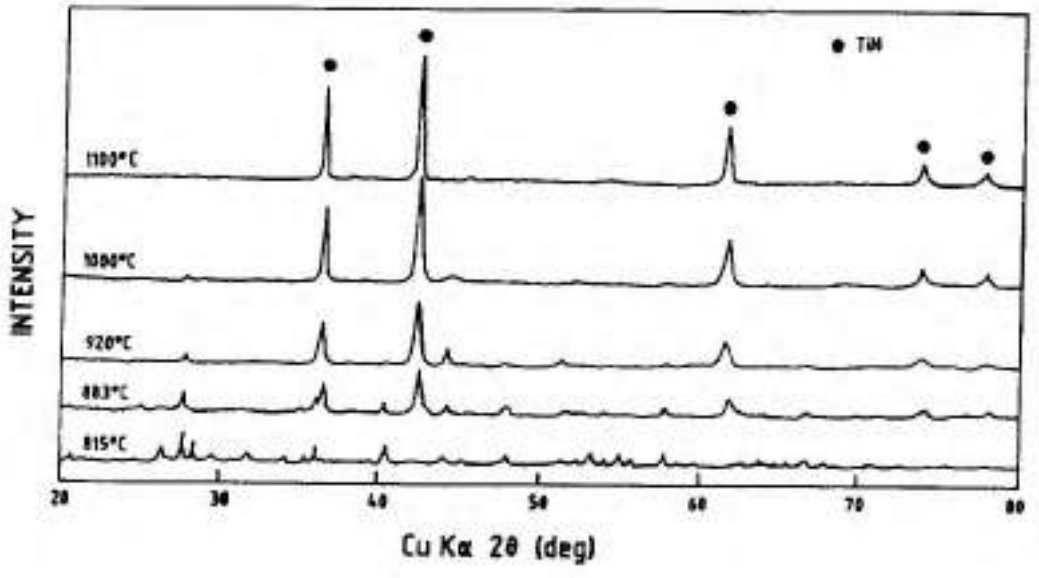

Figure. 8. XRD patterns of TNKC5 reacted at different temperatures in nitrogen.

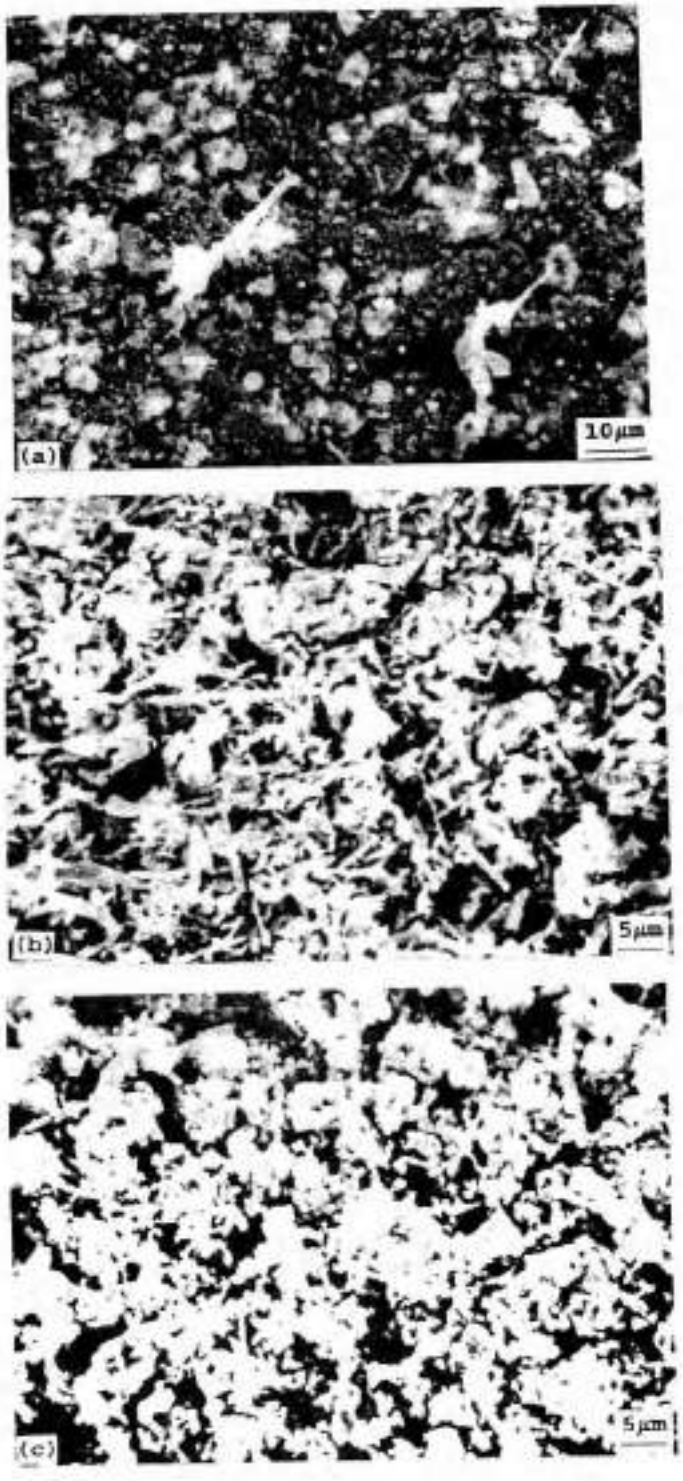

Figure. 9. Morphology of TiN in TNKC2.5 at (a) 815°C, (b) 1000°C and (c) 1100°C.

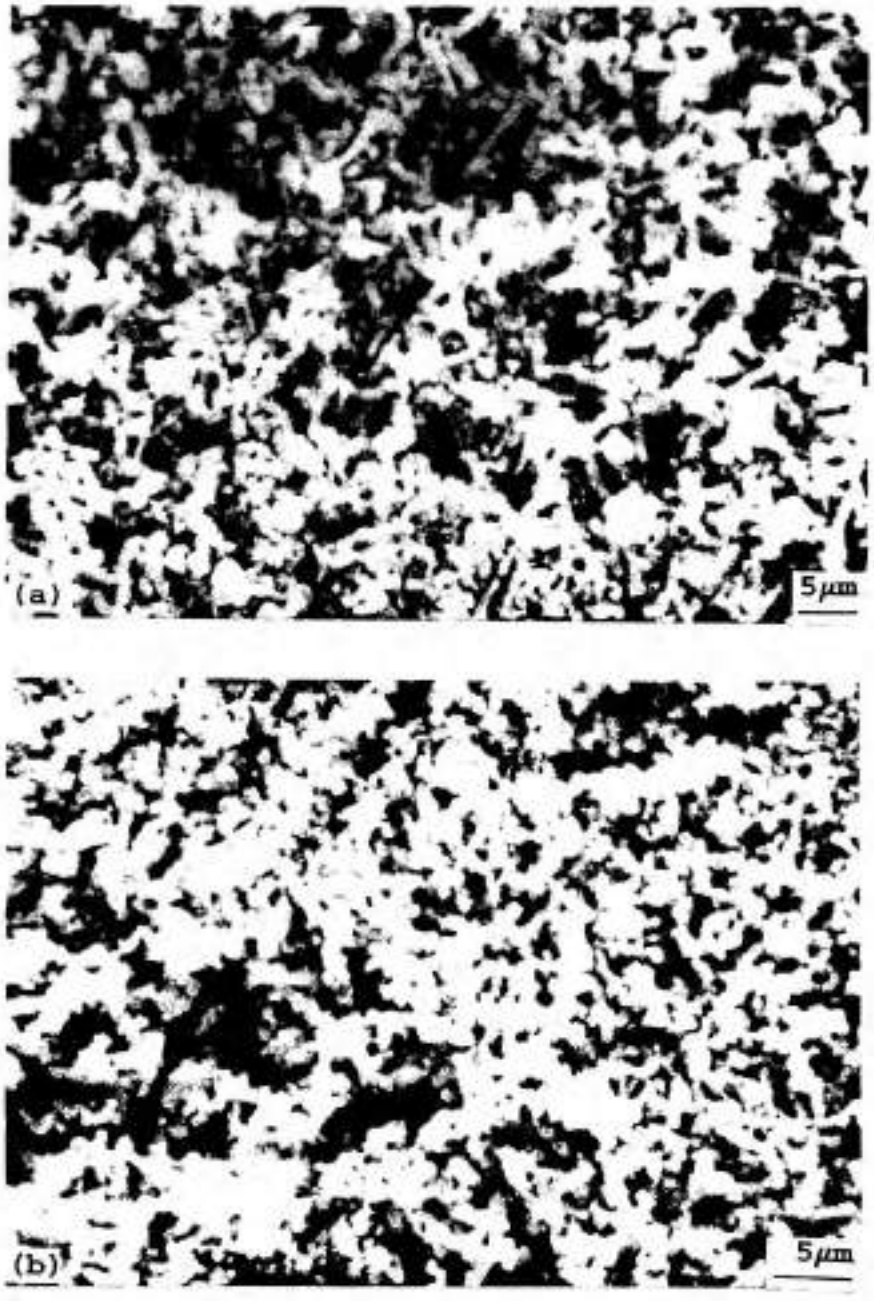

Figure. 10. Morphology of TiN in TNKC5 at (a) 815°C and (b) 1100°C

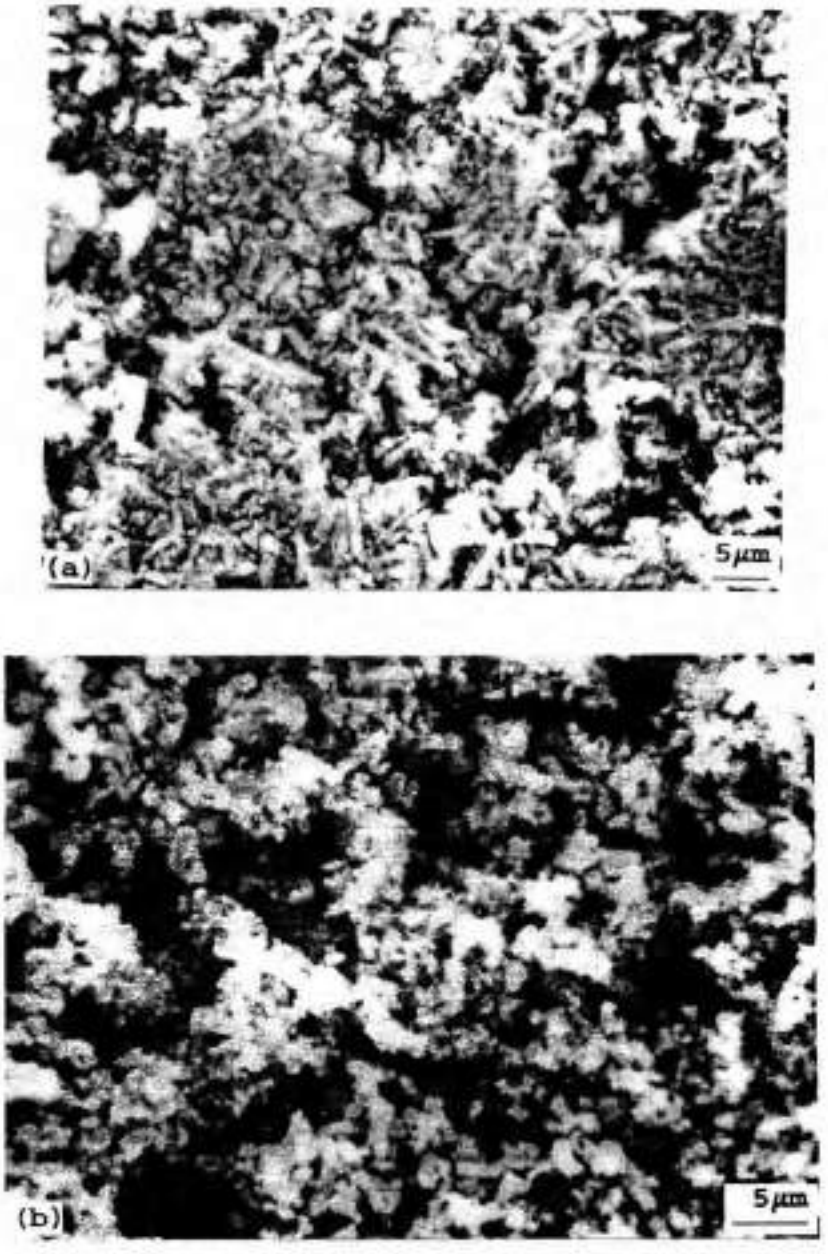

Figure. 11. Morphology of TiN in TNKC7.5 at (a) 815°C, and (b) 1100°C.

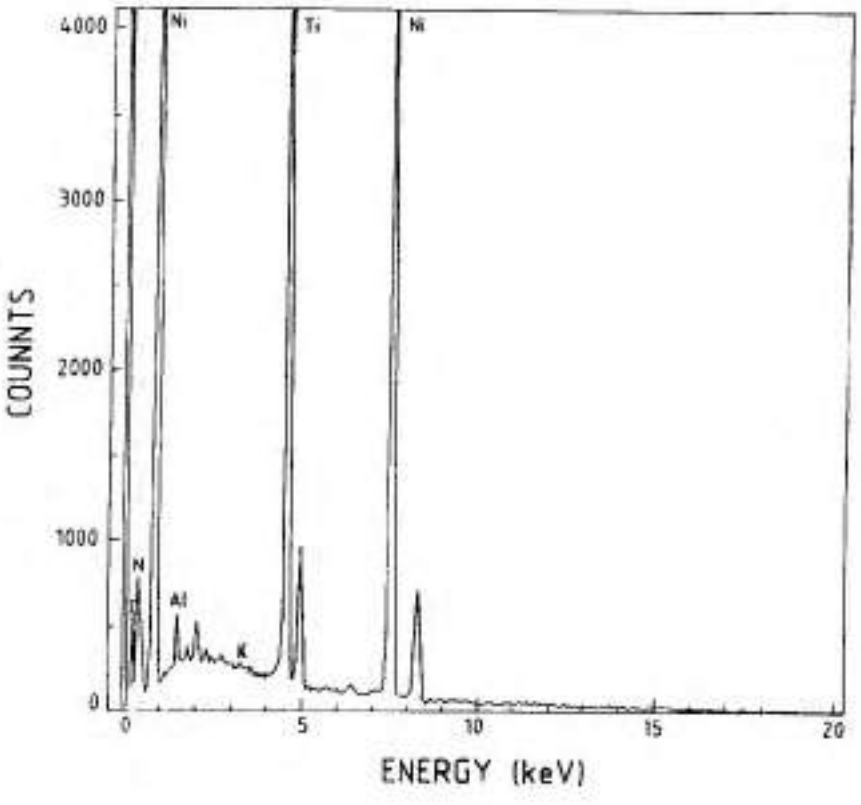

Figure. 12. EDX of spherical tip of TiN whisker formed in TNKC2.5 after slow heating to 1100°C.

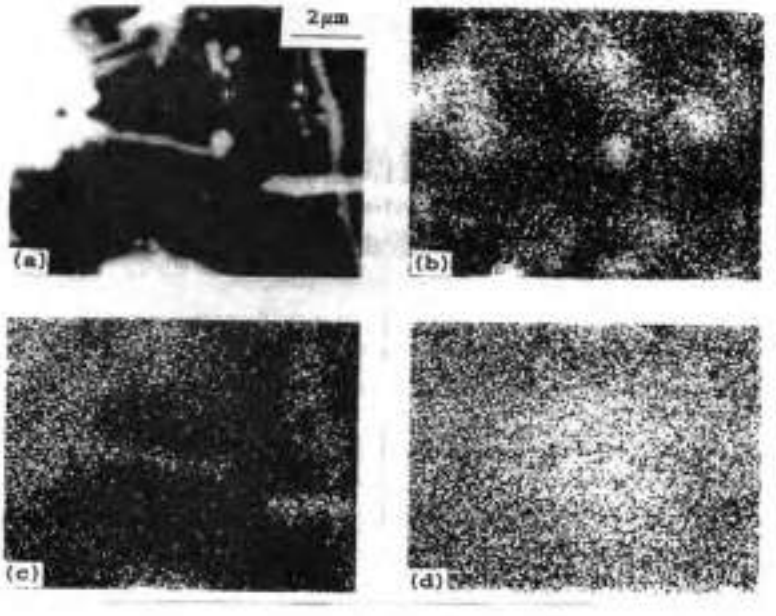

Figure. 13. EPMA anlysis of TiN whisker formed in TNKC2.5 after slow heating to 1100°C. (a) SEM, (b) Ni X-ray map, (c) C X-ray map, and (d) Ti X-ray map.

Phase Evolution on Carbothermal Reduction of 1:2 Molar Mixture of MoO_3 and SiO_2

Tarasankar Mahata and Beant Prakash Sharma
Powder Metallurgy Division
Bhabha Atomic Research Centre
Vashi Complex, Navi Mumbai - 400 705

email : <tsmahata@rediffmail.com> ; <beant@mailcity.com>

ABSTRACT

Carbothermal reduction of 1:2 molar mixture of MoO_3 and SiO_2 has been carried out by stepwise heating under vacuum upto 1600 °C. At least three reaction steps have been identified, namely, reduction of MoO_3 to MoO_2 (600 - 800 °C), reduction of MoO_2 to Mo/Mo_2C (850 - 950 °C) and simultaneous reduction of SiO_2 and formation of Mo-silicides (1100 - 1300 °C). Under optimised processing condition, the loss of Mo could be minimised. However, loss of Si in the form of its suboxide (SiO) is found to be inherent to the process. Consequently, Si/Mo atom ratio in the product remains well below 2.0 and the product contains unreacted carbon. The different phases identified in the product are : $MoSi_2$, $Mo_{4.8}Si_3C_{0.6}$ (Nowotny phase), SiC and C. To study the formation of $Mo_{4.8}Si_3C_{0.6}$, mixtures of $MoSi_2$ and graphite in different molar ratio (C/ $MoSi_2$ = 0.2, 0.4, 1.0, 1.8, 2.6) are prepared and heated to 1600 °C under vacuum better than 10^{-3} mbar. $MoSi_2$ reacting with C forms $Mo_{4.8}Si_3C_{0.6}$ and SiC. $Mo_{4.8}Si_3C_{0.6}$ (Nowotny phase) has been seen to be the most stable phase in the Mo-Si-C system. It has been reported in literature that combination of phases like $MoSi_2$, $Mo_{4.8}Si_3C_{0.6}$ and SiC can form a useful material having high temperature oxidation and creep resistance.

INTRODUCTION

Carbothermal reduction of 1:2 molar mixture of MoO_3 and SiO_2 is aimed at producing $MoSi_2$ which is a promising high temperature material because of its high melting temperature (2030 °C) and excellent oxidation resistance at high temperatures[1,2]. Among other processes for the synthesis of $MoSi_2$ powder, the most popular are the self-propagating high-temperature synthesis (SHS)[3-5] process and mechanical alloying[6,7]. These processes use the elemental Mo and Si powder as starting materials. As the carbothermic process uses oxides of Mo and Si, and graphite as starting materials, the process is expected to be more economical. Also the handling of the raw materials is much easier. However, the carbothermic process has not got much attention as it is difficult to produce single phase $MoSi_2$ by this process. This is largely due to uncontrolled loss of Si in the form of its suboxide during processing. As part of oxygen comes out with Si, the product is left with carbothermally unreacted carbon. In such situation the product is likely to be composed of different phases in the Mo-Si-C system. Suzuki et. al.[8] has mentioned advanced high

Present article deals with the identification of different phases evolved in the carbothermic reduction of 1:2 molar mixture of MoO_3 and SiO_2. Qualitative evaluation has been done on the coexistence of different phases.

THERMODYNAMIC ANALYSIS

Thermodynamic analysis has been done for the probable reactions that could occur during heating a mixture of MoO_3, SiO_2 and graphite powders under vacuum. The following reactions have been taken into consideration.

Evaporation of MoO_3 : $MoO_{3\,(s)} = MoO_{3\,(g)}$ (1)

Reduction of MoO_3 : $MoO_{3\,(s)} + 0.5\,C_{(s)} = MoO_{2\,(s)} + 0.5\,CO_{2\,(g)}$ (2)

Evaporation of MoO_2 : $MoO_{2\,(s)} = MoO_{2\,(g)}$ (3)

Reduction of MoO_2 : $MoO_{2\,(s)} + 2.5\,C_{(s)} = 0.5\,Mo_2C_{(s)} + 2.0\,CO_{(g)}$ (4)

$MoO_{2\,(s)} + 2.0\,C_{(s)} = Mo_{(s)} + 2.0\,CO_{(g)}$ (5)

Formation of $MoSi_2$: $0.5\,Mo_2C_{(s)} + 2.0\,SiO_{2\,(s)} + 3.5\,C_{(s)} = MoSi_{2\,(s)} + 4.0\,CO_{(g)}$ (6)

$Mo_{(s)} + 2.0\,SiO_{2\,(s)} + 4.0\,C_{(s)} = MoSi_{2\,(s)} + 4.0\,CO_{(g)}$ (7)

Other two reactions prevalent in the system are reaction between SiO_2 and graphite to form $SiC_{(s)}$ and $SiO_{(g)}$. The reactions are:

$SiO_{2\,(s)} + C_{(s)} = SiC_{(s)} + CO_{(g)}$ (8)

$SiO_{2\,(s)} + C_{(s)} = SiO_{(g)} + CO_{(g)}$ (9)

Reactions (1), (2) and (9) are of importance since these involve loss of Mo, Mo and Si respectively from the system.

In reduction of SiO_2, elemental Si formation reaction has not been considered in isolation and has been associated with $MoSi_2$ or SiC formation reaction [reactions (6) through (8)]. Also, for convenience in thermodynamic analysis only $MoSi_2$ compound has been taken into consideration among the Mo-silicides of different stoichiometry.

The energetics of the reactions have been compared after calculating the equilibrium partial pressures of the gaseous product species of the different reactions. The equilibrium partial pressure values are given in Table 1. In these calculations the activity of each solid specie has been taken to be unity. For comparison of energetics of different reactions this may be a good approximation. Thermodynamic calculations show that the vapour pressure of MoO_3 is sufficiently high above 1000 °C to affect its loss from the system. On the other hand, vapour pressure of MoO_2 remains below 10^{-5} mbar even at 1300 °C. Thus, to prevent loss of Mo from the system reaction (2) must be complete preferably below 800 °C. Also reduction reactions (4) and (5) should be complete below 1300 °C. Although $MoSi_2$ and SiC formation reactions [reactions (6) through (8)] can start at around 1000 °C, higher reaction temperature is needed for completion of the reaction as the reactants are in solid state. SiO gas formation reaction is prevalent above 900 °C and render loss of Si. However, before escaping from the system SiO can react with Mo /Mo_2C and C to form $MoSi_2$ and SiC respectively. Due to this, in large batch fraction loss of Si is expected to be less.

EXPERIMENTALS

The purity, particle size and source of the raw materials used in the experiments are given in Table 2. MoO_3, SiO_2 and graphite powders were mixed in molar ratio 1 : 2 : 6.5 by wet ball milling in ethyl alcohol for 6 hours using zirconia balls of 3 mm dia. In an initial experiment the mixtures (100 gm raw material batch) were heated under vacuum at 200 °C/hr to a maximum temperature of 1600 °C. Vacuum conditions inside the chamber at different

observations of the initial experiment, the mixture was heated stepwise, holding the different stages of reactions for prolonged time, till the vacuum improves to better than 10^{-4} mbar in each stage. The reaction products were chemically analysed. The phases were identified by X-ray diffraction (Philips Analytical, UK). In another set of experiments, MoSi2 and graphie powders were mixed and heated to 1600 °C and the products were analysed by X-ray diffraction.

RESULTS AND DISCUSSION

Figure 1 shows the vacuum condition inside the reaction chamber for the carbothermic process. At least three reaction stages involving gas evolution can be identified from the figure. Accordingly, the mixture was heated holding at 800, 1000 and 1600 °C to obtain the intermediate and final reaction products. Table 3 gives the list of different phases identified. The results indicate that the reduction of MoO_3 by carbon takes place in the temperature range 600 – 800 °C as per the reaction (2). Thermodynamic calculations show that free energy change (ΔG) for this reaction is negative at a temperature and a pressure of practical interest. However, to activate the process elevated temperature (about 600°C) is required. Materials balance does not indicate ant Mo loss.

The XRD analysis of the intermediate product obtained after pyrovacuum treatment at 1000 °C indicates that it consists of Mo, Mo_2C and unreacted SiO_2 and C. The reaction in the temperature range 850 – 950 °C is attributed to the reduction of MoO_2 according to the reactions (4) and (5).

Figure 2 shows the XRD pattern of the final product obtained after treatment at 1600°C. Phases have been identified to be a mixture of $MoSi_2$, $Mo_{4.8}Si_3C_{0.6}$ (Nowotny phase), SiC and unreacted graphite (C). The most prominent peaks are of $Mo_{4.8}Si_3C_{0.6}$ phase. No unreacted SiO_2 was detected. SiC peak was not prominent. The chemical analysis shows: Mo – 68.3; Si – 24.4; C – 7.3 and O – 0.1. Material balance indicates about 35% loss of silicon and no significant loss of Mo. The loss of Si has occurred through the reaction (9). The Si to Mo stoichiometry in the product is 1.28. Also as part of oxygen comes out with Si, unreacted carbon is present in the product. The reaction practically completes at 1600 °C as there is no noticeable weight even after heating at 1800 °C.

In an attempt to minimise the loss of Si, the reaction was allowed to occur at 1300 - 1400 °C for more than 4 hrs and subsequently the temperature was raised slowly maintaining vacuum level better than 10^{-4}. In this case also the reaction product consists of $MoSi_2$, $Mo_{4.8}Si_3C_{0.6}$ (Nowotny phase), SiC and unreacted graphite (C) as shown in Figure 3. However, the intensity of graphite peak has decreased and that of $MoSi_2$ peak has increased. Chemical analysis shows : Mo – 65.2; Si – 31.3; C – 3.5 and O – 0.18.

The formation of $Mo_{4.8}Si_3C_{0.6}$ has been studied by heating a mixture of $MoSi_2$ and graphite in different molar ratio (C/ $MoSi_2$ = 0.2, 0.4, 1.0, 1.8, 2.6) upto 1600 °C. XRD observations are briefed in Table 4. Qualitative analysis of the XRD result show that as the C/ $MoSi_2$ ratio increases amount of $Mo_{4.8}Si_3C_{0.6}$ and SiC phases increases. This indicates that $MoSi_2$ reacting with C forms $Mo_{4.8}Si_3C_{0.6}$ and SiC. The reactions can be written as follows.

For C/ $MoSi_2$ < 1.45 :

$MoSi_2 + x\,C = (1-v)\,MoSi_2 + v/4.8\,Mo_{4.8}Si_3C_{0.6} + (x - 0.125)\,SiC$

For C/ $MoSi_2$ = 1.45 :

$MoSi_2$ + 1.45 C = 1/4.8 $Mo_{4.8}Si_3C_{0.6}$ +1.375 SiC

For C/ $MoSi_2$ = 1.45 :

$MoSi_2$ + x C = 1/4.8 $Mo_{4.8}Si_3C_{0.6}$ + 1.375 SiC + (x-1.45) C

In our present experiment free carbon is seen when the C/ $MoSi_2$ ratio is above 1.45. Thus with the carbothermic product with carbon content there is a possibility of forming a product consisting of composite phases $MoSi_2$, $Mo_{4.8}Si_3C_{0.6}$, and SiC.

CONCLUSIONS

In carbothermic reduction of 1:2 molar mixture of MoO_3 and SiO_2, loss of Mo could be prevente and loss of Si could be minimised through controlled heating. The different phases identified in the product are : $MoSi_2$, $Mo_{4.8}Si_3C_{0.6}$ (Nowotny phase), SiC and C. Free C when present in combination with $MoSi_2$ reacts together to form $Mo_{4.8}Si_3C_{0.6}$ phase. With controlled heating there is a possibility of forming a product consisting of composite phases $MoSi_2$, $Mo_{4.8}Si_3C_{0.6}$, and SiC without ant free carbon. It has been reported in literature that combination of phases like $MoSi_2$, $Mo_{4.8}Si_3C_{0.6}$ and SiC can form a useful material having high temperature oxidation and creep resistance.

ACKNOWLEDGEMENTS

The authors would like to acknowledge the support of Analytical Chemistry Division and Applied Chemistry Division of BARC in carrying out various analytical works. Thanks are also due to P. K. Sinha and M. Shyambabu for their help in various stages of the work.

REFERENCES

1. K. Ito, T. Yano, T. Nakamoto, H. Inui and M. Imaguchi, *Intermetallics*, 4 (1996) 119.
2. D. A. Berztiss, R. R. Cerchiara, E. Gulbransen, F. S. Petit and G. H. Meier, *Mater. Sci. Eng. A*, 155 (1992) 165.
3. S. Zhang and Z. A. Munir, *J. Mater. Sci.*, 26 (1991) 3685.
4. S. C. Deevi, *J. Mater. Sci.*, 26 (1991) 3343.
5. S. W. Jo, G. W. Lee, J. T. Moon and Y. S. Kim, *Acta Metall. Mater.*, 44 (1996) 4317.
6. R. B. Schwarz, S. R. Srinivasan, J. J. Petrovic and C. J. Maggiore, *Mater. Sci. Eng. A*, 155 (1992) 75.
7. B. K. Yen, T. Aizawa and J. Kihara, *J. Am. Ceram. Soc.*, 79[8] (1996) 2221.
8. Y. Suzuki and K. Niihara, *Intermetallics*, 6 (1998) 7.

Table 1 : Equilibrium partial pressure (mbar) of gaseous product species as a function of temperature (°C)

Reaction		Temperature (°C)				
		527	727	927	1127	1327
$MoO_{3\,(s)} \rightarrow MoO_{3\,(g)}$	MoO_3	2.59×10^{-13}	2.94×10^{-8}	3.46×10^{-5}	3.54×10^{-3}	1155 °C b.p. to polymeric species
$MoO_{3\,(s)} + 0.5\ C_{(s)} = MoO_{2\,(s)} + 0.5\ CO_{2\,(g)}$	CO_2	> 1000	> 1000	> 1000	> 1000	> 1000
$MoO_{2\,(s)} \rightarrow MoO_{2\,(g)}$	MoO_2	6.88×10^{-24}	1.88×10^{-16}	1.53×10^{-11}	4.55×10^{-8}	1.70×10^{-5}
$MoO_{2\,(s)} + 2.5\ C_{(s)} = 0.5\ Mo_2C_{(s)} + 2.0\ CO_{(g)}$	CO	26.7	>1000	>1000	>1000	>1000
$MoO_{2\,(s)} + 2.0\ C_{(s)} = Mo_{(s)} + 2.0\ CO_{(g)}$	CO	3.17	700	>1000	>1000	>1000
$0.5\ Mo_2C_{(s)} + 2.0\ SiO_{2\,(s)} + 3.5\ C_{(s)} = MoSi_{2\,(s)} + 4.0\ CO_{(g)}$	CO	3.72×10^{-9}	4.82×10^{-5}	2.53×10^{-2}	2.15	59.2
$Mo_{(s)} + 2.0\ SiO_{2\,(s)} + 4.0\ C_{(s)} = MoSi_{2\,(s)} + 4.0\ CO_{(g)}$	CO	1.08×10^{-8}	1.16×10^{-4}	5.36×10^{-2}	4.19	104
$SiO_{2\,(s)} + C_{(s)} = SiC_{(s)} + CO_{(g)}$	CO	5.64×10^{-9}	6.40×10^{-5}	3.09×10^{-2}	2.48	65.1
$SiO_{2\,(s)} + C_{(s)} = SiO_{(g)} + CO_{(g)}$	CO	8.13×10^{-11}	2.36×10^{-6}	2.13×10^{-3}	2.67×10^{-1}	9.74

Table 2 : Purity and particle size of the raw materials used in the experiments

Raw Materials	Purity (%)	Median Particle Size (μm)	Source
MoO_3	99.5	2.6	M/s Thomas Baker Chemicals Mumbai, India
SiO_2	99.99	<0.2	M/s Thomas Baker Chemicals Mumbai, India
Graphite	98.5	0.65	M/ s Graphite India Ltd. (ground and leached inhouse)

Table 3 : Phase analysis of the products obtained at various stages of reaction

Product obtained after treatment at temp.	Identification of phases
800 °C	MoO_2 Unreacted SiO_2 and Graphite
1000 °C	Mo, Mo_2C Unreacted SiO_2 and Graphite
1600 °C	$MoSi_2$, $Mo_{4.8}Si_3C_{0.6}$ (Nowotny phase), SiC Unreacted graphite

Table 4. Relative intensities of maximum peaks for the phases

Initial sample composition ($C/MoSi_2$)	$MoSi_2$	$Mo_{4.8}Si_3C_{0.6}$	SiC	Graphite
0.2	100	3.47	2.43	No peak
0.4	100	36.77	22.92	No peak
1.0	69.44	100	44.44	No peak
1.8	22.78	100	51.25	20.66
2.6	No peak	100	45.13	32.78

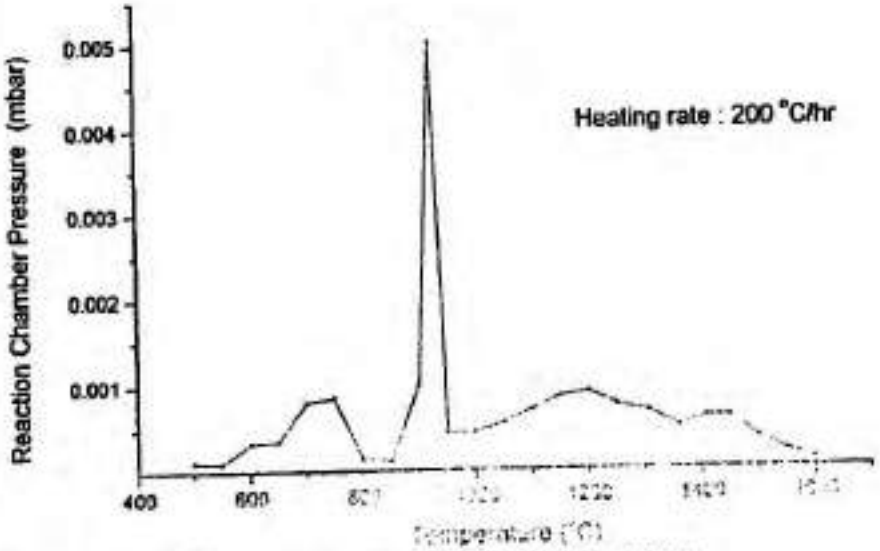

Figure 1 : Plot of reaction chamber pressure with temperature

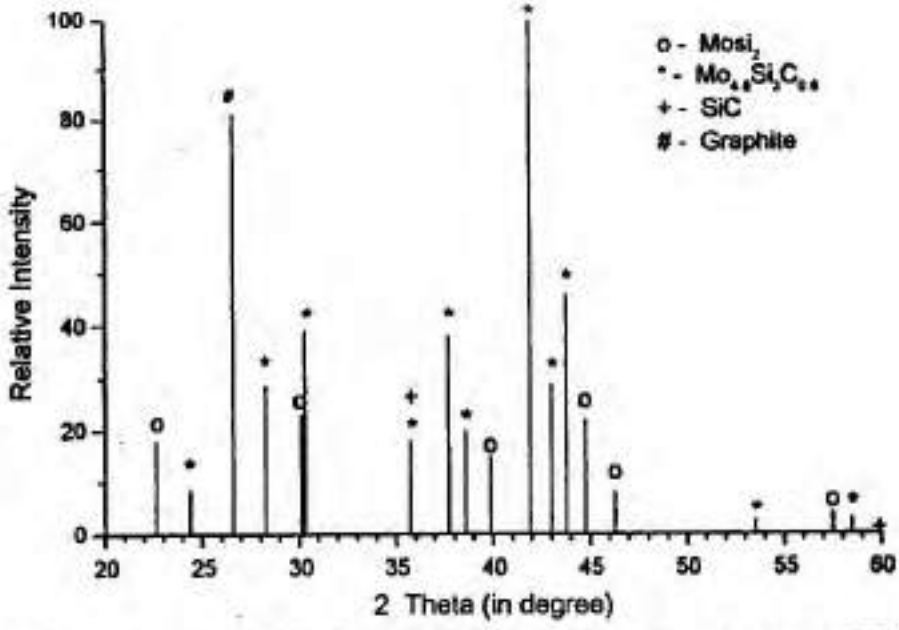

Figure 2 : XRD pattern of the product obtained by carbothermic process (heating rate 200 °C / hr)

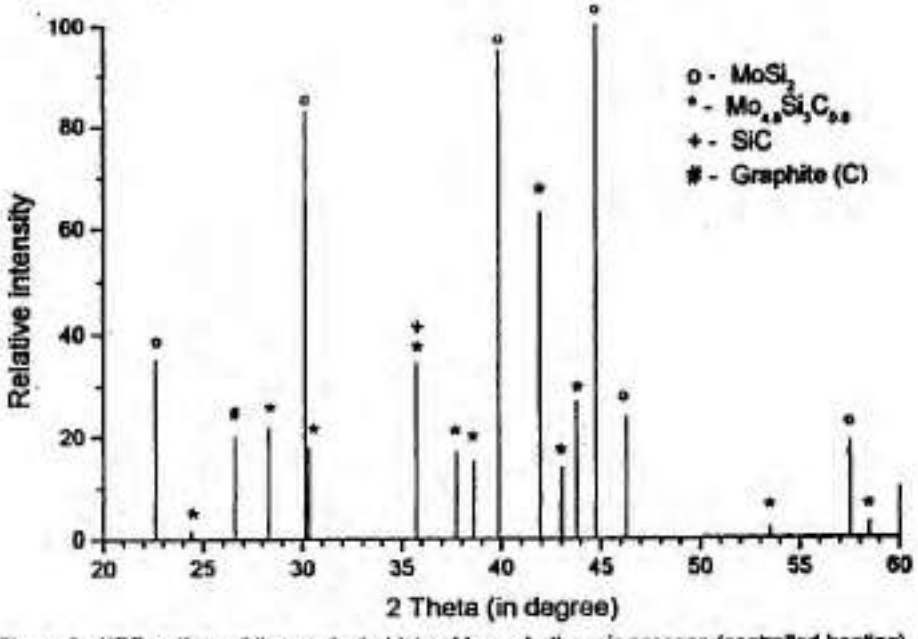

Figure 3 : XRD pattern of the product obtained by carbothermic process (controlled heating)

INFLUENCE OF DENSITY ON THE ROLLING CONTACT FATIGUE BEHAVIOR OF SINTERED STEELS

N. Rajiv, N. Govindarajan, R. Gnanamoorthy, K. Gopinath,
Y. Miyahsita*, Y. Mutoh*

Department of Mechanical Engineering
Indian Institute of Technology Madras
Chennai 600 036, INDIA

* Department of Mechanical Engineering
Nagaoka University of Technology
Nagaoka- shi 940-2188, JAPAN

ABSTRACT

Powder metal bearings and gears find increasing application because of their economical and technical advantages. Presence of pores acts as lubricant pocket and also as vibration and noise dampers and improves the performance of the overall machine. However the presence of porosity may also decrease the mechanical strength and thereby reduce the life of the bearings and gears. In order to understand the effect of density on the contact fatigue behavior it is necessary to conduct a systematic investigation using specimens with different densities on the contact fatigue life. The rolling contact fatigue behavior of sintered and heat-treated steel rollers are investigated using a fatigue test machine designed and fabricated for the purpose. The powder metal specimens are made of pre-alloyed powders followed by sintering and thorough hardening. The sintered rollers are mated against the standard steel rollers of high hardness. The endurance limit stress under rolling contact fatigue depends strongly on the porosity and the wrought steel exhibited very high endurance limit stress compared to the sintered steels investigated. Large surface peeling failures were observed in the sintered steels in addition to the pitting type failure in contrast to only pitting type of failure in the wrought steels.

1.0 INTRODUCTION

Sintered structural parts are gaining more and more significance because of the economical advantages of producing a large number of components with complicated shapes and high dimensional accuracy. Sintered gears and bearings are few of the structural elements, which find increasing application in many engineering industries. Newly developed sintered materials combined with the new densification processes make the powder metallurgy products suitable for medium and heavy-duty applications. Gears and bearings are subjected to severe cyclic loading during service and mostly fail by surface contact fatigue. In addition designing these structural elements require considerable knowledge about the

contact fatigue behavior and the parameters influencing them. The design of gears and bearings also require a material property data, called surface endurance fatigue limit of the material. The mechanical properties of the sintered materials are strongly influenced by the density, type of porosity, composition, processing, etc., [1]. Among these, density is the one of important parameter that influences the mechanical and physical parameters of the sintered material. The effects of density on the tensile and fatigue properties of the sintered steels have been reported [1-3]. Chen et al. [4] have reported about the influence of density on the fracture toughness of sintered steels and have reported increasing fracture toughness with density of the material in the range of 6.4 gm/cc to 7.1 gm/cc. Fatigue crack growth behavior of sintered steels was studied by Pompe et al. [5]. The porosity was found to have no effect on the exponent of the fatigue crack propagation law but it increases the crack velocity for a given stress intensity factor range. Very few publications are available on the rolling contact fatigue behavior of sintered steels [6]. No systematic investigation has been reported about the effect of different parameters on the rolling contact fatigue behavior of sintered steels one of the important properties required for understanding and designing the structural machine elements such as gears and bearings.

This paper reports some of the results of the on going research project on the rolling contact fatigue behavior of sintered steels. Influence of density on the rolling contact fatigue behavior of sintered steels is reported. Comparisons are made between the properties of sintered steels with the low alloy wrought steels, which has more or less similar composition to that of the sintered sample under identical testing conditions.

2.0 TEST MATERIALS AND EXPERIMENTAL PROCEDURE

Sintered steels with the composition shown in Table 1 are considered for the current investigation. The wrought EN 24 steel, which has the more or less similar composition compared to sintered steel composition is also considered for investigation. The samples are made from prealloyed powders, compacted and sintered. The sintered samples with two different densities are considered for the current investigation, 7.15 gm/cc and 7.00 gm/cc.

Table 1 Chemical composition of test and standard rollers (in wt %).

Material	C	Si	Mn	Ni	Cr	Mo	Cu	V	W	Co
Sintered roller	0.43	0.20	0.10	3.46	0.30	0.20	1.5	-	-	-
Wrought roller	0.37	0.20	0.40	0.95	0.95	0.20	-	-	-	-
Standard roller	1.02	0.30	0.30	0.18	3.91	4.52	-	1.93	5.69	0.24

The sintered steel rollers are heat treated to ~ 40 - 42 Rc by cold oil quenching and subsequent tempering. The standard roller against which the sintered specimens are mating is made of a hard tool steel heat treated to ~ 62 Rc. The standard roller is

ground after heat treatment for smooth finish. The dimensions of the test and standard rollers are shown in Figure 1.

Rolling contact fatigue tests were performed using a simple twin disc type test machine in which the standard roller is driven using an induction motor. Test roller is mounted on the linear motion slide and a contact load is gradually applied using hydraulic means. The applied load is measured using a load cell and pressure gage connected to the hydraulic cylinder and continuously recorded. The hydraulic power pack is equipped with an accumulator in order to maintain the constant load throughout the test duration. The lubricant oil used in the current investigation is SAE 80W90 oil. The lubricant oil is gravity fed to the contact point. The output oil temperature is continuously measured using the thermometer connected at the exit point of the oil. The sound level near the junction point is measured using a sound level meter kept about ~ 20 cm from the rollers. The vibration level of the sintered roller mount is also monitored using an accelerometer mounted on the roller support. The speeds of the test and standard roller shafts are also monitored continuously.

The endurance limit curve for the sintered rollers with different densities was generated using the RCF test facility described above. The density, surface roughness, weight and dimensions of each roller are measured before conducting the experiments. Test load is applied gradually after running the standard roller at full speed and supplying the lubricant oil. The vibration level and sound level of the test rig is continuously monitored for detecting the failure of the sintered roller. In addition the rollers are inspected using a magnifying glass at periodic intervals. Each sintered roller is mated with the fresh surface of standard roller and at least three rollers were used for each stress level. Tests were run up to failure or until $5x10^6$ cycles. Failure analysis of the sintered rollers was performed using optical microscope. The subsurface analysis was also carried out in order to analyse the crack initiation sites using metallographically prepared specimens.

3.0 RESULTS AND DISCUSSIONS

The rolling contact fatigue behavior of wrought EN24 steel is shown in Figure 2. The rolling contact behavior of sintered steels with 7.00 and 7.15 gm/cc are shown in Figures 3 and 4 respectively. Three tests were conducted at each contact stress level and the average values are considered due to the limited number of specimens available. All the specimens showed a significant increase in the sound level and vibration level when the specimens failed even with less than 4 % of surface damage. Number of cycles run at this stage is considered as the life of the specimen in the present investigations.

The contact fatigue behavior of sintered rollers and standard steel rollers are compared in Figure 5. The endurance limit stress of the 7.00 gm/cc material is only 1000 MPa while that for the 7.15 gm/cc material is marginally high, 1065 MPa. The endurance limit stress under the identical testing conditions for the EN24 steel was

very high compared to the sintered steel indicating the significant effect of porosity on the rolling contact fatigue endurance limit stress (Figure 6).

In order to understand the micro mechanisms of failures in sintered and hardened steel, failed specimens are investigated using optical microscope. A different damage appearance was observed for sintered and hardened steel specimens depending on the density and applied contact stress. In general two types of failure modes are observed in sintered and hardened steels in contrast to typical pitting type of failure in the wrought steels.

- Pitting failure showing a number of small pits
- Surface peeling failure showing a larger area of material loss

Although sintered steels also failed in pitting mode also, the size of pits in the sintered specimens ranged in order of few hundred microns while the size of pits in the wrought steels are in the order of few millimeters. However a much severe type of localized type of failure, surface peeling, was observed at one or two places indicating severe mode of failure, which was not observed in the wrought steels. Julia et al. [6] have also reported occurrence of similar type of failure in high-density sintered specimens. Pitting is a type of surface fatigue failure characterized by particles of material breaking out of the surface after a certain number of stress cycles. It is well established in the case of wrought materials that the maximum shear stress for two cylinders under contact occurs at a distance of about 0.786 times the contact width at which the fatigue cracks initiate [7]. These cracks after initiation at a depth propagate towards the surface and lead to pitting. Subsurface analysis of the sintered specimens carried out also indicates the crack initiation at the subsurface at a distance of about 0.8 times the surface contact width and crack propagating towards the surface.

4.0 CONCLUSIONS

Rolling contact fatigue behavior of sintered and hardened steels with two different densities 7.00 gm/cc and 7.15 gm/cc and wrought steel with nearly similar chemical composition and hardness are investigated. It is observed from the investigations that the presence of the porosity significantly reduces the contact fatigue behavior of sintered and hardened materials. Increasing the density improved the rolling contact fatigue behavior of the sintered and hardened steels. A severe surface peeling type of failure was observed in sintered and hardened steels, which was not observed in the wrought steels. The size of pits observed in the sintered steels is very small compared to the wrought steel investigated.

5.0 ACKNOWLEDGEMNETS

This research work is supported by the Ministry of Human Resources and Development, India. Authors are very much thankful for the support provided by

M/s Mitsubishi Materials, Niigata, Japan in preparation of the sintered and standards rollers used in the current research work.

6.0 REFERENCES

1. G.F.Bocchini "The influence of porosity on the characteristics of sintered materials", The International Journal of Powder Metallurgy, 22 (1986) P.185.
2. B Lidnqvist "Influence of microstructure and porosity on fatigue properties of sintered steels", Metal Powder Report, (1989) P.443.
3. P.Beiss "Fatigue strength of sintered steels", Metal Powder Report, (1987) P. 244.
4. Y.T.Chen "Fracture toughness testing of PM materials', Metal Powder Report, June (1989) P.425.
5. W.Pompe, G.Leitner, K.Wetzig, G.Zies and W.Grabner "Crack propagation and processes near crack tip of metallic sintered materials", Powder Metallurgy, 27 (1984) P.45.
6. A.W.Julia, P.D.Nurthen and P.R.Brewin "Rolling contact fatigue testing of P/M high speed steels", The International Journal of Powder Metallurgy, 26 (1990) P.345.
7. K.L.Johnson "Contact Mechanics", Cambridge University Press, Cambride (1985).

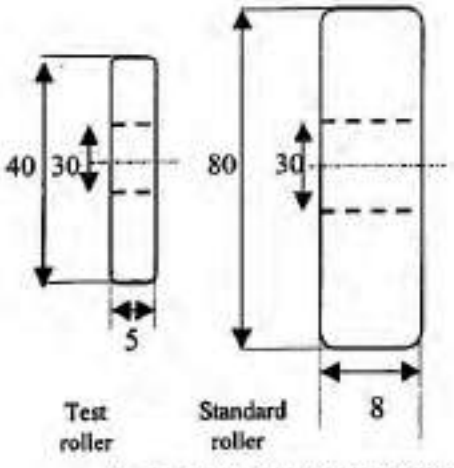

Fig. 1. Geometry of test specimens (Dimensions are in mm)

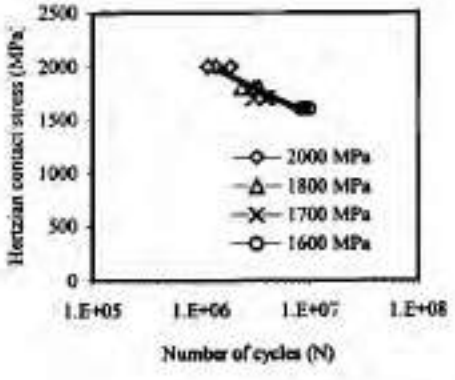

Fig.2. Contact fatigue data for EN24 steel

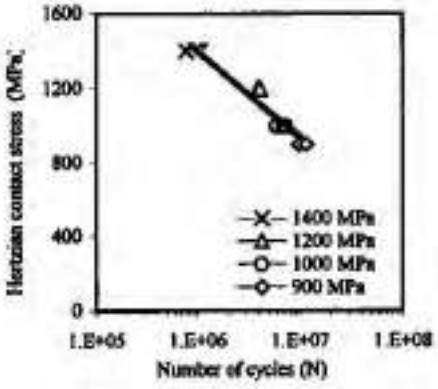

Fig.3. Contact fatigue data for sintered steel with 7.00 gm/cc

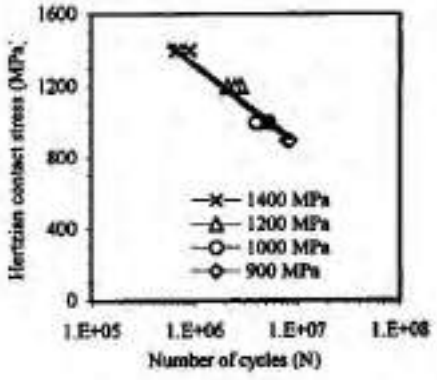

Fig.4. Contact fatigue data for sintered steel with 7.15 gm/cc.

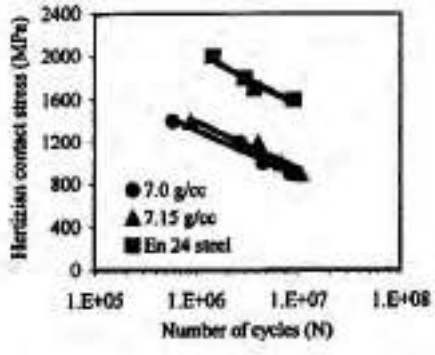

Fig.5 Contact fatigue behavior of sintered and wrought steels.

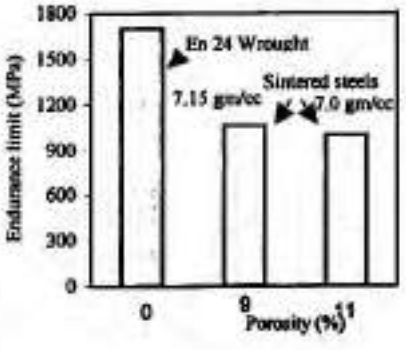

Fig.6 Endurance limit stress for the materials investigated.

Effects of elastic plastic deformation on thermal barrier coatings

Nilima Roy, Debasish Mahanty, Kersi M Godiwalla

and

Ashok K Ray

National Metallurgical Laboratory

Jamshedpur-831007, Bihar, India

Abstract

The present paper highlights some of the results on modeling of deformation behaviour in elastic plastic condition under bending, for miniature test specimens of thermal barrier coatings (TBCs) on Ni base superalloys. These tests were performed with plasma spray coated zirconia, bonded by a MCrAlY layer to Ni -base superalloys (Inconel 617 & CMSX-4). Such thermal barrier composites are currently considered as candidate materials for advanced gas turbine stationary components. Coating as a protective layer improves the surface properties of the substrate.Load vs. centre-point deflection data were obtained from each of the above tests. Four point bend tests on these TBCs at room temperature, in as received and oxidised conditions had revealed that after the yield point of the of the substrate is reached, a high threshold load was required for penetration of the crack front further into the bond coat. The crack never penetrated and propagated into the substrate. At a temperature of 800°C,the crack propagation was found to be confined to the TBC (ceramic layer), as the ductile bond coat offers an attractive sink for stress relaxation. The experimental data was then simulated mathematically using beam elements in Finite Element Analysis. A computer code was developed considering elastic-plastic finite elements, for four point bend specimens with two degrees of freedom at each node. A similar analysis was also conducted using the ANSYS (ver.5.5) software. The analysis indicated concurrence of displacements, for each load case, with the experimental results in the elastic regime. Reasonable extent of concurrence was also obtained in the early stages of plastic deformation of elements. However, minor deviations occurred from experimental results in the case of large loads, i.e.' large plastic deformation.

1. Introduction:

TBCs represent an attractive materials approach of enhancing the high temperature limits for systems such as gas turbines, aircraft engines and diesel engines. Industry and academia in the recent years are actively pursuing research on evaluating the lifetime and thermomechanical behaviour of candidate materials in turbine blades and vanes being subjected to high mechanical stresses and aggressive environments [1-11]. These blades and vanes are made of superalloys with ceramic thermal barrier coatings (TBCs).

The Ni-base superalloys which have been developed for this application are made of superalloys having a γ matrix (solid solution based on nickel) strengthened

by both solid solution and precipitation of the γ'-Ni_3 (Ti,Al) phase. The demand for higher efficiencies and durability has resulted in directionally solidified alloys, single crystals, alloys strengthened by oxide dispersion (ODS) or by carbide fibres [1]. Crack propagation studies and failure mode of TBCs on (i) Ni-base superalloy having a γ' phase > 50% [2] and (ii) Inconel-617 under bending for gas turbine vanes have been studied and reported elsewhere [2,3]. The significant differences in properties between ceramic and metal, as well as the severe temperature gradients applied in such systems, cause thermal stresses that can lead to cracking, delamination and ultimately spalling of the coating. It was established that under conditions simulating jet engine applications [4-5], one significant contributor to such spalling is oxidation of the bond coat. Many studies have concentrated on the time to spalling as a function of heat flux [6-9] and as a function of surface stresses and crack tip opening [9].

In recent years, concentrated efforts have been made to understand the mechanisms of crack initiation and propagation in TBCs under controlled experimental conditions [9-11]. Keeping this in view, an attempt was made to study the crack propagation behaviour in TBCs at room temperature in the as received and oxidized conditions as well as at a higher temperature (1073 K) [2,3]. The elastic modulus of the bond coat has been simulated by modifying the existing model for two - layered composite beam specimen to a three layered composite beam specimen [12]. FEM (finite element) analysis for all types of tested specimens was conducted with ANSYS software using a 2-D isoparametric solid element, defined by four nodal points having two degrees of freedom at each node. Simulations were carried out all specimens with selected load conditions in the elastic region of the stress-strain curves. The outputs of the stresses along the direction of global axes i.e. σ_x, σ_y (component stresses), the shear stress σ_{xy}, the principal stresses σ_1, σ_2, σ_3 and the equivalent stress, σ_{eq} have been presented and discussed[12].

The aim of the present work is to mathematically simulate the experimental data for the deformation curves in elastic plastic condition using beam elements in finite element analysis and to derive analytical models in the elastic plastic regime of the deformation curves in TBCs, since there appears to be a huge plastic zone in the deformation curves.

2. Experimental:

Ni-base superalloy (a) Inconel-617 from source A and (b) CMSX-4 from source B containing γ' phase (~67%) were the substrate material for the TBCs. A NiCrAlY type metallic undercoat or bond coat was first generated by plasma spraying to insure the bonding and the adherence of the thermal barrier on the substrate and to improve the corrosion resistance of the TBC. Thereafter, zirconia (stabilized with 8 wt% yttria) based thermal barrier coating was plasma sprayed on the bond coat. Before initiation of the plasma spray, the substrate was treated through reverse transfer arc sputtering to remove any traces of oxide that may have formed during preheat. The coating distribution is determined by computer- controlled gun and part motion. Although the substrate material of the TBCs from two different sources were different, the plasma spraying parameters were maintained nearly the same. In the case of bond coat, in order to achieve theoretical bulk density and extremely high adhesion strength, plasma spray is carried out in inert gas chamber and in a reduced pressure. The plasma spraying parameters are reported in [2,3]. From the as received plate-shaped vane components four point bend (FPB) specimens were machined using ultrasonic cutting and spark erosion technique. The height (h), width (b) of the various FPB specimens, along with the thickness of the ceramic layer (d_c) and the thickness of the bond coat (d_b) are listed in Table1. Fig.1 shows the unetched microstructure of the TBC composites from source A and B. The load deflection curves are shown in Fig.2.

The failure behaviour of the TBC systems was studied in bending tests with in situ observation of the cracking mechanisms and it has been explained in details in [2,3,12]. The ceramic layer (TBC) is on the tensile surface of the composite beam specimen.

Metallographic interpretation of the substrate, bond coat and ceramic layer are reported in [2,3,12].

3. Finite Element Formulation

There are two approaches to the elastic-plastic analysis of beams: Non-layered approach and Layered approach. In the present work we have considered the Layered approach. In the Non-layered approach, the whole cross-section of the beam is assumed to become plastic instantaneously when the bending moment reaches the

yield moment. Where as in the Layered approach it is assumed that as soon as the stress in the middle of the outer layers reaches the yield value, then the outer layers become plastic, while the rest of the layers remain elastic. The beam is thus divided into a number of layers each of which may become plastic separately.

Consider a beam of depth t in which the breadth b varies with depth symmetrically about the neutral axis (Fig.3). The beam is subjected to a distributed loading of intensity q.

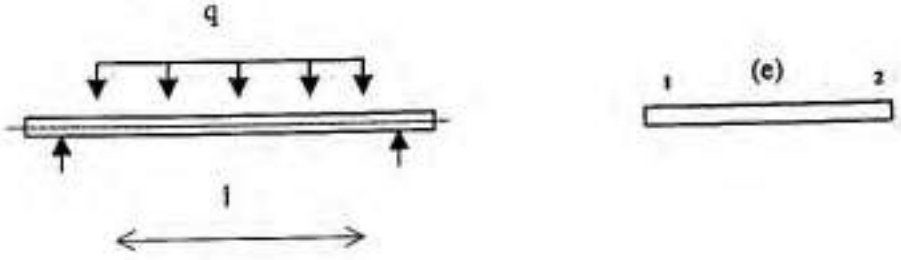

Fig.3 A typical beam problem and its element representation

If the beam undergoes a set of virtual lateral displacements δw, virtual normal rotations δθ and associated virtual curvatures $-z[d(\delta\theta)/dx]$ and virtual shear strains δβ then the virtual work equation can be written as

$$\int_0^l \int_{-t/2}^{t/2} \int_{b(-t/2)}^{b(t/2)} \left(-z\frac{d(\delta\theta)}{dx}\sigma_x + \delta\beta\,\tau_{xz}\right) dx\,dy\,dz - \int_0^l \delta w q\,dx = 0$$

$$\int \left(\frac{d(\partial\theta)}{dx} M + \partial\beta Q\right) dx - \int \partial w q\,dx = 0$$

where the bending moment

$$M = EI\left(\frac{-d\theta}{dx}\right)$$

the shear force

$$Q = GA\beta$$

and EI is the flexural rigidity and GA, the shear rigidity.

3.1 Strain and Displacement relation

The curvature-displacement relationship is

$$\varepsilon_f^{(e)} = \left[0, \frac{1}{l^{(e)}}, 0, \frac{-1}{l^{(e)}}\right] \begin{bmatrix} w_1^{(e)} \\ \theta_1^{(e)} \\ w_2^{(e)} \\ \theta_2^{(e)} \end{bmatrix} = B_f^{(e)} \phi^{(e)}$$

where B_f is the curvature-displacement matrix and ϕ is displacement vector of an element e.

The shear strain-displacement relationship is

$$\varepsilon_s^{(e)} = \left[-\frac{1}{l^{(e)}}, \frac{-(x_2^{(e)} - x^{(e)})}{l^{(e)}}, \frac{1}{l^{(e)}}, \frac{-(x^{(e)} - x_1^{(e)})}{l^{(e)}}\right] \begin{bmatrix} w_1^{(e)} \\ \theta_1^{(e)} \\ w_2^{(e)} \\ \theta_2^{(e)} \end{bmatrix} = B_s^{(e)} \phi^{(e)}$$

Where B_s is the shear strain-displacement matrix.

3.2 Stiffness matrix evaluation

Given the element strain-displacement relationships, Hughes [13] has shown that using a virtual work approach the governing equations can be expressed as

$$\left[K^f + K^s\right]\phi - f = 0$$

the submatrices of K_f, K_s and subvectors of f for element e can be written as

$$K_f^{(e)} = \int_{x_1^{(e)}}^{x_2^{(e)}} \left[B_f^{(e)}\right]^T (EI)^{(e)} B_f^{(e)} dx$$

$$K_s^{(e)} = \int_{x_1^{(e)}}^{x_2^{(e)}} \left[B_s^{(e)}\right]^T (GA f)^{(e)} B_s^{(e)} dx$$

$$f^{(e)} = \int_{x_1^{(e)}}^{x_2^{(e)}} \left[N_1^{(e)}, 0, N_2^{(e)}, 0\right]^T q dx$$

N_1 and N_2 are shape functions.

In the layered approach EI and GA are evaluated as

$$EI = \sum_i E_i b_i z_i^2 t_i$$

$$GA = \sum_i G_i b_i t_i$$

where b_i is the layer breadth

t_i is the layer thickness

z_i is the z-coordinate at the middle of the layer

E_i is the Young's modulus of the layer material

and G_i is the Shear modulus of the layer material.

The state of stress at the middle of a layer is taken as representative for the entire layer. Contributions to the stress resultants M and Q are found for each layer separately by integrating over the layer thickness only. The bending moments and shear forces are then found from the contributions of all the layers of the beam element. However, if the stress at the middle surface of a layer reaches the uniaxial yield stress of the layer material, the whole layer is considered to be plastic and E_i is replaced by

$$E_i\left(1 - \frac{E_i}{E_i + H'}\right)$$

Where H' is the uniaxial strain hardening parameter.

4. Analytical Method

Fig.4 depicts a simply supported beam of length 2l, width b and height 2h. Two loads each of magnitude P act on the beam at locations l_1 from the ends of the beam.

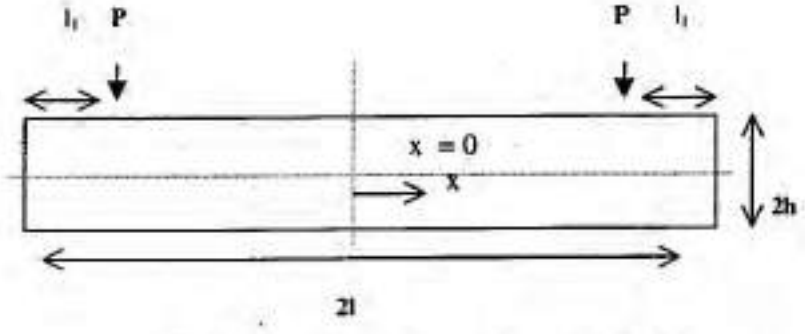

Fig.4 Schematic of a simply supported beam

The curvature of the beam is given by

$$\frac{d^2y}{dx^2} = \frac{\sigma_y}{E\eta}$$

E is elastic modulus.

Solving the equation with appropriate boundary conditions yields the deflection at the centre of the beam as follows:

$$y = \frac{\sigma_y L^2}{2E}\sqrt{\frac{b\sigma_y}{3(b\sigma_y h^2 - Pl_t)}}$$

5. Results and Discussion

Fig 1 shows that the percentage of porosity in the TBC from source B is less (18-20%) than that in the TBC from source A (~30%). Even the bond coat in the composite beam specimen from source B was found to contain less porosity than that in the composite beam specimen from source A.

The TBC layer does not contribute to the toughness of the composite beam as has been experimentally demonstrated. As such, the thickness of the TBC layer has NOT been considered in simulating the experimental results. Furthermore, it was observed that the bond coat acts as an attractive sink for stress relaxation. This prevents the crack front from propagating into the substrate.

For simulating the experimental results, we have subtracted the height of the TBC layer from the specimen. A beam element was chosen for the purpose of simulation. BEAM23 is a uniaxial element with tension-compression and bending capabilities. The element has three degrees of freedom at each node i.e. translation in nodal X and Y direction and rotation about nodal Z direction. Two nodes, the cross-sectional area, moment of inertia, and the height of the rectangular beam define the element.

A 2-D finite element model of the element was developed using ANSYS. Suitable real constants and material properties were specified. In particular, the

The origin x = 0 is selected at the centre of the beam. The axial stress in the beam within the elastic limit of the material is given by

$$\sigma_x = \frac{My}{I}, \; |y| < n$$

where M is the bending moment acting for a given load, y is the distance from the neutral axis, I the moment of intertia. When the loads exceed the yield stress σ_y of the material at the outermost fibres of the beam, the axial stress is denoted by

$$\sigma_x = Siny, \; |y| > n$$

The bending moment can be separated into its elastic and plastic components as:

$$M = \frac{\sigma_y I_{el}}{\eta} + \sigma_y S_p$$

where

$$I_{el} = 2\int_0^{\eta} by^2 dy \quad and \quad S_p = 2\int_{\eta}^{h} bydy$$

i.e.,

$$I_{el} = \frac{2}{3}\sigma_y b\eta^3 \quad and \quad S_p = b\sigma_y (h^2 - \eta^2)$$

Therefore

$$M = \frac{2}{3}\sigma_y b\eta^2 + b\sigma_y (h^2 - \eta^2)$$

and

$$\eta = \sqrt{\frac{3(b\sigma_y h^2 - Pl_y)}{b\sigma_y}}$$

specimen was assumed to follow a bilinear kinematic behaviour. Suitable values for tangent modulus and yield stress were specified to simulate the plastic behaviour of the specimen. The specimen was meshed using BEAM23 elements. The meshed finite element model had 500 nodes. The first and last nodes were constrained in the X and Y direction. The specimen was loaded at two points, which is equidistant from the two ends. This simulates a perfect bending condition (Four-point bend test).

The simulated results are shown in table 1. The results are compared with those obtained through analytical formulation. In another study, the results obtained while using ANSYS for loads within the elastic regime, compared reasonably well with experimental measurements. However, in the present analysis, theoretical predictions could approximate experimental results only for moderate deflections beyond the elastic limit of the material.

These deviations in the case of large deflections could be due to (a) non-availability of true stress-strain curves for each of the materials investigated, (b) only an approximate value of the yield stress is used in the present analysis, (c) experimental uncertainty. Further studies are necessary to account for these deviations.

The validation of experimental data using Finite Element formulation based on layered approach is under progress.

6. Conclusion

Analysis indicated concurrence of displacements, for each load case, with the experimental results in the elastic regime. Reasonable extent of concurrence was also obtained in the early stages of plastic deformation of elements. However, minor deviations occurred from experimental results in the case of large loads, i.e.' large plastic deformation.

Acknowledgement

The data presented in this paper is the outcome of an in house R&D project at National Metallurgical Laboratory, Jamshedpur. The authors are grateful to Prof. P. Ramachandra Rao, Director, NML Jamshedpur for his kind permission to publish this manuscript.

References

1. C. Duret - Thual, R. Morbioli, P. Steinmetz, A Guide to the Control of High Temperature Corrosion and Protection of Gas Turbine Materials CEC (Commision of the European Communities) COST Energy, EUR 10682 EN, 1986. (Edited by O. Morocutti: Commission of the European Communities, Brussels, Belgium).
2. A.K.Ray . Inter. J. Turbo & Jet Engines, 17 (1) 1 (2000)
3. A.K. Ray and R.W. Steinbrech, J. Euro. Ceram. Soc , 19, 2097 (1999) .
4. R. A. Miller and C. E. Lowell, Thin Solid Films., 95 , 265 (1982).
5. W. J. Brindley and R. A. Miller, Surf. Coat. Technol,43-44 , 446(1990).
6. R. A. Miller and C. C. Berndt, Thin Solid Films. , 119, 195 (1984).
7. C. H. Liebert and R. A. MillerInd. Eng. Chem.Prod.,Res.Dev.,12, 334 (1984).
8. J. T. DeMasi, K. D. Sheffler and M. Ortiz, Thermal Barrier Coating, Life Prediction Model Development, NASA CR 182230, National Aeronautics and Space Administration, Dec (1989).
9. K. Kokini and C. D. Choules and Y. R. Takeuchi, J. Therm. Spray. Tech. (JTTEE) ASM International., 6(1),43 (1997) .
10. L. Lelait, S. Alperine, C. Diot and M. Mevrel, , Mater. Sci. Eng A . , 120 – 121, 475 (1989).
11. K. Kokini and Y. R. Takeuchi, Mater. Sci. Eng. A. , 189, 301 (1994).
12. K.M. Godiwalla, N. Roy, S. Chaudhuri and A.K. Ray, Inter. J. Turbo & Jet Engines, 17 (3) (2000) in press.
13. T.J.R. Hughes, R.L. Taylor and S. Kanoknukulchai, Int.J.Num.Meth.Engng, 11, 1529 (1977).

Table.1: Dimension and coating thickness of the TBC specimens for FPB experiments

Type	Source	Test temperature °C	h (mm)	b (mm)	d_c (mm)	d_b (mm)
I. As received	A	RT-25	1.71	2.64	0.60	0.1
II. As received	B	RT-25	1.83	2.61	0.50	0.1
III.-Oxidised at 1000°C for 200 hours	A	RT-25	2.42	2.31	0.27	0.11
IV. As received	B	800	3.00	3.88	0.50	0.20

Table 2 Deflection of the centre of the beam for various loads for different material type

Material Type	LOAD, N	Deflection, mm (ANSYS)	Deflection, mm (Analytical)
I	20	0.0456	0.132
	40	0.0912	0.146
	60	0.137	0.165
	80	0.182	0.195
	100	0.242	0.249
	120	0.311	0.413
II	40	0.0559	0.129
	60	0.0839	0.142
	100	0.14	0.184
	120	0.168	0.228
	140	0.209	0.337
III	40	0.0162	0.069
	60	0.0244	0.071
	80	0.0325	0.0733
	100	0.0406	0.0757
	120	0.0487	0.0784
	180	0.07314	0.088
	200	0.0812	0.092
IV	80	0.0112	0.057
	100	0.0140	0.058
	120	0.0168	0.059
	140	0.0196	0.0595
	160	0.0223	0.0601

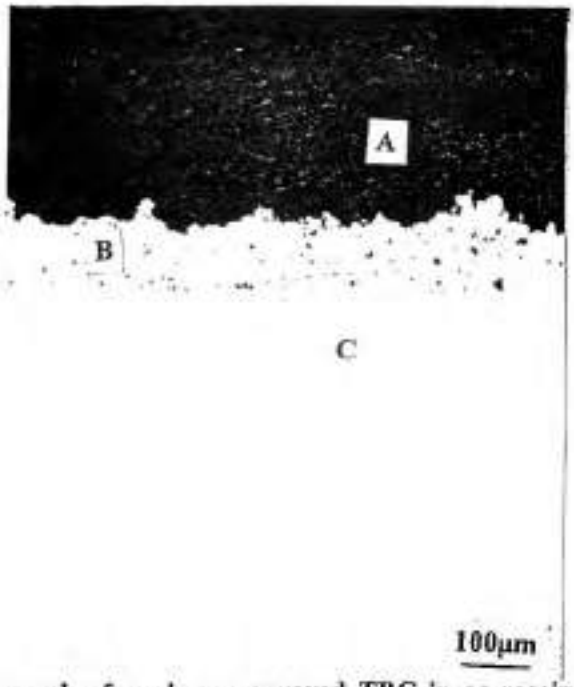

1a. Micrograph of a plasma sprayed TBC in as received condition (TypeI, source A). The sample is polished and unetched.
A- TBC (ceramic layer)
B- Bond coat
C-Substrate

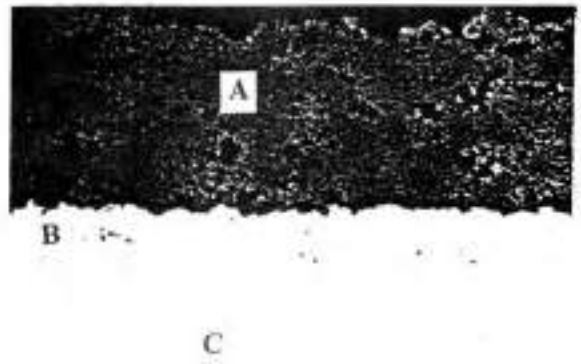

1b. Micrograph of a plasma sprayed TBC (Type II, source B). The sample is polished and unetched. The TBC (ceramic layer) has less % porosity and defect compared to the one reported in Fig. 1a.
A- TBC (ceramic layer)
B- Bond coat
C-Substrate

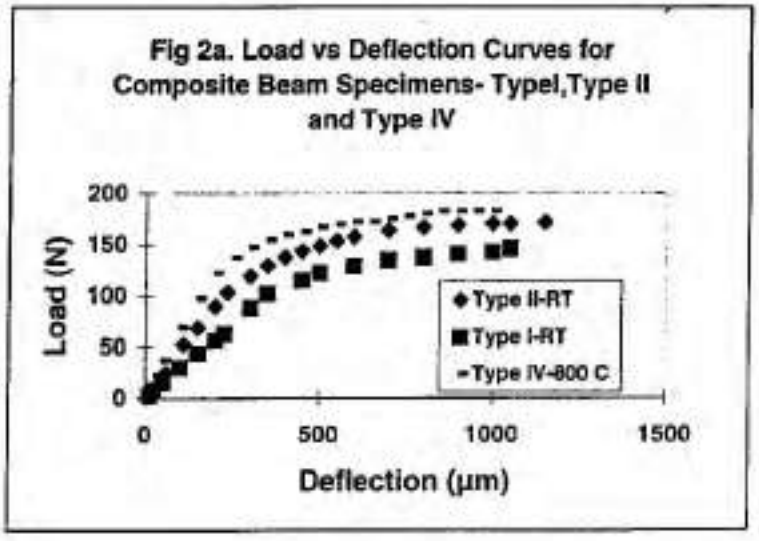
Fig 2a. Load vs Deflection Curves for Composite Beam Specimens- Typel,Type II and Type IV
Load (N)
200
150
100
50
0
0
500
1000
1500
Deflection (μm)
Type II-RT
Type I-RT
Type IV-800 C

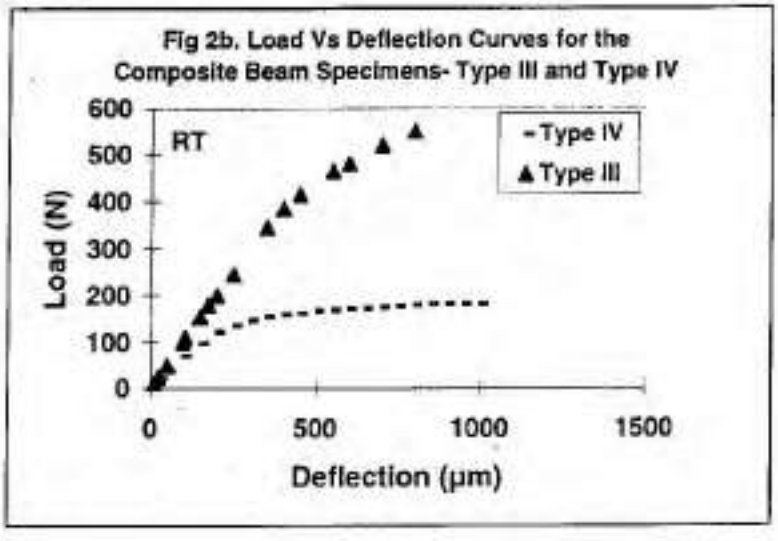
Fig 2b. Load Vs Deflection Curves for the Composite Beam Specimens- Type III and Type IV
RT
Load (N)
600
500
400
300
200
100
0
0
500
1000
1500
Deflection (μm)
Type IV
Type III

A simple model for viscosity of PIM mixes; Iso-viscosity contour maps for PIM processing

J. Janardhana Reddy, M. Vijaykumar*, T.R.RamaMohan# and P. Ramakrishnan#*

** Defence Metallurgical Research Laboratory, Hyderabad, India*
 # Indian Institute of Technology, Bombay, Mumbai, India

Abstract- A simple model is proposed for the prediction of viscosity of PIM mixes incorporating independent parameters like shear rate, powder/binder content and temperature. The viscosities of mixes with powders of coarse silica and fine alumina and polymer-wax based binder systems were measured using capillary rheometry at different shear rates, temperatures and binder contents. The experimental viscosity data shows excellent correlation with the proposed combined equation. The non-linear dependence of viscosity on these parameters is presented in a graphical fashion as iso-viscosity contour maps. The maps provide a useful guide to select the processing regimes of powder injection moulding mixes.
KEYWORDS: Viscosity, Shear rate, CBVC, Model, Processing Maps, Powder Injection Moulding mixes

I. INTRODUCTION

The mould filling of powder injection moulding (PIM) mix is dependant on the viscous flow of the mix into the die cavity. If the mix is highly viscous, then complete mould filling is not possible. If the viscosity is too low, then the non-uniform filling results in segregations [1]. Thus a thorough understanding of flow behaviour of PIM mix is essential for the success of powder injection moulding. But the flow of PIM mixes is a complex subject as it is governed by the properties of the powder and binder, their contents and operational/experimental conditions.

A few authors [2-9] measured viscosities of PIM mixes and presented the viscosity variation as a function of individual parameters like shear rate or particle size, shape and distribution or powder content or temperature etc. Though this type of presentation of data is easier, the understanding and correlating the viscosity to the practical process conditions where a number of parameters are at dynamic conditions, is complicated. Hence, even the available limited experimental data remained useless without any significant contribution to processing conditions. This is due to absence of a combined model for the viscosity of PIM mixes with all the parameters and thus, the selection of regime of optimum processing conditions based on sound principles remained as illusion. Hence the processing conditions are continued to be selected by trial and error method.

In order to predict the viscosity of PIM mix for all operational conditions, a new model was proposed by Janardhana Reddy et.al (10), combining some of the existing models for viscosity with individual parameters as,

$$\eta = m \cdot \gamma^{n-1} * (1\text{-CBVC})/(\text{BVC-CBVC}) * \eta_{\infty} \cdot e^{E/R(1/T-1/T_0)} \quad (1)$$

where m is the consistancy coefficient, n is the flow behaviour index, CBVC is the critical binder volume concentration of powder, BVC is the binder volume in mix, E is the activation energy for the flow and R is gas constant. The equation (1) was further simplified by combining the binder and powder constant terms like m, η_{∞} and CBVC etc. and linearized as,

$$\text{Ln}(\eta \cdot \Delta B) = \ln a + (n-1)\ln \gamma + E/R.1/T \quad (2)$$

where a is constant and ΔB is the binder content in excess of CBVC (i.e., BVC-CBVC). If the parametric constants are calculated from a limited number of viscosity measurements of any binder or PIM mix, then the viscosity data for the whole operational conditions can be generated from the model. The authors in this paper, have compared the experimental viscosities of some of the PIM mixes with those from model and drawn Iso-viscous contour maps for their processing and explored the possibility to define the suitable processing regimes of PIM mixes.

II. EXPERIMENTAL

Five types of polymer -wax binder systems with two constituents (3.1) were selected for the experiments. The major constituent of binder was to give the required fluidity and minor constituent was to modify the flow and to help during debindering. First binder system was a complete wax based system. Second one contained wax as major binder system. Third was polymer major system. The other two were also polymer rich binder systems with addition of 5 vol.% surfactants. The binder systems were prepared by mixing the appropriate constituents at suitable temperatures till the uniformity of the mix was observed. The binder systems compositions, notations, mixing temperaturs and times are given in table 1.

Table 1: The binder systems, notations, mixing temperatures and times

Nota-tion	Binder composition, vol.%	Mixing temp, C	time, hrs
#10	75% PW+ 25% MW	70	2
#20	75% MW + 25% PE	120	3
#30	75% PE + 25% MW	150	3
#30ST	71.5% PE+ 23.5% MW + 5% S.A.	150	3
#30P	71.5% PE + 23.5% MW + 5% PMMA	150	3

Paraffin Wax (PW) was of food grade type fully refined with melting point 61°C from China and Microcrystalline Wax (MW) was of amber type with melting point 67°C from Japan. The Polyethylene (PE) (flow rate FR-190/2.16 = 21.4 gms), Stearic acid (S.A) and Poly MethylMethacrylate (PMMA) were procured locally.

Coarse Silica powder (fused) of average particle size 35μm with broad distribution from 6 to 100μm from Remet Corp., USA and alumina powder of particle size 1.9μm of mono model distribution from 1 to 5μm from Alcon, USA were used for the present experiments. The CBVC values of the silica and alumina powders were estimated as 26% and 43% by torque and temperature measurement methods using mixer of Brabender torque rheometer [11,12].

Powder-binder mixes were prepared for each binder/powder in different proportions of binder contents by mixing the appropriate percent weights of powders and binders in rheometer mixer at specified temperatures for about 45 minutes at 50 rpm. The silica powder-binder mixes 1S, 2S, 3S, 4S, 5S were having binder contents 50, 36, 32, 30 and 28 vol.% respectively. Similarly the alumina powder-binder mixes 1A, 2A, 3A, 4A were having binder contents 50, 46, 44 and 43 vol.% respectively. The mixes notation for any composition was arrived by combining the binder and powder codes. For example a mix code 30S represents all the mixes of #30 binder with silica powder. The mixes uniformity was ensured by allowing the mixing till the torque stabilization. Then the mixes were crushed into fine globules to facilitate their filling in the capillary die for viscosity testing.

Viscosity measurements of the binders and PIM mixes were done on Instron machine, model 4483 with a die having capillary of 1.5 mm at temperatures, above the softening point and below the melting point. The temperatures were selected such that both binder, powder-binder mix were processed in the same temperature range. Processing at a lower temperature was possible with binder, but the mix viscosity would be very high with high powder loadings. At higher temperatures mixes could be processed with lower loads, but the binder required very low loads, this would result in high errors in viscosity measurements. Temperatures of 60, 90° C for #10, #20 and 125° C for #30, #30ST & #30P were selected for binder systems and powder-binder mixes processing. The piston speeds were selected to give shear rates from 10 to 1000 s^{-1}. With the load and the piston speed data, the viscosities of binder systems and powder-binder mixes were calculated using the standard equations [13] at different shear rates and temperatures. The polymer rich binder system #30 had a larger range of operating temperature, so viscosities were measured at 125, 135, 145 and 155° C temperatures. Other binders were tested in a shorter range. Binder #20 was tested at 70, 75, 80 and 90° C and binder #10 at 50, 55 and 60° C. The 4S, 1A powder mixes with the binders were used for viscosity measurements over these temperature ranges. Thus the viscosity measurements of PIM mixes were done with different powders, loadings, binders, surfactants over a range of shear rates and temperatures.

III. RESULTS AND DISCUSSION

The PIM mixes with binder system #10 were too sensitive to temperature and binder was getting squeezed out during viscosity testing. Hence the data of these mixes was excluded from the analysis. The experimental viscosity data with other binders, mixes was used to calculate the parametric constants of the equation 2 by multiple linear regression (MLR) analysis. These values were same even after Rabinowitch correction (14) application to viscosity for non-Newtonian flow. Using the constant values, the viscosities of the powder-binder mixes were calculated using the model equation at different shear rates, binder contents and temperatures. The graphs of experimental viscosity with calculated viscosity from the model were linear and the fits were very good and within the experimental errors for all the mixes. The values of parametric constants and the correlation coefficients for the fit are presented in table 2. The correlation coefficients for different PIM mixes between the experimental and calculated viscosities were excellent, thus validating the model for viscosity prediction for PIM mixes at different process conditions.

Table 2. Values of parametric constants obtained by MLR analysis of viscosity data using the model equation.

Mix code	constant, a	Sh. rate exp., n	E, kJ/mol	corr. coef.
20	5.1×10^{-11}	0.33	91	0.9738
20S	2.4×10^{-16}	0.31	129	0.9582
20A	1.7×10^{-15}	0.37	123	0.9202
30	11.7	0.57	12	0.9544
30S	7.4	0.52	17	0.9832
30A	3.4×10^{-2}	0.53	34	0.9572
30P	1.21	0.53	21	0.9265
30PS	4×10^{-3}	0.56	40	0.9846
30ST	8.2×10^{-3}	0.55	29	0.9758
30STS	4.6×10^{-3}	0.57	36	0.9316

Iso-Viscosity contour maps

Thus, it is clear that the viscosity of the PIM mixes under various conditions of shear rate, binder content and temperature can be effectively systematized using the model and described by the four constants of the equation, viz. the constant term a, the shear rate exponent n, the critical binder content CBVC, and the energy of activation E. These parametric constants are useful in describing the relative behaviour of different binder systems. However, the non-linearity of the dependence of the viscosity on shear rate, binder content and temperature makes it very difficult to infer or visualize the useful operating regimes of these variables directly from such parametric constants. A graphical technique using contour mapping to visualize the effects of such multiple variables has been explored. Such processing maps are in vogue in other disciplines of material processing [15-16].

Fig. 6(a) -(d) presents the iso-viscosity contours for the four binder systems studied. The viscosity contours are mapped at an interval of 20 Pa.s in the shear rate range of 1-1000 s^{-1}, and the temperature range appropriate for the

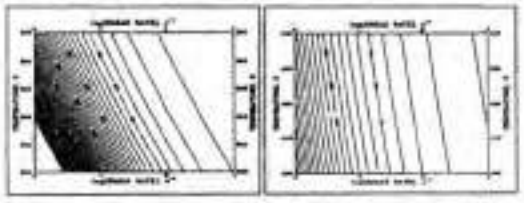

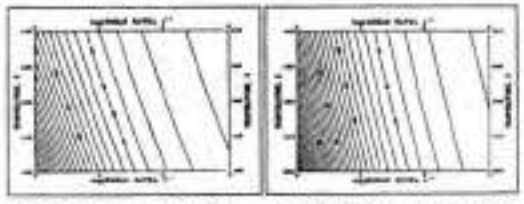

binder. These maps show clearly the higher sensitivity of viscosity of binder #20 compared to that of binder #30 with temperature and shear rate. It is clearly seen from the maps that the surface modifiers, stearic acid or PMMA enlarge the operating regimes of the parameters compared to the basic binder system #30, and the effect is more dramatic with stearic acid than PMMA. Using Weir criterion [17], one can put a limit on the maximum viscosity that is appropriate for successful injection moulding as 1000 Pa.s. in the shear rate range of 1-1000 s^{-1}. It is clear from the figures that all the binders have viscosities satisfying this criterion easily.

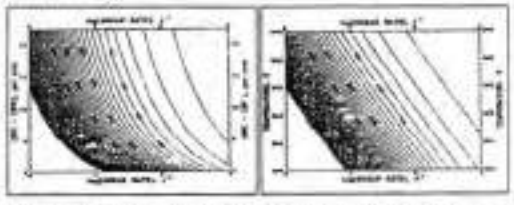

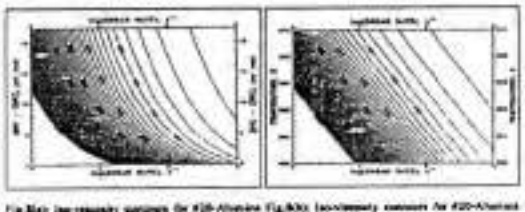

Fig. 7(a)-(b) & 8(a)-(b) represent the iso-viscosity contour maps for the #20 binder system mixed with silica and alumina powders respectively. A comparison of these maps reveals that there is marginal, though not significant, difference between the behaviour of silica and alumina mixes. A similar difference is also noticed between the two powders mixed with #30 binder system.

A comparison of the figs. 6 & 7 shows that once the binders are mixed with a high volume fraction of the powders, the viscosities of the mixes increase by over an order of magnitude. Because of this, the viscosity contour interval had to be changed to 200 Pa.s in figs. 7 & 8,compared to 20 Pa.s in figs. 6. Also, compared to just two controlling parameters, viz. shear rate and temperature, in the case of only binder system, the powder - binder mixes have an additional parameter, viz. the binder content in excess of the CBVC, (BVC-CBVC). As a result, the iso-viscosity contours have been drawn in separate graphs, choosing two parameters at a time. Figs. (a) show the contour map with log(shear rate) and (BVC-CBVC), while figs. (b) use log(shear rate) and temperature. Thus figs. (a) & (b) together represent the viscosity regions with all the three variables. It is also interesting to note from the figures that the temperature and log(shear rate) scale linearly for a given viscosity, while the excess binder and log(shear rate) scale in a non-linear fashion. The iso-viscosity contour maps for #30S mix are shown in fig. 9(a) & (b).

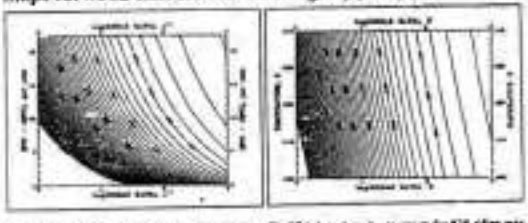

Apart from the Weir criterion referred to earlier, according to which the viscosity of the injection moulding mix may not exceed 1000 Pa.s in the useful operating region, it is also suggested [3,5,6] that the viscosity should not be sensitive to minor changes in the magnitude of operating variables, shear rate, binder level and temperature. The density of the iso-viscosity contour lines in the maps depicts this sensitivity. An examination of the maps in the figs. 7 to 10 reveals that the right-hand upper region is the domain where variations in the viscosity with respect to the variables are the least. That implies that it is ideal to operate at the extreme values of the operating variables. However, practical considerations preclude such a usage. In the case of shear rate, for a given component, it will not be possible to decrease the size of the gate, which determines the shear rate, below a limit. Or, the material may degrade at higher shear rates because of the heat of viscous dissipation. Similarly, high temperature also degrades the binder. In addition, higher temperature leads to higher moulding shrinkages, and hence, not advisable. In terms of the excess binder, one would like to use a level of excess binder just sufficient enough to achieve successful injection moulding, as any excess contributes to shrinkage during debindering.

From the above discussion, it is clear that the Weir criterion of 1000 Pa.s limit on the viscosity can be used to define the minimum values of the variables, shear rate, excess binder and temperature. The upper limit of these variables has to be decided in a qualitative way. Together, they define the region of the parametric variables that is the

best suited for successful injection moulding. Fig. 10 shows the iso- viscosity contour maps for 90, 94 & 98% of CPVC loading of alumina powders in #30 binder. The contours show the senaitivity of viscosity of mix with binder content near the CBVC and also with temperature and shear rate.

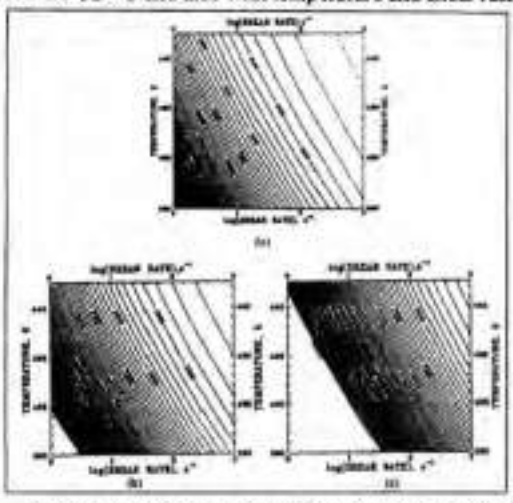

Fig.10. Iso-viscosity contours for #30-alumina mixes with powder loadings of a) 90%, b) 94%, C) 98%.

Use of Iso-viscosity maps for practical Injection moulding

Appropriate viscosity is the key for successful injection moulding of the mix. For this the available machine variables are pressure, temperature and shear rate. The first two factors are limited by the machine, where as the last one by the mould and gate size. Apart from this the viscosity can be varied inherently with the binder content and type, particle size, shape and distribution. If shear rate is fixed by the mould and gate design, machine fixes the pressure limitation, which in turn fixes the viscosity that can flow. Hence one can select the temperature range for processing the mix. If that temperature range is not sufficient for injection of the mix, then the binder content has to be changed. Similarly, one can say whether injection moulding is possible with the binder and estimate whether the machine is suitable from these graphs.

The temperature dependence of the viscosity should be small to avoid sharp viscosity changes that reduce the flow into the chilled cavity and cause undue stress concentrations, cracking and distortion in the moulded components[18]. Large viscosity variation with small shear rate change will lead to a lot of moulding difficulties and result in surface imperfections, uneven filling, unequal densities, high stress levels, warpage and differences in linear shrinkage. It is therefore important to mould at the part of the viscosity vs. shear rate curve where the effect of shear rate is minimal. Such regimes can be identified from these contour maps with ease. In actual moulding conditions these variations are quite large because of small gate and thick moulds.

Thus iso-viscosity contour maps show the viscosity sensitivity to temperature, shear rate and binder content. For smooth operation, the region of distant contours is to be selected, as there the sensitivity to temperature and other terms will be less and so the segregations, stresses can be minimized. Thus these graphs are useful not only for selection of equipment, processing conditions, but also to improve the consistency and quality of product.

IV. CONCLUSIONS

1. The viscosities predicted by proposed combined model have shown excellent correlation with the measured viscosities at shear rates 10 to 1000 s^{-1}, temperatures and binder contents with different low viscosity PIM mixes.
2. Iso-viscosity maps are drawn from the predicted viscosity data of the model to depict the viscosity variation with different parameters. These maps are useful in identifying the PIM processing conditions.

Acknowledgements: Authors deeply acknowledge DRDO, Govt. of India for the financial support and Dr. Dipanker Banerjee, Director, DMRL for his constant encouragement and permission to publish the results.

V. REFERENCES

1. R.M.German: Reviews in Particulate Materials, 1(1993)109.
2. M.J.Edirisinghe, H.M.Shaw and K.L.Tomkins: Ceramic International, 18(1992)193.
3. B.C.Mutsuddy: Key Engineering Materials, vols. 56-57, Trans Tech Publications, Switzerland, (1991)265.
4. M.J.Edirisinghe and J.R.G.Evans: Brit. Ceram. Trans. J., 86(1987)18.
5. M.J.Edirisinghe and J.R.G.Evans: Material Science and Engineering, A, 109(1989)17.
6. M.J.Edirisinghe and J.R.G.Evans: J. of Mater. Sci., 22(1987)269.
7. Y. Li, B. Huang and X. Qu: Powder Metallurgy, 42(1)(1999)86.
8. T. Honma, H. Masaki and S. Wada: Proc. of 3rd Int. Symp. on Ceramic materials and Components for Engines, Ed. Tennery, V.J: Am.Cer.Soc. Inc., (1989)42.
9. B.C.Mutsuddy and L.R.Kahn: Advances in ceramics, vol. 9(1984)251.
10. J.J.Reddy, "Rheology of powder injection moulding mixes with low viscosity binders" 1998, Ph.D Thesis,IIT, Bombay, Mumbai, India.
11. J.J.Reddy, M.Vijayakumar, T.R.Rama Mohan and P.Ramakrishnan: J. of Euro. Cer. Soc., 16(1996)567.
12. J.J.Reddy: Powder Metallurgy, 39(1996)281.
13. Irvin I.Rubin: Injection moulding theory and practice, John Wiley & Sons Inc., Newyork, USA, (1972)214.
14. B.Rabinowitsch: Z. Physik. Chem., A, 145(1929)1.
15. Y.V.R.K.Prasad: Indian Journal of Technology, 28(1990)435.
16. B.V.R.Bhat, Y.V.R.K.Prasad, Y.R.Mahajan: Key Engineering Materials, vol. 104-107(1995)241.
17. F.E.Weir: SPE Trans., 3(1963)32.
18. M.J.Edirisinghe and J.R.G.Evans: J. Mater. Sci., 22(1987)2267.

Author Index

Altekar R.M. 92
Arvind Kumar N. 102

Bagchi T.P. 1, 43, 102
Basak U. 92

Chakraborty A. 64

Dash R.R. 55 , 137

Gnanamoorthy R. 182
Godiwalla Kersi M. 188
Gopinath K. 182
Govindarajan N. 182

Hansda K.L. 55, 137

Kamat S.V. 64,
Krishna Rao K. 34
Krishnarao R.V. 151

Mahanty Debasis 188
Mahata Tarasankar 175
Majumdar S. 92
Malewar Ravindra 1, 43
Mitra R. 64,
Miyahsita Y. 182
Mutoh Y. 182

Pandey V.D. 92

Rajiv N. 182
Rama Mohan T.R. 202
Ramachandran R. 92
Ramakrishnan P. 202
Ramarao V.V. 151
Ray Ashok K. 188
Ray K.K. 64
Reddy Janardhana J. 202
Roy Nilima 188

Sarma Bijoy 1, 43, 102
Schulz Gunther 34
Sharma Beant Prakash 175
Sheikh I.H. 92
Singh M.P. 55, 137
Singh R.J. 55, 137
Subrahmanyam J. 151

Vijay Kumar M. 202